

In-Situ Seismic and Ex-Situ Laboratory Analysis

from

Expedition 364: Chicxulub Impact Basin Peak Ring Hole M0077a

by

Christopher Gordon Nixon

A thesis submitted in partial fulfillment of the requirements for the degree of

Doctor of Philosophy

in

Geophysics

Department of Physics

University of Alberta

© Christopher Gordon Nixon, 2022

## **Abstract**

Although craters with central peak ring morphology are common throughout the solar system, intact examples are rare terrestrially. The central rebound in complex craters is attributed to compressional rebound, but the mechanism that causes these uplifts to form a peak ring above a certain threshold has only been hypothesized. IODP/ICDP Expedition 364 sought to elucidate the mechanisms behind peak ring formation by conducting offshore drilling directly into the Chicxulub Impact Basin's peak ring. By directly sampling 700 m of peak ring impactite core, analysis of Expedition 364 data largely supports the dynamic collapse model of peak ring formation. The work here builds further understanding of the structure in terms of its seismic responses via an in situ vertical seismic profile (VSP) and ex situ by laboratory measurements ultrasonic velocity measurements on representative core samples.

Analysis of the downgoing VSP seismic wavefield indicates that the peak ring impactites display both elevated attenuation and anomalously low seismic wavespeeds relative to that expected for the original granitic rock. These observations are attributed to damage from the hypervelocity impact that is quantified via Grady-Kipp damage parameters that depend on the deficits in the elastic moduli relative to the intact, pore free material. These suggest that the shear elastic moduli have been affected more significantly than the bulk moduli, and this may have implications for the original location of target materials at the time of impact.

The VSP data are further processed to isolate the origin of seismic reflectivity within the structure to assist in calibration of the depths to reflecting events in the surface seismic profiles. The high amplitude seismic reflector, originally interpreted to be the K-Pg boundary, is more complicated as it results from seismic tuning between between an upper dense and high velocity carbonate cap, a middle low velocity layer of highly altered impact breccia, and the lowermost melt and highly damaged peak ring granitoids. As the marine environment is inseparable from the sedimentary cap and hydrologically altered impactites below,

interpretation is discussed regarding hydrological considerations, which may prove extremely relevant in Martian exploration.

A variety of petrophysical characterizations of candidate breccia, melt, and damaged granitoid as well as P- and S-wave velocity measurements were made. All these materials are generally porous with porosities more than 0.1. However, Hg-injection porosimetry and scanning electron microscopy reveal that the breccia and melt pore space is equant with well-defined diameters of  $\sim 1 \mu\text{m}$  while the pore space in the granitoids consists of microcracks with a continuum of apertures from  $\sim 1 \mu\text{m}$  to 10 nm. Interpretation of the petrographic results suggests that a niche for microbial life may exist within crystalline impactites.

Further, the ultrasonic velocity determinations, carried out under confining pressure, indicate non-linear and heterogeneous relations between the wave speeds and pressure. Poisson's ratio at both seismic and sonic frequencies are analyzed within the impactites. These values, too, are anomalously high when compared to similar terrestrial lithology. Taken together, and incorporating thin section analysis, these properties show an extensive and interconnected pore network and attempts to invert velocity data for pore structure have been unsuccessful with existing effective medium theories. This likely occurs because most rock physics theoretical models that all rely on dilute and isolated pores, which is not the case in the highly damaged granitoids.

## Dedication

This dissertation is dedicated to Matheus Nixon (Figure 0.1), the most intelligent, affectionate, adventurous, and talented little cat I have ever met. I will never forget the time you brought me home a live muskrat and I hope you are still getting shoulder rides in kitty heaven.



*Figure 0.1. Matheus Nixon, legendary cat (1994-2016).*



## **Acknowledgements**

Without the tireless support of my wife, Jenise Finlay, parents, Doug & Carol Nixon, and primary care physician, Michael Kordyban, this academic journey would not have been possible. Thank you for being my foundation.

My story of inspirational mentors begins with George Mentz teaching the Outdoor Education program at my junior high school. This man gave me and hundreds of other students an outstanding foundation in outdoor skills and stimulated in me a lifelong passion for exploration and alpine sports. Next, there was a man teaching for Edmonton Public Schools who should be paid at least thrice what he is currently earning: Phil Goldthorpe was my instructor for grade 11 & 12 physics; his love for physics is contagious, and I have not been able to cure myself of it to this very day. Then, in my undergraduate studies at Grant MacEwan, Orla Aaquist introduced me to research, going far beyond his lecturing duties before passing the torch to Jim Pinfeld, a truly charismatic faculty member at the University of Alberta. Jim's chronic curiosity and multidisciplinary talent inspired me, and I was extremely fortunate to be introduced to the world of particle physics through his lens. Particle/nuclear physics will always be my first love, but when things started getting serious, I realized that my passion for the outdoors was going to be a problem.

Although graduate school has been the most difficult and stressful experience of my life, I would probably still do it again. Doug Schmitt (Figure 0.2, right) has been a remarkable mentor to me, believing in me, and giving me some of the most amazing experiences of my life. His mentorship goes well beyond academics, coaching me on the non-technical aspects of both science and life. Doug's compassion for and devotion to his students is unparalleled; when my health took an abrupt nosedive in 2017, he held nothing back in accommodating my new reality. This included talking sense into me all the times

I wanted to quit. No matter where life takes me, I will never forget how far above and beyond Doug went to help me succeed. Thank you, Doug Schmitt, and thank you even more for believing in me.



*Figure 0.2. University of Alberta seismic acquisition team, IODP/ICDP Expedition 364. From left: Randy Kofman, Chris Nixon, and Doug Schmitt (2016).*

Finally, without Randy Kofman (Figure 0.2, left), none of my research would have been possible. Randy is easily the most talented and hardworking researcher I have ever met. Randy, I cannot thank you enough for all the help you supplied over the years we have worked together. They really should be paying you more.

## Table of Contents

Abstract.....	ii
Dedication.....	iv
Acknowledgements.....	v
Table of Contents.....	vii
Lists .....	xiv
Tables.....	xiv
Figures.....	xv
Equations .....	xix
Definitions.....	xxii
Acronyms .....	xxii
Symbols.....	xxiii
Glossary of Terms.....	xxiv
1. Introduction .....	1
1.1 Motivation.....	2
1.2 Confirmed Canadian Impact Structures over 50km.....	6
1.2.1 Manicougan Lake .....	6
1.2.2 Charlevoix Impact Structure .....	8
1.2.3 Sudbury .....	9
1.2.4 Clearwater Lakes.....	10
1.3 Yucatán Geology .....	12

1.4	Expedition 364 Publications.....	16
1.4.1	Physical Properties.....	16
1.4.2	Petrography .....	18
1.4.3	Impact Basin Formation.....	20
1.4.4	Post Impact Hydrothermal System .....	21
1.4.5	Climate Change .....	22
1.4.6	Fossil Record .....	22
1.5	History of Vertical Seismic Profiles .....	25
2.	Theory.....	29
2.1	Seismic Waves.....	29
2.1.1	Elastic Parameters.....	29
2.1.2	Elastic Wave Propagation .....	35
2.2	Vertical Seismic Profiling.....	41
2.2.1	Common VSP Geometries.....	41
2.2.2	Zero-Offset.....	43
2.3	Rock Physics .....	46
2.3.1	Isotropic Polycrystalline Wavespeeds.....	46
2.3.2	Effects of Porosity .....	50
2.4	Hypervelocity Impacts as a Geological Process .....	55
2.4.1	Formation.....	55
2.4.2	Classification of Craters.....	58

2.4.3	Dynamic Collapse Model.....	61
2.5	Shock Metamorphism.....	63
2.5.1	Shock Waves.....	63
2.5.2	Hugoniot-Rankine Conditions.....	63
2.5.3	Experiments in Shocked Mineralogy.....	65
2.6	Segue.....	75
3.	Assessment of Rock Damage Using Seismic Methods: Wave Speeds and Attenuation from Borehole Measurements in the Chicxulub Impact Structure.....	77
3.1	Abstract.....	77
3.2	Introduction.....	78
3.3	Geological Background.....	79
3.4	Vertical Seismic Profile Acquisition.....	81
3.5	Data Processing.....	83
3.5.1	Wavelet Arrival.....	84
3.5.2	Wavefield Separation.....	85
3.5.3	Windowing.....	87
3.5.4	Spectral Ratios.....	87
3.6	Results and Discussion.....	89
3.7	Conclusion.....	91
4.	Borehole Seismic Observations from the Chicxulub Impact Drilling: Implications for Seismic Reflectivity and Impact Damage.....	92
4.1	Introduction.....	94

4.2	Background .....	97
4.2.1	Chicxulub Structure.....	97
4.2.2	Expedition 364 Geology .....	100
4.2.3	Expedition 364 Physical Properties.....	102
4.3	Methods.....	108
4.3.1	Downhole Sonic logs .....	108
4.3.2	VSP Acquisition during Expedition 364 and raw profiles.....	108
4.3.3	Analysis of Horizontal Components .....	111
4.3.4	Determination of Wave Speeds .....	112
4.4	Results.....	115
4.4.1	VSP and log derived wave speeds.....	115
4.4.2	Intrinsic wave speeds of undamaged peak ring materials.....	115
4.5	Discussion.....	118
4.5.1	Nature of the K-Pg reflection event .....	118
4.5.2	Relationships of Velocities .....	119
4.5.3	Assessment of Damage in Peak Ring Materials .....	123
4.5.4	Characterization of block sizes.....	126
4.5.5	Implications for future extraterrestrial seismic investigations.....	128
4.6	Conclusions .....	129
5.	Petrophysical properties of Chicxulub Peak Ring Shocked Granitoids and Impact Melts .....	132
5.1	Abstract.....	132

5.2	Introduction .....	133
5.2.1	Damage and physical properties.....	136
5.2.2	Structural complications .....	137
5.3	Methods & Results.....	139
5.3.1	Acquisition.....	139
5.3.2	Porosimetry.....	141
5.3.3	Ultrasonic Wavespeeds.....	146
5.4	Discussion.....	154
5.4.1	Character of Pore Space.....	154
5.4.2	Damage Parameters.....	155
5.4.3	Elastic Moduli.....	158
5.4.4	Pore characterization implications .....	159
5.5	Conclusion.....	161
6.	Conclusion.....	163
6.1	Future Work.....	163
6.1.1	Attenuation .....	163
6.1.2	Pore Structure Inversion.....	166
6.1.3	Thin Sections .....	168
6.2	Concluding Remarks.....	171
	Permissions .....	174
6.3	Data Sets .....	175

7. Works Cited.....	176
7.1 Articles .....	176
Appendix .....	214
Appendix A - Supplementary Methods for Chapter 3 .....	214
Software Package.....	214
Windowing .....	214
Trouble region.....	215
Spectral Decay.....	217
Variable band .....	218
Slope Matrix .....	220
Q-factor matrix.....	220
Results.....	222
Appendix B - Supplementary Methods for Chapter 4 .....	224
Vertical Seismic Profiling (VSP) .....	224
Acquisition Details. ....	227
Processing of Vertical Component.....	230
Horizontal Components and Processing.....	232
Additional Information.....	234
Acknowledgements.....	235
Appendix C - Supplementary Methods for Chapter 5.....	236
Ultrasonic Processing.....	236



Geological details.....	242
Appendix D - Publications.....	244
Peer Reviewed Publications (First Author) .....	244
Peer Reviewed Publications (Contributing Author).....	245
Peer Reviewed Publications (Contributed).....	246
Technical Reports.....	246
Conference Abstracts (First Author) .....	247
Conference Abstracts (Contributing Author).....	248
Appendix E - IODP 364 OSP Logo Contest Entry .....	249

## Lists

### Tables

2.1. Elastic parameter Identities. ....	35
2.2. Kuster Toksoz geometric weighting factors. ....	54
2.3. Categories of shock metamorphism. ....	65
2.4. Discoveries of shock effects in quartz. ....	67
2.5. Feldspar shock effects ....	71
2.6. Dunite shock effects. ....	72
2.7. Basalt shock effects. ....	73
4.1. Primary constituent minerals elastic moduli. ....	116
5.1. Summary of petrophysical measurements, M0077a samples. ....	143
5.2. Physical properties of Gassman adjusted samples. ....	151
5.3. Elastic moduli and density for primary minerals in M0077a samples. ....	153
A 1. Interpreted geological intervals. ....	228
A 2. Details of seismic acquisition. ....	230
A 3. Block velocity model. ....	232
A 4. Correlation coefficient values, synthetic vs. real. ....	235
A 5. Acronyms used in chapter 5. ....	235
A 6. Sample depths and geological interpretations. ....	242
A 7. Mineralogy from Expedition 364 Onshore Science Party. ....	243

## Figures

0.1. Matheus Nixon.....	iv
0.2. University of Alberta Seismic Acquisition Team, Expedition 364.....	vi
1.1. Barringer Crater.....	1
1.2. Crater disparity.....	4
1.3. Confirmed Impact Craters worldwide.....	5
1.4. Major confirmed impact structures of the Canadian Shield.....	7
1.5. Yucután Peninsula surficial geology.....	13
1.6. Yucután Peninsula core correlation cross sections.....	15
1.7. Symbolic images from Expedition 364.....	16
1.8. Schrödinger impact crater.....	20
1.9. Early synthetic VSP.....	27
2.1. Bulk modulus definition for a sphere.....	30
2.2. Young’s modulus definition for a rod.....	31
2.3. Poisson’s ratio definition in a rod.....	31
2.4. Shear modulus definition.....	33
2.5. Relationship between Poisson’s and $V_p/V_s$ ratios.....	34
2.6. Elastic Snell’s law.....	36
2.7. Reflection and transmission through an impedance contrast.....	37
2.8. Spectral ratios slope illustrated.....	40
2.9. Horizontal vs Vertical seismic acquisition geometry.....	41
2.10. Commonly utilized VSP geometries.....	42
2.11. Simple seismogram for a 3-layer model.....	43

2.12. Primary VSP processing steps.....	45
2.13. Polycrystalline Voigt limit.....	47
2.14. Polycrystalline Reuss limit.....	47
2.15. Impactite Venn diagram.....	55
2.16. Initial shock compression phase.....	56
2.17. Peak pressure isobars during compression phase.....	57
2.18. Zones of impact effects.....	58
2.19. Simple crater cross section.....	58
2.20. Lunar Impact, March 17th, 2013.....	59
2.21. Complex crater continuum.....	59
2.22. Tycho Crater, Luna.....	60
2.23. Multi-Ring Impact Basins.....	61
2.24. Dynamic collapse model.....	62
2.25. Hugoniot-Rankine equation of state for Quartz.....	64
2.26. Analogy between hole M0077a and shocked rock physics.....	75
3.1. M0077a location compared to previous seismic surveys.....	79
3.2. VSP experimental configuration.....	82
3.3. Peak ring portion of VSP shown after pre-processing.....	83
3.4. VSP physical properties.....	84
3.5. P-wavelet windowing.....	86
4.1. Location of Chicxulub structure.....	95
4.2. Peak ring cross sections.....	98
4.3. Simplified lithostratigraphy compared to physical properties.....	104

4.4. Details of physical properties associated with the K-Pg reflection.....	106
4.5. Raw vertical component VSP record.....	109
4.6. Separated upward-going wavefield.....	110
4.7. Optimization of Shear Wave Arrivals.....	111
4.8. Wave speeds determined from VSP, Sonic logging, and modelling.....	113
4.9. Observed and modelled seismic reflection responses.....	114
4.10. VP versus VS cross-plots.....	120
4.11. Poisson’s ratio for various lithologies.....	121
4.12. Vp/Vs ratio in the Suevitic Low Velocity Zone.....	123
4.13. Damage parameterization of peak ring granitoids.....	127
5.1. Chicxulub Impact Crater location.....	138
5.2. Sampling points in M0077a.....	139
5.3. Helium pycnometry results.....	142
5.4. Mercury injection porosimetry.....	145
5.5. Ultrasonic confining pressure experimental configuration.....	146
5.6. Sample 155 waveform windowing.....	148
5.7. Confining pressure wavespeed curves.....	150
5.8. Grady Kipp damage parameters under confining pressure.....	157
5.9. Elastic moduli ranges observed under confining pressure.....	158
5.10. Normalized wavespeed curves under confining pressure.....	160
5.11. Microscopy on samples representative of lithology.....	161
6.1. Peak amplitude loss in the VSP of M0077a.....	163
6.2. Q matrix, using variable band method.....	164

6.3. Natural filtering layer at 936 mbsf.....	165
6.4. Kuster Toksoz pore aspect ratio inversion.....	167
6.5. Triplanar thin sections prepared for EBSD analysis.....	170
A 1. Effects of windowing on one particular trace at 698 m depth.....	215
A 2. Windowing performed on the full VSP.....	216
A 3. Spectral decay.....	217
A 4. Fixed band best fit logarithmic spectral ratio plots.....	218
A 5. Variable band best fit logarithmic spectral ratio plots.....	219
A 6. Logarithmic spectral ratio matrices.....	221
A 7. Q factor matrices.....	222
A 8. Q factor compared with lithostratigraphy.....	223
A 9. Geometry of zero-offset VSP.....	225
A 10. Major VSP processing steps.....	226
A 11. Vertical component processing flow.....	229
A 12. VSP vertical component processing.....	231
A 13. Raw radial and tangential components.....	233
A 14. Horizontal components processing flow.....	234
A 15. Advancing sweep wavelet windowing and cross correlations.....	237
A 16. P and S windowed wavelet averages.....	238
A 17. Fixed window wavelet windowing and cross correlations.....	239
A 18. Cross correlation lag times.....	240
A 19. Velocity results for sample 135.....	241
A 20. Onshore Science Party T-Shirt Logo Contest Entry.....	249

## Equations

2.1. Bulk Modulus Definition.....	29
2.2. Bulk Modulus for a Sphere Under Confining Pressure.....	30
2.3. Young's Modulus Definition.....	31
2.4. Poisson's Ratio Definition.....	31
2.5. Lamé's First Parameter.....	32
2.6. Lamé's second Parameter.....	33
2.7. Isotropic Hooke's Law.....	33
2.8. Isotropic P-Wavespeed.....	33
2.9. Isotropic S-Wavespeed.....	34
2.10. Elastic Snell's Law with Ray Parameter.....	36
2.11. Seismic Impedance.....	36
2.12. Normal Incidence Reflection Coefficient.....	37
2.13. Normal Incidence Transmission Coefficient.....	37
2.14. Definition of Quality Factor.....	39
2.15. Anelastic wavefront decay in the plane-wave approximation.....	39
2.16. Spectral Ratios to Q relationship.....	39
2.17. Linear best fit Q estimate.....	39
2.18. Voigt theoretical isotropic upper limit for bulk modulus of a mineral.....	46
2.19. Voigt theoretical isotropic upper limit for shear modulus of a mineral.....	46
2.20. Reuss theoretical isotropic lower limit for bulk modulus of a mineral.....	47
2.21. Reuss theoretical isotropic lower limit for shear modulus of a mineral.....	47
2.22. Strain/Compliance matrix relation.....	48

2.23. Voigt-Reuss-Hill average of bulk modulus.....	48
2.24. Voigt-Reuss-Hill average of shear modulus.....	48
2.25. Isostress polycrystalline limit of bulk modulus.....	48
2.26. Isostress polycrystalline limit of shear modulus.....	48
2.27. Isostrain polycrystalline limit of bulk modulus.....	49
2.28. Isostrain polycrystalline limit of shear modulus.....	49
2.29. Polycrystalline Bulk Density.....	49
2.30. Porosity as a function of density.....	50
2.31. Porosity as a function of water saturation.....	50
2.32. Gassmann's Shear Modulus Relation.....	52
2.33. Gassmann's Saturated Bulk Modulus Relation.....	52
2.34. Gassmann's Dry Bulk Modulus Relation.....	52
2.35. Kuster-Toksoz bulk modulus relation.....	53
2.36. Kuster-Toksoz shear modulus relation.....	53
3.1. Spectral Ratios to Q relationship.....	87
3.2. Linear best fit Q estimate.....	88
4.1. Normal Incidence Reflection Coefficient.....	107
4.2. Voigt Reuss bulk modulus limits.....	115
4.3. Voigt Reuss bulk modulus limits.....	116
4.4. Voigt Reuss P-wavespeed limits.....	116
4.5. Voigt Reuss S-wavespeed limits.....	116
4.6. Aporous polycrystalline density.....	116
4.7. Poisson's ratio and seismic wavespeed relation.....	119



4.8. Grady Kipp P-damage parameter.....	125
4.9. Grady Kipp S-damage parameter.....	125
4.10. Grady Kipp bulk damage parameter.....	125
5.1. Helium pycnometry equation.....	142
5.2. Porosity as a function of density.....	142
5.3. Washburn’s equation.....	144
5.4. Lenormand crack width.....	144
5.5. Dry shear modulus.....	151
5.6. Dry bulk modulus.....	151
5.7. Gassmann scaling factor.....	152
5.8. Saturated bulk modulus.....	152
5.9. Saturated shear modulus.....	152
5.10. Saturated S-wavespeed.....	152
5.11. Saturated P-wavespeed.....	152
5.12. Saturated density.....	152
5.13. Theoretical Voigt-Reuss-Hill bulk modulus.....	153
5.14. Theoretical Voigt-Reuss-Hill shear modulus.....	153
5.15. Grady Kipp compressional-wavespeed damage parameter.....	156
5.16. Grady Kipp shear-wavespeed damage parameter.....	156
A 1. Spectral Ratios to Q relationship.....	220
A 2. Linear best fit Q estimate.....	220

## **Definitions**

### **Acronyms**

**CCF** -Cross-Correlation Function

**DEM** – Differential Effective Medium

**F-K** – Frequency/Wavenumber

**ICDP** – International Continental scientific Drilling Program

**IODP** – International Ocean Discovery Program

**K-Pg** – Cretaceous/Paleogene

**LFR** – Low Frequency Reflector

**MSCL** – Multi Sensor Core Logging

**OSP** – Onshore Science Party

**PDF** – Planar Deformational Features

**PETM** – Paleocene/Eocene Thermal Maximum

**PF** – Planar Features

**STUC** – Suevite/Transitional Unit Contact

**USD** – United States of America Dollars

**VSP** – Vertical Seismic Profile

## **Symbols**

$D_p$  – Grady-Kipp P wave damage parameter.

$D_s$  – Grady-Kipp S wave damage parameter.

$E$  – Young’s Modulus

$G_a$  – Giga annums (ago)

$GPa$  - Gigapascals

$K$  – Bulk Modulus

$Kyr$  – kilo years

$M$  – P-Modulus

$m$  - mass

$Ma$  - Mega annums (ago)

$mwsf$  - meters wireline sea floor

$mbsf$  – meters below sea floor

$MPa$  - Megapascals

$P$  – pressure

$R$  – reflectivity coefficient

$Q$  – Quality factor

$V_p$  - Compressional wave group velocity

$V_s$  - Shear wave group velocity

$\lambda$  – Lamé’s First Parameter

$\mu$  – Shear Modulus

$\rho$  – density

$\nu$  - Poisson’s Ratio

## Glossary of Terms

**Acoustic fluidization** - A proposed mechanism where an aggregate of solids may behave like a fluid due to intense vibrations.

**Adakite** – Igneous rocks with geochemical characteristic which suggest formation by partial melting.

**Aporous** – A material with porosity exactly equal to zero.

**Auxetic** – A material which becomes more narrow under uniaxial compression (negative poisson's ratio).

**Borehole** – North American terminology for a geologically drilled hole.

**Bulk Density** – Overall combined density of an object (volume divided by mass).

**Cataclasite** - Cohesive granular fault zone, also known as comminution zone.

**Cenote** – Karstic sinkhole in the Yucatán peninsula, popular for swimming.

**Cenozoic** – Current geological era on Earth, beginning 66 Ma.

**Chondrite** – Trace burrowing fossil which resembles the roots of a plant. Origin currently unknown.

**Compliance** – *Flexibility* i.e. inverse of stiffness. Generally describes a tensor in the context of elasticity.

**Cratonic** – Geologically stable and ancient interior portion of continental crust.

**Damage Parameter** – A unitless number between 0 and 1 describing how close to total failure a solid is.

**Dynamic Collapse Model** – A proposed mechanism for peak ring formation in complex impact craters where the central uplift collapses down and outward while the transient crater rim simultaneously collapses inward.

**Elastic** – A mechanical process where energy is perfectly converted between 2 forms and none is lost to friction, noise, etc.

**Granitoid** – Impactites in M0077a which began life as granite.

**Hole** - European terminology for a geologically drilled hole.

**Hookean (linear elastic)** - A material whose restoring force is proportional to the displacement

**Huygen-Fresnel Principle** – Every point on a wavefront is itself a point source of a new wavefront, thereby enabling diffractive properties of waves.

**Ichnological** – Trace fossils, such as tracks or burrows.

**Impact Basin** – A larger impact structure i.e. complex crater.

**Impact Crater** – A smaller impact structure i.e. simple crater.

**Impact Structure** – Structure left behind by hypervelocity impact.

**Isostrain** – Uniform strain throughout a material, can be accomplished with layers parallel to direction of stress.

**Isostress** - Uniform stress throughout a material, can be accomplished with layers orthogonal to direction of stress.

**Nested Melt Cavity Hypothesis** - A proposed mechanism for peak ring formation in complex impact craters where a central melt sheet is contained by an unmelted ring of shocked material, which results in the central melt sheet tunneling downward.

**Noachian** – Geological age of Mars corresponding to the heavy bombardment, roughly 4.1 to 3.7 Ga.

**Palynology** – The study of palynomorphs, which are defined as organic walled fossils between 5-500  $\mu\text{m}$ .

This does not include silicious or carbonate shelled organisms.

**Peak Ring** – Annular central mountain structure within a complex crater.

**Petrophysics** – The study of physical and chemical properties of rocks with a focus on interaction with fluids.

**Poisson Solid** – A solid with equal 1<sup>st</sup> and 2<sup>nd</sup> Lamé parameters, i.e. a Poisson's ratio of 0.25.

**Polymict** – Containing angular clasts of different lithologies.

**Porosity** – Void space within a material, which can in theory range from 0 to  $0.\overline{999}$

**Pycnometry** – Use of a gas to determine skeletal density.

**Shocked** – A material which has experienced a shockwave, usually on the order of GPa

**Sieche** – A long standing wave within a body of water where water piles up on one end.

**Siliciclastic** – Sedimentary rocks composed of weathered terrestrial grains and non-carbonate in origin.

**Stiffness** – *Resistance to strain* i.e. inverse of compliance. Generally describes a tensor in the context of elasticity.

**Stress**. – Force applied to material, divided by area.

**Strain** – Deformation of material under stress.

**Strain-Energy Function** – A function which relates stored elastic energy to the strain gradient.

**Suevite** – Impactite breccia which contains impact melt. The term is somewhat controversial.

**Tektites** – Small glassy impact ejecta, often aerodynamically shaped during flight.

**Ultra-Cataclasite** – Cataclasite where matrix takes up greater than 90% of total volume.

**Wavespeed** – Group speed of P or S wave.

## 1. Introduction

Despite the obvious existence of craters on the moon, impact cratering as a continuing and significant geological process on the earth was slow to be accepted in the scientific community. Barringer's insightfully correct identification of Coon Mountain, Arizona (Figure 1.1) as the site of a hypervelocity impact in 1905 was largely rejected up to the time of his death in 1929; and it took nearly two generations before a forward-thinking young graduate student discovered naturally occurring coesite, a high pressure polymorph of quartz, in the rocks at the rim of Barringer's crater (Chao et al., 1960). Fortunately, nuclear weapons had been invented, and underground test sites made holes very similar to suspected impact craters (Short, 1965). Looking at the affected minerals microscopically yielded direct mineralogical evidence of the metamorphic effects of shock waves and spurred a major shift of paradigm (Short, 1970). The parallel fields of geology, shock physics, and astronomy had been successfully united by the verification of Barringer's crater hypothesis, and the race to discover shocked minerals and impact craters on Earth had begun.

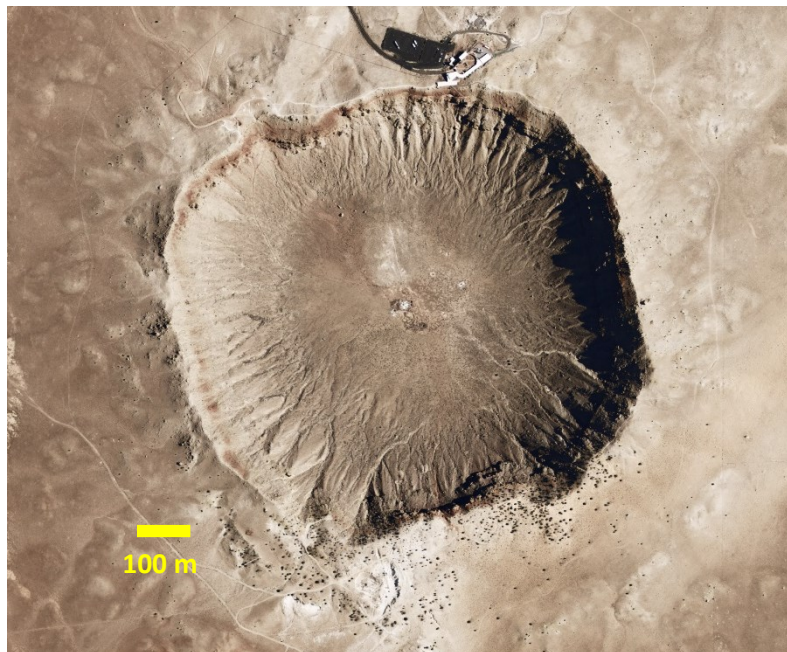


Figure 1.1. Barringer Crater, Arizona. Image credit: NASA.



## 1.1 Motivation

Why study impact structures? There was perhaps a time when scientists could just say “because we can learn things”. However, the age of scientific dilettantes is diminishing, and researchers are increasingly under pressure to show practical applications to secure funding. However, if you are reading this, you are probably a scientist, and I don’t need to convince you of economic benefit to keep your interest.

Although impact cratering is thought to be the most important geological process in our solar system, it remains the most poorly understood. The Moon’s entire surface has been reworked by impacts and continues to be reworked by micrometeorites in the present day (Heiken et al., 1991). Even the existence of the Moon is thought to be from a giant collision between early Earth and another planet, similar in size to Mars (Canup & Asphaug, 2001; Lee et al., 1997). Earth’s extensive water inventory is suspected to have been brought in extra-terrestrially (Albertsson et al., 2014; Robert, 2001), and some researchers suspect the organic building blocks for early life were similarly seeded (Flynn et al., 2003; Hayatsu et al., 1977). Looking beyond Earth, it is easy to see impact effects within the Solar System, with obvious cratering on every rocky planet and the majority of moons (Michel & Morbidelli, 2007; Zahnle et al., 2003). According to the nebular hypothesis, even the existence of planets whatsoever is dependent on inelastic collisions between growing objects in young planetary nebulae (Chiang & Youdin, 2010).

Currently, 190 terrestrial impact structures have been confirmed with further 100 more being potential candidate structures (Spray, 2021). Although craters tend to be circular, not all circles are craters.

Conversely, owing to tectonic and erosional deformation, older impact scars may not be circular at all.

Therefore, unequivocal proof accepted for verifying a crater includes the existence of shatter cones, planar deformational features, or high-pressure mineral phases. While this vetting process is necessary, it can stall confirmation of likely craters due to unsuitable target lithology (eg. Bow City, Alberta (Glombick et al., 2014; Wei Xie, 2014)) or where only remote sensing is available. Given the heavy bolide

bombardment thought to have occurred during the Hadean/Archean eons, it is likely a vast repository of impact structures remains buried within crystalline basements.

While one may seek to confirm a crater by directly sampling via costly drilling, or by improving lithological identification methods on soft, low quartz target lithology, many easy-to-identify surface craters likely remain hidden in plain sight. It is no secret that economic prosperity is directly linked to scientific funding, and impact research is no exception. If one compares confirmed craters to regional wealth within a continent, it becomes apparent that many craters could remain undiscovered within poor regions of the world (Figure 1.2). Europe leads confirmed impact structure density, likely owing to a combination of heavy investment in research and high population density. Then, if we assume crater and wealth distribution are uncorrelated, global crater distribution is homogenous, and Europe's confirmed crater density is near the asymptotic limit, then back of the envelope calculations suggest more than 300 impact structures remain to be discovered with currently available methods, not including Antarctica.

Surficial crater morphology is fairly well understood, with enough observable impact structures in the solar system to develop statistical relations between diameter, depth, gravity, lithology, and complex crater features (Güldemeister et al., 2015). However, knowledge on the bulk of the structure hidden below the surface remains limited to remote sensing and geophysical surveys, as well as pricking the surface for drill sampling on Earth. As such, our knowledge of impact structure is extremely limited and is heavily reliant on modelling. Additionally, while knowledge of shocked mineralogy is steadily improving, information of their elastic properties is nearly nonexistent. This is primarily due to the lack of large mineral grains in these exotic polymorphs. With direct measurements unavailable, the alternative is to assess how rocks are elastically altered by impact events and then invert backwards to

constituent minerals. Unfortunately, taking this route would require extensive sampling in order to constrain the unknown elastic parameters in shocked minerals.

### Regional Wealth vs. Confirmed Impact Structure Density

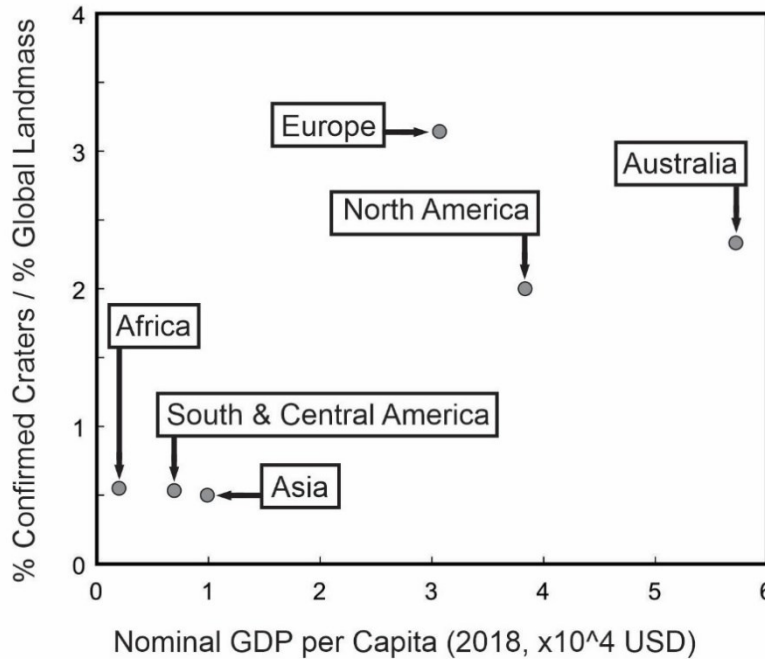


Figure 1.2. Crater Disparity. Confirmed impact structure density appears to correlate with regional wealth. Data sources: Impact Structures, Earth Impact Database (Spray, 2021); Population, United Nations (DESA, 2019); Economic, International Monetary Fund (Long & Ascent, 2020).

The world is moving toward a second space race and with it will come a new golden age of geophysics. The Earth has been thoroughly geophysically investigated, with scientists seeking out deeper and more specialized niches for further discovery. However, other bodies in our solar system have merely been scratched, with the bulk of data originating from remote sensing. Future discovery on heavily cratered bodies will be inseparable from shock effect. Construction projects on the Moon will likely take place in areas of low elevation with smooth topography, i.e., impact basins. Similarly owing to their low initial elevation, sedimentary impact basins will be an important target of research in the search for water and life on Mars. On Earth, it is difficult to delineate impact structures from interactions with water, and understanding these processes here can help in our search for evidence of ancient water elsewhere. Additionally, hydrological activity is the main process driving mineral concentration into ore bodies, and

better understanding of these processes within impact structures will help unlock the vast resource potential beyond Earth's atmosphere.

Earth's ecosystem is fragile, yet it has endured repeated hypervelocity impacts throughout its lifetime (Figure 1.3). These impacts often affected the ecosystem, and our own civilization is equally vulnerable.

Bolides will strike Earth again; it is only a question of when. Better understanding the risk posed by a candidate impactor and mitigation measures should therefore be a top priority on Earth and in future settlements throughout the solar system.



*Figure 1.3. Confirmed Impact Craters worldwide. Figure credit: Earth Impact Database. Maps data: Google.*

## 1.2 Confirmed Canadian Impact Structures over 50km

Canada is a vast country with equally vast resources. The Canadian shield is no exception, with 3 (4 for a certain interpretation of size) of the world's 15 largest confirmed impact structures located within a 600 km radius (Figure 1.4e).

### 1.2.1 Manicougan Lake

Colloquially known as “The eye of Quebec” (Figure 1.4b), the Manicougan Impact Structure was once suspected to be part of a late Triassic multiple impact event simultaneously creating the Rochechouart (France), Saint Martin (Canada), Obolon’ (Ukraine), and Red Wing (USA) Impact structures (Spray et al., 1998). Improvements in dating techniques have since delineated these events by tens of millions of years (e.g., Schmieder et al., 2014 ). At 100 km diameter, Manicougan has a highly heterogeneous melt sheet, with thicknesses up to 1500m (Spray & Thompson, 2008). Although it has a clear peak ring, Spray and Thompson also found a central uplift structure and argue that Manicougan may not fit into current crater classification schemes. An extensive review of Manicougan’s metamorphic province, Grenville, is available (Indares & Dunning, 2018), and it is possible that the apparent central peak is simply a manifestation of target metamorphic rock heterogeneity. Although Manicougan is one of the 10 largest confirmed impact structures on Earth, paleomagnetic analysis has revealed that this 214 Ma impact likely did not affect Earth’s geodynamo (Eitel et al., 2016).

Located in Northern Quebec, the lake can be reached by highway in less than ten hours from Quebec City. Manicougan Lake has many advantages for advancing impact structure knowledge: it is undeformed, is relatively well preserved, has been extensively drilled for mineral exploration, and is mostly exposed (Spray et al., 2010). In addition, Spray puts forward the Manicougan impact structure as an analogue for Martian and Lunar structures, largely on the basis of similar mineralogy and hydrothermal systems. Finally, Manicougan is an excellent source of insight on the primary physical

properties of impact melt bearing breccia, known as suevite, providing a terrestrial perspective on suevite production in a near absence of water during the impact event (Thompson & Spray, 2017).

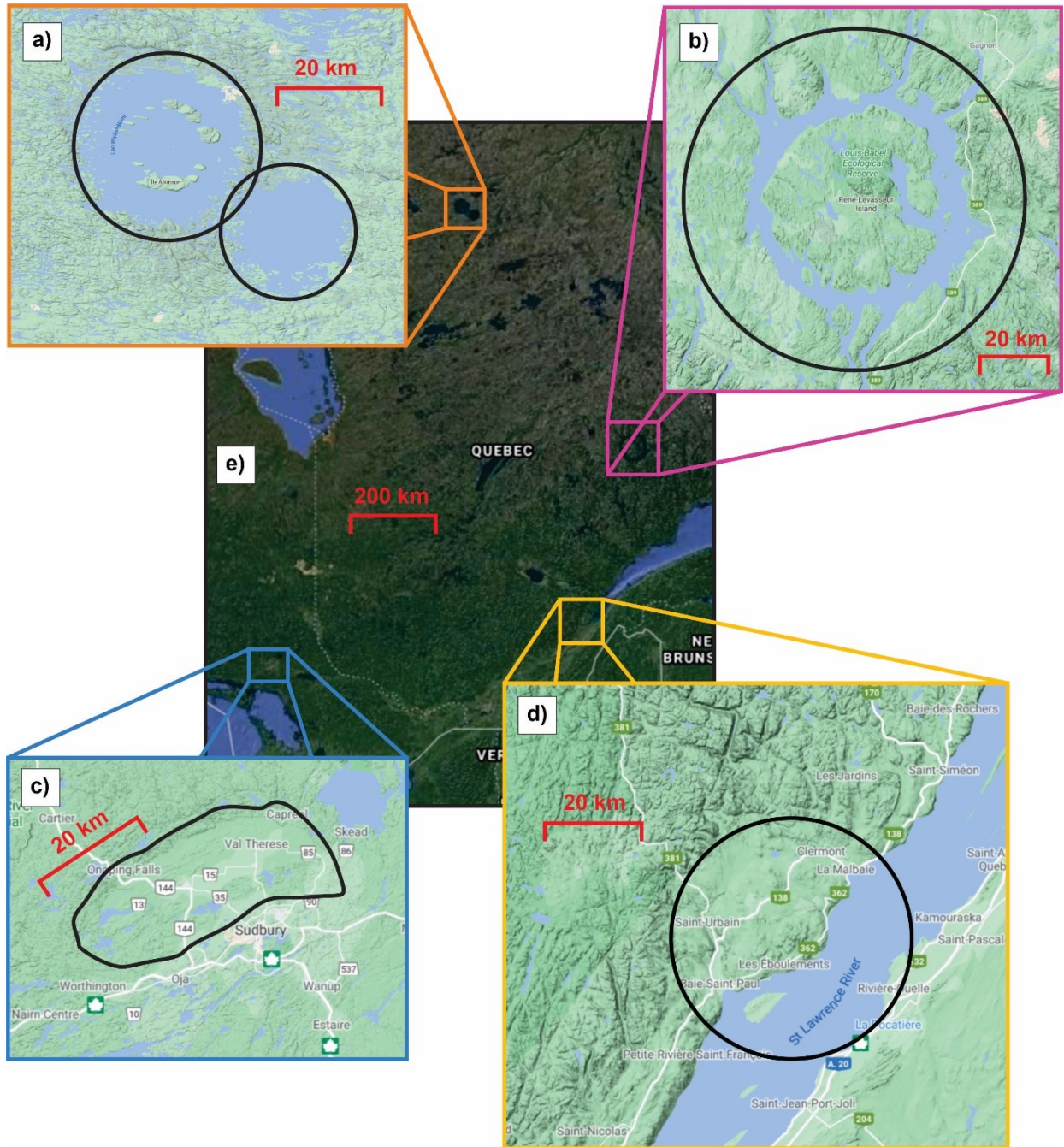


Figure 1.4. Major confirmed impact structures of the Canadian Shield. a) Clearwater Lakes, a formerly suspected binary impact. b) Manicougan lake. c) Sudbury Impact Structure, extensively deformed. d) Charlevoix Impact Structure, partially under the St. Lawrence River. Maps data: Google.



### 1.2.2 Charlevoix Impact Structure

Located conveniently en-route to Manicougan Lake (Figure 1.4d), the eroded Charlevoix impact structure is of low topographical relief and higher population density compared to the surrounding Appalachians. The crustal target rock is easy to sample throughout the structure and continuously onto the surrounding unshocked host rock. As such, it was possible to extensively map out the prevalence of deformational features in non-displaced shocked quartz and feldspar target rock (Robertson & Grieve, 1975). Based on the correlation between planar deformation features (PDFs) and peak shock pressure, Robertson was able to map the peak pressure of the radiating shock wave at the Charlevoix impact (Robertson, 1975b). Extensive analysis of shocked quartz grains found evidence of post-shock annealing (Trepmann & Spray, 2006). Calcium rich evidence of hydrothermal alteration was found in intensely fractured areas (Trepmann et al., 2005), confounding analysis of shock specific effects. Charlevoix's age has recently been further constrained with uranium-lead analysis of shocked zircon grains, placing Charlevoix's age at ~450 Ma.

The annulus of impact melt bearing breccia is surprisingly thin, possibly due to impact ejecta being washed out to sea, as the St Lawrence river system already existed at the time of impact (Rondot, 1971). Rondot further argues gravitational adjustment from deep listric faults could account for the "zone of silence" around the central uplift of Charlevoix (Rondot, 2000). Indeed, the structure is intensely faulted and straddles the intersection of the Grenville province, Cambrian-Ordovician sediments, and accreted Appalachian orogen (Lemieux et al., 2003). The Charlevoix Seismic Zone is the most seismically active in Eastern Canada; inevitably, seismic and impact analysis continually confound each other (Lamontagne et al., 2000; Yu et al., 2016).

### 1.2.3 Sudbury

Owing to extensive economically exploitable hydrothermal mineralization (Molnár et al., 1999), extensive geological, geophysical, and drilling data is available for the Sudbury Basin. For example, the Government of Ontario has made available an extensive guide on the geology of the Sudbury formation (Rousell & Brown, 2009). However, we will limit to a very brief discussion here. The Sudbury Basin is yet another example of civilization filling the topographically smooth niche left behind by an astrobleme (Figure 1.4c). Although the Sudbury Basin is the second largest confirmed terrestrial impact structure, it has been extensively deformed; a review on the topic concludes that it is still unclear whether Sudbury is a central uplift or multi-ring structure (Riller, 2005). Owing to extensive reworking and deformation, the original size of the now elliptical Sudbury basin is poorly constrained, although estimates place the original diameter at 150-250 km (Grieve & Osinski, 2020). This diameter places Sudbury well within the dimensions of peak ring basins, and Grieve suggests there is trace evidence of a peak ring. Significant effort has been placed on reconstructing the post impact evolution of the Sudbury structure (Grieve et al., 2010). It has been suggested that the impact breccia continued to migrate long after initial crater formation (Göllner et al., 2019). Additionally, Sudbury has been shown to have a robust post-impact hydrothermal system (Ames et al., 2006).

Surprisingly little work has been done on the impact melt bearing breccia associated with the Sudbury impact, particularly about its physical properties. An apparent lack of work may be related to the roaming terminology, with various interpretations of suevite associated with the Sudbury impact being referred to as Onaping Breccia (French, 2021), Sudbury Breccia (O'Callaghan et al., 2017), or Accretionary Lapilli (Huber & Koeberl, 2017), as a few examples. Fortunately, recent work has been completed to unite the fragmented terminology surrounding Sudbury (Debono, 2018). Regardless, the answer to the question of whether the Sudbury Breccia was impact created is resoundingly positive (Kawohl et al., 2021; Lafrance et al., 2008).



#### 1.2.4 Clearwater Lakes

Also known as Lac Wiyâshâkimî (Figure 1.4a), the combined length of the slightly overlapping impact structures Clearwater West and Clearwater East is ~60 km. Likely owing to its conspicuous peak ring island structure, Clearwater West has been intensely studied. For example, a 3-part study was released by NASA during the Apollo era, and separated into field geology, structure, and bulk chemistry (Simonds et al., 1978), petrology (Phinney et al., 1978b), and fine grained SEM petrology (Phinney et al., 1978a). Conversely, the Clearwater East structure is entirely submerged and further overlain with significant sedimentation. As such, very little is known about Clearwater East, with the bulk of knowledge relying mainly on geophysical surveys and two drill cores from the 1960s (Osinski et al., 2015).

Although originally interpreted to be a Permian dual-impact event (e.g., Reimold et al., 1981), the vast majority of recent discussion has been focused on improvements in dating methods. Argon isotope (Schmieder et al., 2014), Osmium isotope (Daly et al., 2018), and paleomagnetic (Gattacceca et al., 2019) analysis have all led to the conclusion that Clearwater West and East are temporally separated by hundreds of millions of years.

With the dual impact debate appearing to be settled, authors have been looking at the Clearwater Impact Structure from other perspectives. Analysis of shocked quartz grains have been used to estimate maximum shock pressure within West Clearwater (Rae et al., 2017). Integrating these constraints with iSALE shock physics code, Rae concludes that the existing structure can be explained by dynamic collapse of a central uplift and estimates that the 35-40 km original structure has been eroded by approximately 2km, which removed all the impact ejecta. Analysis of melt veins via optical microscopy, electron microprobe, and bulk chemistry suggests that the impact melts at West Clearwater were formed in situ at the center of the crater and were injected further outward (Wilks, 2016). Although extremely limited sampling still exists for East Clearwater, there has been some renewed interest

around analysis of these samples, with analysis of the post-impact hydrothermal system as one exciting example (King, 2019).

There is a small physical overlap of the boundaries between the two Clearwater Impact structures.

Drilling and sampling the twice-shocked central region of Lac Wiyâshâkimî could lead to unprecedented insights in radiometric dating and shocked rock properties. This is a rare opportunity on Earth, although multiple impact events to the same target are extremely prevalent on the Moon.

### 1.3 Yucatán Geology

With the above overview of a few Canadian impact structures, it is time to turn to the topic of the Chicxulub Impact structure that forms the basis of the current thesis. Although a full review on previous geological work on Yucatán and the Chicxulub Impact Basin would be appropriate, Chapters 3 & 4 already contain a substantial background. Thus, we will here limit to a brief overview of the state of current knowledge of the Yucatán Peninsula, Mexico in order to help prepare the reader for the later material.

The marine impact excavation created the Chicxulub sedimentary basin, a site of productive marine sedimentation that was filled by the middle Miocene. Sedimentary processes were influenced by the existence of this basin, with non-diagenetic carbonate dominance within the basin and dolomitization seen at the outer edges (Leticariu et al., 2006). Present day Yucatán is dominated by Paleogene marine sediments (Pope et al., 1993), with most of the current topography north of the Ticul fault (Figure 1.5) lower than 50 m in elevation, and significant parts of the coast only a few meters in elevation. These low lying carbonates are heavily karsted and highly permeable (Moreno-Gómez et al., 2019), leaving much of the Yucatán Peninsula vulnerable to sea level rise, including the popular tourism destination of Cancun.

Significant work has been published on understanding the target lithology. An extensive review on the surrounding marine and surficial geology is available (Ramos, 1975), and Jurassic reconstruction of the Gulf of Mexico has been accomplished by having the Yucatán block rift away from North America (Marton & Buffler, 1994). At the time of the Chicxulub impact, the target consisted of a shallow ~100m deep sea, ~3 km of marine Mesozoic carbonates atop the crystalline basement (see Figure 4, Kring, 2005). The 2-layer target has been a gift to understanding, as both Ries and Chicxulub show sedimentary and crystal ejecta dominance at distal and proximal final resting locations, respectively. Although the Mantle was not quite penetrated by the transient crater, the Mohorovičić discontinuity appears to

have been uplifted by ~1 km (Kring, 2005). Presently, the entire impact structure is buried under hundreds of meters of younger marine sediment (Ward et al., 1995). However, the structure still affects surface geology (Pope et al., 1996), most conspicuously in the Cenote ring at ~90 km radius from the center (Rebolledo-Vieyra et al., 2011). This question is an active area of research, however the cenote ring does appear to coincide with both crater rim faults and the outer periphery of the impact melt sheet (Pope et al., 1996; Rebolledo-Vieyra et al., 2011). Authors have suggested that the impermeable

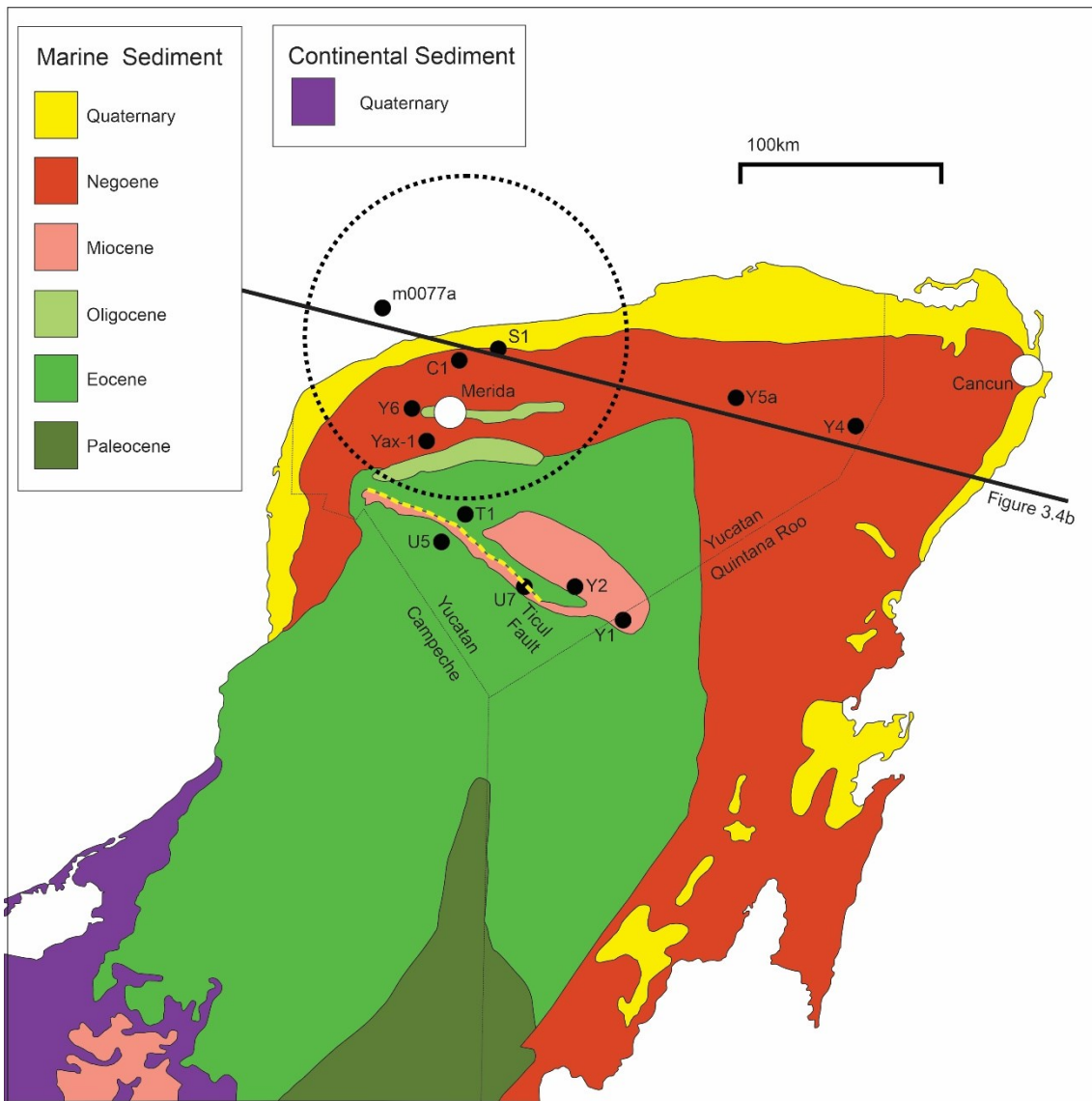


Figure 1.5. Yucatán Peninsula surficial geology, modified from Kring (2005).  
Projected cross section line for Figure 1.6b shown.

and gradually thinning melt sheet redirects geothermally upwelling fluid within the slump faults to its periphery, where there is high permeability (Monroy-Rios & Beddows, 2015). Here, we incorporate this hypothesis with core interpretations from Ward et al. (1995), updated with core interpretations from hole M0077a (Gulick, 2017), and integrated with seismic interpretation from Christeson et al. (2021) & Nixon et al. (2022, in press), to put forward new cross section models of the Chicxulub Impact Structure for 2 orientations: isotropic radial (Figure 1.6a) and East-West projected transects (Figure 1.6b). Ward et al. (1995) and Rebolledo-Vieyra (2011) are both vague on the interpretation of what they label as (?) at the upper Jurassic contact. In the model presented here, the (?) stratigraphy is interpreted mainly based on physical properties, with whatever process created the (?) stratigraphy leading to high permeability. We note in Figure 1.6 that the transient crater rim collapse breccia has not been sampled by drilling, it is recommended here to prioritize exploration of the poorly understood infill breccia in order to further constrain hydrocode modelling of complex crater peak ring formation.

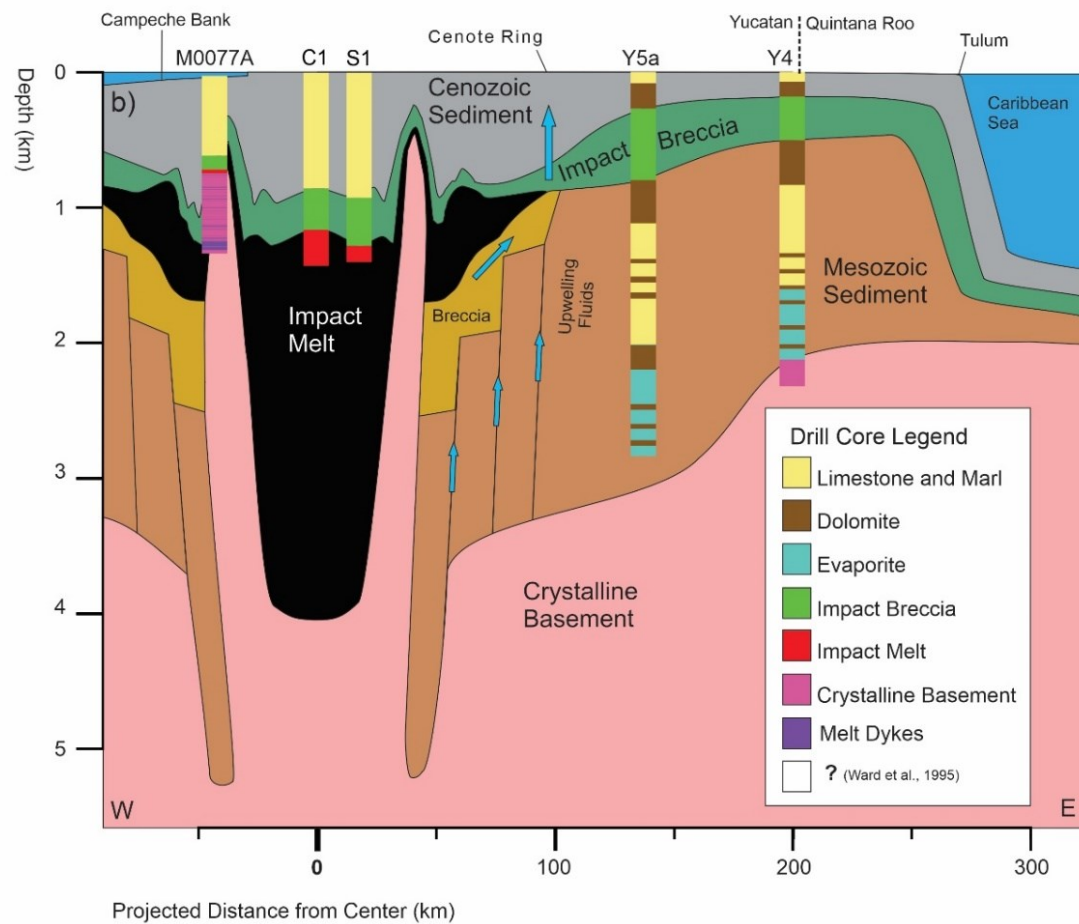
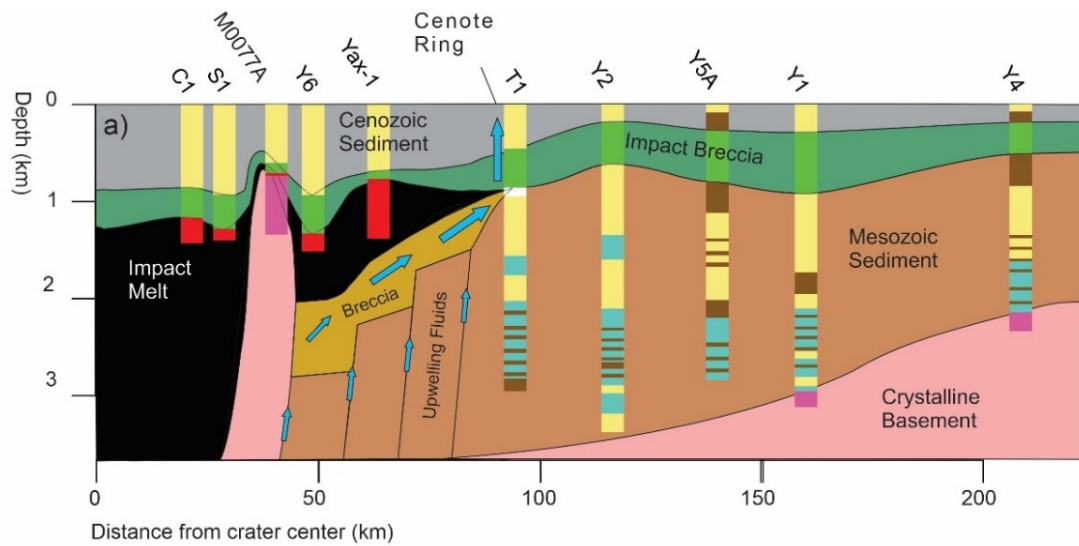


Figure 1.6. Integrated cross section model of Chicxulub Impact Structure for a) Isotropic radial interpretation and b) Projected cross section (line b from Figure 1.5).

The new model is developed here by integrating together the upwelling fluid hypothesis for Cenote ring formation from Monroy-Rios and Beddows (2015), core interpretations from Ward et al. (1995) & hole M0077a (Gulick, 2017), and seismic interpretation from Christeson et al. (2021) & Nixon et al. (2022, in press).

## 1.4 Expedition 364 Publications

At a final cost of 10 million USD, Expedition 364 (Figure 1.7a) aboard the Lift Ship Myrtle (Figure 1.7b), targeted a prominent region of the Chicxulub Impact Basin's peak ring (site M0077) and drilled 1325 mbsf to create hole M0077a (Gulick et al., 2017a). As the expedition was a heavy investment in multi-disciplinary science, it is worthwhile to provide this brief yet unique review of peer reviewed publications specifically resulting from Expedition 364. A less up-to-date but expanded list of publications, including conference proceedings, can be found at <http://publications.iodp.org/proceedings/364/364title.html#bib>.

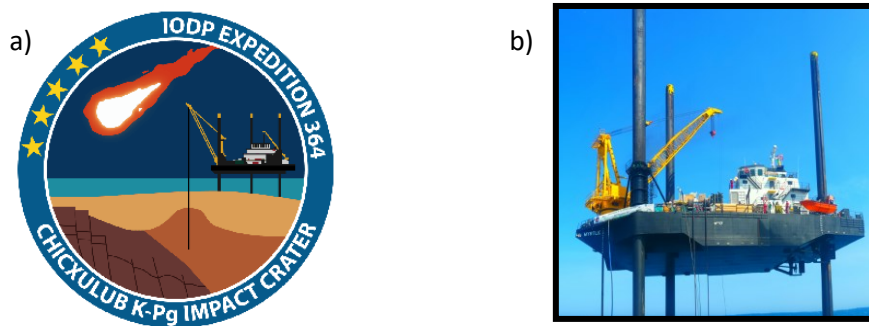


Figure 1.7. Symbolic images from Expedition 364. a) Official Exp. 364 logo.

b) View of L/S Myrtle, operation vessel for Exp. 364.

### 1.4.1 Physical Properties

First shown by Christeson et al. (2018), M0077a peak ring rocks have unusual physical properties.

Laboratory petrophysical measurements on the shocked granitoids show high porosity (0.08-0.13), low bulk density (2.39-2.44 g/cm<sup>3</sup>), and low dry  $V_p$  (4-4.2 km/s). Typical values for unaltered granite are ~0, 2.6 g/cm<sup>3</sup>, and 6 km/s, respectively. This study also found velocity, density, and porosity of 2.9-3.7 km/s, 2.06-2.37 g/cm<sup>3</sup>, and 0.2-0.35 for peak ring suevite and 3.7-4.4 km/s, 2.26-2.37 g/cm<sup>3</sup>, 0.19-0.22 for impact melt sheet rock. They concluded that shocked peak ring lithologies are among the most damaged in an impact basin, as is consistent with numerical modelling. Further, they combined the results with

previous seismic profiles to map suevites within the Chicxulub Basin and showed that the suevite layer is thicker within the central basin than peak ring.

The highly damaged granitoids of M0077a have been subjected to attenuation analysis at seismic frequencies; unsurprisingly, the highly damaged and porous seawater saturated media is found to be highly attenuating, with  $Q$ -factors as low as ten, although  $Q$  does increase with depth in M0077a (Nixon et al., 2020). This VSP data has been fully processed including application to damage parameterization (Nixon et al., 2022, in press) which includes integration with high frequency sonic logs (Lofi et al., 2018).

The extraordinarily high porosities with M0077 granites have been shown to be caused primarily by shock-induced microfracturing (Rae et al., 2019). Rae found preferential orientations to the shock induced fractures, which can be predicted to correspond with the directions of the principal stresses calculated during numerical simulations of the dynamic collapse model. Feather features (short, parallel to sub-parallel lamellae within quartz grains) were quantified and compared to the principal stress axis of the shockwave, showing feather features are generally confined to orientations parallel to the direction of shock wave propagation (Ebert et al., 2020). An analysis of eleven M0077a granitoid samples found 99.8% of quartz grains shocked (Feignon et al., 2020). They measured 963 PDF sets across the 352 quartz grains investigated, finding homogenous PDF orientations. They were also able to constrain the peak-shock pressure to between 16 and 18 GPa and noted slightly higher shock pressures at higher elevations in the core.

While quartz shock effects are extremely well understood and heavily used for impact ‘fingerprinting’, hole M0077a presents a unique opportunity for investigating shock effects in other minerals. An analysis of 560 apatite grains ( $\text{Ca}_5(\text{PO}_4)_3(\text{F},\text{Cl},\text{OH})$ ) found this mineral’s shock deformation response to be highly variable with an uptake of MgO in shock-recrystallized grains. Little is known about shocked titanite ( $\text{CaTiSiO}_5$ ); however, two new modes of mechanical twinning have been discovered in hole M0077a



(Timms et al., 2019). An analysis of high pressure zircon ( $ZrSiO_4$ ) phases found twinning, granular zircon, and its high pressure polymorph reidite (Zhao et al., 2021); shock pressure of up to 30 GPa in the suevite has been constrained from this zircon analysis. The reidite mineral phase has never been observed in a large impact basin on Earth before this, which the authors attribute to rapid cooling by seawater. Further investigation of the shocked zircon suggests shock pressure can be amplified by impedance contrasts within the target material (Wittmann et al., 2021).

#### 1.4.2 Petrography

Laying directly atop the granitoids, the 46 m thick impact melt consists primarily of two parts mixed in a marble like texture: a black aphanitic/trachyandesitic component and a green clay mineral/sparitic calcite component (Schulte et al., 2021). Schulte asserts that this texture resulted from the violent interaction of impact melt rock with a debris/seawater mixture, and subsequent hydrothermal alteration. Similarly, the 130 m melt bearing breccia directly atop the impact melt has undergone an explosive molten fuel-coolant interaction with seawater, which was subsequently deposited subaqueously to form a well-sorted sequence (Osinski et al., 2020). They argue that subaqueous impact melt bearing breccia does not meet the current classification criteria for suevite, and a new classification scheme should be developed for shallow marine impactites.

Petrographic analysis in M0077a has largely been focused in and around the suevite layer. An extensive analysis of suevite and impact melt rock petrographic analysis has been conducted with the goal of identifying original target lithologies (Van Gaever, 2019). The suevite has been divided into three layers on the basis of distinct petrography and geochemistry (Kaskes et al., 2021). Rapid emplacement of the bottommost 5.6 m thick non-graded suevite unit is estimated to have occurred within the 30 minutes after impact, resulting from violent interactions between the first arrival of seawater and hot impact melt rock. Following is an 89 m thick graded unit, deposited over several hours by rock debris rich seawater. Indeed, the suevite sequence is reported as having among the highest known deposition rates

in the sedimentary record (Gulick et al., 2019). After the rapid first days of Cenozoic deposition, Kaskes estimates that the uppermost 3.5 m thick layer of bedded suevite took up to 20 years to deposit. In-depth analysis of the clasts within the suevite layer has been compared to 8 other marine impact sites, and a new method for estimating impact magnitude is proposed through a relationship between water depth, projectile diameter, clast frequency, and sample location within the crater (Ormö et al., 2021).

The uppermost layer, and transitional unit to normal marine sedimentation have been closely analyzed (Whalen et al., 2020), noting multiple repetitive layers of normally graded suevite. Whalen concludes that although timing on the bedded layers is difficult, tsunamis and sieches likely operated for weeks post impact but potentially as long as years, due to subsequent continental margin collapse. The 75 cm thick transitional unit is a micritic limestone which has been found to be a global marine K-Pg feature varying from 4 cm to 17 m at 30 other sites worldwide (Bralower et al., 2020). Additionally, elevated Iridium is reported in the upper portion of the transitional unit (Goderis et al., 2021), further supporting that the Chicxulub Impact structure is linked to the global K-Pg iridium anomaly.

Geochemical and petrographic analysis were performed on granitoid, dolerite, felsite, and zircon throughout the M0077a peak ring. Elemental analysis of the granitoids revealed elevated  $K_2O/Na_2O$ ,  $LaN/YbN$  and  $Sr/Y$  ratios and very low Yb and Y ratios (Zhao et al., 2020). In felsites, these anomalous elemental ratios are thought to be due to partial melting of altered and subsequently subducted basalt. Geochemically, felsitic rocks of this composition are known as adakites, although there is not yet a consensus on how adakites are formed, Zhao argues that adakitic dominance of the M0077a granitoids is likely due to partial melting of thickened crust. Zhao describes the felsitic dykes within the granitoid peak ring as shoshonitic whereas the doleritic dykes appear to be more closely related ocean island basalts. Zhao suggests a tearing slab break off model, although recent work with Uranium-Lead dating, trace element analysis, and zircon grains shows the target basement rock originated as a carboniferous continental volcanic arc (Ross et al., 2021).

### 1.4.3 Impact Basin Formation

Impact craters whose diameter exceeds a certain threshold, which is dependent on target gravity and lithology, have an annular central uplift known as a *peak ring* (Figure 1.8). Although peak rings are poorly understood, two competing models exist for their formation: the Dynamic Collapse Model and the Nested Melt Cavity Hypothesis (see section 2.4.3). Cross cut dykes, shear zones, low density, and low seismic velocity were all found in M0077a which is argued as evidence for vertical fluxes in large impacts, and therefore, support for the dynamic collapse model. The dynamic collapse model continued to gain rapid support following geological results within the first year after Expedition 364 (Kring et al., 2017). That the basement rocks are fractured, shocked, and uplifted has been succinctly cited as evidence supporting the Dynamic Collapse Model (Urrutia-Fucugauchi et al., 2019). The dynamic collapse process has been numerically modelled to increasingly higher temporal and spatial resolution,

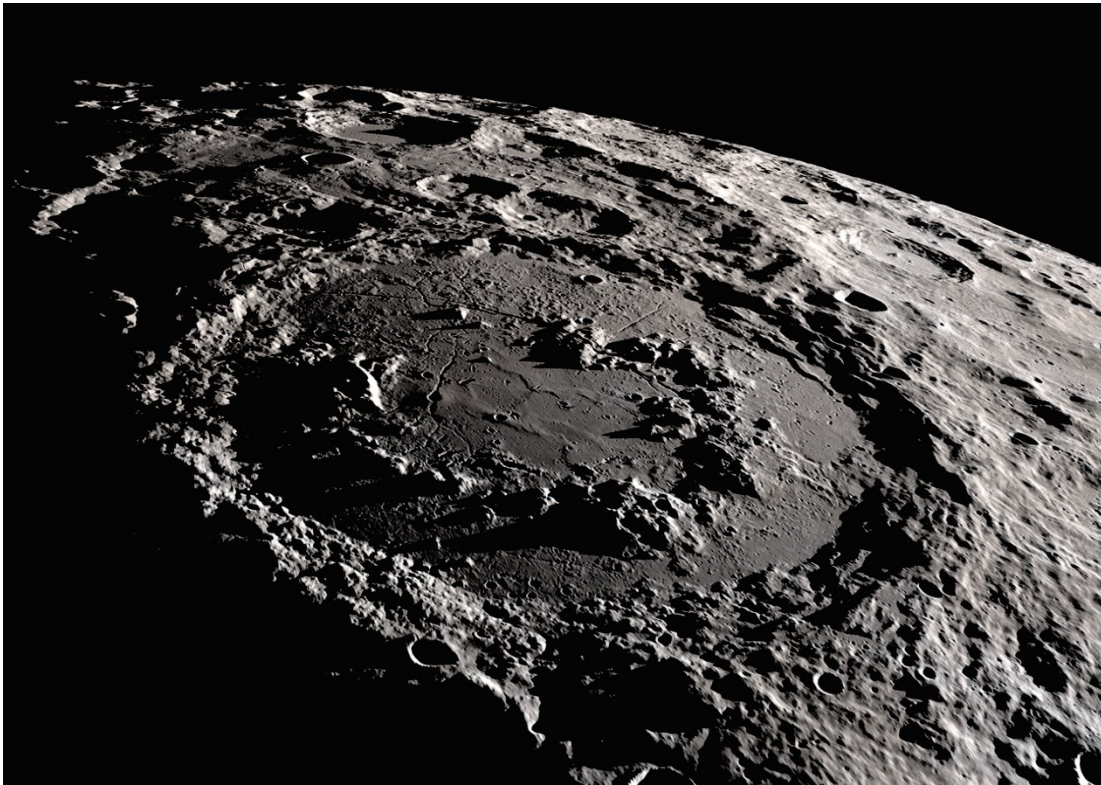


*Figure 1.8. Schrödinger impact crater as photographed from Lunar orbit. Annular peak ring is apparent in center. Total crater diameter is ~300km. Image credit: NASA.*

and the results are remarkably consistent with extensive and diverse observations from M0077a core . However, Rae asserts that some component of ‘acoustic fluidization’ (Melosh & Gaffney, 1983) is necessary to fully produce the deformations of Dynamic Collapse Model. Cataclasite and ultracataclasite zones are interpreted as the initially dominant mechanism for acoustic fluidization, giving a much smaller block size than initially assumed. Feather features are used to trace block rotation, with the interpretation that the rock within M0077a behaved as a semi coherent mass as permitted by acoustic fluidization (Ebert et al., 2020). CT scan and line scan imaging has revealed preferred orientation of dipping toward crater center and tangential to the peak ring for cataclasite and ultracataclasite zones, respectively (McCall et al., 2021); these orientations are consistent with hydrocode modelling for peak ring formation and further support the process of acoustic fluidization. Additionally, improved mapping of the Chicxulub Peak Ring structure has recently been provided by integration of M0077a borehole data with regional mapping (Christeson et al., 2021).

#### 1.4.4 Post Impact Hydrothermal System

The geological stable sedimentary deposition that has subsequently blanketed the Chicxulub Impact structure since its formation provides unique opportunity to study a well-preserved peak ring on Earth. However, hydrological alteration has severely confounded analysis of shock effects; indeed, preliminary analysis immediately revealed that hydrothermal alteration has affected all lithologies, particularly within the upper suevite. Detailed analysis of hydrothermal effects within the suevites revealed alteration phase dominance of Fe-Mg clay minerals, zeolites, alkali feldspars, calcite, minor sulfides, sulfates, opal, and Fe-Ti oxides, with the most intense alteration near lithological contacts (Simpson et al., 2020). Hydrothermal lead depletion within the shocked titanite has been applied to uranium-lead dating to confirm the age of the impact event (Timms et al., 2020). A similar approach has been applied to shock fractured zircon, which suggests that the intense post-impact hydrothermal circulation controlled uranium-lead age resetting, rather than the impact itself (Rasmussen et al., 2019). Detailed

analysis of the core, including paleomagnetic analysis, and integration with hydrothermal modelling, suggest the Chicxulub Impact Basin's hydrothermal system persisted for more than one million years, perhaps as high as two million (Kring et al., 2020). Kring estimates  $1.4E5 \text{ km}^3$  of rock has been hydrothermally modified by this system.

#### 1.4.5 Climate Change

While climate change from the Chicxulub impact is widely regarded as the most direct cause of the end-Cretaceous extinction, marine sediment archives reveal that impacts typically do not cause significant environmental change (Lowery et al., 2019). Charcoal, a sign of wildfires, is found within M0077a, which, combined with depleted sulfur-rich evaporites, is interpreted as support for a K-Pg impact-induced winter (Gulick et al., 2019). The target rock composition was also critical in creating such a global winter, with polycyclic aromatic hydrocarbons from M0077a core suggesting a large fossilized carbon sink within the target rock (Lyons et al., 2020). Lyons estimates  $7.5E14$  to  $2.5E15$  g of organic black carbon was ejected during the Chicxulub impact, further cooling the planet and exacerbating the impact winter. They further assert that wildfires were somewhat delayed and the smoke released played a more minor role in the impact winter than previously thought. New constraints on impact angle and target composition from M0077a allowed for updated hydrocode modelling, producing estimates of sulfur and  $\text{CO}_2$  released during the impact of 325 and 425 Gt, respectively (Artemieva et al., 2017). Impact modelling with a focus on impactor angle variation has been compared with the geophysical observations of up to and including Expedition 364, with the conclusion that the Chicxulub Impactor likely arrived from the North-East at an inclination angle of 45-60 degrees (Collins et al., 2020); they regard this inclination angle to result in the maximum release of climate changing gases. .

#### 1.4.6 Fossil Record

Fossil analysis of the post-impact sedimentary rock core was a significant portion of data collection on Expedition 364. The post-impact hydrothermal system within M0077a was found to host pyrite

framboids which metabolized reduced sulfates within porous niches (Kring & Bach, 2021; Kring et al., 2021). Furthermore, elevated biomass was found within the present day impact suevite as well as elevated cell abundance at impact induced interfaces within the biologically sparse granitoids (Cockell et al., 2021) who also assert that the present-day subsurface biosphere continues to be influenced by the impact induced improvements in nutrient transport.

Although the end of the Cretaceous marks a mass extinction event, some species were ideally suited to the apocalyptic conditions. Palynological analysis of post-impact M0077a core has identified Dinoflagellate cyst *Trithyrodinium Evittii* as a likely disaster taxa at ground zero of the Chicxulub impact (Smith et al., 2021), with the Paleocene core having nearly no other evidence of palynomorphs. Within 30 kyr, the ecosystem at ground zero had returned to high-productivity (Lowery et al., 2018), with ocean resurge and subsequent tsunami nutrient deposition initiating cyanobacteria blooms until 200 kyr after the impact event (Schaefer et al., 2020). Recovery within the impact basin continued rapidly, with full recovery to an abundance of Zoophycos, Chondrites<sup>1</sup>, and Planolites occurring within 700 kyr (Rodríguez-Tovar et al., 2020), although full termination of disaster taxa within the Chicxulub Impact basin was delayed by 500 kyr as compared to other sites.

Expedition 364 yielded many firsts for the fossil record that are not directly related to the impact; the first Paleocene-Eocene Thermal Maximum (PETM) microfossil floral assemblage from Mexico, Central America, and the northern Caribbean shows average PETM sea surface temperatures of 37.8 °C (Smith et al., 2020a). One of the first Paleocene palynological records from Mexico/Central America revealed elevated pollen and spores in the PETM organic rich shale (Smith et al., 2020b). The first record of floral recovery inside the Chicxulub impact basin discovered a new genus and five new species of angiosperms

---

<sup>1</sup> Trace burrowing fossil, not to be confused with chondrite meteorites.

(Smith et al., 2020c). Additionally, M0077a core was applied to a new Python-based computer ichnological analysis with results that are easy to correlate with core data (Casanova-Arenillas et al., 2020).

## 1.5 History of Vertical Seismic Profiles

A vertical seismic profile (VSP) refers to a family of techniques in which seismic observations are made using seismic receivers at a series of depths in the earth. This differs from normal 2D seismic profiles in which both the source and the receivers are limited solely to the earth's surface. Such profiles are useful for calibrating the surface seismic results, for accurately determining in situ velocities, and to allow direct measurements of seismic attenuation. The data, too, can be processed to better understand the source of seismic reflectivity and this is a major component of later chapters where the details of how this is accomplished are provided in more detail. In this section, however, a short overview of the history of this technique is given.

Locking downhole geophones were pioneered as early as the 1950s, and enabled major advances even with the analog seismic analyses in the pre-digital age (Jolly, 1953). Jolly's innovation enabled in situ observation and amplitude decay of the down-going wave-pulse, precise depth determination of reflectors and reflector coefficients, and correlation of in-situ reflections with reflections recorded at the surface.

Following directly from Jolly's work, attenuation of high frequency signal was established in a study of downhole seismic surveys in eight separate wells (Levin & Lynn, 1958). With studies similar to those aforementioned growing in popularity, the term "vertical seismic profile" first appeared in print as a methods paper as early as the 1960's (Demidenko, 1969). A high impact article on VSPs (Gal'perin, 1974) triggered a flurry in development of the VSP technique. Wuenschel (1976) was a strong advocate for downhole seismology, arguing that "signal to noise ratio can be controlled to any level when the noise is due to scattering from layers shallower than the depth to array". He further demonstrated this by completing cross-hole VSPs (i.e., observations with source in one borehole and receivers in another) beneath highly attenuating glacial debris. He additionally demonstrated the utility of the VSP in this



study for identification and mitigation of multiples and ghosts (i.e., reverberations), a problem which continues to plague surface-based reflection seismology today.

Downhole seismic methods, however, can also be plagued with their own unique problem that make analysis problematic with the worst of these being 'tube' waves (i.e., high amplitude guided wave modes that are similar to the modes encountered in optical fiber). The borehole is an excellent conduit for high amplitude P-waves within the fluid. Although tube waves generally travel much slower ( $\sim 1500$  m/s) than the compressional (longitudinal) wave speed  $V_P$  of almost all rocks, their propagation speed can be quite similar to the shear (transverse) wave speed  $V_S$ , and these strong waves can confound discrimination of the primary P-reflections. Hardage (1981) sought to address this problem and recommended the application of techniques used in the reduction of ground roll (surface waves) in surface profiles as the first line of defense against tube waves, one example of this would be use of a 2-D f-k filter in the frequency-wavenumber domain. He recommended increasing source-borehole offsets as one way to try to reduce the tube waves. However, he cautions that velocity filters, while excellent for resolving in situ velocities, can prohibit further analysis of the waveform.

Wyatt (1981) eliminated tube waves by developing systematic equations for calculating a synthetic VSP from a velocity model. The recursive method developed by Wyatt meant that the detail of the synthetic VSP is limited only by the detail of the velocity model, and therefore the computational power available. The velocity model could be as simple as a block model (Figure 1.9) or a much more detailed sonic log. Although a synthetic VSP has advantages in tracing back primary reflections and multiples to their exact point of origin, the greatest application today is in attenuation analysis through comparing the real and synthetic VSPs. Balch et al. (1982) argued for the utility of VSP aided elucidation of surface seismic interpretation in three main ways: First, by tracing surface reflections to their exact origin within the Earth, second, by delineating the surface detectability of a specific layer within the borehole, and third,

by direct correlations between the in situ seismic properties and physical properties of stratigraphy within the borehole.

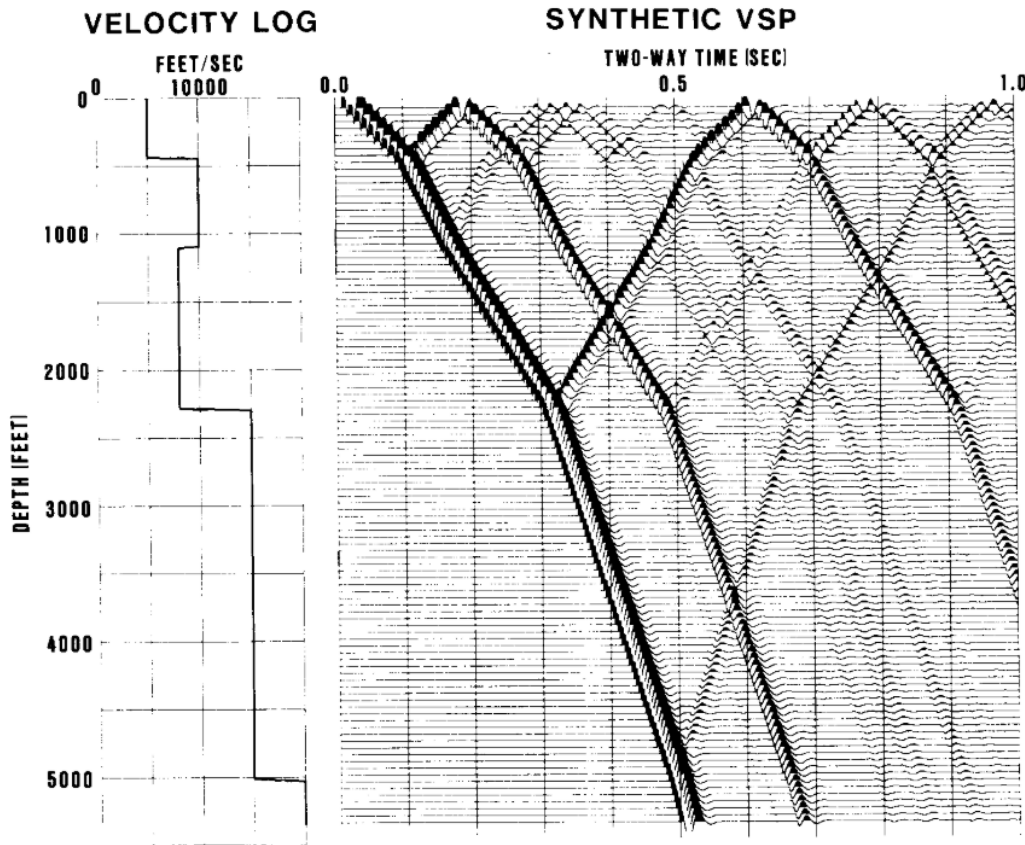


Figure 1.9. Early synthetic VSP from a simple 5 block velocity model. Reproduced from Wyatt (1981).

As with nearly all science, the true potential of the VSP was not realized until computers became involved. Methods for computer processing of the raw VSP wavefield were put forward (Lee & Balch, 1983), with the authors emphasizing the importance of wavelet shaping, wavefield separation, computation of transfer functions, and calculation of acoustic impedance logs. However, with increasing popularity of the VSP method, workers began noticing discrepancies between sonic and seismic velocities (Stewart et al., 1984). They analyzed this discrepancy (sonic vs seismic “drift”) in detail, concluding that the main factor controlling the drift in attenuation occurring from velocity dispersion. Complexity of VSP geometries continued to increase, giving rise to non-unique inversion requirements.

Recognizing this, Stewart (1984) pioneered least-squares travel time inversion for calculating interval velocities, a method that is particularly important with sparse receiver spacings.

With the rising popularity of computer analysis, Mallick & Frazer (1988) helped segue VSP analysis into the digital age by developing reliable and rapid algorithms for calculating the synthetic response of a walkaway VSP, which included the consideration of frequency dependent dispersion. By 1990, the VSP had become a staple of geophysical exploration. The in-situ records provided were invaluable to both the advancement of surface seismic methods and resource prospecting risk management. However, today the popularity of the geophone-based VSPs is declining due to the development of lower cost digital acoustic sensing methods.

I had originally planned to include here a review of VSPs on impact structures. However, to date, there have only been three that we are aware of: M0077a, collected from the Chicxulub Peak Ring and discussed in chapters 3 & 4, that collected in the central peak of the complex crater (Schmitt et al., 2007) at Lake Bosumtwi, Ghana, and a low resolution check shot survey in the Ries Crater, Germany (Angenheister & Pohl, 1974). All 3 found diminished seismic wavespeeds with respect to similar unshocked lithologies.

## 2. Theory

### 2.1 Seismic Waves

Many texts provide comprehensive discussions and derivations to link the elastic moduli, Newton's law, and stress-strain constitutive relationships to arrive at the concept of P and S waves and their speeds (Aki & Richards, 2002; Malvern, 1969). As such, we will provide here a summary of the key concepts utilized in this work.

#### 2.1.1 Elastic Parameters

As all the data discussed in subsequent chapters was collected in 1-D and analysis is therefore limited to an isotropic assumption, it is convenient to discuss some isotropic elastic parameters. Elastic moduli are always in units of pressure, and generally reported in GPa. It is important to outline here some of the differing elastic moduli that will appear in later chapters. As just noted, two independent elastic stiffnesses are necessary to describe an isotropic material. However, there are a number of different ways these can be expressed, and any two of these can be described using simple equations by any other two isotropic moduli.

##### *Bulk Modulus*

The bulk modulus,  $K$ , is defined as how much an object compresses under confining pressure, and this is quantified by change in its volume for a given increment in uniform hydrostatic pressure.

$$K = -V \frac{dP}{dV} \quad (2.1)$$

*Bulk Modulus Definition.*

In the example of a sphere of initial radius  $r_o$  which contracts by  $D r$  due to application of a hydrostatic compression  $P$  (reckoned positive sign) (Figure 2.1), the bulk modulus can be found from simple geometry to be:

$$K = \frac{-P}{1 - \left(\frac{r_0 - \Delta r}{r_0}\right)^3} \quad (2.2)$$

*Bulk Modulus for a Sphere Under Confining Pressure.*

Although certain materials such as engineered composites e.g. (Wang & Lakes, 2005), metamaterials e.g. (Ding et al., 2007), and single celled foam e.g. (Moore et al., 2006) can be interpreted to display negative bulk moduli under special circumstances, negative bulk moduli are considered forbidden by thermodynamics and naturally occurring materials unilaterally compress under stress.

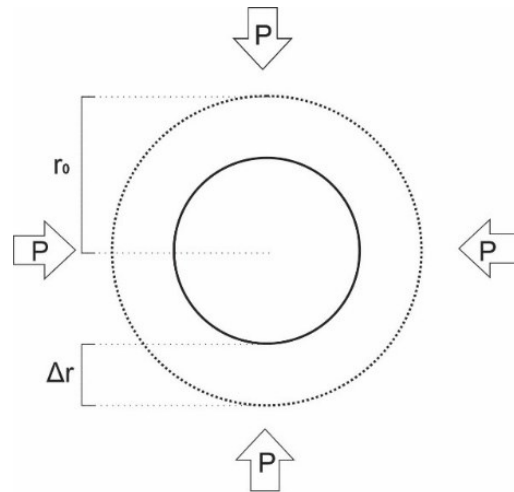


*Figure 2.1. Depiction of bulk modulus definition for a sphere.*

### *Young's Modulus*

Young's modulus was an idea originally developed by Euler (Euler, 1980), which may explain the parameter's letter choice,  $E$ . It became associated with Young's name due to a series of lectures in the 19<sup>th</sup> century (Young, 1807).  $E$ , also known as the tensile or elastic modulus is a very simple measure of the ratio of an applied uniaxial normal stress  $\sigma$  to the change in the length  $L$  of the object expressed as the linear strain  $\varepsilon = \Delta L/L$  in the same direction (Figure 2.2):

$$E_{ii} = \frac{\sigma}{\epsilon} \quad (2.3)$$

*Young's Modulus Definition.*

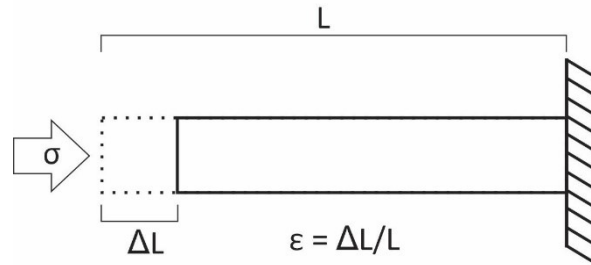


*Figure 2.2. Depiction of Young's modulus definition for a rod.*

*Poisson's Ratio*

Although not technically an elastic modulus, Poisson's Ratio,  $\nu$ , is one of the most useful elastic parameters in the study of seismic wave propagation. The Poisson effect is the observation that most materials thicken perpendicular to the axis of compression and similarly thin when stretched (Poisson, 1838). Formally, Poisson's ratio is defined as the ratio of axial strain to transverse strain (Figure 2.3)

$$\nu_{ii} = -\frac{\epsilon_{jj}}{\epsilon_{ii}} \quad (2.4)$$

*Poisson's Ratio Definition. Note that the repeated indices Einstein notation is not applied.*

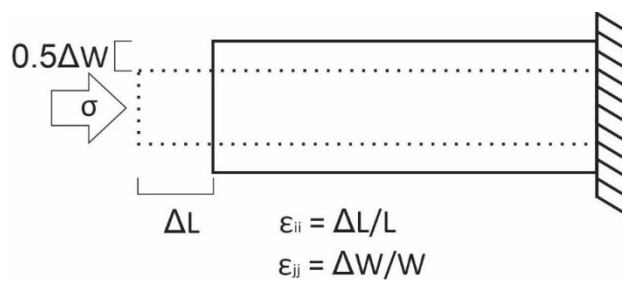


*Figure 2.3. Depiction of Poisson's ratio definition in a rod.*

Although many single crystal minerals and even some types of wood are observed to be *auxetic*, which means they have a negative Poisson's Ratio (Lakes, 2017), the vast majority of typical solids have a  $\nu$

somewhere between 0.2 and 0.3. In the case where both Lamé parameters are equal, the material has a  $\nu$  of 0.25 and is said to be a *Poisson Solid*.

#### *Lamé Parameters*

The two elastic parameters introduced by Gabriel Lamé (1852) are useful for alternate forms of Hooke's Law as well as identities connecting various elastic moduli. These moduli are particularly useful in seismology as they lead to simplification of the wave equation.

Lamé's first parameter,  $\lambda$ , while having no real physical interpretation except in fluids where it is the same as the bulk modulus is derived from the off diagonal terms of the stiffness tensor but may be readily calculated if  $\nu$  and  $E$  are known:

$$\lambda = \frac{\nu E}{(1+\nu)(1-2\nu)} \quad (2.5)$$

*Lamé's First Parameter.*

Lamé's second Parameter,  $\mu$ , is interpreted in solids as the shear modulus, and is alternatively defined as the ratio of shear stress to the Engineering shear strain  $\gamma_{ij}$  (Figure 2.4):

$$\mu = \frac{E}{2(1+\nu)} = \frac{2\sigma_{ij}}{\gamma_{ij}} \quad (2.6)$$

Lamé's second Parameter, ie. Shear Modulus.  $\gamma_{ij}$  is the angle of shear strain (Figure 2.4).

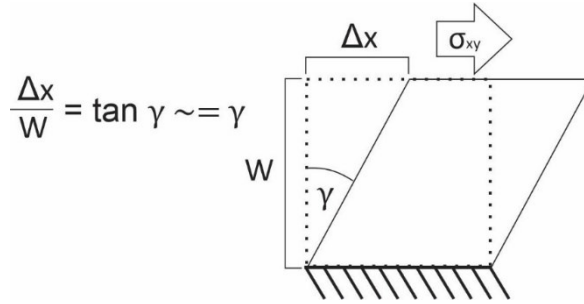


Figure 2.4. Depiction of shear modulus definition.

An application of the Lamé parameters in isotropic materials is a convenient form of Hooke's Law:

$$\sigma_{ij} = 2\mu\varepsilon_{ij} + \lambda\varepsilon_{kk}\delta_{ij} \quad (2.7)$$

Isotropic Hooke's Law, where  $\delta_{ij}$  is the Kronecker delta ( $= 1$  if  $i=j$ ,  $=0$  if  $i \neq j$ ).

Here the Einstein repeated summation applies so that  $e_{kk} = e_{11} + e_{22} + e_{33}$ .

#### Elastic Wavespeeds

Armed with the bulk and shear moduli, we can now put forward the most common expression for the elastic wavespeeds. Compressional (P) waves, with oscillation parallel to the direction of propagation, have a well-defined wavespeeds ( $v_p$ ), which can be predicted if the density ( $\rho$ ), bulk modulus  $K$ , and shear modulus  $m$  are known:

$$v_p = \sqrt{\frac{K + \frac{4}{3}\mu}{\rho}} \quad (2.8)$$

Isotropic P-Wavespeed.

It is worthwhile to note that in the Geophysics literature for convenience the numerator of equation 4.15 of  $K + 4m/3$  is referred to at the P-wave modulus. Shear (S) waves, with oscillation orthogonal to



the direction of propagation, similarly have a well-defined and much simpler wavespeed ( $v_s$ ), which only requires the shear modulus and density to be known:

$$v_s = \sqrt{\frac{\mu}{\rho}} \quad (2.9)$$

*Isotropic S-Wavespeed.*

In the isotropic case, all elastic parameters are connected with simple identities. If one can measure any 2 elastic parameters, then one can receive the others readily. For convenience, an extensive table of elastic identities is reproduced here (Table 2.1), (Smidt, 2009).

By inspection, we note that  $v_p/v_s$  is related to Poisson's Ratio; indeed, the two ratios are referred to interchangeably in the literature and authors argue about which provides the most sensitivity to material properties. In Figure 2.5a, one can observe the theoretical asymptotic upper limit of 0.5 for which would be the value expected for a fluid that cannot sustain any shear stress, as well as a lower  $v_p/v_s$  limit of  $\sqrt{2}$  for non-auxetic materials. Figure 2.5b shows the  $v_p/v_s$  vs  $\nu$  function expanded around values typically encountered, with the exact values for a Poisson solid marked. This knowledge is particularly useful in seismic interpretation, as shear waveform interpretations giving  $v_p/v_s > 2$  or  $< 1.6$  should be evaluated more carefully.

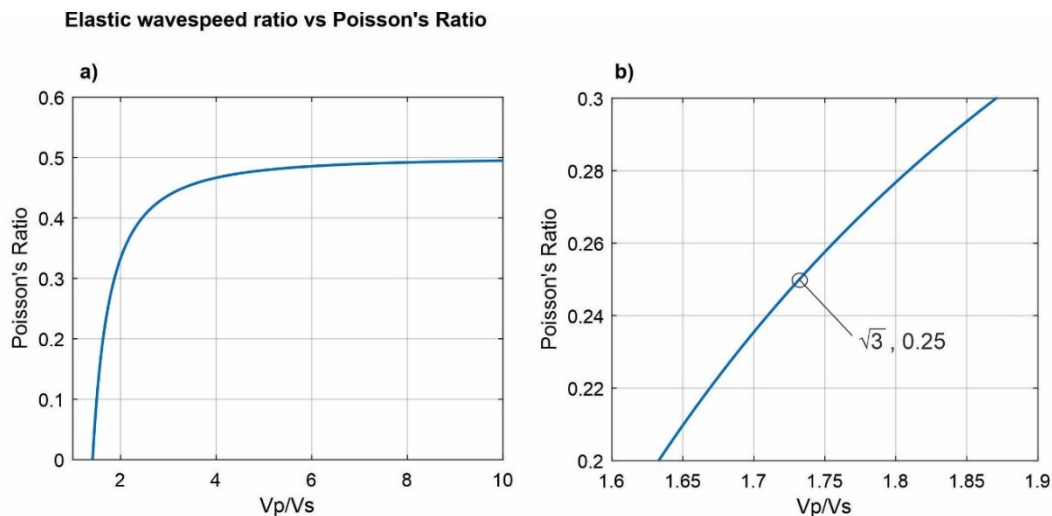


Figure 2.5. Relationship between Poisson's and  $V_p/V_s$  ratios. Ratio of a poisson solid is labelled in b).

Function of	Young's Modulus E =	Poisson's Ratio ν =	Bulk Modulus K =	P- Modulus M =	Lame Parameter λ =	Shear Modulus μ =	Lame Ratio λ / μ =	P-Wavespeed V <sub>p</sub> =	S-Wavespeed V <sub>s</sub> =	P-S Ratio V <sub>p</sub> / V <sub>s</sub> =
(E, ν)			$\frac{E}{3(1-2\nu)}$	$\frac{E(1-\nu)}{(1+\nu)(1-2\nu)}$	$\frac{E\nu}{(1+\nu)(1-2\nu)}$	$\frac{E}{2(1+\nu)}$	$\frac{2\nu}{1-2\nu}$	$\sqrt{\frac{E(1-\nu)}{\rho(1+\nu)(1-2\nu)}}$	$\sqrt{\frac{1-\nu}{2\rho(1+\nu)}}$	$\sqrt{\frac{1-\nu}{0.5-\nu}}$
(E, K)		$\frac{3K-E}{6K}$		$3K\frac{3K+E}{9K-E}$	$3K\frac{3-E}{9K-E}$	$\frac{3KE}{9K-E}$	$\frac{3K}{E}-1$	$\sqrt{\frac{3K(3K+E)}{\rho(9K-E)}}$	$\sqrt{\frac{3KE}{\rho(9K-E)}}$	$\sqrt{\frac{3K+E}{E}}$
(E, μ)		$\frac{E-2\mu}{2\mu}$	$\frac{\mu E}{3(3\mu-E)}$	$\mu\frac{4\mu-E}{3\mu-E}$	$\mu\frac{E-2\mu}{3\mu-E}$			$\sqrt{\frac{\mu(4\mu-E)}{\rho(3\mu-E)}}$	$\sqrt{\frac{\mu}{\rho}}$	$\sqrt{\frac{4\mu-E}{3\mu-E}}$
(ν, K)	$3K(1-2\nu)$			$3K\frac{1-\nu}{1+\nu}$	$3K\frac{\nu}{1+\nu}$	$\frac{3K(1-2\nu)}{2(1+\nu)}$	$\frac{2\nu}{1-2\nu}$	$\sqrt{\frac{3K(1-\nu)}{\rho(1+\nu)}}$	$\sqrt{\frac{3K(1-2\nu)}{2\rho(1+\nu)}}$	$\sqrt{\frac{1-\nu}{0.5-\nu}}$
(ν, μ)	$2\mu(1+\nu)$		$\frac{2\mu(1+\nu)}{3(1-2\nu)}$	$2\mu\frac{1-\nu}{1-2\nu}$	$\mu\frac{2\nu}{1-2\nu}$			$\sqrt{\frac{2\mu(1-\nu)}{\rho(1-2\nu)}}$	$\sqrt{\frac{\mu}{\rho}}$	$\sqrt{\frac{1-\nu}{0.5-\nu}}$
(ν, λ)	$\lambda\frac{(1+\nu)(1-2\nu)}{\nu}$		$\lambda\frac{(1+\nu)}{3\nu}$	$\lambda\frac{(1-\nu)}{\nu}$		$\lambda\frac{(1-2\nu)}{2\nu}$		$\sqrt{\frac{\lambda(1-\nu)}{\rho\nu}}$	$\sqrt{\frac{\lambda(1-2\nu)}{2\rho\nu}}$	$\sqrt{\frac{1-\nu}{0.5-\nu}}$
(K, μ)	$\frac{9K\mu}{3K+\mu}$	$\frac{3K-2\mu}{2(3K+\mu)}$		$K+\frac{4}{3}\mu$	$K-\frac{2}{3}\mu$			$\sqrt{\frac{K+\frac{4}{3}\mu}{\rho}}$	$\sqrt{\frac{\mu}{\rho}}$	$\sqrt{\frac{K+\frac{4}{3}\mu}{\mu}}$
(K, λ)	$9K\frac{K-\lambda}{3K-\lambda}$	$\frac{\lambda}{3K-\lambda}$		$3K-2\lambda$		$\frac{3}{2}(K-\lambda)$		$\sqrt{\frac{3K-2\lambda}{\rho}}$	$\sqrt{\frac{3(K-\lambda)}{2\rho}}$	$\sqrt{\frac{2K-\frac{4}{3}\lambda}{2K-2\lambda}}$
(μ, λ)	$\mu\frac{3\lambda+2\mu}{\lambda+\mu}$	$\frac{\lambda}{2(\lambda+\mu)}$	$\lambda+\frac{2}{3}\mu$	$\lambda+2\mu$				$\sqrt{\frac{\lambda+2\mu}{\rho}}$	$\sqrt{\frac{\mu}{\rho}}$	$\sqrt{\frac{\lambda+2\mu}{\mu}}$
(V <sub>p</sub> , V <sub>s</sub> )	$\frac{\rho v_s^2(3v_p^2-4v_s^2)}{v_p^2-v_s^2}$	$\frac{v_p^2-2v_s^2}{2(v_p^2-v_s^2)}$	$\rho(v_p^2-\frac{4}{3}(v_s^2)^2)$	$\rho v_p^2$	$\rho(v_p^2-2v_s^2)$	$\rho v_s^2$	$(\frac{v_p}{v_s})^2-2$			

Table 2.1. Elastic parameter identities, modified from Smidt, 2009.

### 2.1.2 Elastic Wave Propagation

#### Snell's Law

The Huygen-Fresnel principle asserts that every point on a wavefront is a point for a spherically propagating wave, and each of these individual waves interfere. The end result of constructive interference is observed as a wavefront. The Huygen-Fresnel principle neatly explains diffractive behaviour, as well. The Huygen-Fresnel principle can be used to derive an updated version of Snell's law for elastic waves (Sheriff & Geldart, 1995):

$$p = \frac{\sin \theta_1}{V_{P1}} = \frac{\sin \theta_2}{V_{P2}} = \frac{\sin \phi_1}{V_{S1}} = \frac{\sin \phi_2}{V_{S2}} \quad (2.10)$$

*Elastic Snell's Law with Ray Parameter.*

Where  $p$  is the very convenient *ray parameter* which remains unchanged for a ray travelling through parallel isotropic layered media (Figure 2.6).

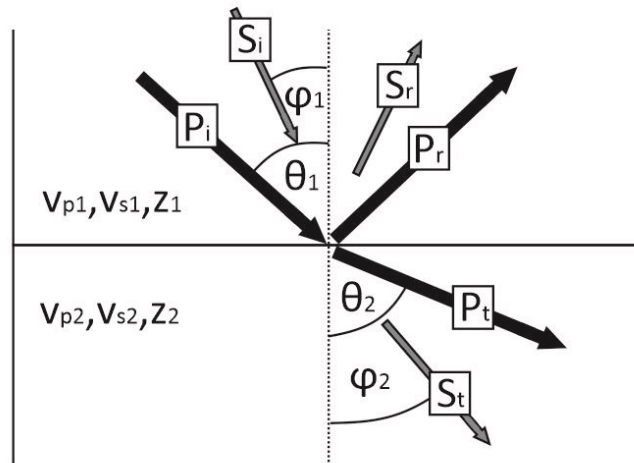


Figure 2.6. Depiction of elastic Snell's law with incident ( $P_i, S_i$ ), reflected ( $P_r, S_r$ ), and transmitted ray paths ( $P_t, S_t$ ). Ray parameter,  $p$ , is conserved.

### *Impedance*

In the most broad sense, impedance describes how well a medium resists (impedes) the disturbance. Waves with the same energy intensity have lower amplitudes in a material of higher impedance. In the context of elastic waves, a material's elastic stiffness and its inertia (via density) conspire to resist disturbance; however, as the disturbance is brief and not allowed to reach steady state, the inertia resists the propagating disturbance as well. Seismic impedance is then defined as:

$$z_{p,s} = \rho v_{p,s} = \sqrt{\rho \delta_{p,s}} \quad (2.11)$$

*Seismic Impedance.*

With  $\delta_{p,s}$  being your choice of P-wave or shear modulus. P-Impedance is often referred to as acoustic impedance, as what animals perceive as sound is, in fact, P-waves within fluids.

Impedance contrast between different media is what empowers seismic imaging. For a wavelet incoming normalized amplitude = 1 travelling at normal incidence through an impedance discontinuity between layers of impedances  $z_1$  t  $z_2$  (Figure 2.7), the amplitude of the reflected wavelet is given by:

$$R = \frac{z_1 - z_2}{z_1 + z_2} \quad ( 2.12 )$$

*Normal Incidence Reflection Coefficient.*

And the transmitted wavelet by:

$$T = 1 - R = \frac{2z_1}{z_1 + z_2} \quad ( 2.13 )$$

*Normal Incidence Transmission Coefficient.*

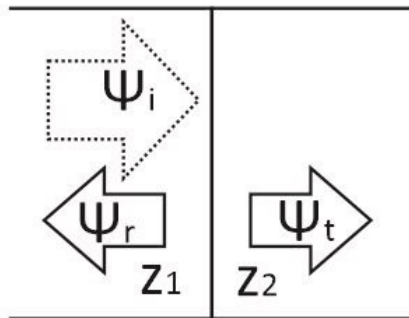


*Figure 2.7. Reflection and transmission through an impedance contrast.*

While the above assumption is useful in very limited cases, such as a zero-offset VSP, incidence angles in practice are rarely normal. Like any wave, elastic waves refract at an interface; reflection and transmission coefficients for non-normal incidence have been derived from Hooke's Law (Zoeppritz, 1919), with the fascinating result of P to S wave and vice-versa conversions at the discontinuity (Figure 2.6) as a necessary condition.

### *Attenuation*

Attenuation is defined as reduction in the waves intensity and amplitude as it propagates, which can be either elastic or inelastic. It is debatable whether geometrical spreading qualifies as a component of elastic attenuation; nonetheless, geometric spreading, often approximated as spherical spreading of the wavefield area in inverse proportion to the square of the distance most usually contributes the most to the decay of the amplitude. Additionally, although phase velocity is often ignored in seismic processing, velocity dispersion contributes to elastic amplitude loss as pulse time duration 'fattens'. In an inhomogeneous medium, scattering further contributes to elastic amplitude loss, as well. Scattering is heavily frequency dependent, as the scale of heterogeneity will be similar to the wavelength being scattered.

In contrast, anelastic attenuation includes those processes in which energy is permanently lost to heat. Anelastic attenuation is highly frequency dependent, and characterizing it is a prioritized field in research as it is intrinsically related to fluid and porosity characteristics of the host rock, such as inter/intra pore fluid flow and grain boundary friction. Separating the geometric, scattering, and anelastic effects from observations of seismic amplitude decay remains challenging.

### Quality Factor

The Quality factor ( $Q$ ) is defined by the ratio of waveform energy ( $E$ ) to the energy lost in one cycle ( $\Delta E$ ):

$$Q = 2\pi \left( \frac{E}{\Delta E} \right) \quad ( 2.14 )$$

*Definition of Quality Factor.*

By inspection, one sees that less energy lost per waveform cycle results in higher  $Q$  and less attenuation:

$Q$  is inversely related to attenuation. Amplitude  $A$  decay between two points  $x_0$  and  $x$  in a planar wavefront at frequency  $f$  propagating with speed  $v$  can then be described by:

$$A(x, f) = A(x_0, f) e^{\frac{-\pi f}{Qv}(x-x_0)} \quad ( 2.15 )$$

*Anelastic wavefront decay in the plane-wave approximation.*

Taking the natural logarithm of both sides gives:

$$\ln \frac{A(x, f)}{A(x_0, f)} = -\frac{\pi \Delta x}{Qv} f + \ln G \quad ( 2.16 )$$

*Spectral Ratios to  $Q$  relationship.*

Equation 16 is a convenient way to analyze attenuation, as the spectral ratio relationship does not require any information about the source wavelet or contributions of elastic attenuation all of which combine into a geometric terms  $G$ . By plotting the natural log of the ratio of amplitudes as a function of frequency (Figure 2.8), we can fit a linear slope ( $m$ ), and estimate  $Q$ :

$$Q = \frac{-\pi \Delta x}{mv_p} \quad ( 2.17 )$$

*Linear best fit  $Q$  estimate*

It is important to note that this practical method assumes  $Q$  is fixed for all frequencies. In reality,  $Q$  is generally higher for lower frequencies. A much more extensive description of the spectral ratios method

and attenuation in general can be found in Atten (2004). One problem with this method, however, is that it is particularly susceptible to noise that may be instrumental or even considered to due to complications (e.g. reflections and multiples) in the wavefield.

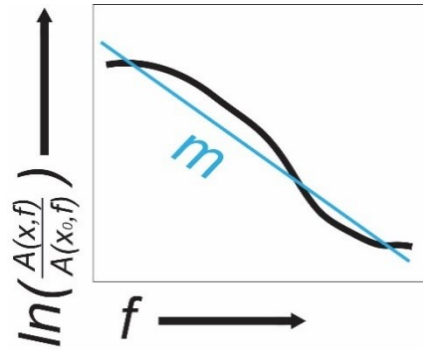


Figure 2.8. Spectral ratios slope illustrated.

## 2.2 Vertical Seismic Profiling

As a much more detailed description of analytical methods used for chapter 4 is available in the appendix, we provide here a very brief description of Vertical Seismic Profiling.

### 2.2.1 Common VSP Geometries

In widely used surface seismic surveys, receivers are typically spaced out along the surface of the earth with the source repeated at a horizontal offset,  $\Delta x$ , from the various receivers (Figure 2.9a). The only difference with a zero offset vertical seismic profile is the receivers are located vertically within a hole, with the source repeated at a vertical offset,  $\Delta z$  (Figure 2.9b).

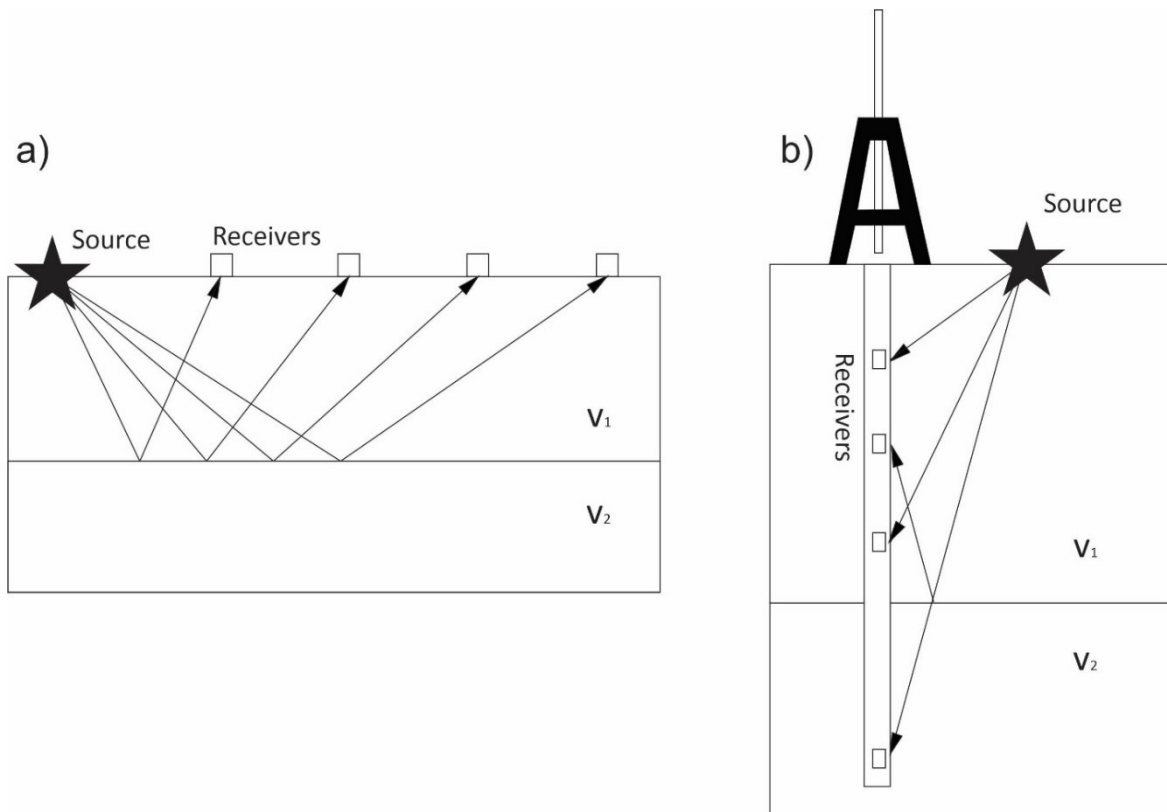


Figure 2.9. Horizontal vs Vertical seismic acquisition geometry. a) Horizontal, i.e., surface seismic.

b) Vertical, i.e., downhole seismic.



While the geometry utilized here is the simplest zero offset orientation, which produces a 1-D velocity structure, vertical seismic profiles can be collected in various configurations: A ‘far-offset’ configuration (Figure 2.10a) is more likely to convert detectable S-waves, although the offset complicates processing. Data from the ‘walk-away’ configuration (Figure 2.10b) can be inverted for 2-D structure, and when a well is significantly deviated from vertical, the ‘walk-above’ technique (Figure 2.10c) is advantageous for tomographic mapping. ‘Cross-well’ methods (Figure 2.10d) are advantageous due to extremely low noise levels and are able to detect heterogeneity within the stratigraphy. A ‘while-drilling’ VSP (Figure 2.10e) is unique in that the drill bit is used as the signal and is mainly used to look ahead of the drill. Finally, the ‘multi-azimuthal’ or ‘walk-around’ geometry (Figure 2.10f) is inverted for 3D velocity structure (Labo, 1987).

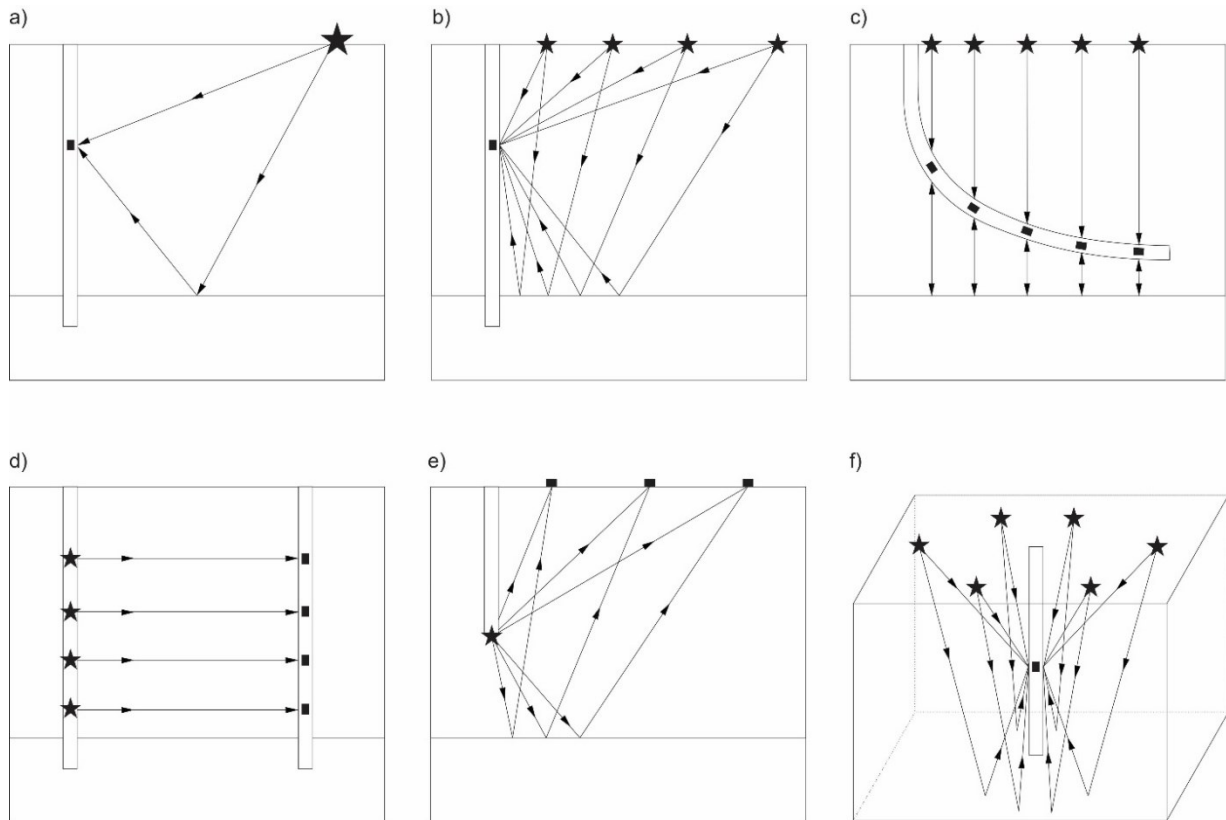


Figure 2.10. Commonly utilized VSP geometries. a) Far-offset. b) Walk-away. c) Walk-above. d) Cross-well. e) While-drilling. f) Walk-around.

### 2.2.2 Zero-Offset

Unlike the majority of geophysical imaging techniques, the zero-offset VSP produces unique solutions. This is enabled by the zero-offset and parallel ray path assumptions, although near field effects can be problematic for non-horizontal stratigraphy. There are two major purposes to the processing described immediately below. The first is to obtain true direct measures of the in situ wave speeds that can only be inferred from surface seismic data. The second is to provide a calibration seismic trace that highlights the depths from which primary reflections originate, and to allow direct comparison to the surface seismic images. The primary steps are illustrated (Figure 2.12), reproduced from appendix (Figure A 10) for a conceptual 3-layer model in the zero-offset method as follows:

- 1) The receiver is lowered into the borehole and a source is triggered at the surface, near enough the borehole that it can be treated as directly above. The pulse then travels directly downward, passing through the receiver that records the initially downgoing wavelet (Figure 2.11a). After encountering an impedance boundary, the pulse will be reflected upward and also registered as second wavelet (Figure 2.11b) at the receiver. Reflections at greater depths (Figure 2.11c) will be recorded as well.

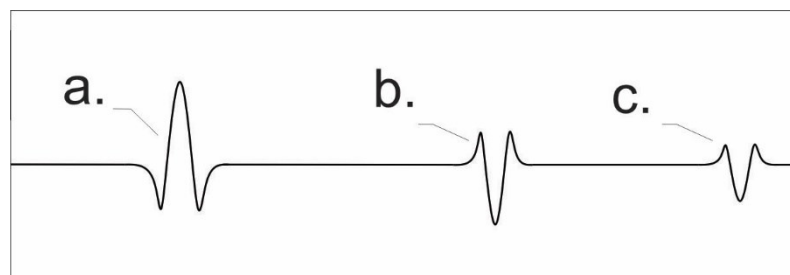


Figure 2.11. Simple seismogram for a 3-layer model.

- 2) The receiver is then lowered to a different spot along the borehole and step 1 is repeated at predetermined depth intervals ( $\Delta z$ ). One can then organize the recorded seismic traces by depth giving a raw VSP (Figure 2.12a). The initial wavelet arrival throughout the borehole (Figure 2.12a, Figure 2.12a, fb) is known as the first break (FB). Subsequent reflection wavelets are

shown (Figure 2.12b, c, Figure 2.12a, r1, r2). At this point, one can quickly extract a 1D velocity model, as the dotted line's slope in Figure 2.12a is in units of velocity.

- 3) More useful information can be obtained from this data set as it is particularly useful in highlighting the true depth at which seismic reflections originate, and it is useful to briefly outline the data processing steps used. First, each trace is then statically shifted to the left by its FB time value (Figure 2.12b). This 'flattens' the downgoing wavefield into a series of perfectly straight wavelets, the purpose of doing this is that the downgoing portion of the wavefield can more readily be separated from the upgoing. With the data in this arrangement, the downgoing wavefield (Figure 2.12c) can usually be accurately estimated using a median filter, although other techniques that employ various transforms of the image such as the  $z$ - $p$  and F-K are alternatives.
- 4) The downgoing wavefield (Figure 2.12c) is then subtracted from the flattened VSP (Figure 2.12b), and the remaining difference is the reflected wavefield (Figure 2.12d). The steps up to this point are known as wavefield separation.
- 5) The reflected wavefield is then right shifted back the right by double the first break amount, converting the time axis to two-way travel time (TWT), which has the effect of flattening the reflected wavefield. Everything within the trace prior to the first break and up to a certain time,  $\Delta t$ , after the first break (usually 100-200ms) is deleted. All that remains is a narrow strip of the traces immediately following the initial arrival, known as a 'corridor' mute (Figure 2.12e). This step is performed to eliminate multiples, as only the immediate reflections near boundaries make the cut.
- 6) Every corridor muted trace is then 'stacked' (summed at constant time) together giving a single seismic reflection trace in TWT (Figure 2.12f) which can then be directly compared to existing surface seismic profiles.

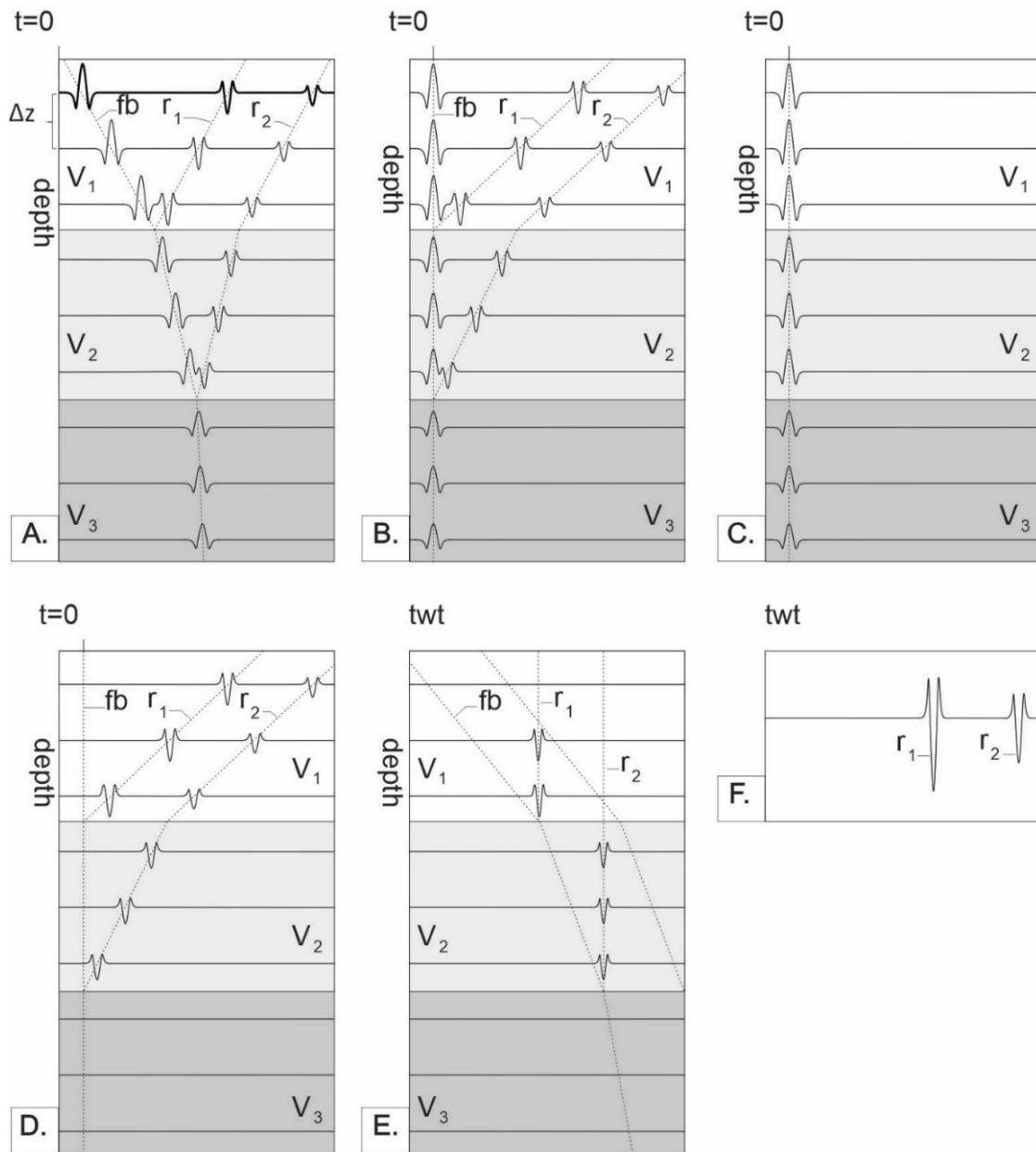


Figure 2.12. Primary VSP processing steps. a) Raw VSP. b) Flattened to first break. c) Downgoing wavefield. d) Reflected wavefield. e) Corridor mute. f) Seismic reflection profile.

## 2.3 Rock Physics

Later chapters also include the use of various models in rock physics that attempt to predict seismic wave speeds from knowledge of the rock's constituents. More precisely, the models are used to determine the moduli of the composite rocks that are then used with the density to determine wave speeds. The inverse problem of finding moduli from the observed wave speeds will be important to find moduli that can then be used to constrain damage. These models are briefly reviewed here as a convenience for the reader.

### 2.3.1 Isotropic Polycrystalline Wavespeeds

Knowing that the macroscopic properties of a crystal is controlled by repetition of highly ordered atomic lattices, it is no surprise that all minerals show at least some amount of anisotropy. Even the cubic unit cell will show anisotropy in elastic parameters depending on whether measurement is parallel or diagonal to the atomic bonds. However, elastic tensors are complex and many of the polycrystalline aggregates we study have randomly oriented mineral grains and are macroscopically isotropic.

#### *Voigt-Reuss Bounds*

The simplest models for composite material seek to bound the moduli and within the context of elasticity these models were developed nearly a century ago by Reuss and Voigt. Analogous to resistors in series (Figure 2.13), the upper possible limit for an isotropic elastic modulus of a single mineral component, pore-free, polycrystalline material can be calculated under the assumption of isostress (Voigt, 1928). Given the elastic stiffnesses  $C_{ij}$  (in the condensed Voigt notation) corresponding Voigt upper bound bulk and shear moduli for a specific mineral, respectively, are:

$$K_V \text{ mineral} = \frac{1}{9} [(c_{11} + c_{22} + c_{33}) + 2(c_{12} + c_{23} + c_{13})] \quad (2.18)$$

$$\mu_V \text{ mineral} = \frac{1}{15} [(c_{11} + c_{22} + c_{33}) - (c_{12} + c_{23} + c_{13}) + 3(c_{44} + c_{55} + c_{66})] \quad (2.19)$$

*Voigt theoretical isotropic upper limit for bulk and shear moduli of a mineral.*

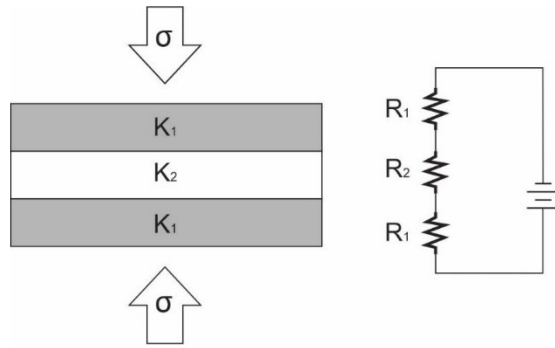


Figure 2.13. Voigt limit (isostress), analogous to electrical resistors in series.

Conversely, analogous to resistors in parallel (Figure 2.14), the lower possible limit for an isotropic elastic modulus can be calculated under the assumption of isostrain (Reuß, 1929). Reuss's lower bound corresponding bulk and shear moduli for a specific mineral, respectively, are:

$$K_{R \text{ mineral}} = \frac{9}{[(s_{11}+s_{22}+s_{33})+2(s_{12}+s_{23}+s_{13})]} \quad (2.20)$$

$$\mu_{V \text{ mineral}} = \frac{15}{4(s_{11}+s_{22}+s_{33})-4(s_{12}+s_{13}+s_{23})+3(s_{44}+s_{55}+s_{66})} \quad (2.21)$$

Reuss theoretical isotropic lower limit for bulk and shear moduli of a mineral.

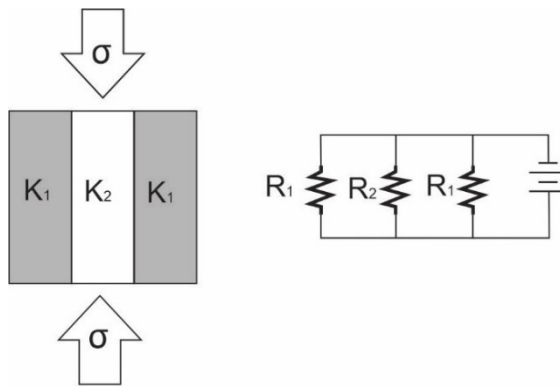


Figure 2.14. Reuss limit (isostrain), analogous to electrical resistors in parallel.

It is somewhat inconvenient that equations 28 and 29 require compliances while 26 and 27 use stiffnesses, and alternative forms of equations 28 and 29 are available where the compliances have been substituted for equivalent expressions in terms of stiffness (Watt, 1979, 1986). However, today's handheld electronic devices exceed the combined computational power of the entire world when the

aforementioned expressions were derived (Hilbert & López, 2011), and most may choose to leave inversion to the machines, utilizing the following identity:

$$\mathbf{C} = \mathbf{S}^{-1} \quad ( 2.22 )$$

*Strain/Compliance matrix relation.*

The Voigt-Reuss bounds can constrain a mineral's moduli quite tightly for many cases, and a simple arithmetic mean of the limits (Hill, 1952), is often presumed (but not guaranteed) to be close to experimentally derived values. Referred to as the Voigt-Reuss-Hill average, the following formulae can be applied to mineral or polycrystalline moduli:

$$K_{VRH} = \frac{K_R + K_V}{2} \quad ( 2.23 )$$

$$\mu_{VRH} = \frac{\mu_V + \mu_R}{2} \quad ( 2.24 )$$

*Voigt-Reuss-Hill average of elastic moduli.*

And the Voigt bulk and shear limits for an isotropic and aporous (crack free) polycrystal composed of  $n$  minerals are:

$$K_V = \sum_{i=1}^n \varphi_i K_{VRH \text{ mineral } i} \quad ( 2.25 )$$

$$\mu_V = \sum_{i=1}^n \varphi_i \mu_{VRH \text{ mineral } i} \quad ( 2.26 )$$

*Isostress (Voigt) Polycrystalline Limits of elastic moduli.*

Similarly, the Reuss bulk and shear limits for an isotropic and aporous polycrystal composed of  $n$  minerals are:

$$K_{R m} \left( \sum_{i=1}^n \frac{\varphi_i}{K_{VRH \text{ mineral } i}} \right)^{-1} \quad ( 2.27 )$$

$$\mu_{V m} \left( \sum_{i=1}^n \frac{\varphi_i}{\mu_{VRH \text{ mineral } i}} \right)^{-1} \quad ( 2.28 )$$

*Isostrain (Reuss) Polycrystalline limits of elastic moduli.*

Where  $\varphi_i$  is the volumetric abundance of the  $i^{\text{th}}$  mineral.

Although the Voigt-Reuss-Hill average is often a very good estimate, the upper and lower limits can be poorly constrained in certain situations. For rigor beyond what is required here, one may consult the work of Simmons & Wang (1971), who derived theoretical limits for every crystal class *other* than triclinic based on the principles of Hashin & Shtrikman (1962).

#### *Mineral Density*

If the  $i^{\text{th}}$  mineral densities are readily available, then the bulk density for an aporous polycrystal composed of  $n$  minerals is:

$$\rho_m = \sum_{i=1}^n \varphi_i \rho_{\text{mineral } i} \quad ( 2.29 )$$

*Polycrystalline bulk density.*

Now armed with the theoretical rock frame properties of  $K$ ,  $\mu$ , and  $\rho$ , it is very quick to find the intrinsic, crack free wavespeeds of a polycrystal via equations 15 and 16. However, although mineral moduli and densities appear to be widely available, in practice they are not usually easy to measure. Methods to directly determine mineral density rely on accurate measures of mass and volume, making the Archimedean method reliable only when a sufficiently large pure aporous crystal can be grown. Alternatively, Boyle's law can be exploited with much smaller grains via helium pycnometry (Lowell et al., 2012), although a pure sample of the mineral is still required. Additionally, values reported with helium pycnometry may be less than the true mineral density, as there may be pores within the frame



which are fully inaccessible by any fluid. For minerals not available in large single crystals, samples can be made into a powder and X-Ray diffraction can tightly constrain the dimensions of a mineral's unit cell. Since the molar mass can be calculated precisely from first principles, X-ray crystallography is potentially the most accurate method of obtaining true mineral density. These issues do impact our capacity to fully understand the highly shocked materials discussed in later chapters as currently there do not exist adequate measurements of these materials.

### 2.3.2 Effects of Porosity

Although the previous method is useful for carefully grown and annealed aporous rocks perhaps originating from the Earth's mantle or a laboratory, real rocks have pores. Porosity,  $\Phi$ , is defined as the volumetric fraction of a rock that is not rock. If one has the theoretical rock frame density available (equation 37), then the difference from bulk density can be used to estimate porosity:

$$\Phi = \frac{V_{void}}{V_{total}} = \frac{\rho_m - \rho_{bulk}}{\rho_m} \quad (2.30)$$

*Porosity as a function of density.*

Equation 38 is also applicable if the grain density can be directly measured such as with helium pycnometry. Similarly, a simple method for determining porosity utilizes water where the mass of a sample is measured dry and saturated:

$$\Phi = \frac{m_s - m_d}{V \rho_{water}} \quad (2.31)$$

*Porosity as a function of water saturation.*

This method can provide good estimates for well-connected pores although uncertainty in the sample's volume and surface wetting can contribute significant error. This method was used to estimate porosities in the core samples at the Expedition 364 Sampling Party.

Although obvious that introducing porosity will alter the density of an aporous rock, the specifics can be quite complex with the exception of complete pore saturation with a single fluid. In this case, the pore saturated density can be found simply by considering the fluid as an  $i^{\text{th}}$  mineral in equation 37. For this purpose, gaseous fluids can be approximated as zero density. Additionally, one could estimate mixtures of fluids within pore space by substituting multiple  $i^{\text{th}}$  terms, although the theoretical details of partial fluid saturation would be a thesis project all on its own.

Introducing porosity to a rock frame will unilaterally decrease the density, which would by itself cause seismic wavespeeds to increase due to density being in the denominators of equations 15 and 16. However, the pores also decrease elastic moduli in the numerators, and the overall effect of porosity is most usually to decrease seismic wavespeeds, although the competing of effects of moduli and density must always be considered. One definition of a fluid is any material with a shear modulus of zero; thus, if we swap the pore saturation of one fluid (eg. air) for one with a higher density (eg. water), the shear modulus will be zero in either case, yet the bulk density is higher for water saturation, which causes a decrease in  $V_s$ . However, water's bulk modulus is 3 orders of magnitude greater than air's, which would cause an increase in  $V_p$  for the water saturated example. Although the differences in density and elastic moduli are not as extreme as with air and liquids, taking advantage of this divergent saturation dependence has obvious economic applications in the case of oil vs. water saturation.

#### *Gassmann's Model*

Using the assumption of that static deformation moduli will apply to low frequency seismic wave propagation for a fully saturated porous isotropic solid, relatively simple expressions for saturated moduli have been developed (Gassmann, 1951). In developing his equations, Gassmann further assumed no chemical interaction between the fluid and mineral, that there is only one mineral in the rock, and that the fluid does not affect the rock's shear modulus. This final assumption is very critical, as it implies the dry and saturated shear moduli are equal:

$$\mu_s = \mu_d \quad (2.32)$$

*Gassmann's shear modulus relation.*

The forward and inverse versions relating dry to saturated bulk moduli are:

$$K_s = K_d + \frac{\left(1 - \frac{K_d}{K_m}\right)^2}{\frac{\phi}{K_f} + \frac{K_d}{K_m} - \phi} \quad (2.33)$$

$$K_d = \frac{\left(\frac{\phi K_m}{K_f} + 1 - \phi\right) K_s - K_m}{\frac{\phi K_m}{K_f} - 1 - \phi + \frac{K_s}{K_m}} \quad (2.34)$$

*Gassmann's bulk modulus relations.*

Owing mainly to their simplicity, Gassmann's equations are very popular. However, seismic wave propagation is not a static (zero frequency) phenomenon and these equations should only be used as an estimate, as the deviation from true values can be quite significant, particularly at low pressure (He & Schmitt, 2006). Incorporating viscoelastic behaviour of fluids within the pore space is frequency dependent: in a sufficiently permeable medium, the entire fluid body acts with "global flow" (Biot 1956a,b), a process that is dominant at seismic frequencies, with an upper limit of pore diameter being on the same order as wavelength. Unfortunately, Biot's method requires knowledge of at least 14 physical parameters which is far beyond the 2 to 4 generally available. Full descriptions of Biot's global flow analysis methods can be found in several contributions (Bourbié et al., 1992; Johnson, 1986; Smeulders, 2005). Conversely, at high frequencies local flow is more significant. The squirt model is dependent on compressible pores of high aspect ratio (cracks) oriented both parallel and orthogonal to the direction of stress, such that fluid is *squished* from the compressed cracks and *squirts* into the uncompressed cracks (O'Connell & Budiansky, 1977). Frequency response of squish-squirt flow is highly

dependent on crack density, permeability, and crack characterization. As such, frequency response can be resonant, particularly for homogenous crack properties (Hilpert et al., 2000). Although much work has been done investigating local flow viscoelasticity, developing non-empirical equations has proven problematic (Schmitt, 2015).

#### *Kuster-Toksoz Model*

Long wavelength scattering theory was used to develop the Kuster-Toksoz (KT) model, which can incorporate the combined effects of different inclusions, such as fluid filled pores (Kuster & Toksöz, 1974). As with most models, KT assumes dilute non-interacting pores. Although this is not strictly valid for extensively damaged media, it has been included since analytical inversions are possible for a single pore type, and multi-pore inversions can grant insight to pore type distribution.

The KT forward method is to sum the volumetric contributions of the difference in elastic moduli between the inclusion and rock frame, which is weighted by a geometric factor ( $P^{mi}$ ,  $Q^{mi}$ , Table 2.2). The total of this summation can then be compared to the discrepancy between KT predicted elastic moduli and rock frame moduli, as follows:

$$(K_{KT} - K_m) \frac{3K_m + 4\mu_m}{3K_{KT} + 4\mu_m} = \sum_{i=1}^N x_i (K_i - K_m) P^{mi} \quad (2.35)$$

$$(\mu_{KT} - \mu_m) \frac{\mu_m + \xi_m}{\mu_{KT} + \xi_m} = \sum_{i=1}^N x_i (\mu_i - \mu_m) Q^{mi} \quad (2.36)$$

*Kuster-Toksoz model moduli relations, where  $P, Q^{mi}$  are the geometric weighting factor for inclusion type  $i$  (table 4.1),  $x_i$  is the volumetric fraction of inclusion type  $i$ ,  $K$  and  $\mu$  are bulk and shear moduli, respectively, with subscripts  $KT$ ,  $m$ , and  $i$  denoting Kuster Toksoz prediction, rock frame, and inclusion, respectively.*

Inclusion Shape	$p^{mi}$	$Q^{mi}$
Spheres	$\frac{3K_m + 4\mu_m}{3K_i + 4\mu_m}$	$\frac{3\mu_m + 4\xi_m}{3\mu_i + 4\xi_m}$
Needles	$\frac{3K_m + 3\mu_m + \mu_i}{3K_i + 3\mu_m + \mu_i}$	$\frac{1}{5} \left( \frac{4\mu_m}{\mu_m + \mu_i} + 2 \frac{\mu_m + \gamma_m}{\mu_i + \gamma_m} + \frac{3K_i + 4\mu_m}{3K_i + 3\mu_m + \mu_i} \right)$
Discs	$\frac{3K_m + 4\mu_i}{3K_i + 4\mu_i}$	$\frac{\mu_m + \xi_i}{\mu_i + \xi_i}$
Penny Cracks	$\frac{3K_m + 4\mu_i}{3K_i + 4\mu_i + 3\pi\alpha\beta_m}$	$\frac{1}{5} \left( 1 + \frac{8\mu_m}{8\mu_i + \pi\alpha(\mu_m + 2\beta_m)} + \frac{6K_i + 4(\mu_i + \mu_m)}{3K_i + 4\mu_i + 3\pi\alpha\beta_m} \right)$
Algebraic Tidying Coefficients		
$\beta = \mu \frac{3K + \mu}{3K + 4\mu}$	$\gamma = \mu \frac{3K + \mu}{3K + 7\mu}$	$\xi = \mu \frac{9K + 8\mu}{6K + 12\mu}$

Table 2.2. Geometric weighting factors for the Kuster-Toksoz elastic moduli model, table modified from Liu & Sun (2015).

## 2.4 Hypervelocity Impacts as a Geological Process

Geologists prefer to classify a rock by the most recent of the three fundamental geological processes it underwent. These processes occur on the order of thousands to millions of years, and are even known to exceed academic timescales. Impact events, however, are extremely rapid, with all three fundamental geological processes occurring over a period of seconds to minutes. Depending on exactly where a rock originally sat in the target lithology, an impactite may have one (e.g., spall, sedimentation), two (e.g., ejecta, sedimentation and metamorphism), or all three (e.g., suevite) of the fundamental geological processes involved. As such, I provide here a Venn diagram illustrating this overlap (Figure 2.15). Impactite classification is under continual debate and official terminology appears to be a moving target (e.g., King & Petruny, 2003; Stöffler & Grieve, 1994; Stöffler et al., 2018).

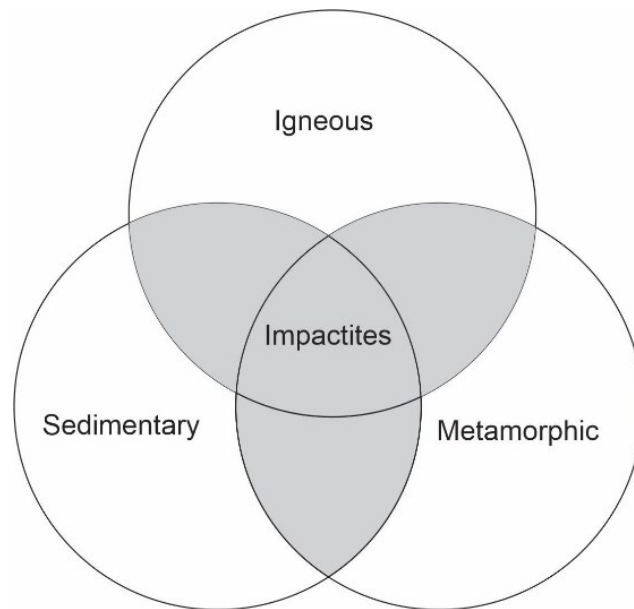


*Figure 2.15. Venn diagram illustrating the author's perspective on the difficulty of classifying impactites within the 3 classical categories of rock formation.*

### 2.4.1 Formation

Impact structure formation is largely controlled by the weakest of the four fundamental forces in nature: gravity. Unlike most geological processes, impact structures form very quickly: on a scale of

seconds to minutes. What happens when an unstoppable force meets an immovable object (Watson, 2003)? Modelers have decided on 3 main stages of impact formation: compression, excavation, and modification.

### *Compression*

When the orbits of two objects meet at the same point in time and space, and the smaller object (i.e., bolide) is large enough to survive the trip through the larger object's atmosphere, an impact structure is formed. Even in the unusual case of an asteroid having very little velocity differential with Earth, the gravity well to Earth's surface is 11 km/s deep. If the bolide's size is sufficient for atmospheric drag to be negligible, then any contact with an asteroid is in the realm of hypervelocity impacts. The initial contact, known as the compression phase, lasts a fraction of a second. Modelling suggests that bolide penetration depth is up to twice the bolide's diameter (Kieffer & Simonds, 1980; O'Keefe & Ahrens, 1982) with nearly all of the former bolide's kinetic energy converted to heat and compression of the target rock; however, a small amount of energy does remain in the kinetic form to power jetting of melt and vapor. The bolide is initially compressed, as well, although when the shock wave reaches the unconstrained upper surface of the bolide, it is reflected downward as a rarefaction wave. Although the transition from compression to excavation is a continuum, the end of the compression phase can be defined as the moment this reflected rarefaction wave reaches the bolide/target interface (Figure 2.16),

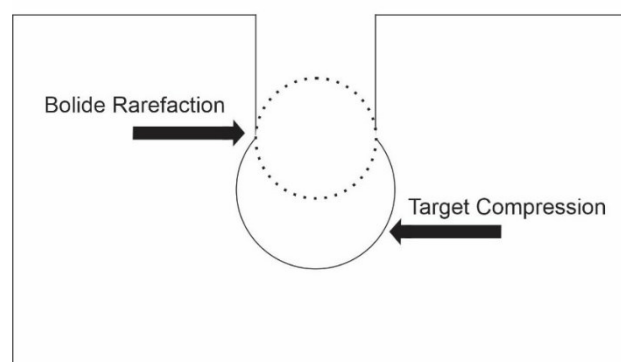


*Figure 2.16. Initial compression phase, in the first instants of target contact. Modified from Kieffer and Simonds (1980).*

(Kieffer & Simonds, 1980). Although fragments of smaller bolides have been found to survive impact, all that remains of the original impactor large enough to create a complex crater is a geochemical signature.

### *Excavation*

The shockwave front propagates hemispherically from the projectile's penetration depth, and rarefaction reflections from the free surface destructively interfere with the shock front of peak pressure resulting in an altered-hemispherical peak pressure distribution (Figure 2.17). The rapid decline of peak shock pressure near the surface should result in some material not exceeding the elastic limit and therefore being ejected with no shock alteration, a process known as spalling. With the primary rarefaction wave close behind, the direction of material displacement is orthogonal to peak pressure isobars. This means that near the surface, material is ejected upward, at middle depths material is displaced outward, and material at the greatest depths is displaced downward and outward (Figure 2.18). The resulting structure has an aspect ratio is  $\sim 3:1$  (Croft, 1985), is gravitationally unstable, and is referred to as the transient crater.

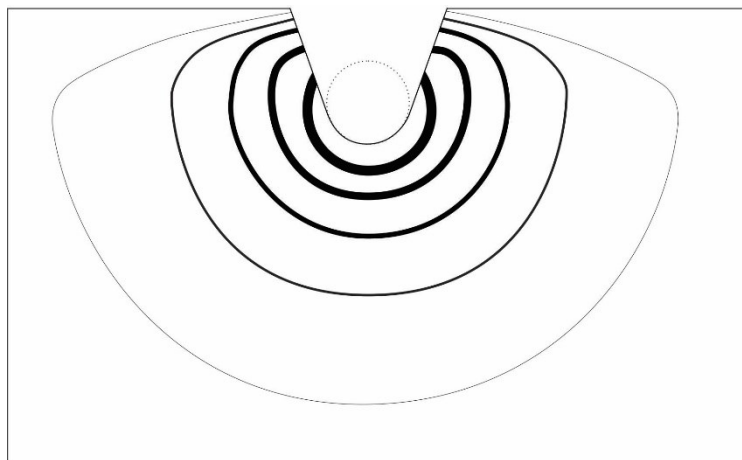


*Figure 2.17.. Peak pressure isobars during compression phase, thicker lines corresponding to higher pressure. Modified after French (1998).*



### Modification

Transition from the shock wave controlled excavation to the gravity controlled modification stages is gradual and may occur at different times at different points in the crater (Melosh, 1989). The modification stage includes rebound of the compressed crater floor, and gravitational collapse of various unstable transient structures. Of the three stages of crater formation, the modification stage is the longest lasting, most complex, and most poorly understood.

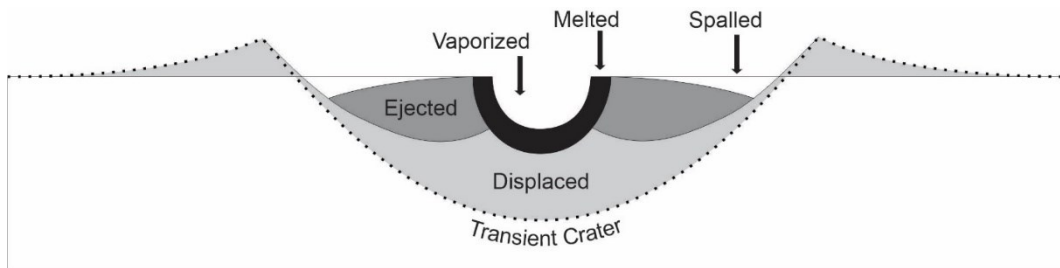


Figure 2.18. Zones of impact effects. Modified after French (1998).

### 2.4.2 Classification of Craters

#### Simple

Also known as a bowl shaped crater, simple craters (Figure 2.19, Figure 1.1) go under relatively little modification. The transient crater walls collapse, which can increase the diameter of the apparent structure by as much as 20%, and a fallback lens of ejecta collects within (Figure 2.19), filling the transient cavity by  $\sim$  half its original depth.

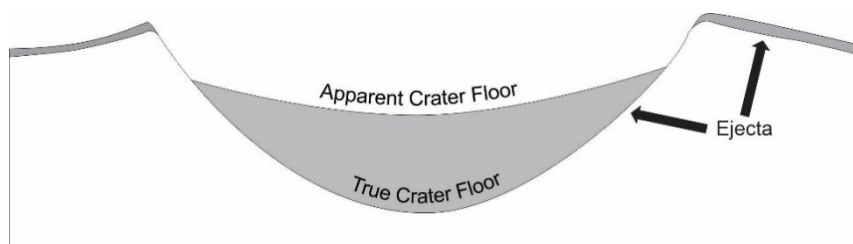


Figure 2.19. Simple crater cross section. Modified from French (1998).

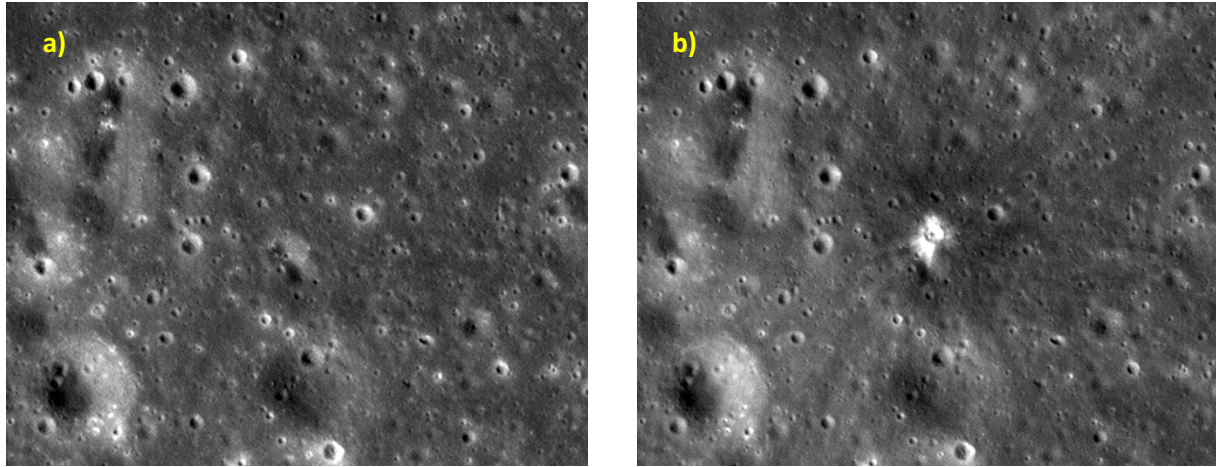


Figure 2.20. Lunar Impact, March 17<sup>th</sup>, 2013. a) Pre-impact (2012/02/12). Regolith is relatively homogenous in color. b) Post impact (2013/07/28). Regolith shows light colored ejecta near center and a dark colored ejecta blanket radiating outward. Image credit: NASA.

### Complex

At a certain size that is controlled mainly by the target's gravity, upward rebound of the target floor will compete with inward collapse of the transient rim, and the transient rim undergoes much more extensive collapse modification. Target lithology strength constrains the transition from simple to complex craters as well, with the upper limit for simple terrestrial craters at 2 to 4 km for sedimentary and crystalline targets, respectively (French, 1998). The Moon, however, shows transition from simple to complex structure at 20km diameter indicating the strong control of gravity on the structure's formation.

### Central Uplift

Rebound of the complex crater floor results in a central uplift which can be further subcategorized (Figure 2.21) into a central peak (Figure 2.22), a central peak-basin, or a peak ring basin roughly dependent on the structures size. The three categories are somewhat arbitrary, as they lay among a



Figure 2.21.. Complex crater continuum. a) Central peak. b) Central peak basin. c) Peak ring basin.

continuum of the central uplift modification process (Figure 2.21). The details of the central uplift process are currently an active area of research; by assuming target rock fluidization (Riller et al., 2018), modelers have been successful in replicating central uplift structure for hypervelocity impacts (Morgan et al., 2016). Geological sampling of complex crater structure provides important constraints, with central uplift materials originating at a depth of  $\sim 1/10$  the final impact structure diameter (Grieve et al., 1981).

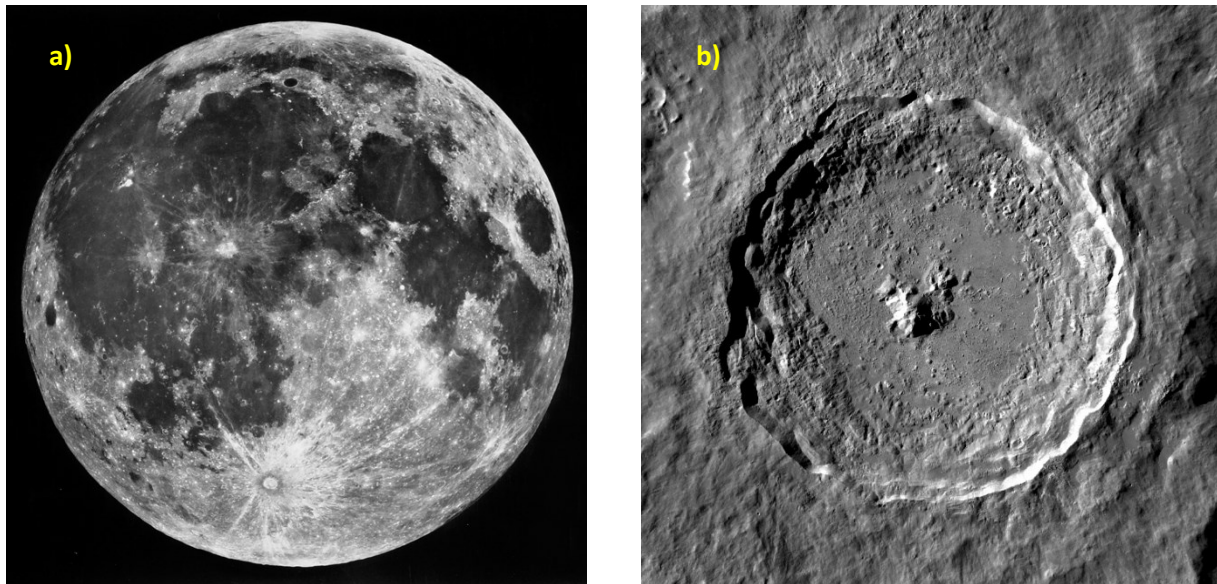
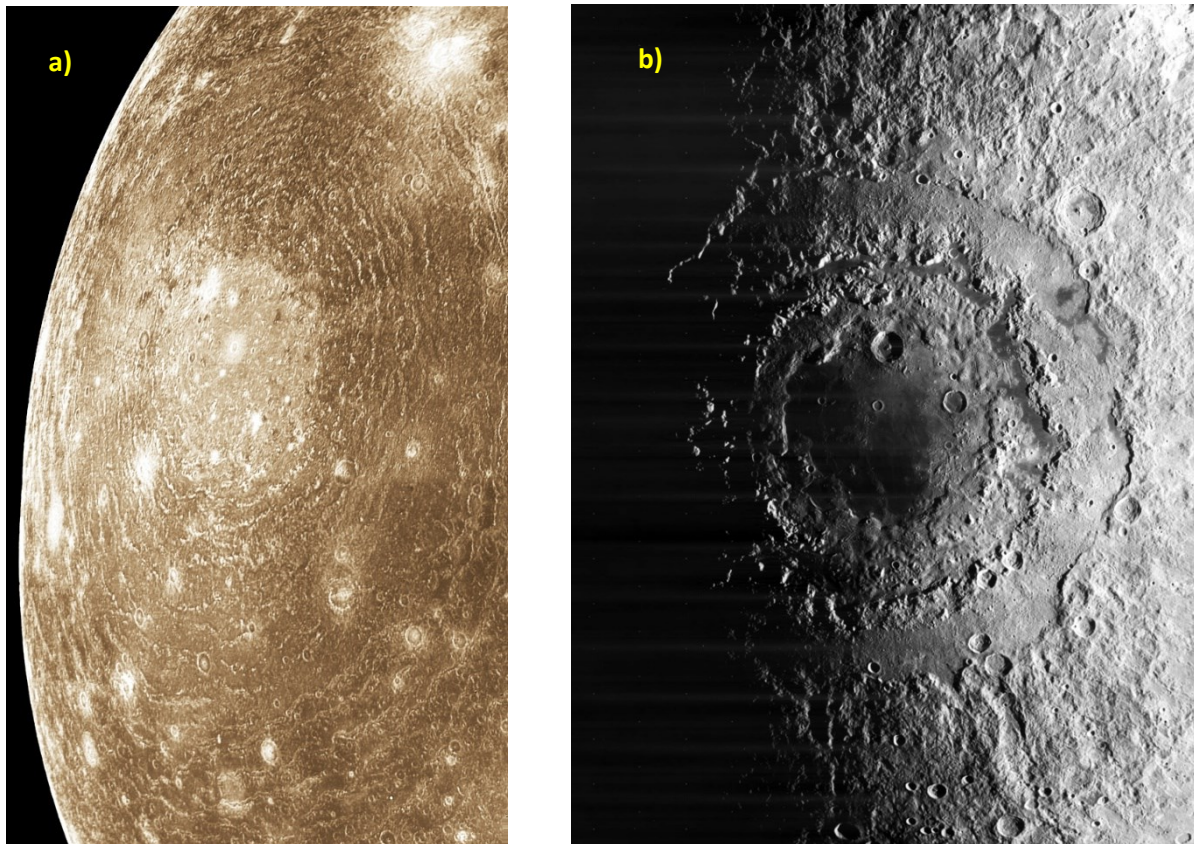


Figure 2.22. Tycho Crater, Luna. a) Light color ejecta pattern seen radiating from crater (bottom middle). b) Overhead view with prominent central uplift. Image credit: NASA.

### Multi-Ring

The most poorly understood and largest impact structures display multiple concentric structures and are hundreds to thousands of kilometers in diameter. The transition from central uplift to multi ring basin also appears to be controlled by the target's gravity, with the multi ring threshold on the Moon around 600 km (French, 1998). Multi-ring basins are prevalent on the Moon and Calisto (Figure 2.23), yet rare on Ganymede and nonexistent on Mercury or Mars. Such interplanetary heterogeneity suggests target lithology may be a critical parameter in multi-ring basin formation. Various definitions of multi-ring

basins have been put forward, largely depending on the author's desired interpretation. One definition considers faint features outside the crater rim to qualify as multi-ring, making Chicxulub a multi ring structure (Morgan & Warner, 1999). Another example of multi-ring by definition is the 20km Silverpit Structure in the North Sea, with a 2km suspected crater surrounded by concentric ring faults (Osinski & Pierazzo, 2012).



*Figure 2.23. Multi-ring impact basins. a) Valhalla Crater, Callisto. Total diameter ~ 3000 km, bright central area 700 km.*

*b) Mare Orientale, Luna. Total diameter ~ 900 km. Image credit: NASA.*

### 2.4.3 Dynamic Collapse Model

Although peak ring formation is still being discussed, two competing models have emerged to explain the dynamics of their formation. The first is the nested melt cavity (NMC) hypothesis that postulates that a trapped central melt cavity tunnels downward leaving the unmelted shocked “shell” as a peak



ring (Head, 2010). Although the NMC model may prove to be valuable in elucidating multi-ring basin structure, drilling of the Chicxulub Peak Ring provided evidence strongly in support of the Dynamic Collapse Model (DCM), (Morgan et al., 2016). Although experiments at small scale do not appear to be able to create a peak ring structure (Dörfler & Kenkmann, 2020), extensive hydrocode modelling has been successful in reproducing peak ring structures that support the DCM. In this model (Figure 2.24), the target rock behaves as a fluid in the seconds to minutes post impact: the central uplift becomes extremely high rebounding to elevations similar to the depth of excavation of the transient crater. This unstable central uplift then collapses downward, and gains enough downward momentum that it continues to flow outward. Rock fluidization then subsides, and the subdued 'ripple' is frozen as a peak ring.



Figure 2.24. Dynamic collapse model. a) Isostatic rebound overshoots stability. b) Central uplift collapses downward and outward. c) Outward momentum continues until rock fluidization subsides.

## 2.5 Shock Metamorphism

With obvious exceptions such as seismic and volcanic events, metamorphic processes are generally quite slow on human timescales. Although higher temperature phases of solid materials have been known for quite some time, allowing materials to cool naturally is a slow enough process to allow reversion back to ambient polymorphs. However, rapidly cooling, i.e., quenching (Stöffler et al., 1991) can allow a higher order polymorphs to exist at ambient pressures and temperatures not ordinarily permitted by adiabatic phase diagrams. This quenching phenomenon has been known since at least the middle-ages in the case of tempering steel, and is used extensively today in metal fabrication. The opposite of quenching, known as annealing, is the process of allowing a material to cool very slowly from higher order phases. This generally has the effect of refining grain structure and improving ductility and homogeneity of the low order phase (Digges et al., 1966).

### 2.5.1 Shock Waves

When a hypervelocity projectile impacts, a large fraction of its kinetic energy compresses the target material at the projectile/target interface (Figure 2.16). This zone of extreme compression immediately seeks to radiate away to uncompressed material around it. The nearly discontinuous extreme rise in wave front pressure, followed by the reflected rarefaction wave, provides the rapid quenching procedure for higher order polymorphs to survive in ambient surface conditions. The hypervelocity shock wave rapidly attenuates geometrically, and mellows out into a P-wave at some distance from ground zero. The peak pressure of an impactor's shock wave can easily exceed 100 GPa.

### 2.5.2 Hugoniot-Rankine Conditions

A key component of understanding impact metamorphism is the material-specific equation of state known as a Hugoniot curve (Figure 2.25). The Hugoniot Rankine conditions are simply an experimentally determined adiabatic relationship between pressure and specific volume (Short, 1966). Although nearly trivial for fluids, the general shape for a mineral's Hugoniot curve for a given material contains three

distinct regimes in pressure versus specific volume (i.e. reciprocal of density) space delineated by differing types of behaviour that include:

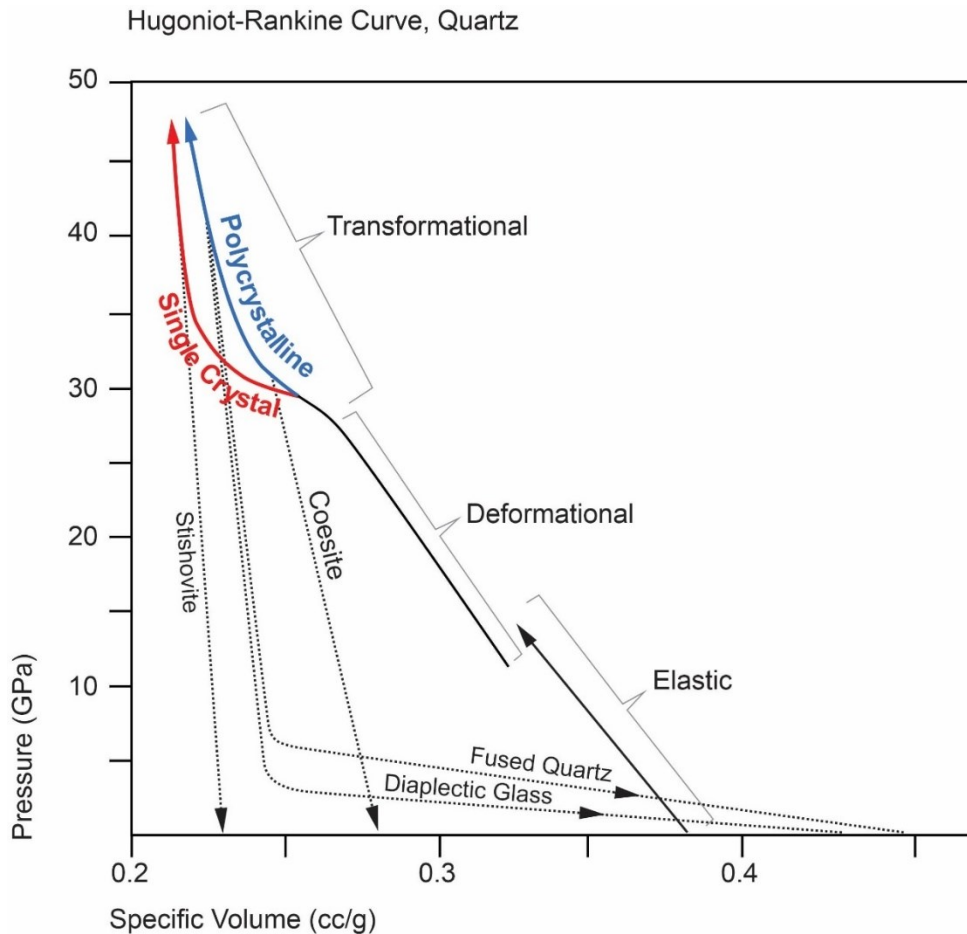


Figure 2.25. Hugoniot-Rankine equation of state for Quartz.

**Elastic deformation.** At low pressures the material deforms elastically with a linear relationship between density and pressure. This regime persists to the elastic limit of the material, usually referred to as the Hugoniot Elastic Limit (HEL).

**Brittle/plastic deformation.** Once the HEL pressure is exceeded, the material enters a combined elastic /plastic deformation zone. The material loses most of its shear rigidity above the HEL and behaves more fluid-like. Permanent structural changes occur at the micro and macro level.

**Transformational.** Many minerals will undergo solid state phase transformation to denser forms dependent upon the stress and temperature. Shock pressures in large impacts are often sufficient to convert the minerals to their high pressure polymorphs with different crystal structure. Further, the deformation can also produce partial intragranular melting. This portion of the phase diagram ends with total melting and can continue with the Hugoniot curve for the fluid of the constituent molecules.

An early database of known Hugoniot curves for 18 minerals was compiled just prior to the space race and ensuing golden age of shock recovery experiments (Anderson & Kanamori, 1968). It shall be seen that, in general, the brittle deformation portion of this curve dominates the observed. Based on peak pressure achieved in crystalline target rocks, stages of shock metamorphism are roughly categorized in Table 2.3 (French, 1998).

Pressure (GPa)	Effects
<2	Fracturing and brecciation, without development of unique shock features.
2-30	Shatter cones, with distinctive microscopic deformation features above 10 GPa
8-25	Microscopic planar deformation features in individual mineral grains, most prevalently quartz and feldspar. See section on quartz for more detail.
25-40	Transformation to diaplectic glasses without melting. Accompanied frequently by high pressure mineral polymorphs.
35-60	Selective melting of individual minerals, particularly feldspar.
60-100	Complete melting of all minerals to form a rock melt.
>100	Complete rock vaporization. No preserved minerals formed at these pressures.

Table 2.3. Categories of shock metamorphism.

### 2.5.3 Experiments in Shocked Mineralogy

In this section we present a brief overview of lab induced shock metamorphism in various rocks and minerals. The collective term shock recovery experiment is used in the literature for many processes with fundamentally the same working principle (Stöffler & Langenhorst, 1994):

- 1) A target mineral is placed in a metal vessel
- 2) A metal plate is accelerated toward the containment vessel, generally with a pneumatic cannon or conventional explosive of some type.



- 3) Upon contacting the metal vessel, a shock wave is produced which reflects many times through the containment vessel. Due to this interference prior to arrival of the rarefaction wave, peak pressure is often much higher than the initial shock wave propagation.
- 4) The target mineral is recovered from the metal containment vessel and investigated for shock alteration effects.

### *Quartz*

As the classic fingerprint of shock effects, no discussion of shock metamorphism would be complete without quartz, thus our discussion begins here. Shock induced transformations in quartz were first reported in 1959 (De Carli & Jamieson) which spurred extensive further studies showing the diverse nature of shocked quartz; the specific and unique nature of shocked quartz is instrumental to identifying astroblemes, and this irrefutable evidence was critical for overcoming resistance in the geological community to bolides being a significant and continuing geological process on Earth.

Much of the literature on shocked quartz has previously been reviewed (Stöffler & Langenhorst, 1994), thus we will begin with a short summary of this work.

An important assumption in the study of impact shocked quartz is as follows: In the Earth's upper crust, the only stable form of  $\text{SiO}_2$  is trigonal  $\alpha$ -quartz. Given that bolides strike the crust's surface, the assumption is that all terrestrial quartz containing impact sites will show shock metamorphism effects to trigonal  $\alpha$ -quartz. However, hexagonal  $\beta$  quartz is present in the lower crust which can be affected by the largest impactors and thus  $\beta$  quartz should not be ignored for a complete discussion of shock metamorphism.

All the major effects in shock induced quartz were unravelled from 1959-1968 (Table 2.4). De Carli & Jamieson (1959) spurred the shocked quartz research frenzy by demonstrating that single crystal quartz becomes amorphous during shock compression

Author	Discovery	Experiment or Locality
(Coes Jr, 1953)	Coesite	Synthesis by Static Compression
(De Carli & Jamieson, 1959)	Amorphized Quartz	Shock Recovery Experiment
(Stishov & Popova, 1961)	Stishovite	Synthesis by Static Compression
(Chao et al., 1960)	Natural Coesite	Barringer Crater, USA
(Chao et al., 1962)	Natural Stishovite	Barringer Crater, USA
(McIntyre, 1962); (Englund & Roen, 1963)	Planar Microstructures	Clearwater Lakes, Canada; Middlesbo, USA
(Bunch & Cohen, 1964)	Crystallographic Orientation of Planar Microstructures	Barringer Crater, USA
(De Carli & Milton, 1965)	Stishovite	Shock Recovery Experiment
(Stöffler, 1966); (von Engelhardt, 1967)	Amorphized quartz is diaplectic quartz glass	Ries Crater, Germany.
(Engelhardt et al., 1968; Müller & Défourneaux, 1968)	Planar Microstructures	Shock Recovery Experiments

Table 2.4. Discoveries of shock effects in quartz. Modified from Stöffler & Langenhorst (1994).

Quartz is well suited to laboratory study and it is well established that pure  $\alpha$  quartz has a brittle yield strength very close to the theoretical elastic limit (Doukhan & Trépiéd, 1985). However, the presence of trace amounts of water results in ductile behaviour known as hydrolytic weaking (Griggs & Blacic, 1965) which is an extremely slow process when compared to shock effects.

Mechanical twinning in quartz, also known as 0001 twinning, can only be caused by extremely rapid deformation (McLaren et al., 1967) and shock waves (Goltrant et al., 1992). As such, it is a useful diagnostic feature for impact events since it has never been observed in tectonically deformed quartz. The lower limit required for “unequivocal shock induced effects” (Stöffler & Langenhorst, 1994) in quartz is its HEL at 5 GPa this continues up and spans up to 50 GPa after which complete melting occurs.

The variety of pressure specific alterations possible in quartz make it a powerful tool for mapping topographically eroded astroblemes. General unordered fracture networks are also pervasive in shocked quartz, yet this is not a unique shock induced feature and will be omitted from discussion. As such, the following classification scheme has been developed:

## Low Pressure Regime:

1. Planar microstructures
  - 1.1 Planar fractures parallel to rational low index crystallographic planes
  - 1.2 Planar deformation features (PDFs) parallel to rational low index crystallographic planes
    - 1.2.1 Non-decorated PDFs
    - 1.2.2 Decorated PDFs
2. Mosaicism

## High pressure regime:

3. Diaplectic quartz glass (amorphized quartz = short-range-order phase)
4. High pressure polymorphs (coesite, stishovite)
5. Liquid (quenched to silica glass = lechatelierite)
6. Vapor (condensed to silica glass)

Caution should be used when applying these results, as it has been shown that the effects of temperature can vary the shock effects quite significantly (Langenhorst et al., 1992).

## Low Pressure Regime

The bottom end of the low temperature regime is defined strictly by the Hugoniot elastic limit (HEL), at which point brittle failure can occur. The HEL is not isotropic, however, and varies in quartz between 3.5 and 8 GPa depending on the shock direction through the crystal. However, 5 GPa is typically defined as the lower limit for onset of shock related effects with 7 GPa as the most probable threshold for true shock related effects. The upper end of the low pressure regime is derived from the inflection point between deformational and transformational points in quartz's Hugoniot curve from shock recovery experiments (Figure 2.25). Thus, the generally accepted range for the low pressure regime in shock altered quartz is considered to be 5-35 GPa.

Irregular, non-planar fracturing is common throughout shocked quartz, yet this feature can be created through elastic shocks below 5 GPa and is not a strictly shock feature. However, general fracturing intensity has been used successfully to calibrate shock intensity at low pressures (Short, 1968).

#### Planar Microstructures

With the aid of optical microscopes, planar microstructure is a clear indicator of shock alteration. Planar fractures (PF) are parallel sets of open fractures with a spacing of at least 20 micrometers. PFs act as grain boundaries and are the lowest energy feature specific to shocked quartz.

Associated with higher pressures, planar deformational features (PDF) are similar to PFs but are more tightly spaced (2-10 micrometers). PDFs are thought to develop after PFs as PDFs develop within the grain boundaries created by PFs. PDFs become more regular and closely spaced with increasing shock intensity. PDF microstructure has been thoroughly described by (Engelhardt & Bertsch, 1969). PDFs that are not easily resolvable in the microscope are termed non-decorated, as opposed to the more common decorated-PDF which can easily be observed using optical microscopes. It is thought that decorated PDFs are secondary structures that develop during annealing of the target rock. This is supported by decorated PDFs being the most common type in annealed breccias and slow cooled crater floors, as well as the complete absence of decorated PDFs in rapidly quenched laboratory target rock samples.

Mosaicism is an optical characteristic of shocked quartz showing PDFs as the spacing is near enough to cause optical diffraction.

In addition to aforementioned effects, shocked  $\alpha$  quartz also shows anomalous biaxial optics. Optic axial angles in unshocked quartz of up to  $10^\circ$  are commonly reported, sometimes as high as  $28^\circ$  (Short, 1970). However, quartz containing multiple PDFs has yielded birefringence of up to  $70^\circ$  (Langenhorst & Deutsch, 1993). Anomalous densities as low as 2.28g/cc for shocked quartz have been accurately measured (Langenhorst & Deutsch, 1994), whereas single crystal alpha quartz has a density of 2.65g/cc.

## High Pressure Regime

It has been shown that the vast majority of quartz (>95%) shocked above 35 and below 50 GPa (the high pressure transformational regime) is transformed to an amorphous, low density glass known as diaplectic glass (Stöffler, 1984). Diaplectic glass is easily distinguished from regular silica glass by its higher index of refraction, as well as coesite and stishovite inclusions. At pressures above 50 GPa, quartz is fully shock melted which can cool rapidly to a glass known as lechatelierite. Although common in impact craters, lechatelierite is absent from the shocked quartz portions as the phase diagram permits only liquid quartz at pressures above 50 GPa. Shock produced lechatelierite is similar to synthetic silica glass, however, it is the textural setting which distinguishes it as shock induced.

The truly exotic minerals unique to shocked quartz are coesite and stishovite with densities of 2.92 g/cm<sup>3</sup> and ~4.3 g/cm<sup>3</sup>, respectively, at room conditions. These are considerably denser than normal  $\alpha$ -quartz with a density of 2.65 g/cm<sup>3</sup>. Although counterintuitive to the Hugoniot curve (Figure 2.25), stishovite generally forms at lower shock pressures than coesite. This is because stishovite forms during shock compression, whereas coesite forms during release from the pressurized phase.

Coesite is a fine grained and colorless to brownish polycrystalline aggregate 100-200 micrometers in size. Individual crystals in coesite are generally around 1 micrometer. The highest concentrations of coesite are found in highly vesiculated quartz exposed to pressures very near the melt limit of 50 GPa. Stishovite, although difficult to identify with optical microscopes, is indicative of moderately shocked rocks that were rapidly quenched. Stishovite is often found subparallel to PDFs, and is the densest of the shocked quartz polymorphs. Stishovite is also the second hardest oxide known. It is important to also note that these phases are metastable at surface conditions on the earth.

Stöffler & Langenhorst (1994) conclude their description of shock metamorphosed quartz minerals by summarizing pressure ranges expected for Stishovite and coesite: Stishovite can be expected in trace

amounts in rocks exposed to shock pressures of 12-45 GPa, whereas coesite can be formed in clasts of peak pressures between 30 and 60 GPa. However, quenching is often necessary for these polymorphs to survive.

Spurred by the space race and retrieval of lunar samples assumed to be shocked, the late 1970s saw prolific research in laboratory shocked minerals. In the following, we detail a few of the key results of that era.

*Feldspars*

Due to its co-prevalence with quartz in felsic rocks such as granite, feldspar minerals have not been as thoroughly investigated as quartz in the context of shock metamorphism. However, feldspar has still been well investigated and yields similarly to shock processes as quartz. Single crystal shock experiments on sanidine, orthoclase, microcline, oligoclase, and labradorite (all different chemical forms of plagioclase) yielded the following maximum pressure categories (Ostertag, 1983).

Pressure (GPa)	Feldspar Shock Feature
< 10.5	Fracturing starts to develop
10.5-14	Planar elements
18-26	Mosaicism
26-34	Diaplectic glass
> 42	Melt glass

*Table 2.5. Feldspar shock effects.*

*Microcline*

Single crystal microcline sample were shock loaded at pressures of up to 41.7 MPa in 15 shock recovery experiments (Robertson, 1975a). Robertson found that microcline deformed similarly to quartz and other alkali feldspars. Planar fractures develop slightly below and above the Hugoniot elastic limit (6-8.5 MPa), and planar deformational features begin to appear at 13.5 to 14.5 MPa. Some planar deformation is converted to mechanical twinning at the lower threshold of 20 MPa. Diaplectic glass is reported in

minor amounts at all pressures investigated. Microcline is unique as it retains weak birefringence even at 45 GPa.

### *Olivine*

A clear distinction between thermal and pressure induced shock effects has been shown in olivine and is greatly dependent on porosity (Bauer, 1979). Shock melting is seen to occur as low as 20 GPa in porous samples, but single crystal samples will only melt at pressures greater than 75 GPa. Effects below 50 GPa are generally dominated by fracturing. Bauer proposes olivine as a sensitive pressure calibration tool due to largely mechanical failure in the high-pressure regimes where quartz and feldspar show dominantly thermal effects. Olivine crystals show prevalent planar deformational features at pressures of 5-43 GPa (Müller & Hornemann, 1969).

Dunite is an ultramafic rock representative of the earth's upper mantle and compose nearly entirely of olivine. Samples of dunite from Aheim were shock loaded at a variety of pressures between 5 & 59 GPa (Reimold & Stöffler, 1978). Progressive stages of alteration were categorized as follows (Table 2.6). In order of degree of alteration, the observed changes in dunite are irregular fracturing, planar fracturing, mosaicism, intergranular brecciation, intragranular solid state recrystallization, and intergranular melting with recrystallization. Reimold & Stoffler also found that intergranular brecciation textures in the 29-45 GPa range closely resemble lunar dunite samples.

Pressure (GPa)	Alteration
>5	Irregular & planar fracturing
15-30	Mosaicism & planar fracturing
38-45	Planar fracturing, mosaicism, & intergranular brecciation
45-59	Planar fracturing, intragranular solid state recrystallization, and intergranular melting with recrystallization.

*Table 2.6. Dunite shock effects.*

## Basalt

Comparison of shock loaded lunar and terrestrial basalt samples up to 100 GPa revealed feldspars of Lunar origin to be more resistant to high pressure melting (Schaal & Hörz, 1977). The authors conclude a dominant role of micrometeorites in lunar geology due to a lack of hand sized shocked samples and prevalence of smaller glass spheres and agglutinates in the lunar regolith. They classed shocked basalt by peak pressure as follows (Table 2.7). Due to the stepped mineral melt pressures, deformation features in shocked basalt can be utilized as a fairly accurate shock measure at pressures well above quartz's melting point.

Pressure (GPa)	Effect
< 25	Brittle and plastic deformation. Shock lamellae in plagioclase.
25-45	Complete transition of plagioclase to maskelynite.
45-60	Feldspar fusion (mostly along grain boundaries).
60-80	Vesicular and flowed feldspar melts. Loss of target texture.
> 80	Melting of pyroxene, plagioclase, and ilmenite. Whole rock melting.

Table 2.7. Basalt shock effects.

## Zircon

Uranium impurities are typical in zircon crystals, and thus the uranium to lead decay chain has been fundamental in geological dating. It is fortunate that shock events can, at least partially, reset the uranium clock and constrain the age of astro-geological events.

Shock induced textural effects in zircon were first reported by acid etching scanning electron microscopy techniques in K/T ejecta collected from Berwind Canyon, Colorado (Bohor et al., 1993). The texture was shown to increase progressively with peak pressure, along with resetting of the U-Pb isotopic system.

Zircon has much more resistance to pressure than quartz, and shock recovery experiments with tunnelling electron microscope analysis have shown Planar Deformational Features around 20 GPa (Leroux et al., 1999). The authors found partial conversion to the scheelite polymorph at 40 GPa and



complete conversion to scheelite at 60 GPa. This confirms an earlier study from the golden age of mineral shock recovery where the onset of scheelite conversion begins at 30 GPa and completes quantitatively by 53 GPa (Kusaba et al., 1985). Kusaba et al. also discovered single crystal decomposition to tetragonal  $ZrO_2$  at 94 GPa. At this pressure, most minerals vaporize or at least melt, thus giving a probe for the higher pressures.

The deformational features caused by shock in zircon can cause lead daughter products of uranium inclusions to escape. It has been shown that the amount of shock induced textural deformation in zircon is correlated to the degree of isotopic resetting. Thus, using a curve of various ejecta samples, both the age of the target rock and impact event can be resolved (Krogh et al., 1993).

An exciting feature of the U-Pb method in dating shocked zircon is the requirement of “hot shock” to remove the lead. In peak temperatures below 700 °C, although shock pressure induced features can be present, the lead daughter isotopes remain and the nuclear decay clock is not reset (Moser et al., 2011); the implication being that shocked zircon can be used to constrain both pressure and temperature in distal ejecta samples.

## 2.6 Segue

Incidentally, this thesis is structured similarly to the scientific hole it is discussing (Figure 2.26). The preceding chapters have hopefully been interesting and important in themselves, as they provide background and context. However, a hurried reader could happily bypass the top half of this thesis and begin with the main course below. This is analogous to hole M0077a from a rock physics perspective: The post-impact sediments are like the introduction; these carbonates are interesting and have their own scientific value, but the peak ring and its rare impactites below is what we really came to study.

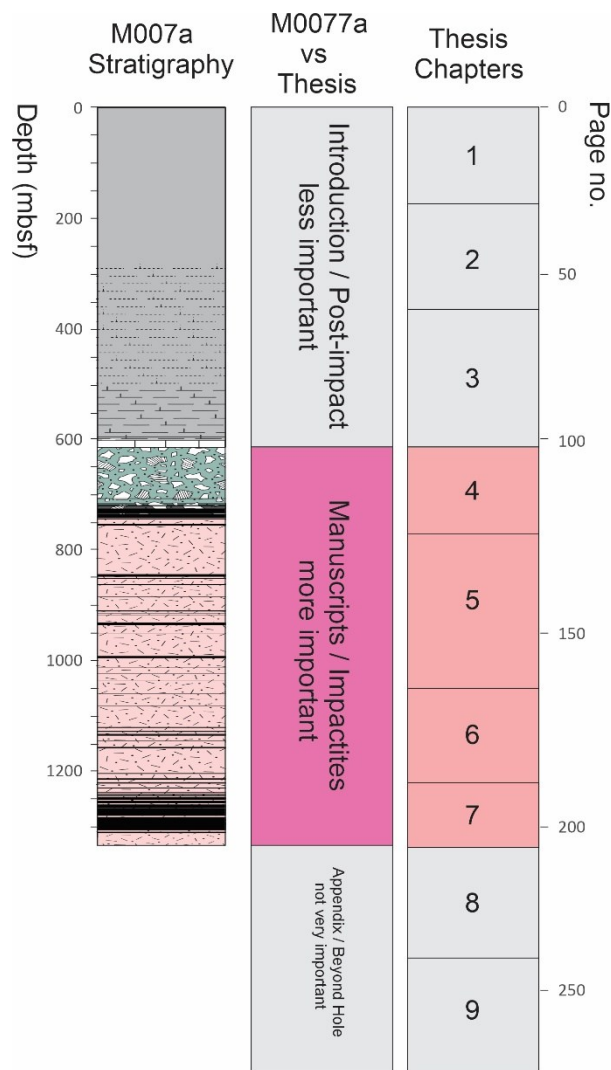


Figure 2.26. Analogy between hole M0077a and the proverbial 'rabbit-hole' of shocked rock physics. More important parts are colored for emphasis.

The following three chapters are manuscripts ordered by their respective stage of progress, ranging from fully published to not yet submitted. The bizarre physical properties observed within Hole M0077a are discussed and analyzed with a particular emphasis on the peak ring impactites. The reduced seismic wavespeeds observed in M0077a are utilized for novel quantification of attenuation (Chapter 3) and damage parameters (Chapter 4). Petrophysical characterization of M0077a impactites is presented in Chapter 5 with the goal of inversion for pore characterization, although presently available rock physics models may prove to be insufficient for shocked rock physics.

### 3. Assessment of Rock Damage Using Seismic Methods: Wave Speeds and Attenuation from Borehole Measurements in the Chicxulub Impact Structure.

*This chapter has been previously published in 54th US Rock Mechanics/Geomechanics Symposium as:*

Nixon, C.G., Kofman, R., Schmitt, D.R., Gulick, S.P.S., Christeson, G.L., Sastrup, S., Lofi, J. and Morgan, J.V., 2020, June. Assessment of Rock Damage Using Seismic Methods: Wave Speeds and Attenuation from Borehole Measurements in the Chicxulub Impact Structure. In *54th US Rock Mechanics/Geomechanics Symposium*. OnePetro. [onepetro.org/ARMAUSRMS/proceedings-abstract/ARMA20/All-ARMA20/ARMA-2020-1307/447518](https://onepetro.org/ARMAUSRMS/proceedings-abstract/ARMA20/All-ARMA20/ARMA-2020-1307/447518)

#### 3.1 Abstract

Anomalous values of in-situ compressional wave speeds ( $V_p$ ) and quality factors ( $Q$ ), determined from analysis of borehole seismic measurements are found within the highly damaged rock mass in the peak ring materials of the K-Pg Chicxulub impact structure. The data is obtained from vertical seismic profiling of IODP/ICDP hole M0077A, drilled to 1335 m depth.  $V_p$ , calculated by local slope regression, are  $\sim 4$  km/s, only about 60% that for similar unshocked polycrystalline granite. Attenuation is quantified using the spectral ratios method that gives low  $Q$  factors of 10 to 35, values that are significantly less than expected for unshocked granites. Previous in-situ studies measuring physical properties of complex crater central uplifts remain rare; the extraordinary geo-mechanical results from these analyses are presented as impetus for future studies on the poorly understood physical properties and formation of impact basin peak rings as well as providing insight into seismic wave propagation through highly damaged rock masses.

## 3.2 Introduction

Geophysical investigations provide a means to remotely characterize a rock mass prior to drilling. In applied seismology, most efforts focus on developing increasingly better resolved images of subsurface structures. However, inversion of these data can provide spatial maps of a rock mass's physical properties which in turn can provide indications of composition, density, porosity, and fluid content. Seismic methods, for example, are used almost exclusively to directly measure the compressional  $V_p$  and shear  $V_s$  wavespeeds within the rock mass or to infer impedances and density. These may then be transformed to the more fundamental characteristics using a variety of theories or empirical relationships. However, propagating waves attenuate due to a combination of intrinsic absorption and scattering; this attenuation can also provide additional important information on in situ conditions and fine-scale structure. Although attenuation remains challenging to accurately measure and in situ measurements of attenuation remain rare, attenuation can provide sensitive indications of fluid saturation and porosity. This is particularly important in assessing rock materials that are highly damaged by strong dynamic stress waves or by nearly reaching failure conditions. Attenuation can provide proxy information that relates to the degree of damage in the material; however, finding appropriate sites to make measurements in the field is difficult.

Borehole seismic studies were carried out as part of the ICDP/IODP Expedition 364 Chicxulub drilling of hole M0077A off the coast of the Yucatán Peninsula, Mexico (Gulick et al., 2017a),(Figure 3.1); this provided a rare opportunity to measure wave speeds and attenuation within materials highly damaged during a large hypervelocity impact. In this contribution, we describe the methodologies used to obtain seismic frequency band measurements of the anomalous attenuation and reduced wave speeds from the hole drilled into the severely damaged rock mass within the peak ring of the Chicxulub Impact Structure.

### 3.3 Geological Background

The 66 Ma Cretaceous-Paleogene (K-Pg) boundary marks a major extinction event in earth history. Thin deposits at this boundary are highly enriched in iridium, the origin of which was hypothesized to result from incoming extraterrestrial material distributed by a large hypervelocity impact to the earth (Alvarez et al., 1980). Such an event must have produced a significant crater, but at that time no responsible impact structure was known. Potential field reconnaissance by PEMEX in the 1970s had detected anomalous structures (Penfield, 1981) in the western Yucatán, Mexico; however, it was not until the early 1990s that this structure was more firmly linked to the K-Pg event (Hildebrand & Stansberry, 1992; Hildebrand et al., 1991; Koeberl, 1993; Kring et al., 1991).

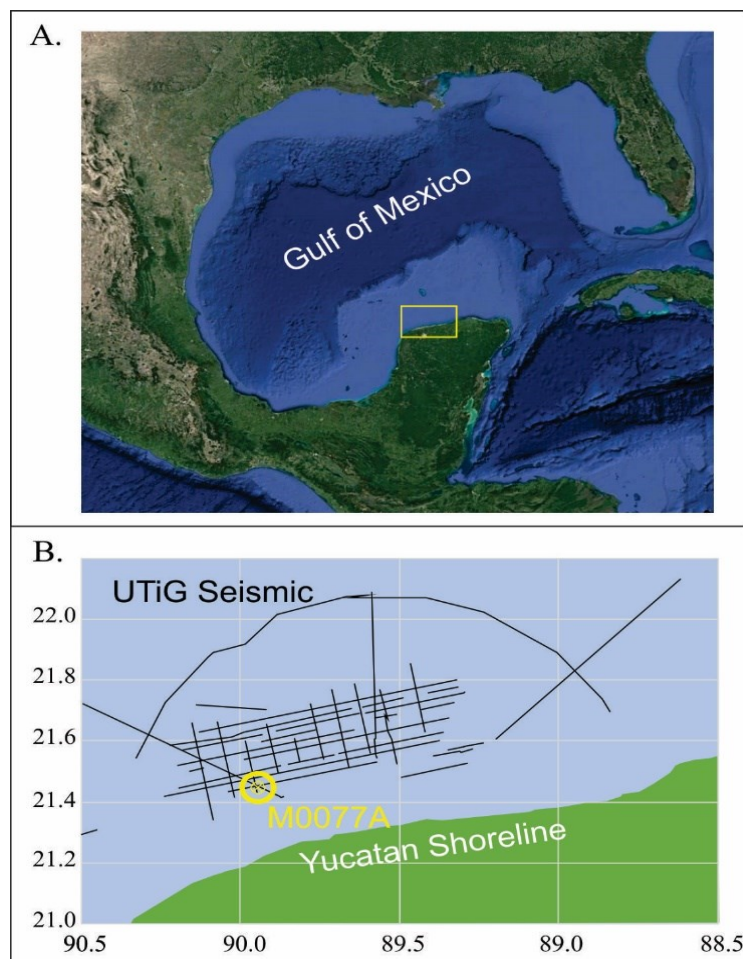


Figure 3.1. a) Gulf of Mexico with offshore region of the Chicxulub impact basin (Figure 3.1b) shown in yellow box. b) Location borehole M0077A, shown with previous seismic profiles.

Further geophysical mapping of the structure revealed a pronounced annular uplift ~80 km in diameter surrounding the basin's center (Morgan et al., 2000), similar to the peak-rings common in large complex craters throughout the solar system. On earth, central peaks and peak rings are topographic highs that, in most cases, are prone to rapid erosion accelerated by the fact that the rock is highly damaged and displaced during the impact. Consequently, there are few, if any, other good examples of peak rings on earth; the unique state of preservation of the Chicxulub peak ring can be attributed to the continual blanketing of the structure with sedimentary carbonates.

A number of 2D marine reflection seismic surveys (Figure 3.1b) were acquired to better delineate the structure e.g., (Gulick et al., 2013; Gulick et al., 2008; Morgan et al., 1997); subsequent tomographic analyses associated the topmost portions of these structures with anomalously low compressional wave speeds. These seismic images were key in site selection of the IODP/ICDP Expedition 364 that drilled into the peak ring in mid-2016 (Morgan et al., 2016). The project sought to answer numerous questions related to the K-Pg mass extinction and reveal specifics of how peak rings form. Drilling reached a final depth of 1335 m below sea level, the bottom sections completely coring the peak ring. The peak ring material consists of zones of melt, mixed melt & breccia (suevite), and highly damaged granite. Dynamic models of the impact suggest that this damaged granite may have originated at depths near 10 km, been displaced laterally by up to 20 km, and experienced peak shock pressures in excess of 40 GPa during impact (Morgan et al., 2016).

A typical undamaged granite is characterized by vanishing porosity and  $V_p$  of ~6 km/sec. However, the damaged granite core is as much as 10% porous (Christeson et al., 2018). Further geophysical logging (Lofi et al., 2018) and vertical seismic profiling (Nixon et al., 2017) yields  $V_p$  of ~4 km/s. Such values are highly anomalous and indicate the degree of damage within such normally competent rock.

### 3.4 Vertical Seismic Profile Acquisition

Drilling and seismic operations were all carried out from the deck of the liftboat L/S Myrtle. The downhole seismic measurements were made using a set of four 3-component geophone sondes (Sercel Slimwave™). The sondes lock into the borehole at each recording station with mechanically deployed arms. The seismic records are digitized within each sonde, then transferred to the surface for recording, thus eliminating inductive analog noise from the long wireline. The 4 triaxial sondes were separated by 15 m each, which together, with the top data transfer sonde, makes for a total tool string length of 60 m (Figure 3.2). Depending on operational constraints, seismic records were obtained with depth spacings from 5 to 1.25 m and digitally sampled at 250 ms for 3 seconds. A minimum of 5 separate records were taken at each station to allow for noise reduction by stacking. The seismic source was a small airgun (30/30 Sercel MiniGI™) deployed at ~1 m water depth and operated with ~14 MPa of compressed air pressure. Marine biologists maintained watch during operations should marine mammals or turtles come close to the platform.

The system was deployed 3 times in May and June of 2016 after geophysical logging had confirmed hole stability, yet here we focus here on analysis of the seismic records obtained within the lowest section in the peak ring from 700 mbsf to 1335 mbsf.



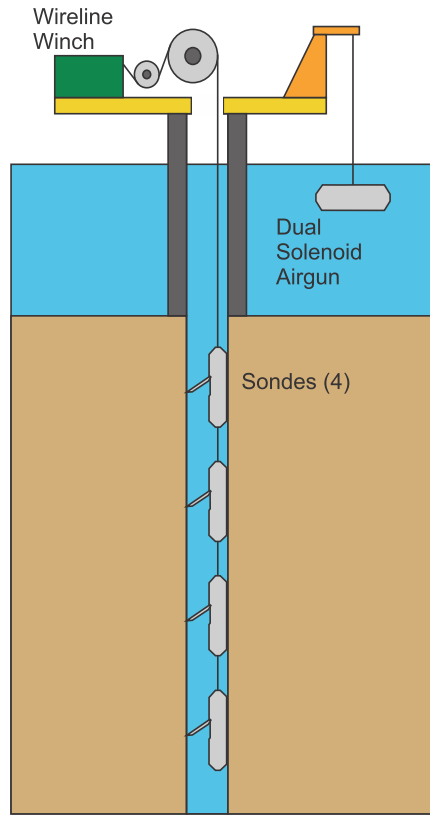


Figure 3.2. VSP experimental configuration. The four sondes are 15 m apart.

### 3.5 Data Processing

Pre-processing steps applied to the data include:

- (i) Editing of problematic records
- (ii) Stacking to improve signal to noise ratio, and
- (iii) Applying minor static time shifts to account for variations in the depth of the air gun during the three deployments.

The resulting raw vertical component data for the peak ring section is shown in Figure 3.3 with a sonde spacing of 5 m. It is important to distinguish between meters below sea floor which specifically refers to depth measured by counting driller rod and meters wireline sea floor (mwsf). mwsf is estimated by cable counters during logging and was found to have a discrepancy with mbsf of up to ~1% in these VSP operations.

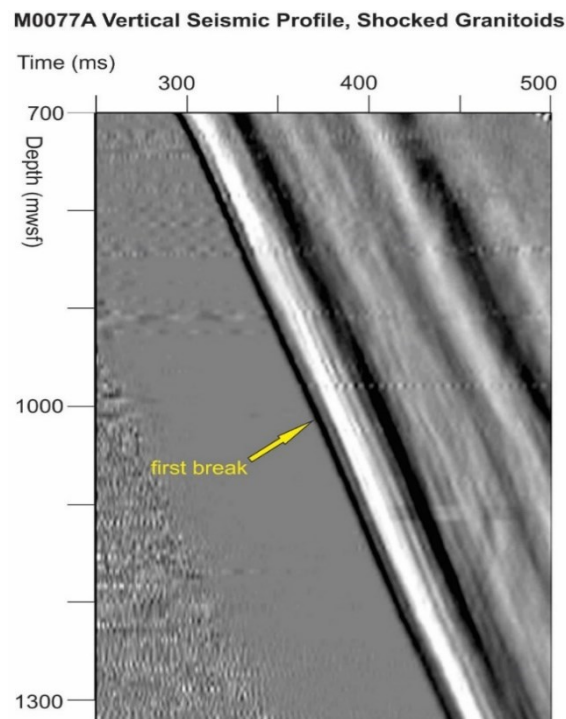


Figure 3.3. Peak ring portion of VSP shown after pre-processing and 1000 ms automatic gain control for display only. Thin black feature is P-wave first energy arrival (first break), denoted by yellow arrow.

### 3.5.1 Wavelet Arrival

After pre-processing, the first and most central processing step was to pick the arrival times of the seismic wave from the airgun source to the receiver (Hardage, 1985). To avoid inconsistency, the arrival time of each trace was declared by the first pulse amplitude minima (Figure 3.3) which provided arrival times versus depths. Interval  $V_p$  were calculated from this relationship by a local slope linear regression algorithm (Schmitt et al., 2007). The local slope method calculates velocity with respect to other nearby traces, which enables following a strong feature in the waveform rather than attempting to discern the exact point at which the wavelet begins to arrive. A second advantage of the local slope method is that uncertainty ranges may be readily determined as part of the regression with the results shown in Figure 3.4d; these are largely the same as those reported initially in Morgan et al., (2016). It is worth noting that we attempted to obtain measures of the shear wave speed  $V_s$  from analysis of the horizontal

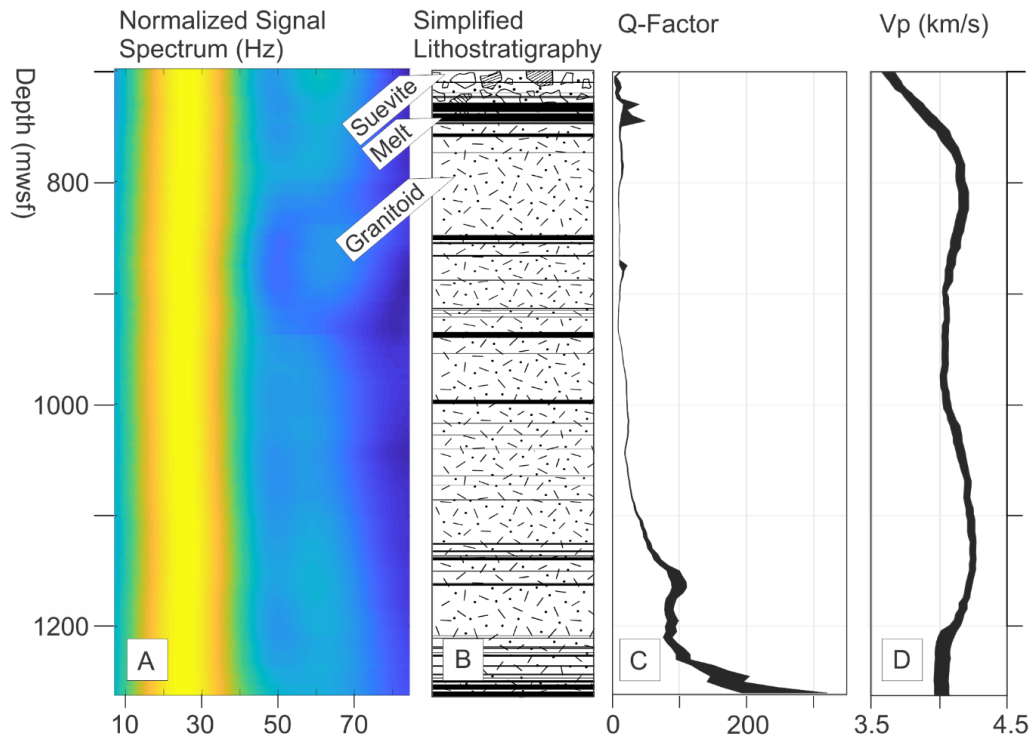


Figure 3.4. VSP physical properties. a) Fourier transform of VSP traces illustrating useful frequency band of 7-85 Hz. b) Simplified lithostratigraphy, listed in order of appearance from top: suevite, melt, granitoid. c) Quality factor  $Q$  versus depth. d) Interval  $V_p$  versus depth as determined using local slope regression.

components, but these were highly uncertain due to the low amplitude of this mode. After pre-processing, the first and most central processing step was to pick the arrival times of the seismic wave from the airgun source to the receiver (Hardage, 1985). To avoid inconsistency, the arrival time of each trace was declared by the first pulse amplitude minima (Figure 3.3) which provided arrival times versus depths. Interval  $V_p$  were calculated from this relationship by a local slope linear regression algorithm (Schmitt et al., 2007). The local slope method calculates velocity with respect to other nearby traces, which enables following a strong feature in the waveform rather than attempting to discern the exact point at which the wavelet begins to arrive. A second advantage of the local slope method is that uncertainty ranges may be readily determined as part of the regression with the results shown in Figure 3.4d; these are largely the same as those reported initially in Morgan et al., 2016. It is worth noting that we attempted to obtain measures of the shear wave speed  $V_s$  from analysis of the horizontal components, but these were highly uncertain due to the low amplitude of this mode.

### 3.5.2 Wavefield Separation

In an ideal determination of attenuation, one would desire a clean down-going pulse uncontaminated by scattering and the reflected up-going wavefield. The raw data of Figure 3.3 primarily shows the strong down-going waves but close inspection reveals reflections with the opposite slopes in time-depth plots. Wavefield separation must be carried out to isolate the down-going wavefield as much as possible. Consequently, in the next step, the raw wavefield is flattened by shifting each trace by its first break time; this has the effect of flattening the traces (Figure 3.5a). Wavefield separation may then be achieved via different image processing methods such as  $f$ - $k$ , median, or  $\tau$ - $p$  filtering, each with its own merits (Kommedal & Tjøstheim, 1989). In this study, median filtering was used because it does not rely on use of a 2D FFT that can introduce spectral artifacts (Amidror, 2013; Learner et al., 1996). We presume that this median filtered result is representative of the down-going wavefield (Figure 3.5a) and is ready for further analysis. It is important to note the relatively rapid decline in the amplitudes (as

shown in false colors) in Figure 3.5a is due largely to attenuation and geometrical spreading of the wave field. The results of the full wavefield separation in which the up-going wavefield is the simple difference between the estimated down-going field and the original observed field has been determined. However, as it is not germane to determination of the attenuation, presentation of these results is delayed to a later contribution. It is important to note that bandpass filters and top mutes were not applied at this stage as preserving the trace frequency spectra as uncontaminated as possible is necessary for determination of the attenuation by the spectral ratios method.

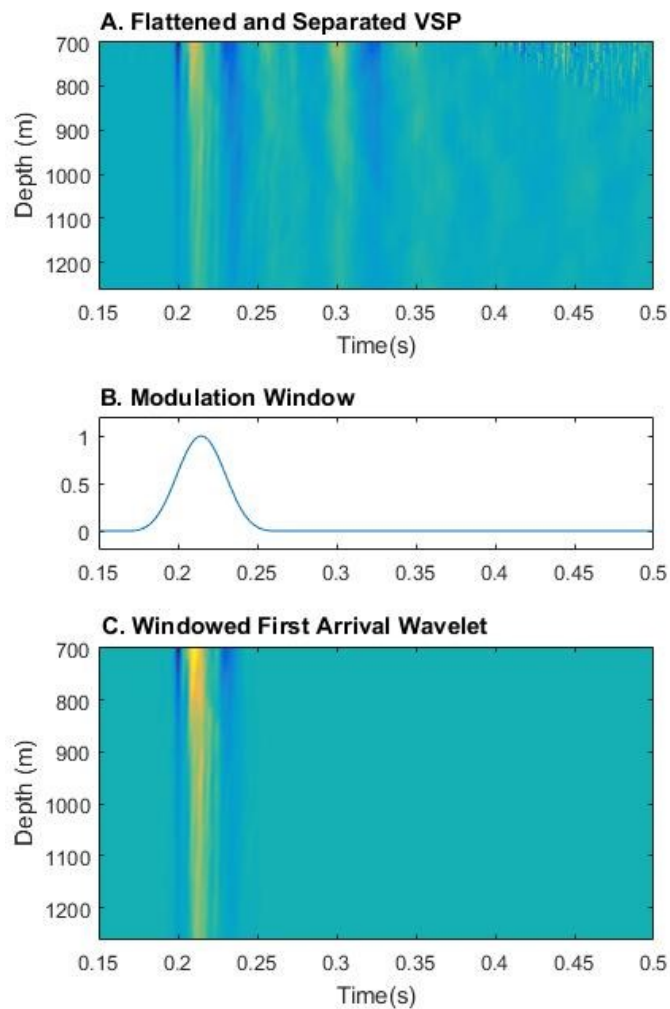


Figure 3.5. P-wavelet windowing. a) Flattened VSP down-going wavefield after shifted in negative time direction by first break time. b) Blackman-Harris modulation window. c) Isolated first arrival wavelet after application of modulation window providing traces for attenuation analysis.

### 3.5.3 Windowing

A further processing step is necessary in order to prepare the traces for attenuation analysis. Significant energy remains in the down-going pulse for a considerable time period beyond the arrival of the main pulse. This is largely due to reverberations of the bubble released by the airgun source and does not contribute usefully to the analysis; to overcome this, the initial wavelet is isolated by modulating it with a smoothly varying Blackman-Harris window function (Harris, 1978) which is similar in appearance to a Gaussian function (Figure 3.5b); however, the Blackman-Harris window has the advantage that it is a finite cosine series which at its outer boundaries vanishes. The down-going wavefield after modulation (Figure 3.5c) provides sufficiently conditioned data for the subsequent spectral analysis (Figure 3.4a).

### 3.5.4 Spectral Ratios

The well-known spectral ratios method was selected for estimation of the attenuation. The reader may find a review of this, for example, in Molyneux and Schmitt, (Molyneux & Schmitt, 2000). The method essentially relies comparing the spectral amplitudes of a pulse observed at locations  $x_o$  and  $x$  which are, respectively, closer and farther from its source. This method assumes that the quality factor  $Q$ , which is a measure of relative dissipation of the energy with each cycle, is almost constant over the frequency band of the pulse. With this simplification, then the spectral ratio at frequency  $f$  of the amplitude spectra of the near  $A(x_o, f)$  and far  $A(x, f)$  pulses, determined from the FFT of the pulses, is the linearized relation:

$$\ln \frac{A(x, f)}{A(x_o, f)} = -\frac{\pi \Delta x}{Qv} f + \ln G \quad (3.1)$$

Where  $\Delta x = x - x_o$ ,  $v$  is the phase velocity,  $G$  is a geometric factor that would include wavefield spreading, and  $Q$  is the quality factor. eqn. 3.1 is a convenient expression for constant  $Q$ ; a plot of

$\ln[A(x,f)/A(x_0,f)]$  versus  $f$  is ideally a line with slope  $m = -\pi\Delta x/Qv$  that may be found readily by linear regression so that  $Q$  is upon rearrangement:

$$Q = \frac{-\pi\Delta x}{mv_p} \quad (3.2)$$

With the down-going P-wavelet isolated (Figure 3.5c), the next step is a Fourier transform to the frequency domain (Figure 3.4a). Although normalization is not required for this method, it has been applied to the spectral amplitudes in order to assist visual quality control and to keep the absolute values on subsequent steps similar. Typically, when the spectral ratios method is applied, the topmost trace is designated as a reference. The ratio of signal amplitudes is then calculated for each frequency between a particular trace and the reference trace (eqn. 3.1, LHS), which results in a negative frequency vs ratio correlation for seismic bandwidths in an attenuating medium. A natural log is then applied to the spectral ratios plot, and a linear regression fit applied. The resulting slope ( $m$ ) can then be inserted into eqn. 3.2, resulting in a measurement of  $Q$  for the trace. Here, the analysis was repeated by using separately each of the 4 topmost traces as the reference. This allowed for some assessment of the uncertainty and as a quality control check on the analysis for each depth point (Figure 3.4c).

### 3.6 Results and Discussion

There are two significant observations from these data with regard to the in-situ material properties. First, as discussed (Christeson et al., 2018; Lofi et al., 2018), the observed wave speeds within the damaged granites range from about 4 km/s to 4.25 km/s. This is substantially less than that expected for silica rich granite which, at pressures sufficient to close the microcrack porosity, will have compressional wave speeds at modest elevated pressures in excess of 6 km/s; this has been found experimentally by many researchers after Birch (1960) and may be calculated using simple Voigt-Reuss-Hill averaging. However, velocities measured at room pressure in such relatively undamaged crystalline rocks may still reach as low as 5 km/s. Second, the quality factors observed over much of the zone fall within the range of 10 to 35, indicating high levels of attenuation. Unfortunately, there are few comparative measures. Wulff et al. (1999) studied the attenuation of granites subject to uniaxial loads up to failure. At ambient room pressures, Wulff found low Q of ~20 that reached as low as ~5 near failure. Schön (2015) provides a recent review of attenuation in crystalline rocks that can reach nearly 1000 and summarizes earlier studies over a range of frequencies that range from 50 to 700 Hz. The in-situ values observed here are clearly low indicating that this cracked medium is strongly attenuating relative to undamaged materials. There are no other attempts to determine attenuation from a VSP survey within an impact structure to our knowledge. Borehole seismic investigations in such structures remain rare. Angenheister and Pohl (1974; 1976) collected a VSP within the Nördlinger Ries crater in Germany, a smaller structure that also has a buried peak ring, and obtained simple measures of average wave speeds to depth of 1000 m. In their attempt to estimate interval velocities, Angenheister and Pohl, (1974) found compressional wave speeds that ranged from ~3800 m/s to over 6500 m/s. It is likely that the large variations seen with depth in their plots result from large uncertainties in wave speed calculation that propagates from errors in transit time measurements, particularly when the adjacent receiver points are close to one another. On the basis of surface seismic profiling, they also noted that  $V_p$  increased with distance from



the center of the crater. VSP studies into the central peak of the Bosumtwi structure, a complex crater in Ghana, also showed considerable deficits in both  $V_p$  and  $V_s$  that increased rapidly with depth (Schmitt et al., 2007). Recent unpublished seismic tomographic studies of the Bow City Structure (Glombick et al., 2014) also indicate significantly reduced  $V_p$  within and beneath the central peak (Xie, 2014).

In practice, attenuation can be a very difficult physical property to measure (Cheng & Toksöz, 1979; Cheng et al., 1982; Johnston et al., 1979; Newman & Worthington, 1982; Watanabe & Sassa, 1996; Winkler & Nur, 1982; Yamamura et al., 2003). Attempts to directly calculate dispersive frequency related velocity relationships, a necessary condition in an attenuating medium (Müller et al., 2010), were unsuccessful with this dataset. The spectral ratios method tested here requires relatively few processing steps and yields reasonable values for the shock damaged and highly-attenuating medium. One advantage of the spectral ratios method is that it exploits the relative differences in the amplitudes in the frequency domain and the relationship is not affected by geometric spreading. However, a major disadvantage of the spectral ratio method is its reliance on a reference trace. If the reference trace chosen has incomplete spectra or the spectrum is biased to high frequencies, processing can give unrealistic results or even nonphysical negative  $Q$  values within the hole. The analysis presented here attempts to reduce this risk by separately employing the topmost four traces to be the reference trace. A deficiency of the current study is that the values of attenuation obtained are representative of the rock mass between the reference and observation trace. Current work is seeking to extract measures that will better reflect the attenuation over more discrete intervals; this may require use of alternative methods that include waveform modeling in order to better represent more local physical properties and to include the potential effects of scattering within such a complex rock mass.

### 3.7 Conclusion

The direct in-situ seismic measurements on the Chicxulub's shocked granitoid peak ring presented here have yielded  $V_p$  values of  $\sim 4$  km/s, depressed by  $\sim 1/3$  of what is normally expected for similar unshocked crustal granite. Although these values appear strangely anomalous, the  $\sim 10\%$  porosity is significantly higher than the near zero value expected for unshocked granite. The hypervelocity impact is almost certainly responsible for these anomalous values, although the exact relationship between the shock induced porosity and seismic wave speed deviations is still under investigation. We have tested the spectral ratios method of attenuation analysis and have shown anomalously low  $Q$  values of 10 to 35 within the shocked granite peak ring. This is one to two orders of magnitude less than what is expected for unshocked crystalline rocks, which can have  $Q$  values as high as 1000. Unfortunately, with very few if any similar previous studies to compare with, it is difficult to accept these results with absolute confidence. However, given the extraordinary physical properties already observed in the shocked granites recovered from IODP/ICDP Expedition 364, it is possible that these extremely low  $Q$  values are accurate and further investigations into  $Q$  values of shocked media are important. Further, linking this work to ongoing laboratory investigations of wave speeds and detailed crack damage may assist to improve rock mass damage assessments remotely obtained by seismic methods.

#### ***Acknowledgements:***

The European Consortium for Ocean Research Drilling (ECORD) implemented Expedition 364 with funding from the International Ocean Discovery Program (IODP) and the International Continental scientific Drilling Project (ICDP).

## 4. Borehole Seismic Observations from the Chicxulub Impact Drilling: Implications for Seismic Reflectivity and Impact Damage

This chapter is currently in press at *Geochemistry, Geophysics, and Geosystems*, (AGU).

### 4.0.1 Key Points

- We present analyses from a vertical seismic profile at Site M0077 on the Chicxulub peak ring.
- Reflectivity is primarily from a low velocity zone of hydrothermally altered impactites at the top of the peak ring below Cenozoic sediments.
- We derive *Grady-Kipp* damage parameters and Poisson's ratios which indicate high damage levels within the peak ring.

### 4.0.2 Abstract

We conducted a vertical seismic profile (VSP) in the borehole of International Ocean Discovery Program/International Continental Scientific Drilling Program Expedition 364 Site M0077 to better understand the nature of the seismic reflectivity and the in situ seismic properties associated with the Chicxulub impact structure peak ring. Extraction of the up-going wavefield from the VSP shows that a strong seismic reflection event imaged in seismic reflection data results from discontinuities in the elastic impedance  $Z$  (the product of density and wave speed) at the top and bottom of a zone of hydrothermally altered melt-bearing polymict breccia (suevite) that are characterized by anomalously low  $Z$ . Below this strong carbonate/suevite reflection event, the upgoing seismic wavefield is chaotic, indicating high levels of scattering from the suevites and underlying melt rocks and shocked granitoids of the peak ring, in contrast to the clear coherent reflections throughout the overlying Cenozoic sediments. We extract shear wave speeds, which, together with those provided from the complementary sonic log and densities from core scanning, allowed determination of  $V_P/V_S$  and Poisson's ratio  $\nu$ . These values are anomalously high relative to comparable terrestrial lithologies. We

also calculate a variety of damage parameters for the disrupted peak ring granitoids. These values may assist in linking seismic observations to shock levels that are necessary to calibrate current impact models and may also be useful in assessing levels of fracturing within major fault zones.

#### *4.0.3 Plain Language Summary*

Seismic profiling over geological features reveal to us both the geometry of the structure and the speeds of the seismic waves within it. Calibrating these profiles using only data from the surface, however, remains challenging but this can be accomplished by making direct seismic measurements in a borehole in a technique called vertical seismic profiling (VSP). Here, we describe the analysis of such a VSP acquired during drilling into the Chicxulub Impact Structure during IODP Expedition 364. Special processing of the waves confirm that the strong seismic reflection seen in surface data originates from abrupt changes in the rock properties related to the juxtaposition of hardened sediments, weak suevites, and melt rock. No seismic reflections could be found originating deeper in the uplifted and highly damaged granitoids of the structure's peak ring. As noted in earlier studies, the seismic wave speeds are anomalously low in these lower materials. These speeds were converted into damage indexes and as such this information may provide a means towards constraining advanced numerical impact modeling and in assessing levels of damage in the subsurface in advance of construction on the surfaces of the Moon and Mars.

## 4.1 Introduction

Complex impact structures are common throughout the solar system and their relatively uneroded surface morphologies have been well studied on the extraterrestrial planets and natural satellites (Phillips et al., 1991; Pike, 1977; Wood & Head, 1976). However, spaceborne remote sensing can only reveal extremely limited details of the subsurface of these craters, such as geological structure or physical properties. These elusive details can elucidate the dynamics of the formation of complex impact structures and are particularly important for the largest impact structures (impact basins) which exhibit peak rings (Melosh, 1989). Geophysical and drilling investigations from the bodies' surface can provide this information, but due to the active hydrological and tectonic cycles acting on weak shock-damaged, faulted rock masses with initially steep topography, there is only one confirmed intact peak-ring structure on Earth (Kenkmann et al., 2014). The ~200 km diameter Chicxulub impact structure's peak ring is fortuitously preserved by nearly continuous limestone blanketing on a geologically stable passive margin since its formation (Kenkmann et al., 2014; Lopez Ramos, 1975). As such, the accessible Chicxulub structure presents opportunities for direct geophysical and sampling investigations to further constrain our understanding of the formation of such structures. Our study focuses on understanding the nature of the seismic wavefield within peak rings through detailed Hole M0077a seismic observations carried out as a component of the International Ocean Discovery Program/International Continental Scientific Drilling Program (IODP/ICDP) Expedition 364 Chicxulub drilling project located off the Yucatán Peninsula, México (Figure 4.1).

Active source seismic profiling has been extensively used in imaging of impact craters since the first focused refraction studies at the complex Ries Crater as early as 1948 (Angenheister & Pohl, 1976) and at the simple Meteor Crater, Arizona in the 1970s (Ackermann et al., 1975). On Earth, complex craters in crystalline targets are typically >4 km in diameter but can have diameters as low as 2 km in softer sedimentary rocks. Complex craters include a central uplift zone, a melt sheet, and a normal faulted rim

where large blocks slumped into the transient crater (French & Hokett, 1998; Melosh, 1989). Active source seismological profiles exist over a number of complex craters, an incomplete listing of which includes the Chesapeake Bay Structure (Catchings et al., 2008), Mjøltnir crater, North Sea (Gudlaugsson, 1993), Siljan structure, Sweden (Juhlin & Pedersen, 1987), Upheaval Dome, Utah, (Kanbur et al., 2000), Manson Structure, Iowa, (Keiswetter et al., 1996), Bosumtwi Structure, Ghana (Scholz et al., 2002), Siljan structure, Sweden (Juhlin & Pedersen, 1987), Upheaval Dome, Utah, (Kanbur et al., 2000), Manson Structure, Iowa, (Keiswetter et al., 1996), Bosumtwi Structure, Ghana (Scholz et al., 2002), El'gygytgyn Structure, Siberia (Niessen et al., 2007), Houghton Structure, Nunavut (Scott & Hajnal, 1988), Sudbury Structure, Ontario (Wu et al., 1995), and Bow City Structure, Alberta (Glombick et al., 2014). The seismic

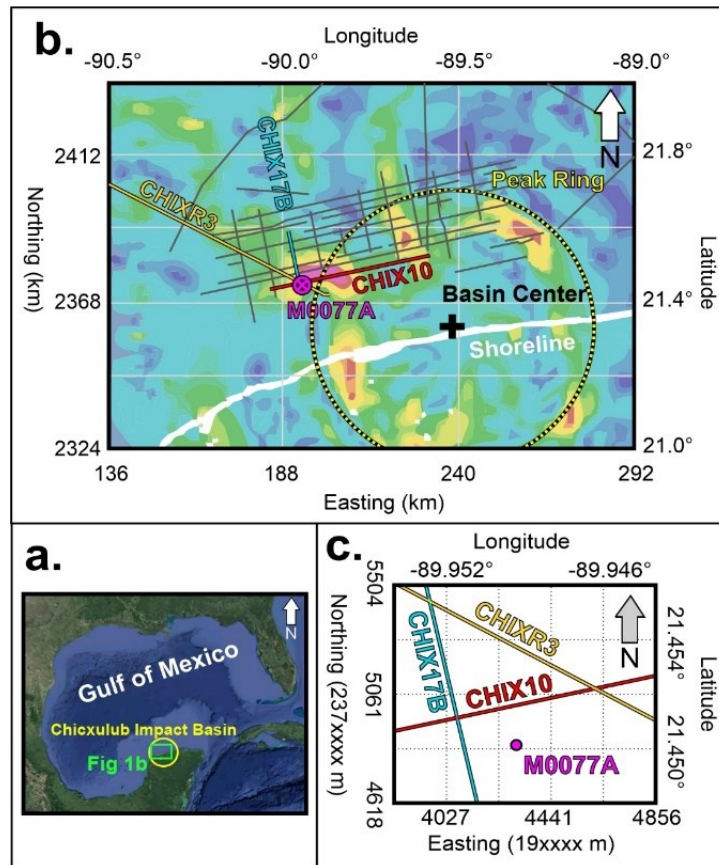


Figure 4.1. Location of Chicxulub structure. a) Within the Gulf of Mexico. b) With radius of the peak ring from the basin center and the nearby surface seismic profiles superimposed on horizontal gravity gradient map after Hildebrand et al. (1998). c) Project Hole M0077A in purple compared to nearby seismic lines, located in UTM zone Q16N. Northing is 2370000 + y-axis, Easting is 190000 + x-axis.

profiles obtained in these studies are consistent with central uplifts and faulted rims of larger complex craters (Melosh, 1989).

To date, the VSP data obtained during the Expedition 364 Chicxulub drilling program have been used in obtaining in situ compressional seismic wave speeds,  $V_p$  (Christeson et al., 2018). However, VSP data can also calibrate the depth to reflectors, improve the understanding of the nature of the seismic wavefield in the complex structure, resolve the details of the reflectivity, and provide additional constraints on the in situ physical properties. Here, we extend the VSP data set to better understand the nature of the seismic reflectivity of the Chicxulub peak ring, overlying impactites, and K-Pg boundary sequence including displaced target rocks (Gulick et al., 2019; Morgan et al., 2016), and to obtain estimates of shear wave speeds,  $V_s$ , to contribute to understanding the unique geological formations produced during large impacts. Additionally, obtaining measures of the seismic wavefield within the highly damaged rock masses of large impact structures may provide additional insight into the anomalous ‘diffusive’ seismic wave propagation on the Moon (e.g., Dainty & Toksoz, 1977; Latham et al., 1970; Pandit and Tozer, 1970) or assist in the interpretation of seismic observations on Mars (e.g., Karakostas et al., 2020; Lognonne et al., 2020).

We begin with an overview of the geological and physical properties found at Site M0077 and of the VSP methodology, provide the results of the structural measurements, and interpret these results with regard to the high degree of shock deformation experienced by the displaced crystalline peak ring materials as well as longer term processes that modified the seismic properties. The wave speeds, observed both in sonic logs and directly from the VSP data, are contrasted against comparable terrestrial analogs. Finally, we derive measures of damage that may be used as metrics in the assessment of deformations predicted by hydrocode impact modelling codes.

## 4.2 Background

### 4.2.1 Chicxulub Structure

The Chicxulub impact structure is centered near the village of Puerto Chicxulub on the Yucatán platform, México. The platform is characterized offshore by carbonate and evaporite depositional facies (Gischler & Lomando, 1999) and onshore by an unconfined flat lying karstic environment (Weide & Faber, 1985). Active source seismic source marine profiling (Camargo-Zanoguera & Suarez-Reynoso, 1994; Gulick et al., 2008; Hildebrand et al., 1998; Morgan et al., 1997) and passive monitoring (Campos-Enriquez et al., 2004; Mackenzie et al., 2001) have provided data used in numerous subsequent analyses: reflection for structure (Bell et al., 2004; Christeson et al., 2018; Gulick et al., 2008) and refraction for velocities (Christeson et al., 2001; 2009); these studies are described in recent reviews by Canales-Garcia et al. (2018), Gulick et al. (2013), and Salguero-Hernández et al. (2020). Together with the knowledge available from prior regional drilling (Ramos, 1975), these data are consistent with an interpretation that the Chicxulub structure is a complex crater which include elements (Figure 4.2) consisting of structural uplift with: i) a ~30 km diameter central zone of uplifted lower and mid crustal rocks blanketed by impactites and a thick melt sheet of near 40 km radius, ii) a topographically high peak ring of upper- and mid-crustal materials displaced upwards and coated with a thin veneer of melt and suevite, and iii) a series of terraced slump blocks of the upper crust and the original Mesozoic platform sediments that collapsed inward during the crater modification stage. This terrace zone bounds and lies beneath an annular trough filled with impactites and melt rock that extends to ~75 km radius, interpreted as the crater rim (Morgan et al, 2000) or inner rim considering the existence of additional ring structures such as offset sediments that define an outer ring at ~100 km radius (Gulick et al., 2008). The Chicxulub structure of Figure 4.2 is consistent with locations where large displacements may occur in numerical hydrodynamic crater modeling (Collins et al., 2008).



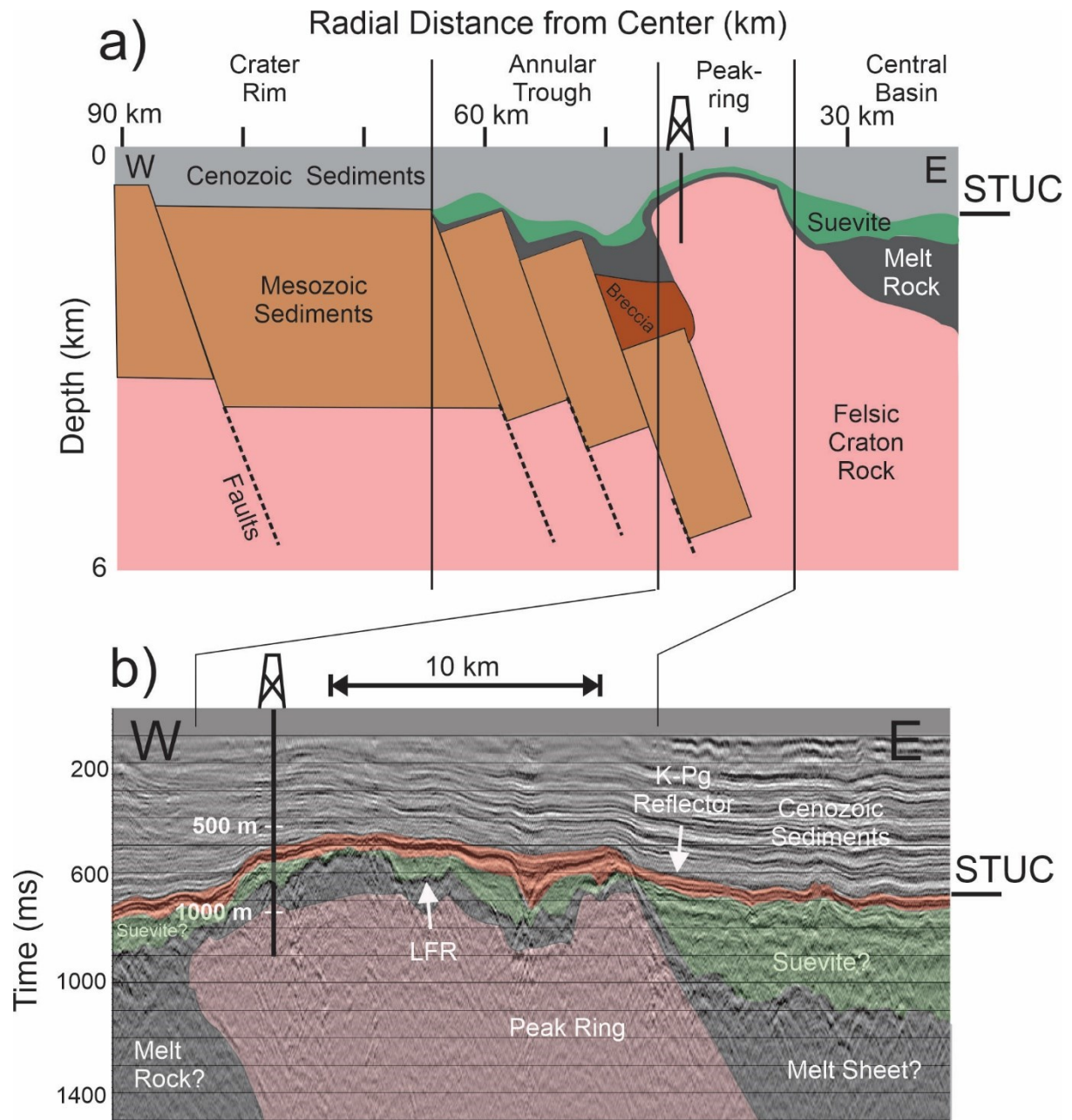


Figure 4.2. a) Conceptual geological cross section with upper contact of K-Pg boundary layer demarked by the Suevite/Transitional Unit Contact (STUC) along radius from crater center adapted from the interpretations of Vermeesch and Morgan (2008), Morgan et al. (2011), and Gulick et al. (2013), updated from Expedition 364 observations following Simpson et al. (2020), and suevite/melt rock/breccia transitions updated from Christeson et al., (2021). b) Portion of the migrated stack of line CHIX10 (Gulick et al., 2008) over the peak-ring with the K-Pg reflector highlighted in red and the underlying low frequency reflector (LFR) indicated. closest offset of Expedition 364 borehole M0077A from Line 10 indicated by small drill rig with depth extent correlating to 2-way time of 890 ms.

A portion of the seismic profile line CHIX10 (Figure 4.2b) is interpreted following Christeson et al. (2018), with detailed rationales provided by Gulick et al. (2008). The profile's features include: i) the layered Cenozoic sediments deposited since the impact, ii) a strong and continuous event present across the profile confirmed by the drilling to be associated with the upper K-Pg boundary, iii) the peak-ring formed by uplift and dynamic collapse of the central uplift immediately following the K-Pg impact, iv) suevite bounding and capping the peak-ring, and v) a thick zone of melt rock within the central basin, the top of which is delineated by an irregular low frequency reflector. The Suevite/Transitional Unit Contact (STUC) at 617.33 mbsf is a disconformity delineating the transition from rapid suevite deposition to Paleogene marine sedimentation, with the iridium layer being present at 616.6 mbsf (Goderis et al., 2021) and thus marking the top of the K-Pg boundary sequence within the crater. Within the peak-ring, a continuous low frequency and irregular reflector (LFR) lies below the STUC with 130 m layer of suevite and melt rock in between as drilled at Site M0077 (Gulick et al., 2019; Morgan et al., 2016). This LFR has been associated, albeit intermittently, with the base of a thin zone of low velocity found by full waveform inversion (Morgan et al., 2011). Aside from the LFR, there are no laterally coherent reflections within the peak ring, although, numerous diffraction hyperbolae in the time migrated stack indicate a complex scattering regime.

The character in the 2-D surface profiles below the Chicxulub suevite is non-reflective; as there are no laterally coherent events visible, these zones are often said to be 'seismically transparent', meaning that there are no readily traceable coherent events visible. Aside from impact structures (e.g., Scholz et al., 2002), seismic imaging over metamorphic crystalline cratons (e.g., Kneib, 1995) and igneous basalt flows are examples of geological environments that exemplify 'seismically transparent' sections.

Overall, the seismic observations are consistent with the 'dynamic collapse' model (Collins et al., 2002; Ivanov & Kostuchenko, 1997), which accounts for the uplift and subsequent collapse of the central peak as well as the overturning of basement crust on top of the slump blocks of Mesozoic sediments to form

the peak ring (Collins et al., 2002; Morgan et al., 2016a,b). The peak ring in situ densities and seismic wave speeds as determined from gravity modelling and seismic tomographic inversion are significantly diminished relative to the values expected for intact crystalline cratonic crustal rock (Christeson et al., 2018). Resolving this discrepancy from what is expected for the depths of origin of the peak ring rocks and testing the dynamic collapse hypothesis against competing models for the formation of peak ring structures in part motivated Expedition 364 (Site M0077) drilling and sampling of Chicxulub's peak ring in 2016. The borehole stratigraphy is composed of post-impact Cenozoic carbonates overlying impactites, which in turn overlie highly fractured and shock damaged felsic granitoid basement blocks interspersed with impact melt and breccia dikes (Morgan et al., 2016). The composition of the felsic basement rocks is consistent with numerical modelling results, which suggests these materials originated at a depth of ~10 km and were displaced laterally more than 20 km to form the peak ring. Both the low densities and seismic wave speeds of these felsic rocks correlate with their anomalously high porosities (Christeson et al., 2018) produced during shock compression to pressures possibly as high as 20 GPa (Feignon et al., 2020; Morgan et al., 2016; Rae, et al., 2019) . These low wave speeds were clearly observed by full waveform seismic tomography inversion (Christeson et al., 2021; Morgan et al., 2011) and were confirmed by both downhole sonic logging and the zero-offset VSP from Expedition 364 discussed in more detail here.

#### 4.2.2 Expedition 364 Geology

Site M0077 (Figure 4.1c) was drilled during the joint IODP/ICDP Expedition 364 campaign in 2016 at a location estimated to be ~46 km from the center of the impact structure. Summaries of the technical details of the project may be found in Gulick et al. (2017a), of the geophysical logging in Lofi et al. (2018), and of the combined log/core property interpretation in Christeson et al., (2018) (see **Error! Reference source not found.**). The borehole was drilled in three stages dependent upon engineering and key target considerations with cores obtained between 505.7 and the total depth of the hole at

1334.7 meters below sea floor (mbsf) (Morgan et al., 2017). The core was classified based on lithology into four major lithostratigraphic units 1 through 4, that are broadly characterized as post-impact sediments, suevite, impact melt rock, and displaced shocked granitoids, respectively (Smith et al., 2020). Unit 1 (505.7 to 617.33 mbsf) consists of post-impact Paleogene and Eocene pelagic limestones, marls, and claystones, extending to the STUC at 617.33 mbsf. Directly above the STUC is Transitional Unit 1G (616.58 – 617.33 mbsf) which is a micritic limestone likely deposited over a period of a few years (Gulick et al., 2019; Lowery et al., 2018; Whalen et al., 2020), capped by the K-Pg iridium anomaly (Goderis et al., 2021). The approximately 55.93-55.71 Ma Paleogene-Eocene Thermal Maximum manifests as a thin (607.27 to 607.06 mbsf) shale layer bounded by a disconformity to Paleogene carbonate 'hardground' below and bioturbated limestones above (Smith et al., 2020). The Palynological age-depth relationships show low sedimentation rates of 0.22 cm/Kyr on average over the Paleocene section, complicated by numerous unconformities, with high average rates of 2.3 cm/Kyr through the Eocene section (Gulick et al., 2017b).

Lithostratigraphic Unit 2 (617.33 mbsf to 721.61 mbsf) and Unit 3 (721.61 mbsf to 747.02 mbsf) are an ~130 m thick series of impactites deposited immediately following the excavation, rebound, and dynamic collapse of the crater. The upper ~90 m is suevite with generally decreasing particle sizes upwards indicative of rapid deposition of materials carried by ocean resurge into the crater in the hours following the impact (Gulick et al., 2019). The increasing proportions of impact melts mixed with clasts of the target rocks in rocks below ~706 mbsf in Units 2 and 3 are interpreted to indicate that this material was emplaced prior during the initial resurge and underwent explosive interactions between melt and seawater (Gulick et al., 2019; Osinski et al., 2020; Schulte et al., 2021). Unit 3 is dominated by impact melt with poor clast abundance, demarking an approximate limit to the depth of the explosive interaction. The abundance of clays, zeolites, and other secondary alteration products throughout both

units indicates persistent hydrothermal alteration (Kring et al., 2020; Simpson et al., 2020) that is particularly severe in a porous section between ~689 to 706 mbsf.

Unit 4 (747.02 mbsf to 1334.7 mbsf) includes highly damaged and displaced original target felsic magmatic rock (Zhao et al., 2020) containing occasional doleritic dikes that were bisected by zones of breccia and melt dikes during the impact event. Riller et al. (2018) document the types and abundances of different scales of mechanical disruption including intragranular and intergranular tension microcracks, mm to cm thick cataclasites, and hundreds of shear faults with decametric slip displacements all contributing to high porosities and low  $P$ -wave velocities. The microcrack porosity is preferentially oriented at  $45^\circ$  to the principal stress axis during shock (Rae et al., 2019). Detailed investigation of shock induced planar deformation features in quartz grains from the felsic protolith indicate that this material reached shock pressures of 18-20 GPa (Feignon et al., 2020). This zone, too, displays evidence of hydrothermal alteration including intermittent dissolution of quartz that increased porosity values (Kring et al., 2020). The sonic geophysical logs and multi-sensor core logging density measurements (Figure 4.3) correlate broadly, but not universally, to these core-interpretation based lithologic intervals. Shear wave speeds  $V_{s\ log} \lesssim 1.5$  km/s cannot be well constrained with the monopole logging instrument employed due to the interference of much stronger Stoneley wave modes propagating at near the sonic velocity of the borehole fluid (e.g., Paillet & Cheng, 1991); thus, only those values exceeding 1.5 km/s are shown in Figure 4.3.

#### 4.2.3 Expedition 364 Physical Properties

The sonic compressional log velocities through upper sections of post-impact Cenozoic sediments above 585 mbsf are consistent with depth trends seen elsewhere in shallow and primarily carbonate columns (e.g., Eberli et al., 2003; Japsen, 1998). Depths to 590 mbsf had initially been informally separated into two distinct zones from 47.5 m to 280 mbsf and 280 to 590 mbsf on the basis of average VSP transit

time  $P$ -wave speeds of  $2.285 \text{ km/s} \pm 14 \text{ m/s}$  and  $2.567 \text{ km/s} \pm 4 \text{ m/s}$ , respectively (Gulick et al., 2017c).

The reason for the subtle difference between the two zones is unknown but may result from mechanical changes resulting from the transition of biogenic opal-A to opal-CT (e.g., Guerin & Goldberg, 1996; Ishii et al., 2011; Meadows and Davies, 2009), the latter indicated by X-ray identification of significant modal proportions of  $\alpha$ -quartz, cristobalite and tridymite in the core section 505-585 mbsf (Gulick et al., 2017b, table T8). This variation may alternatively be due to other changes in the rock composition as seen in the abrupt change in the natural gamma radiation log (GR) that may indicate greater concentrations of clay minerals above 275 mbsl (Gulick et al., 2017c, Figure F1). Anomalously low  $V_p$  (both log and VSP

~1.800 km/s) exist ~230-280 mbsf and this zone was likely subject to karstification as suggested by the appearance of large ~10 cm diameter vugs in the ultrasonic televiewer images.

Density  $\rho_{core}$ ,  $V_P$  and  $V_S$  (both log and VSP) all rapidly increase at depths 585-617 mbsf which roughly correlates with Subunits 1E-G (Gulick et al., 2017b, Figure F43). The reasons for the increased seismic relevant properties through this interval are not explicitly known, although the gamma ray log drops at 588 mbsf, suggesting reduced clay in increased carbonate lithology. Additionally, these lowest sections of Unit 1 are also distinguished by the absence of both organic carbon (Gulick et al., 2017b, table T6) and

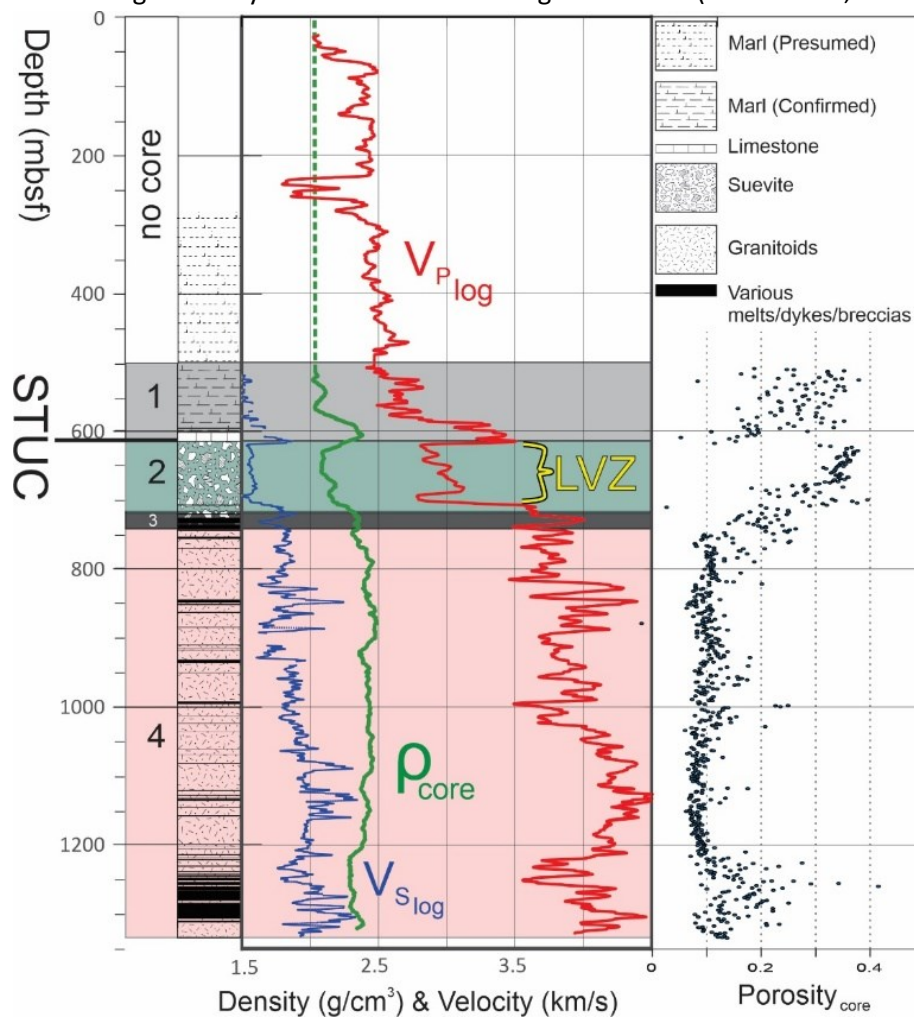


Figure 4.3. Simplified geological column from core and cuttings with the four major units as interpreted from the core (505.7 mbsf to 1334.7 mbsf) compared to running average of density measurements on discrete core samples (green line) and to the running average over 0.5 m of the P-wave (red line) and S-wave (blue line) speeds as measured by the sonic log. Core was not retrieved above 500m and so it is not included in the 4 colored units.

of opal-CT (i.e., as indicated by the lack of cristobalite and tridymite) with  $\alpha$ -quartz being the only silica phase detected in XRD (Gulick 2017 et al., 2017b, table T8). The opal-CT to  $\alpha$ -quartz transition has been linked to changes in mechanical properties (Nobes et al., 1992) that have provided elsewhere sufficient material contrasts that result in clear seismic reflections (Ireland et al., 2010). In addition, the bottommost section of the post impact sediments was most certainly exposed to higher temperature hydrothermal fluid venting for at least 2.1 Myr after the impact (Kring et al., 2020). Stylolites are noted throughout Subunits 1E-G, with the highest concentration toward the bottom of this sequence in Subunit 1F (Goderis, 2019; Gulick, et al., 2017b). The stylolites suggest increased compaction as a contributing factor to elevated  $\rho_{core}$ ,  $V_P$  and  $V_S$  (both log and VSP) at these depths, as well. Regardless of the origin, we refer to this ~35 m thick zone (582-617 mbsf) of post impact hardened sediments as a seismic 'LID', as the contrast in its bounding seismic properties contributes significantly to the observed seismic reflection signature over the peak ring (Figure 4.4).

$V_P$ ,  $V_S$  (both VSP and log), and  $\rho_{core}$  all discontinuously drop across the STUC at 617.33 mbsf into Unit 2 and remain low to 705.5 m depth where increased proportions of melt rock are observed. The mechanical properties in this depth interval clearly differ (Figure 4.4) from that above and below and are hereafter referred to as the low velocity zone (LVZ). Unit 2 is suevite that is highly porous ( $\Phi_{core} \approx 0.2$  to 0.4), with low wave speeds observed in discrete sample measurements and the sonic log, similar to observations of suevite at the Ries Crater, Germany (Heap et al., 2020) and the Bosumtwi Structure, Ghana (Hunze & Wonik, 2007; Meillieux, 2009). In contrast to its top, the base of Unit 2 at ~722 mbsf does not correspond to any discontinuity in the mechanical properties (Figure 4.4). Instead,  $V_P$ ,  $V_S$  (both VSP and log), and  $\rho_{core}$  increase abruptly at 705.5 mbsf in the vicinity of two thin melts near the base of Subunit 2B, and these elevated seismic properties continue through the remainder of Unit 2 and into Unit 3.



Relatively greater wavespeeds and densities (Christeson et al., 2018) persist to the bottom of the borehole through the predominantly impact melt rocks of Unit 3 (721.61 – 747.02 mbsf) and the highly damaged granitoids (Rae, et al., 2019) with occasional dolerite, suevite, and melt dikes of Unit 4 (747.02 – 1334.69 mbsf) (Gulick, et al., 2017b,d). Mechanically, there is no abrupt boundary between the melt rock-rich zone commencing at 705.5 mbsf through to the base of Unit 3 with the underlying peak-ring material. However, we designate these as the seismic ‘MELT’ zone and the ‘PR’ zone due to the clear differences between their composition and suggested means of emplacement (de Graaff et al., 2021; Gulick et al., 2019; Kaskes et al., 2019).

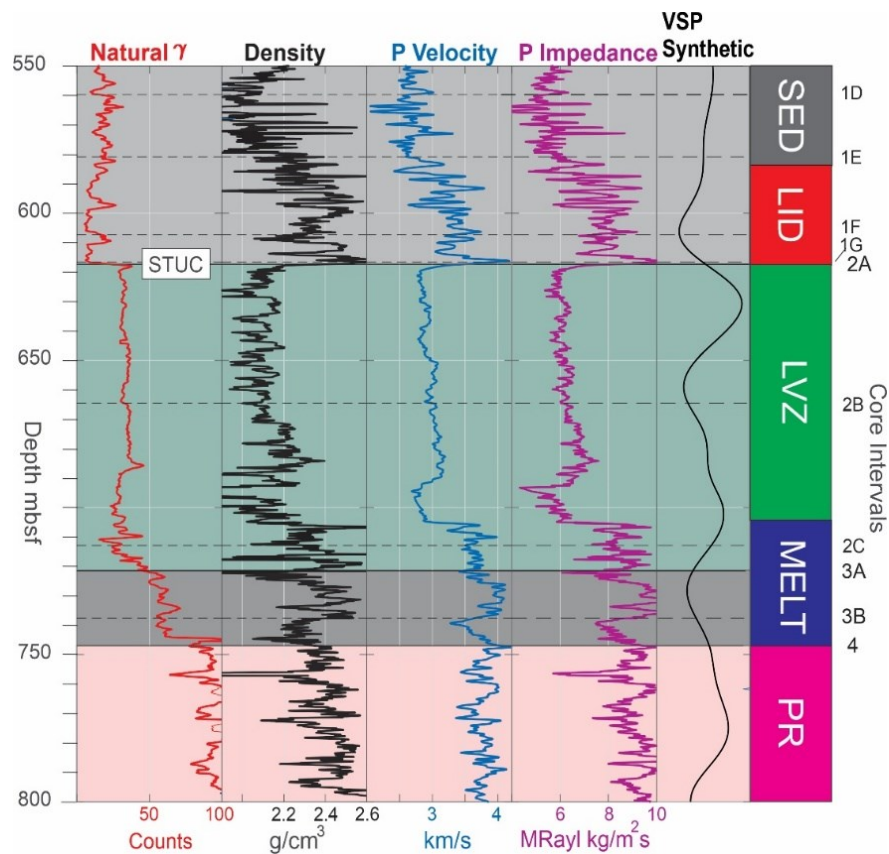


Figure 4.4. Details of physical properties associated with the K-Pg reflection obtained from the multi-sensor core logging including the natural  $\gamma$  radiation, the saturated bulk density determined by  $\gamma$ - $\gamma$  absorption, the P-wave sonic wave speeds obtained from the geophysical logs, and the calculated P-wave impedance. Five mechanical zones are distinguished on the basis of changes in P-wave impedance ( $Z$ ) as sediments (SED), hardened post-impact sediments (LID), low velocity zone (LVZ), melt rich zone (MELT), and displaced peak ring material (PR). The depths of the tops of the geologic intervals and subintervals interpreted from the core are denoted on the right. Discrete data points have been averaged into a continuous function with a filter radius of 5 sampling points.

Understanding the nature of the K-Pg reflection necessitates a close examination of the physical properties responsible for forming this event. Sharp discontinuities in the physical properties are also evident in multi-sensor core logging (MSCL) densities (Figure 4.4) at the STUC and towards the bottom of Unit 2B. The lower discontinuity at 705.5 mbsf is associated with the increased presence downhole of impact melt rock and the higher values of density and wave speed continue through the melt-rock rich unit 3 (Gulick et al., 2019).

The strength of the *P*-wave seismic reflection from the contrast between two elastic media is primarily controlled by the contrasts in their *P*-wave impedance ( $Z = \rho V_p$ ) with the normal incidence reflection coefficient *R*,

$$R = \frac{Z_2 - Z_1}{Z_2 + Z_1} \quad (4.1)$$

where the subscripts 1 and 2 refer to the upper and lower media, respectively. Examination of Figure 4.4 suggests that the two impedance discontinuities at the STUC at 617.33 mbsf and within unit 2B (705.5 mbsf) which bound the LVZ would, at seismic frequencies, have large reflection coefficients of about -0.2 and +0.2, respectively. This is a key point, as large reflections originate from these impedance discontinuities and the strong reflection event is associated with the tuned superposition of these two reflections. Consequently, it is expected that the impedance architecture of this low velocity zone sandwiched between the earliest Cenozoic sedimentary LID and the melt rock rich zone commencing in unit 2B will strongly influence the character of the overall seismic reflection package associated with the STUC (Figure 4.2b).

## 4.3 Methods

### 4.3.1 Downhole Sonic logs

The downhole sonic logs were acquired in open hole conditions with a QL40-FWS (Full Waveform Sonic, ALT/Mount Sopris Instruments) slimline tool. The tool was combined into tool strings and centered with two centralizers (see Morgan et al. (2017) for additional details). The source frequency was 6 kHz (wavelength of  $\sim 50$  cm at 3 km/s). Data were acquired running uphole at 5-cm spacing. The first arrival signal was checked on the way down in the steel pipe to confirm a *P*-wave velocity typical of steel (5.40 km/s). The measured velocity was 5.55 km/s; thus, formation velocities may be slightly overestimated (by  $< 3\%$ ). Data were subsequently processed with the ALT WellCAD software to calculate the compressional and shear velocities used in this work. Due to the good data quality, waveform picking was done automatically with the semblance analysis module performed on 3 receivers (R1, R2, R4), the velocity signal thus being integrated over a 0.8 m thick interval. The compressional velocities look accurate, correlating well with the discrete *P*-wave measurements on samples and with the *P*-wave velocity calculated from the Standard Threshold Pickup Algorithm module using the R1 and R2 receivers (spacing = 20 cm).  $V_{s\ log}$  signal was not always clear and should be used with care especially in the post-impact carbonates. Down-hole depths were calculated from wireline distance and have been corrected to mbsf for consistency.

### 4.3.2 VSP Acquisition during Expedition 364 and raw profiles

Details of the VSP acquisition during Expedition 364 may be found in Gulick et al., (2017e), and a summary of VSP theory and methodology are provided in 0 and at <https://doi.org/10.7939/DVN/D1YY4A> (Nixon, 2021d). In brief, the 3-C records were obtained using wall-locking geophone sondes activated by an airgun source offset a few meters from the borehole. Acquisitions occurred in three separate deployments (Figure 4.5, RHS) because of drilling operations. The raw vertical component VSP (Figure 4.5) displays numerous events, including the down-going pulse

(a), a strong upward-going primary reflection from the vicinity of the STUC (b), and its corresponding down-going water-surface multiple (c), as well as indications of deeper reflected events that appear to originate within the peak ring (e,f). Fortunately, tube waves (d), which can overwhelm the desired signals, only occurred over a limited depth range during stage 3 acquisition and did not seriously complicate the processing.

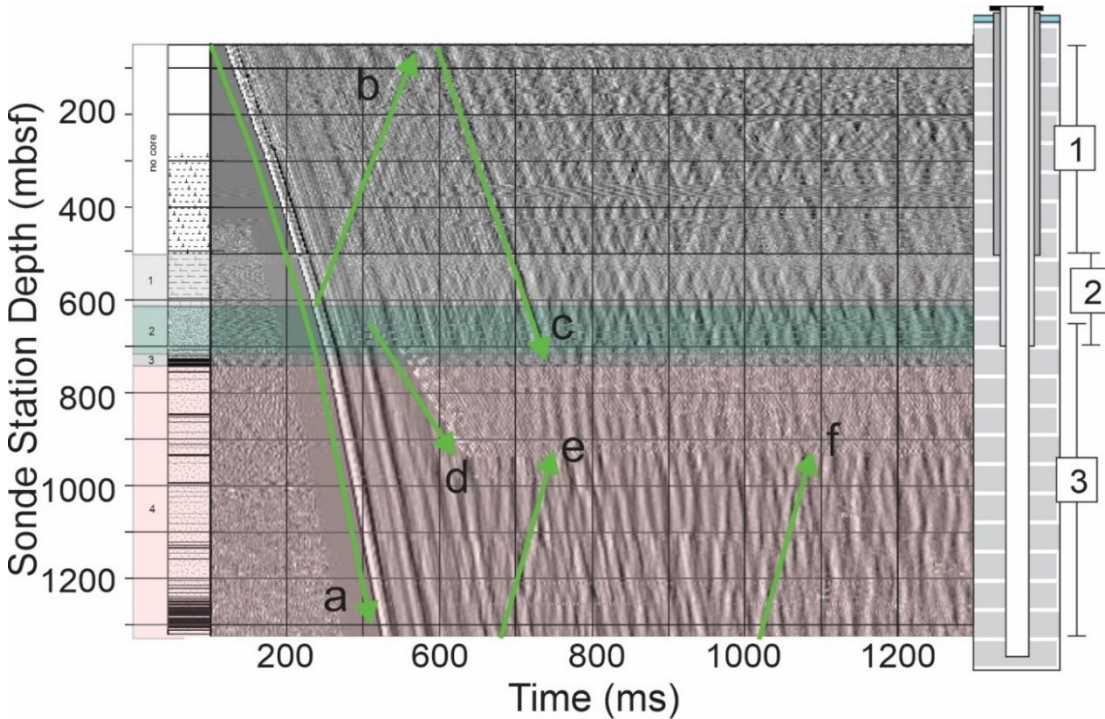


Figure 4.5. Raw vertical component VSP record (first peak normalization and 100 ms automatic gain control) acquired in three stages in rightmost panel (1: 47.5 mbsf – 498.75 mbsf @ 1.25 m/station, 2: 500 mbsf – 696.25 mbsf @ 2.5 m/station, 3: 652.5 – 1325.0 mbsf @ 5 m/station). The various arrivals a – f delineated by upward and downward arrows are described in the text.

One key motivation for obtaining VSP data is that through appropriate processing the down-going wavefield (primarily the strong pulse wavelet) may be separated from the weaker up-going reflections (e.g., Hardage, 1985; Hinds et al., 1996 ) allowing the true depth of such events to be directly linked to the travel-time in the surface seismic reflection data. The up-going wavefields (Figure 4.6), the processing details of which are given in appendix B, indicate that the upward going K-Pg reflection

package is a ~100 ms long event commencing with the higher impedance limestone immediately overlying the STUC at 617 mbsf.

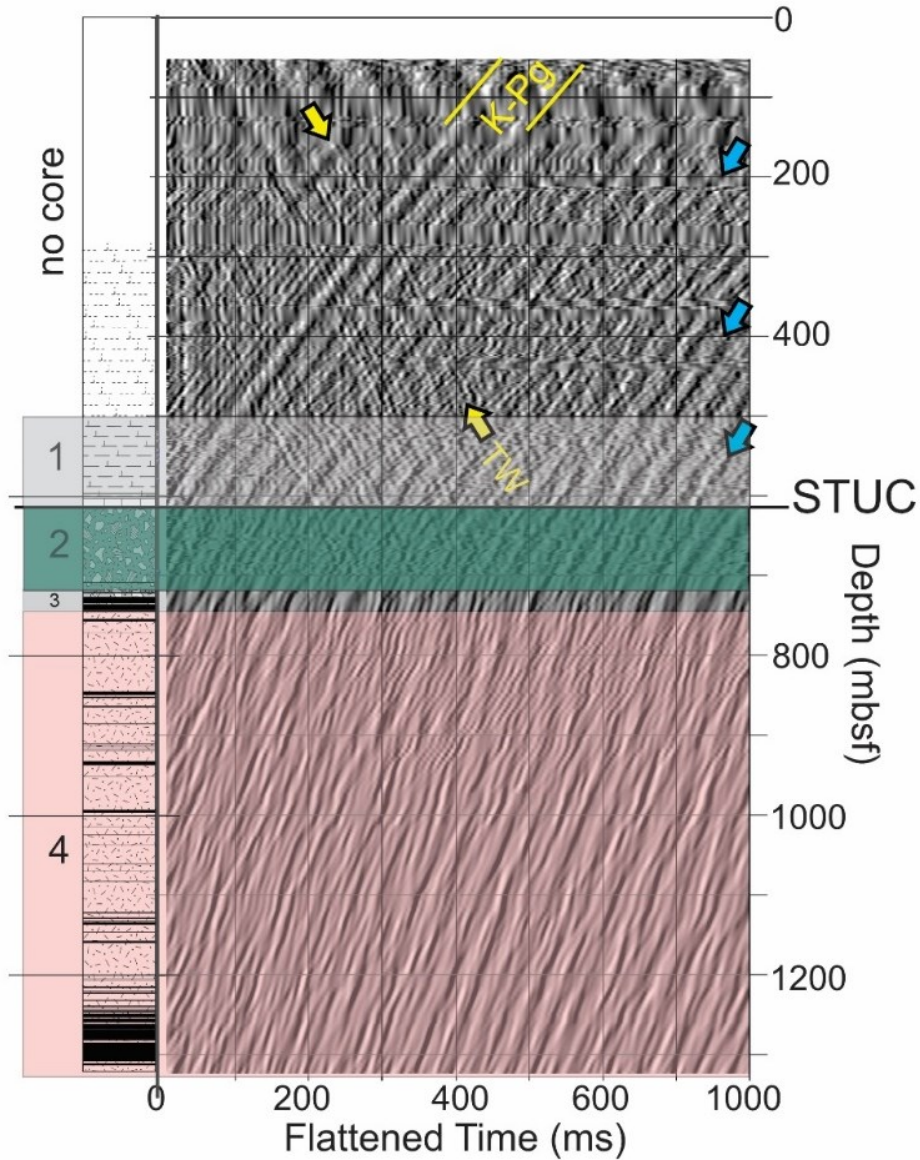


Figure 4.6. Separated upward-going wavefield obtained after wavefield separation compared against lithostratigraphy and four major units as interpreted from core. K-Pg boundary shown both in depth at 617 mbsf and in time. Smaller amplitude down-going tube waves are apparent with one example highlighted by yellow arrows and indicated as TW; these cannot be removed using the median filter. Upward-going events that originate beneath the K-Pg boundary are indicated by blue arrows. Wavefield characters differ above and below the top of the peak ring.



### 4.3.3 Analysis of Horizontal Components

In marine settings, zero-offset VSP data are rarely used to study *S*-waves primarily because of the difficulties associated with directly generating a shear wave using airgun sources in water where, at best, only weak *P*-*SV* conversions are expected. The horizontal radial and tangential polarized geophone signatures (appendix B) in our study are of lower amplitude than the vertical component, as expected, although they do display an *S*-wave arrival due to its polarization transverse to the borehole axis. At each depth, the horizontal components were rotated into a principal polarization direction (details on processing in appendix B) yielding separate profiles for zones mostly above and below the STUC (Figure 4.7). The *S*-wave arrival is enhanced using polarization filtering (Montalbetti & Kanasewich, 1970). As with the vertical component wavefield, the *S*-waves observed in the upper sections of post-impact sediments (Figure 4.7a) show relatively continuous coherent arrivals which differ significantly from the chaotic pattern within the peak-ring (Figure 4.7b).

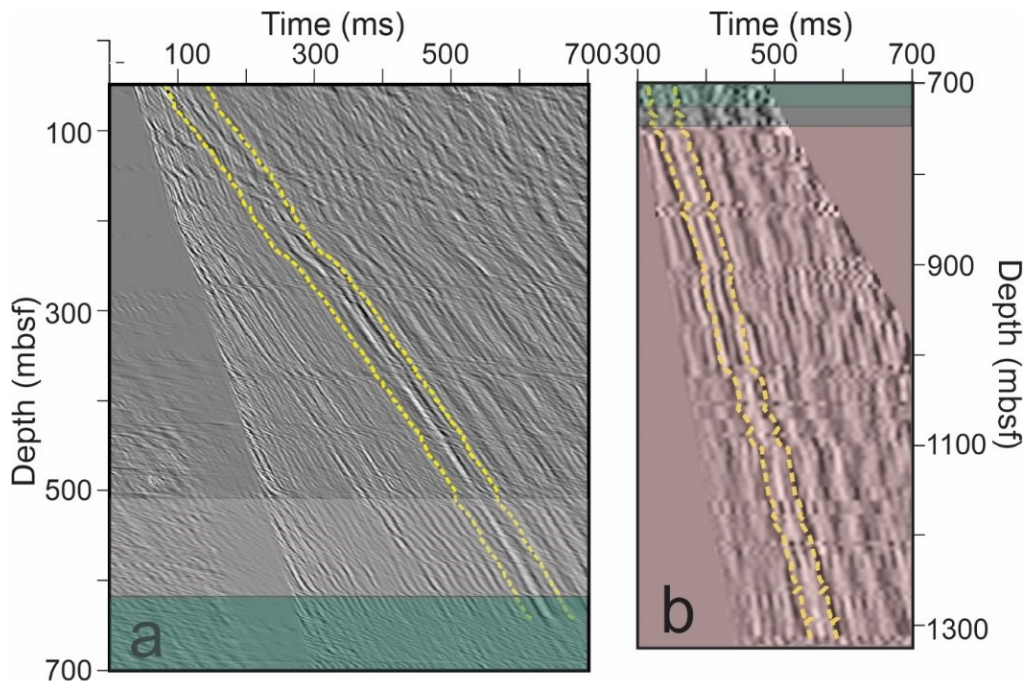


Figure 4.7. Optimization of Shear Wave Arrivals: Maximally rotated horizontal component profiles through a) top of suevite (Interval 2) and post K-Pg sediments, and b) bottom of suevite (Interval 2) through Interval 3 (melt) and Interval 4 (peak ring). Yellow lines bound the polarization analysis time window around converted *S*-wave. Color overlays indicate intervals as in Figure 4.6.

#### 4.3.4 Determination of Wave Speeds

Large receiver spacings in traditional VSP experiments have limited the resolution for the determination of in situ seismic wave speeds because significant errors arise from the uncertainties associated with picking consistent arrival times of the down-going waves for the relatively small delays between receivers. Authors have attempted to overcome this limitation by inverting their sets of observed one-way transit times to depth in VSP studies (Stephen & Harding, 1983; Stewart, 1984).

One significant difference of our data is that the wavefield was sampled at relatively close spacing, as small as 1.25 m along the borehole; this spacing allows use of a more direct 'local slope' method (Schmitt et al., 2007), which provides the in situ interval velocity together with a measure of its uncertainty. This method simply relies on equating the 'local' slope  $\Delta z/\Delta t$  to the velocity via linear least-squares regression of a sequence of adjacent observed one-way VSP transit times versus their depth. The square root of the variance of this slope provides a measure of the uncertainty, the expressions for which may be found in many linear regression texts (e.g., Altman & Krzywinski, 2015) and are shown within 95% certainty envelopes (Figure 4.8). The P-wave arrival time used in this analysis is declared to be that of the first amplitude extremum, a negative amplitude trough of the initial direct down-going pulse. This trough is chosen to avoid complications to the pulse character introduced by interference of the primary pulse with pursuant water surface multiples and ambiguities arising from both the errors and physical meaning of picking the first detectable onset of the wave (Molyneux & Schmitt, 2000). Similarly, the S-wave first arrival time was chosen as the first coherent negative amplitude extremum. Unfortunately, there was not an unambiguous and coherent S-waveform in the region 640 - 755 mbsf and due to local slope method's sampling radius,  $V_{S\ VSP}$  estimates are not available in the interval 633.75 - 780 mbsf. The uncertainties in  $V_{P\ VSP}$  throughout and  $V_{S\ VSP}$  at depths 72 - 628 mbsf (within the Cenozoic section) are determined with reasonable accuracy. In contrast, the 95% envelope for  $V_{S\ VSP}$  at depths >780 mbsf (within the peak ring) is wide, indicating the unreliability in picking an appropriate S-wave

transit time through this zone, as suggested by the complicated structure to the horizontal seismic wavefield (Figure 4.7b). The character of the reflection package arising from the vicinity of the STUC is analyzed by calculating 1-D 'synthetic' normal incidence reflection traces by convolving a representative

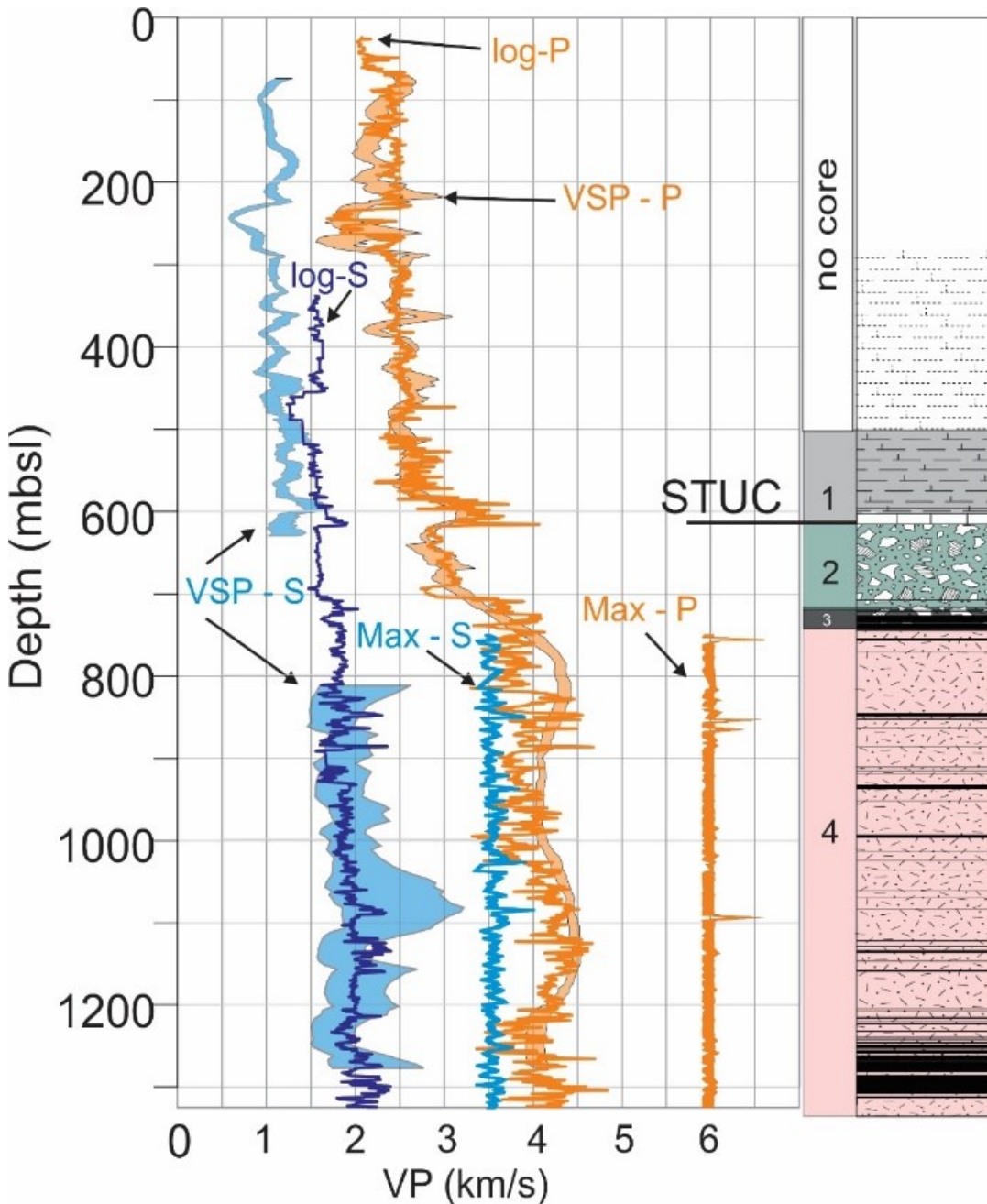


Figure 4.8. Observed wave speeds determined from the VSP P-wave (orange shaded trend) and S-wave (blue shaded trend) arrival times, log-P and log-S speeds interpreted from the full sonic waveforms, and intrinsic Max-P and Max-S speeds estimated for the undamaged rock on the basis of mineral modes within Voigt-Reuss-Hill bounds.



wavelet with an estimated reflectivity time series (e.g., Ganley, 1981). Two different candidate wavelets were used in this basic modelling (see insets to Figure 4.9d,e). The first (Figure 4.9d) is obtained from the estimate of the down-going seismic wavefield directly from the VSP (See Figure A 12). The second is averaged from the wavelet extracted from the nearest 11 seismic traces from migrated reflection profiles CHIX17b, CHIX10, and CHIXR3 using the standard minimum phase wavelet assumption (Kanasewich, 1974). The reflectivity sequence (Figure 4.9i) is calculated from the observed  $V_p$  log and  $\rho_{core}$  from core sampling using a recursive invariant embedding scheme (Kennett, 1974) that includes multiple reflections.

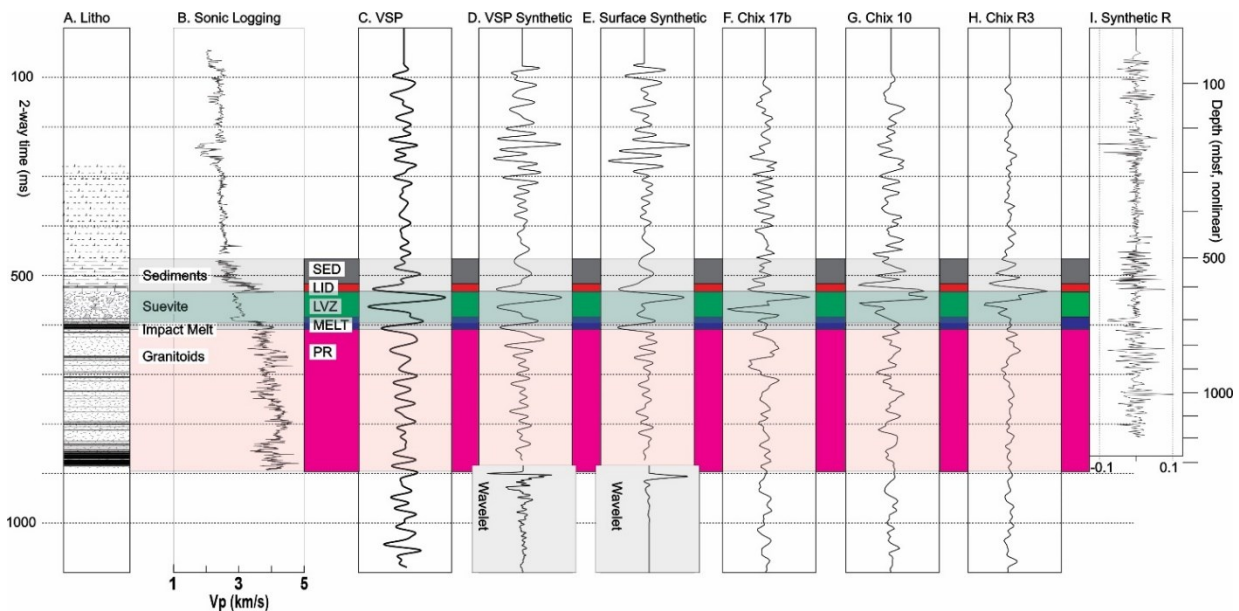


Figure 4.9. Observed and modelled seismic reflection responses with mechanical seismic zones (between panels) and major lithostratigraphic units (within panels). a) Reference Lithology. b) Sonic logging P-wave velocities. c) Final processed VSP trace with corridor stack to mimic normal incidence reflection record. d) Synthetic normal incidence trace from estimate of downgoing wavelet (bottom) from VSP. e) Synthetic normal incidence trace from average estimate of wavelet extracted from migrated lines CHIX17b, CHIX10, CHIXR3. (f-g) average of 5 nearest migrated seismic traces from profiles CHIX17b, CHIX10, and CHIXR3, respectively. Correlation coefficients between various traces are shown in the supplementary methods (Error! Reference source not found.).

## 4.4 Results

### 4.4.1 VSP and log derived wave speeds

The envelopes of the updated VSP derived compressional ( $V_{P\ VSP}$ ) and new shear ( $V_{S\ VSP}$ ) wave velocities (Figure 4.8) mostly track their corresponding sonic log values. The  $V_{S\ VSP}$  are often  $< 1.5$  km/s further reinforcing the difficulties in finding  $V_{S\ log}$  from the sonic logs in these zones as mentioned earlier (Figure 4.3). The  $V_{P\ VSP}$  increases gradually throughout the Cenozoic sedimentary carbonates aside for a low velocity excursion near 250 mbsf. Both the  $V_{P\ VSP}$  and  $V_{P\ log}$  show an abrupt drop in speeds at the top of the STUC below the high-velocity LID. The lower contact of the STUC is smoothed, perhaps in part due to the larger spacings between the sondes (2.5 m) in the depth interval 500-696.25 mbsf compared to a spacing of 1.25 m at depths 47.5-498.75 mbsf.

### 4.4.2 Intrinsic wave speeds of undamaged peak ring materials

The deficit in both the sonic logging and  $V_{P\ VSP}$  relative to the expected lithologies within the peak ring has already been noted (Christeson, et al., 2018) and attributed primarily to the damage-induced porosity. The  $V_{S\ log}$  and the more poorly constrained  $V_{S\ VSP}$  measures described here, too, are significantly below the speeds expected for the target granitoids. We quantify this deficit more fully by calculating the speeds expected for the undamaged mineral crystallite (granite) of the peak ring materials on the basis of the mineral volumetric modal fractions  $\phi_i(z)$  and the corresponding intrinsic isotropic moduli  $K_i$  and  $\mu_i$  (Table 4.1). The constituent mineral phases from the X-ray diffraction core analyses reported in Gulick et al. (2017b, table T5) and Gulick et al. (2017d, table T4) are used to first calculate the undamaged bulk rock  $K_o(z)$  and shear  $\mu_o(z)$ . The upper Voigt  $K_V$  and  $\mu_V$  and lower Reuss  $K_R$  and  $\mu_R$  bounds constrain the allowable values of  $K_o(z)$  and  $\mu_o(z)$  with

$$K_V(z) = \sum \phi_i(z)K_i \geq K_o(z) \geq \left[ \sum \frac{\phi_i(z)}{K_i} \right]^{-1} = K_R(z) \quad (4.2)$$

and

$$\mu_V(z) = \sum \phi_i(z) \mu_i \phi_i(z) \mu_i \geq \mu_o(z) \geq \left[ \sum \frac{\phi_i(z)}{\mu_i} \right]^{-1} = \mu_R(z) \quad (4.3)$$

Hill (1952) suggested that the simple average of these bounds provided an adequate estimate, but we retain both Voigt-Reuss-Hill (VRH) bounds. The bounds for the wavespeeds expected for the nonporous and undamaged rocks are then

$$\sqrt{\frac{K_V(z) + 4\mu_V(z)/3}{\rho_o(z)}} = \sqrt{\frac{M_V(z)}{\rho_o(z)}} \geq V_{Po}(z) \geq \sqrt{\frac{K_R(z) + 4\mu_R(z)/3}{\rho_o(z)}} = \sqrt{\frac{M_R(z)}{\rho_o(z)}} \quad (4.4)$$

where  $M$  is the longitudinal, or P-wave, modulus, and

$$\sqrt{\frac{\mu_V(z)}{\rho_o(z)}} \geq V_{So}(z) \geq \sqrt{\frac{\mu_R(z)}{\rho_o(z)}} \quad (4.5)$$

where the pore-free rock intrinsic density is

$$\rho_o(z) = \sum \phi_i(z) \rho_i \quad (4.6)$$

Mineral	Quartz	Albite	Microcline	Sanidine	Orthoclase	Anorthite	Augite
$\rho$ (kg/m <sup>3</sup> )	2648	2610	2567	2520	2571	2765	3320
$K$ (GPa)	37.8	56.9	55.4	58.8	62	84.2	95
$\mu$ (GPa)	44.3	28.6	28.1	30.1	29.3	39.9	59

Table 4.1. Isotropic elastic moduli and density for primary constituent minerals in peak ring (Bass 1995).

The VRH bounded  $V_{P\ VRH}$  and  $V_{S\ VRH}$  are shown in Figure 4.8 and are the estimates for the unaltered isotropic polycrystalline rock, with no attempt to incorporate pores or microcracks. The values will be in error within the melt rock zones as neither the volume fractions of melt rock nor the glass moduli are well constrained. The observed VSP compressional wavespeeds within the peak ring (~4 - 4.5 km/s) are only about 65% to 75% of the VRH bounds (~6 km/s), illustrating the large deficits in wave speeds caused by shock induced damage and fracturing/faulting during peak ring formation.

The stack of the final VSP corridor (see processing details Figure A 12e) produces a seismic reflection trace in two-way time (Figure 4.9c) that is compared against the neighboring seismic reflection profiles CHIX10, CHIX17b, and CHIXR3 located at distances from the borehole of approximately 160 m, 200 m, and 350 m, respectively. With these offsets of the seismic profiles to the borehole we cannot expect the trace to match perfectly, with a correlation coefficient of 0.4068 between the real VSP trace and nearest profile CHIX10 (**Error! Reference source not found.**). The strong reflection just below 600 m depth (Figure 4.9, Figure 4.6) is the event originally interpreted to be the top of the K-Pg boundary section within the crater. However, the character of this event is not one of a simple primary reflection. As noted, the velocity structure near the STUC consists of rapidly increasing wavespeeds with depth in the Cenozoic sedimentary carbonates of the LID with a sharp decrease into the highly altered underlying suevites of the LVZ followed at ~700 m by a second abrupt increase at the top of the unsorted melt rich suevites, coinciding with the LFR.

The synthetic VSP trace (Figure 4.9d) captures well the character of the observed VSP trace (Figure 4.9c), confirming that the reflection package originates from interference of reflections from the complex impedance structure both above and below the STUC (Figure 4.4). The synthetic calculated using the wavelet extracted from the seismic profile (Figure 4.9e) also captures this behaviour. This extracted wavelet, however, has a broader frequency bandwidth and is sharper in the time domain; this nearly allows for separation of the events originating at the Z discontinuities top and bottom of the LVZ.

## 4.5 Discussion

### 4.5.1 Nature of the K-Pg reflection event

The characteristics of the upward-going wavefields differ significantly above and below the STUC (Figure 4.6). No upward travelling coherent events that could be interpreted as a seismic reflection are apparent in the wavefield within the peak ring granitoids. This contrasts with the continuous events, even those that must originate within the peak ring (with a few indicated by blue arrows, Figure 4.6), that characterize the wavefield above the STUC. These coherent reflections originating from the granitoids may originate from fault planes within the peak ring (Morgan et al., 2016); however, they do not stack well during processing of the surface seismic profile into continuous coherent events, suggesting that the lateral dimensions of the heterogeneity within the peak ring materials may not be larger than the Fresnel zone of the 2005 multichannel seismic data (~500 m width).

Curiously, there is no evidence for the *LFR* seen in the surface profiles throughout at least the full 3 seconds of the VSP record (not shown), even after applying numerous bandpass filters that would enhance lower frequency arrivals. This absence may mean that the conditions necessary to produce the *LFR* may not exist at the borehole location. Differences in the thickness of the MELT zone away from the drill site, for example, might explain the reflector. Alternatively, one cannot discount the possibility that this *LFR* could instead be due to reflections originating out of the plane of Line CHIX10 from the rugose 3D topography of the peak ring; the *LFR* may not result from in-plane physical property contrasts. This issue could only be resolved by conducting a high-resolution 3-D seismic program.

Hydrothermal fluids have altered the mechanical properties and possibly the density of the original impactites and early post-impact sediments. As a result, the local character of the K-Pg seismic event may depend on the duration, fluid fluxes, temperatures, and compositions resulting from the hydrothermal cooling after the impact. Much of the area will have been covered with the impactites which were then subsequently buried by continued sedimentary deposition; however, the mechanical

character of these deposits may depend strongly on the persistent hydrothermal flux. In cooler regions with less fluid flow, such a distinct seismic LID may not have formed and the sharp Z discontinuity at the STUC (Figure 4.4) may not have developed. Many of the rock layers immediately overlying Unit 1D have higher clay content, which may partly explain the rapid change in wave speeds. The increasing  $V_P$  (both log and VSP) in these layers is accompanied by a trend of diminishing porosity; the reasons for this are unknown, but this may be related to precipitation of minerals brought up by the vigorous hydrothermal circulation that occurred for at least 2 Myr post impact (Kring et al., 2020) or by variations in the compaction.

#### 4.5.2 Relationships of Velocities

Although a rock mass' elastic moduli and density contain more fundamental information about a material, often all that can remotely be observed are  $V_P$  and  $V_S$ , and the spatial distribution of these can self-consistently define structure.

Presented here are values of both  $V_P$  and  $V_S$  measured by moderate frequency sonic logs (6 kHz, Figure 4.10a) and seismic VSP frequencies ( $\sim 100$  Hz, Figure 4.10b). Additional insight may be gained from the simple  $R = V_P/V_S$  ratio or the closely related dynamic Poisson's ratio  $\nu$  that for an isotropic material is:

$$\nu = \frac{1}{2} \frac{R^2 - 2}{R^2 - 1} \quad (4.7)$$

In isotropic materials,  $-1 \leq \nu \leq 0.5$  is theoretically allowed, although for rocks the range  $0 \leq \nu \leq 0.5$  ( $R \geq \sqrt{2}$ ) is more realistic. Negative apparent  $\nu$  can appear if anisotropy is not appropriately considered (Wang et al., 2012).

$R$  or  $\nu$  has been used in numerous studies to augment the interpretation of observed  $V_P$  and  $V_S$ , which are nonunique by themselves, over the range of scales from the lithosphere (Golos et al., 2020) to

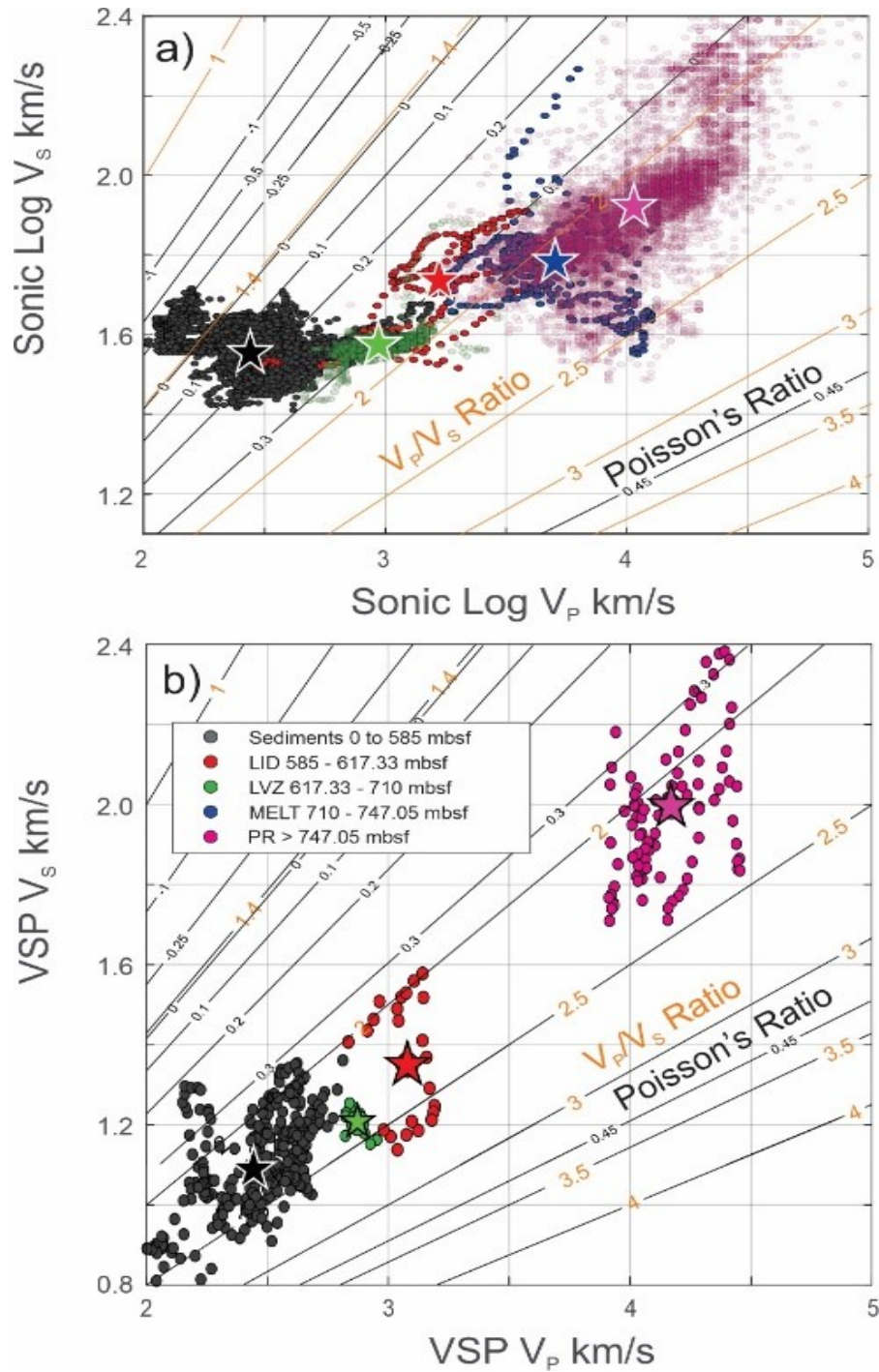


Figure 4.10.  $V_p$  versus  $V_s$  cross-plots with lithologic mechanical lithologies demarcated by colored symbols superimposed on Poisson's ratio and  $V_p/V_s$  ratio contours for a) the sonic log and b) the VSP analysis.  $V_s$  VSP data unavailable for the MELT. Average values for each lithology are denoted by stars.

the near surface. It is useful to review what trends might be expected. For example, in the case of pore-free crystalline igneous rocks,  $\nu$  can often provide some indication of mineralogical content;  $\nu$  is particularly useful with respect to quartz, which has an anomalously low  $\nu$  near 0.06 (Christensen, 1996). In porous sediments,  $\nu$  is sensitive to different factors which include mineralogy, porosity, pore geometry, effective confining stress, pressure, temperature, and saturation state (Hamilton, 1979). Modelling of the effects of crack densities on elastic properties using available theories show that  $R$  generally increases with crack density (e.g., Dunn & Ledbetter, 1995; O'Connell & Budiansky, 1974). Additionally,  $\nu$  is important in controlling the reflection amplitudes' dependence on angle of incidence, thus  $\nu$  is routinely sought during inversion of common midpoint active source seismic profiling (e.g., Li & Zhao, 2014). Figure 4.11 compares the  $\nu$  values observed here separately for the LID, the LVZ, the MELT,

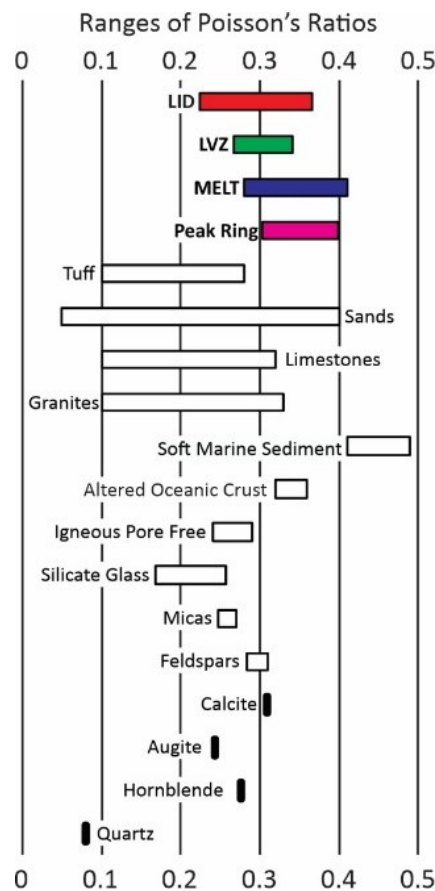


Figure 4.11. Poisson's ratio for various lithologies contrasted with those observed in the Chicxulub borehole.



and the peak ring material against similar terrestrial rocks and their constituent minerals. The mineral values are the Hill averages calculated for isotropic monocrystalline crystallites; aside from the anomaly of quartz, most of the minerals will have  $\nu$  of  $\sim 0.25 - 0.3$ . The values of  $\nu$  for pore free silicate glasses with felsic to mafic compositions increase from 0.168 to 0.257 as the  $SiO_2$  content decreases (Meister et al., 1980). Poisson's ratios for pore free igneous rocks fall within a relatively small range, but the presence of micro-cracks that are open at lower confining pressures strongly influences the material moduli and allow for a much wider range of  $\nu$  as indicated for granite. Limestones and sandstones have large ranges of observed  $\nu$  which are dependent upon the wide range of porosities and compositions encountered. Loosely consolidated siliclastic sediments, primarily muds and sands, are not expected at depth at the drill site; however, they are shown as they illustrate materials with vanishing rigidity.

The ranges for the LID, LVZ, MELT, and PR in Figure 4.11 encompass 95% (mean  $\pm 2$  standard deviations) of the calculated  $\nu$  (equation. 6.7) from the velocity observations at all depths in each interval. (Figure 4.10). The primarily calcite and  $\alpha$ -quartz bearing LID sediments fall within ranges comparable to low porosity limestones with the mean  $\nu$  below that for pure calcite. The  $\nu$  for the post-impact LID sediments is at the high end of that expected for carbonates, and the mean value is close to that for a monocrystalline calcite crystallite. These values are not atypical for low porosity carbonates (e.g., Njiekak & Schmitt, 2019). The  $\nu$  for the LVZ (Figure 4.12), MELT, and peak ring (Figure 4.11) are all anomalously high relative to the closest comparable terrestrial lithologies of tuffs and the constituent silicate melts. Only low velocity oceanic mafic materials, that have also experienced hydrothermal alteration near mid-ocean ridges, have similar values (Figure 4.11). The unusual  $\nu$  ranges for the Chicxulub borehole rocks are likely due to an anomalously low shear modulus as a result of multiple underlying factors. The VSP shear waveform is poorly resolved in the LVZ, which further supports the assumption of an anomalously low shear modulus.

The LVZ is a fining upward breccia with a matrix primarily composed of shocked ejecta particles. However, the fining upward trend is general, and periodically reverts back to coarser grains which modulates the fining upward trend with an oscillatory character.  $\nu$  and clast size both generally increase with depth within the LVZ, and major grain size discontinuities appear at roughly the same depths as discontinuities in  $\nu$  (Figure 4.12). Although there is a correlation between the LVZ fining upward sequence and  $\nu$ , this is not necessarily causative and further investigations into this trend are warranted.

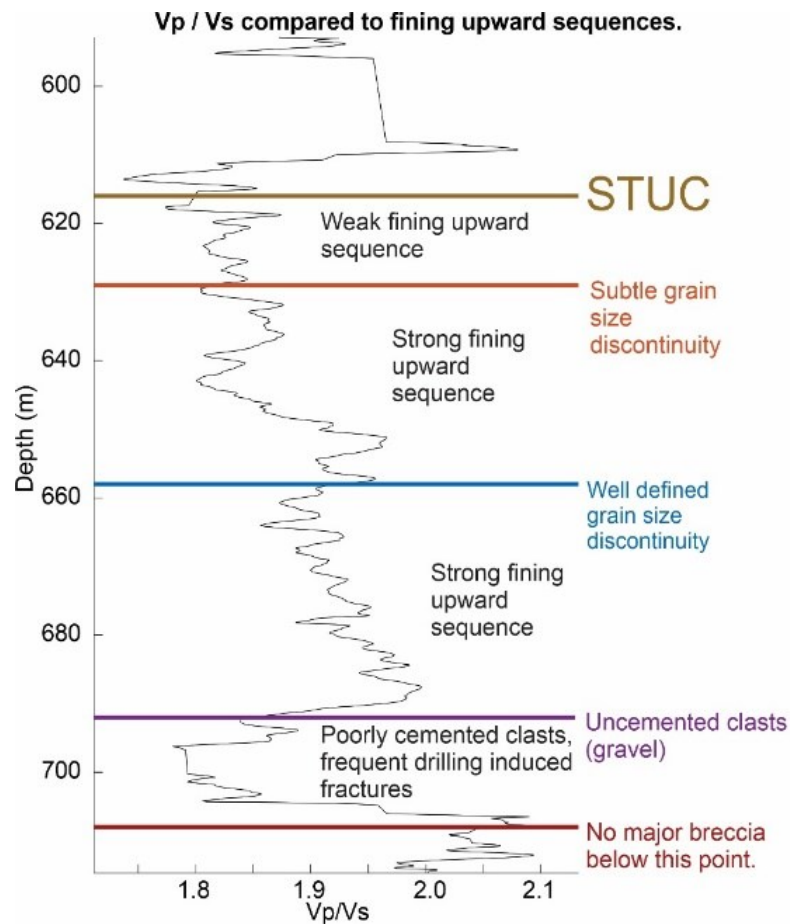


Figure 4.12.  $V_p/V_s$  ratio in the Suevitic Low Velocity Zone (LVZ).

#### 4.5.3 Assessment of Damage in Peak Ring Materials

Numerical models of the formation of large impact structures are one key tool to understanding the evolution pressures, temperature, deformation, and final structure (Melosh et al., 1992; Okeefe & Ahrens, 1993) that have progressively evolved to incorporate increasingly sophisticated estimates of

porosity or damage (Collins, 2014; Collins et al., 2004; Ivanov et al., 1997; Melosh et al., 1992; Wiggins et al., 2019). There are numerous attempts to constrain the models from morphology (e.g., Baker et al., 2016), gravitational signatures (Pilkington & Grieve, 1992), or seismic imaging (e.g., Collins et al., 2002). However, as noted by Collins (2014), calibrating the levels of damage predicted in the models against actual impact structures remains challenging on Earth due to the paucity of available pristine impact structures and the difficulties associated with direct observation through drilling. Mapping of the structures in terms of seismic wave speeds that are sensitive to damaged porosity can potentially provide some additional constraints.

In terrestrial situations, the influence of abundant macroscopic fractures and microcracks in diminishing seismic wave speeds or elastic moduli as manifest by their nonlinear stress dependence has been known for over a century (Adams & Williamson, 1923). The rock engineering community has most directly sought to exploit this link via empirical relationships between P-wave velocities and various measures of rock damage such as the rock quality index (Boadu, 1998; Dickmann et al., 2021; Sjogren et al., 1979). At larger scales, various lines of evidence including trapped modes (e.g., Gulley et al., 2017), seismic tomography (e.g., Cochran et al., 2009; Thurber et al., 2006), and interferometry of ambient noise (e.g., Brenguier et al., 2019) suggest zones of diminished seismic velocities that are interpreted as high levels of damage near fault zones in the brittle upper-crust (Ben-Zion & Sammis, 2003; Caine et al., 1996). Measurements from boreholes using sonic logs (Moos & Zoback, 1983; Stierman & Kovach, 1979), cross-well measurements (e.g., Wong et al., 1983), and near surface refraction (Rempe et al., 2013) also indicate the fracturing significantly lowers the waves speeds relative to laboratory measurements on the intact materials. Generally, both  $V_p$  and  $V_s$  are reduced in such zones translating to increased  $R$  and  $\nu$ . Efforts have attempted to extract the degree of damage from the observed wave speeds (e.g., Benson et al., 2006; Schubnel et al., 2006). However, the correlations may not always be as direct as hoped (Rempe et al., 2018; Swanson et al., 2020).

In developing a model of the dynamic fragmentation of materials that is employed in many impact models, Grady & Kipp (1987) defined the scalar measure of damage  $D$  that is bounded between 0 and 1. These bounds indicate the evolution from a fully intact undamaged material (value of 0) to a state of complete failure and disaggregation (value of 1), such that it cannot support a tensile stress. As such,  $D$  is intended to be an internal state variable that indicates the intensity of fracture damage in the material and is quantified through the reduction of the material's flaw-free elastic modulus  $B_o$  to that for the given level of damage  $B = (1 - D)B_o$ . However, Grady & Kipp (1987) did not specify which elastic modulus should be used. Bearing this concern in mind and using the simple relation  $B = \rho(V_B)^2$ , Ahrens & Rubin (1993) expressed  $D$  in terms of either  $V_P$  or  $V_S$  corresponding to the damaged longitudinal (P-wave)  $M_d = K_d + 4\mu_d/3$  and shear  $\mu_d$  moduli, respectively as

$$D_P = 1 - \frac{M_d}{M_o} = 1 - \frac{\rho}{\rho_o} \left( \frac{V_P}{V_{Po}} \right)^2 \quad (4.8)$$

and

$$D_S = 1 - \frac{\mu_d}{\mu_o} = 1 - \frac{\rho}{\rho_o} \left( \frac{V_S}{V_{So}} \right)^2 \quad (4.9)$$

One could also describe a damage parameter  $D_K$  using knowledge of the damaged  $K_d$  and intrinsic  $K_o$  bulk moduli less directly:

$$D_K = 1 - \frac{K_d}{K_o} = 1 - \frac{\rho}{\rho_o} \left[ \left( \frac{V_P}{V_{Po}} \right)^2 - \frac{4}{3} \left( \frac{V_S}{V_{So}} \right)^2 \right] \quad (4.10)$$

Ahrens & Rubin (1993) simplified equations 8-9 by assuming that  $\rho \approx \rho_o$ , but we retain these terms given the large observed differences here and because damaged  $\rho$  are available from the core.

The damage parameters have been used in numerous high-velocity impact laboratory studies to assess the degree of material disruption.  $D_P$  and  $D_S$  have been particularly useful metrics to track changes in the degree of disruption extending radially from impacts into large target blocks. This is accomplished by

measuring  $V_P$  directly on samples cut from the shocked blocks (Ahrens & Rubin, 1993; Ai & Ahrens, 2007) or indirectly via wave speed tomography (Moser et al., 2013; Raith et al., 2018; Xia & Ahrens, 2001).  $D_P$  has been particularly useful in connecting damage to attenuation and induced micro-crack densities (Liu & Ahrens, 1997) in materials from these experiments, although these the magnitudes of these damage measures were not linked more directly to levels of strain experienced by the sample. Further, we are not aware of any prior damage parameters estimates from rock samples or indirect seismic measurements on terrestrial impact structures.

The in situ seismic wavespeeds in hole M0077a are highly attenuating, as shown by low Q factors (Figure 4.13d) from spectral ratio analysis (Nixon et al., 2020). Curiously, although attenuation decreases with depth within this hole as shown by increasing Q, damage parameters appear to be relatively consistent throughout the hole (Figure 4.13b). The values shown in Figure 4.13b all indicate high levels of damage within the peak ring materials, yet the values of the three damage parameters differ significantly from one another.  $D_S$  is always larger (0.7-0.75) than  $D_P$  (0.5-0.6), with  $D_k$  laying between the two values, by definition of elastic moduli. This indicates that the deficit of  $V_S$  is greater than that for  $V_P$  as was suggested by the elevated values of  $R$ . The reasons for this discrepancy are not yet understood, but may be related to the displaced materials' point of origin within the un-displaced target hemisphere. Wiggins et al. (2019) incorporated tensile and shear damage parameterization into shock physics hydrocode iSALE-2D for hypervelocity impacts from 100m to 100km in diameter in Lunar basalt; both tensile and shear damage with similar values to those shown here ( $\sim 0.5$  and  $0.75$ , respectively) were found on the boundary between the pure shear damage zone and mixed shear/tensile damage zone, at  $\sim 1/10$  of the radius of the transient crater.

#### 4.5.4 Characterization of block sizes

Within the PR,  $V_{P_{log}}$  ( $\lambda \sim 1\text{m}$ ) are  $\sim 5\%$  less than  $V_{P_{VSP}}$  ( $\lambda \sim 50\text{m}$ ); this discrepancy is more pronounced in the upper PR, approaching 15% (Figure 4.8). With a similar trend observed in the longitudinal damage

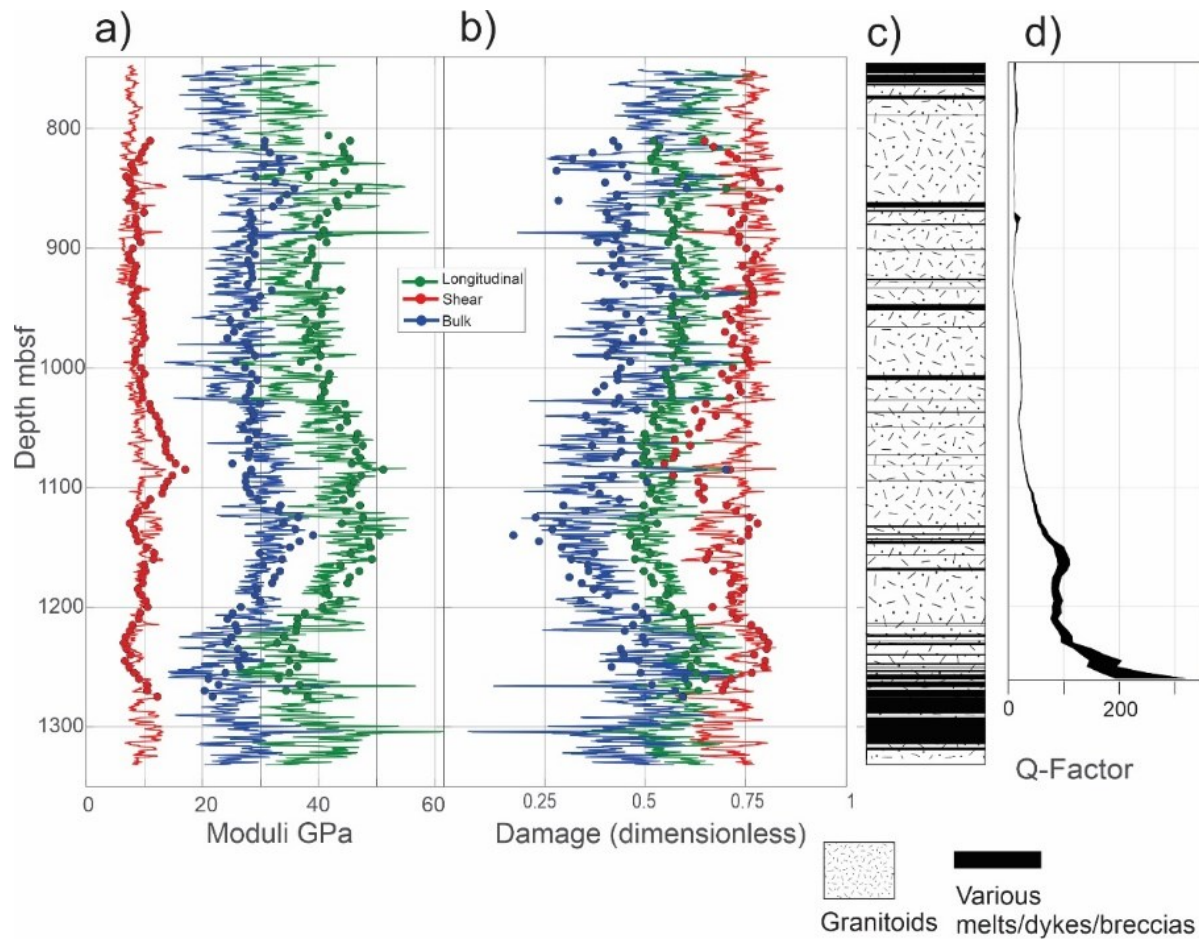


Figure 4.13. Damage parameterization of peak ring granitoids and simplified geological column. a) Dynamic longitudinal or P-wave (green), bulk (blue), and shear (red) moduli. b) Corresponding longitudinal (green),  $D_p$  bulk (blue), and shear (red)  $D_s$  damage parameters. Continuous lines calculated from sonic log velocities. Discrete filled circles calculated using VSP obtained velocities. c) Simplified stratigraphy. d) Quality factor vs. dept, originally from Nixon et al. (2020).

parameter (blue circles compared to solid blue lines in Figure 4.13), this frequency dependent response may be due to dominance of characteristic acoustic fluidization block size (Riller et al., 2018). Riller et al. (2018) suggest a characteristic block size as low as 2.3 m, on the basis of cataclasite and ultra cataclasite zones. This finding is supported by a relatively high cataclasite count in the region 750 mbsf – 850 mbsf, the depth with the greatest sonic/VSP  $V_p$  discrepancy (Figure 4.8). However speculative, dominance of smaller effective acoustic fluidization block size toward the top of the PR granitoids is additionally confirmed intuitively, since smaller blocks would be displaced farther more easily.

#### 4.5.5 Implications for future extraterrestrial seismic investigations

The gross features of the Chicxulub structure remain well preserved, owing to burial by later Cenozoic sediments. As such, it is worthwhile to consider how Chicxulub might serve as an analog to future hypothetical extraterrestrial seismic investigations on the Moon or Mars. Larger impact craters on all of these bodies will typically exhibit central peaks or peak rings, melt sheets, and breccia/suevite veneers. To reiterate, vertical seismic data at site M0077 on the peak ring of Chicxulub includes reflections originating from the discontinuities in impedance at the top and bottom of the LVZ. These contrasts may be influenced by long-term hydrological alteration of the original breccias and suevites with the fluid fluxes potentially also stiffening the sediments of the LID; much of this response relied on the abundance of water. Additionally, the presence of a sorted suevite that makes up the bulk of the LVZ (Units 2a and 2b above 705.5 mbsf) required water in the form of an ocean resurge (Gulick et al., 2019; Ormö et al., 2021).

There is abundant evidence for the existence of surface water in Mars' past from numerous lines of inquiry (Filiberto & Schwenger, 2018), and extensive reservoirs may still reside in its subsurface (Lasue et al., 2019). The presence of abundant water, even if it originates underground, suggests that the impactites on Mars could similarly be subject to post-impact hydrological alteration. Whether the structure might be preserved by subsequent sedimentation would depend critically, as it does on Earth, on the nature and location of the target (e.g., land, liquid water, ice, etc.) and size/speed of the impactor. However, atmospheric conditions on Mars have likely not been conducive to standing bodies of water for nearly 3.7 Ga (Pollack et al., 1987; Wordsworth, 2016), suggesting that any potential analogy between the seismic responses of a sedimentary capped Martian impact structure and the seismic structure of Chicxulub may only be relevant for pre-Noachian and Noachian impacts.

Free water is not expected in any important quantities in the Moon (Honniball et al., 2021), likely precluding any significant hydrothermal alteration of impactites after the volatile depletion period

(Hauri et al., 2015) of lunar history. Older lunar impact structures, however, will be buried by the slow progressive buildup of the regolith. Controlled source seismic tests during the Apollo program suggest that  $V_p$  of the regolith near the surface is very low (Cooper et al., 1974; Kovach & Watkins, 1973). One might reasonably expect the seismic properties of the displaced and damaged 'bedrock' with the proximal blanketing by melt and breccias to be similar to those at Chicxulub described here. Consequently, although there will be no hydrothermal alteration, one could anticipate a strong contrast in seismic impedance between impactites and later deposited regolith.

Although impact structures are rare on Earth, they dominate the crusts of many other rocky bodies. Understanding damage in the near surface lithology will be important for construction projects on our own Moon, of which  $\sim 1/2$  of the surface is impact ejecta and likely all has at least micrometeorite damage (Anders et al., 1973). Indeed, impact basins are flat and low in elevation, both desirable traits for lunar construction projects; understanding the geoengineering response in impact basins is therefore important for successful colonization of the Solar System.

#### **4.6 Conclusions**

Detailed analysis of the vertical seismic profile obtained during the IODP/ICDP Expedition 364 Chicxulub impact structure scientific drilling project reveals the factors controlling the character of the K-Pg seismic boundary reflection event, illustrates the chaotic nature of the seismic wavefield within the highly damaged peak ring, and allows for assessment of damage levels.

Modelling confirms that the character of the seismic reflections at Site M0077 within the impact sequence results primarily from tuning of reflections originating at the abrupt discontinuities in impedance at the top and bottom of a low velocity zone (LVZ) formed dominantly of suevite deposited by ocean resurge. The mechanical and density variations that control the seismic reflectivity at the top of the Chicxulub structure are clear. However, the reasons for the high seismic impedance of the earliest



sedimentary materials relative to the underlying suevite and melt rock of the LVZ are not so apparent. Hydrothermal alteration has been well documented in the LVZ, and the change in mineralogy and porosity will certainly have influenced the wave speeds and density through this zone. These fluid fluxes also likely contributed to stiffening those sediments deposited following the impact forming the higher sedimentation rate portions of Paleocene section of the LID, but whether such circulation could persist long enough to explain the elevated density and wave speeds through the younger Eocene sediments is not obvious. Other mechanisms that could play a role include compaction and cementation. Additional detailed studies, including microscopy to elucidate pore structures and the prevalence of dissolution, or secondary precipitation of minerals, and mechanical wave speed and strength measurements on the core materials through the LID, particularly those above the Paleocene-Eocene Thermal Maximum that have not yet received much attention, will be necessary to better understand the factors influencing the physical properties of these sediments.

The character of the seismic wavefield changes significantly as it passes from the post-impact impactites and sediments into the highly damaged peak ring granitoids. The upgoing vertical component wavefield displays clear reflections in the sediments, whereas no strong coherent events exist within the peak ring. From the horizontal components a weak but distinct shear wave may be followed through the sediments; however, this wavefield becomes chaotic in the peak ring, making tracing a shear arrival tenuous. These observations indicate a highly heterogeneous structure to the peak ring that scatters the seismic energy. A full understanding of this phenomenon is beyond the scope of this contribution, but efforts are underway to better characterize this through various measures such as apparent attenuation (Nixon et al., 2020).

$V_s$  values from both sonic logging and the VSP are anomalously low within the Chicxulub peak ring, consistent with earlier studies that documented anomalously low  $V_p$  and  $\rho$  in this region. Having measures of both  $V_p$  and  $V_s$  allows determination of their ratio  $R$  and of Poisson's ratio  $\nu$ , both of which

are elevated relative to comparable, but undamaged, terrestrial lithologies. As such,  $R$  and  $\nu$  could be useful attributes for mapping the extent of damage beneath impact structures on the terrestrial planets.

The observed velocities were further used to calculate damage parameters  $D_i$  following the definition of Grady & Kipp (1987) that have been used previously to delineate damage zones in laboratory impacts.

We were able to use peak ring mineralogy and core density values to determine  $D_p$ ,  $D_s$ , and  $D_K$  based respectively on the dynamic longitudinal, shear, and bulk moduli. The goal of this analysis is, as with  $R$  and  $\nu$ , to provide observational constraints to assist in refining advanced numerical impact models that currently incorporate *Grady-Kipp* fragmentation concepts in calculating shock induced strain or porosity.

#### *Acknowledgments and Data*

The authors thank J. Melosh and B. Johnson for insight into the inclusion of strain within impact modelling codes, D. Goldberg for advice on sonic log results, and J. Morgan for suggestions on improving the manuscript. This research used samples and data provided by IODP. Samples can be requested at <http://web.iodp.tamu.edu/sdrm>. Expedition 364 was jointly funded by the European Consortium for Ocean Research Drilling (ECORD) and the International Continental Scientific Drilling Program, with contributions and logistical support from the Yucatán State Government and Universidad Nacional Autónoma de México (UNAM). The downhole seismic system was provided by the Canada Foundation for Innovation Leaders Opportunity Fund Grant #31419. The organized data used here are freely available at <https://doi.org/10.7939/DVN/D1YY4A> (Nixon, 2021d). SPSG and GLC were supported by NSF grant OCE-1737351. The authors have no conflicts of interest.

## **5. Petrophysical properties of Chicxulub Peak Ring Shocked Granitoids and Impact Melts**

### **5.1 Abstract**

Here we describe preliminary results from laboratory characterizations of Chicxulub impactites. Previous studies have shown significantly diminished seismic speeds in the highly damaged granitoids and porous impact melts. Porosity is characterized with helium pycnometry and mercury porosimetry, the latter revealing differing distributions of pore sizes between the crack-filled granitoids and the impact melts. Ultrasonic compressional and shear wavespeeds are investigated under air-saturated (dry) confining pressure up to 200 MPa, showing both non-linear and hysterical behavior. We present Grady-Kipp damage parameterization of the confining pressure wavespeeds and discuss in situ implications incorporating considerations from hysteresis, heterogeneity, and fluid saturation.

## 5.2 Introduction

Open porosity strongly influences the geophysical signatures of impact craters on the rocky bodies within the solar system. This porosity is often attributed to ‘damage’, but the nature of this damage is rarely examined in detail. The concentrations and characteristics of this pore space, however, strongly control bulk density, permeability, and seismic wave speeds within and near such structures.

Conversely, geophysical anomalies associated with impact structures are the only means to remotely map the spatial variations of this porosity; information that is key to understanding a structure’s genesis and evolution. Such pores may also play a key role in promoting life throughout the solar system, as they can shelter biological activity from hostile conditions on the surfaces of bodies. As such, it is increasingly important that the characteristics of this pore space be better understood. Below, we address aspects of this problem related to the interpretation of seismological observations using petrophysical characterization of the pore space and laboratory measurements of wave speeds on candidate core samples from the ICDP/IODP Expedition 364 Chicxulub Impact drilling project.

Geophysical investigations are key to finding and understanding impact structures both on the earth and the terrestrial planets, and often these signatures indicate the existence of porosity resulting in diminished density and lowered seismic wave speeds. For smaller impact structures that avoid involving mantle uplift, the decreased densities manifest as central zones of negative Bouguer anomaly on the earth (e.g., Pilkington & Grieve, 1992), the Moon (e.g., Soderblom et al., 2015), Mars (e.g., Johnson et al., 2021, Lewis et al., 2019), and Mercury (e.g., Qingyun et al., 2018). Lower seismic velocities have also been observed via active source surveys in the vicinity of numerous terrestrial impact structures ranging from the simple Barringer Crater (e.g., Ackermann et al., 1975), up through complex craters (e.g., Karp et al., 2002), to the large peak-ringed complex Chicxulub Impact Structure (e.g., Morgan et al., 2011). Lowered velocities are also more directly observed via geophysical logging and borehole seismic measurements through the uppermost sections of the central peak at the Bosumtwi Structure, Ghana

(Hunze & Wonik, 2007; Schmitt et al., 2007), Bow City Structure, Alberta (Xie et al., 2014), and the peak ring of the Chicxulub Structure (Christeson et al., 2018; Nixon, 2021b). Passive seismic methods have only recently been used, and Onwuemeka et al. (2021) showed velocity deficits of over 10% beneath the Charlevoix impact structure in Québec.

Although not capable yet of reaching the strain rates and pressures of a real impact event, the damaged blocks from a number of laboratory cratering tests (e.g. Ai & Ahrens, 2007; Kenkmann et al., 2018; Liu & Ahrens, 1997; Moser et al., 2013; Winkler et al., 2018; Xia & Ahrens, 2001) show patterns of decreasing wave speeds with proximity to the artificial craters; these patterns are largely consistent with field observations. These laboratory tests are carried out on intact blocks of target rock with the patterns of wavespeed deficits reflecting the local distributions of microcrack density. The results taken together suggest that seismic wave speeds may be able to provide real constraints on impact energy (Xia & Ahrens, 2001), be used as a proxy for damage in calibrating advanced numerical impact models (Collins et al., 2004), or utilized as a proxy for damage in calibrating advanced numerical impact models (Collins et al., 2004).

Rock samples from a variety of terrestrial impact sites show evidence of damage at a variety of scales, the most obvious of which are macroscopic shatter cones (Dietz, 1947) that are now taken to be a necessary indicator of hypervelocity impacts (French & Koeberl, 2010) in combination with other petrographic diagnostics such as diaplectic glass, high pressure mineral phases, and cryptographically controlled planar deformation features. It is unlikely, but not yet known, whether these petrographic features would significantly influence the overall seismic properties. We do know, however, that porosity in general and crack-like porosity in particular strongly influences material elastic moduli and hence seismic velocities. Crack-like porosity has long been known to disproportionately influence rock elasticity (Adams & Williamson, 1923) and a variety of differing theoretical developments broadly support this observation (see for example Berge et al., 1993).

While hydrocode modelling of impacts grow increasingly sophisticated (D. M. H. Baker et al., 2016; Wiggins et al., 2019), experimental studies of hypervelocity shocked media remain somewhat uncommon, owing mainly to the scarcity of such material. However, triaxial hypervelocity impacts have been studied in the laboratory in San Marcos granite and Bedford limestone (Ai, 2006). Suevites of the Ries impact crater have been studied for petrophysical and mechanical properties, revealing increased permeability and decreased strength & elastic moduli when compared to terrestrial basalts (Heap et al., 2020). Natural remnant magnetization has been used to constrain shock pressure below 0.5 GPa in the Lonar crater, India, (Agarwal et al., 2016), although the shock pressures discussed in this paper are around the order of 10-20 GPa (Tani et al., 2018). A few examples of impact structures with petrophysical investigations on samples include Bosumti, Ghana (Elbra et al., 2007; Koeberl et al., 2007; Meillieux, 2009), Popigai, Siberia (Pilkington et al., 2002), Keurussellka, Finland (Raiskila et al., 2008), Janisjarvi, Karelia (Salminen et al., 2006), and the earlier drilling at Chicxulub (Vermeesch & Morgan, 2004; Mayr et al, 2008a; Mayr et al, 2088b). Popov et al. (2014) have compared measurements from rock obtained from several impact structures.

The above studies indicate the importance of porosity in controlling physical properties within impact structures. Conversely, using geophysical observations to obtain porosity, particularly through inversion of gravity measurements and seismic wave speeds, may provide a means to better understand the formation of these structures and contribute to calibration of existing modelling algorithms. This chapter provides a preliminary presentation of laboratory characterization of the pore structures within a series of core samples of differing lithologies obtained during the Expedition 364 drilling project. Details of pore structures are investigated using a combination of petrographic and scanning electron microscopy and Hg-injection porosimetry. Mineral densities are obtained from He-pycnometry, and, finally, wave speeds are measured on dry samples under confining pressures. The implications of these preliminary results for understanding the larger structures through inversion are discussed.

### 5.2.1 Damage and physical properties

Although work relating shock damage to physical properties is somewhat sparse, significant work has been completed relating more common forms of terrestrial damage to physical properties (e.g., Dresen & Guéguen, 2004). Rock masses adjacent to major faults are often extensively damaged, with investigations completed on carbonates in the Fucino Basin, Italy (Agosta et al., 2007). Freeze thaw cycles are a ubiquitous source of terrestrial damage associated with microcrack propagation (Zhou et al., 2015), as well as damage resulting from extreme heat (Liu et al., 2020; Sun et al., 2015). Slightly more relevant to shock damage, the mining community is interested in rock damage from explosives use (Silva et al., 2019) and in the vicinity of underground nuclear tests (Hawkins & Wohletz, 1997).

Damage to granite in terrestrial settings is well studied, with physical properties effect of thermal cracking investigated by numerous authors (e.g., David et al., 1999). More recently, research on damaged granite has accelerated looking at the effects of repeated impacts (Wang et al., 2018), supercritical water (Hu et al., 2019), and high temperature treatments (Wang et al., 2021; Yang et al., 2017; Zhang et al., 2018). Mineralogy, both composition and grain aspect ratio, has been shown to affect linear microcrack growth (Ghasemi et al., 2020) and progress is being made in characterizing damage in granite ultrasonically (Chaki et al., 2008; Chen et al., 2014).

Ultrasonic velocity determinations have been used for nearly 80 years to probe the elastic properties of rocks. Some applications in sedimentary rocks include mechanical and physical properties of carbonates (Abdelhedi et al., 2017; Zuo et al., 2020), characterization of progressive fracture damage in carbonates (Martínez-Martínez et al., 2016), and parameterized relations between ultrasonic velocities and physical properties for carbonates, siltstone, and sandstone (Uyanik et al., 2019). Ultrasonic methods are used to monitor damage development in many types of rocks, including salt rock (Li et al., 2018), Lyons sandstone, granodiorite, and Gosford sandstone (Shirole et al., 2018). Additionally, ultrasonic methods are regularly used to evaluate damage on manmade structures made of concrete (Jiang et al., 2017;

Wang et al., 2019), excavation disturbance in tunnels (Falls & Young, 1998), damage from underground blasting (Raina et al., 2000), and even impact damage to polymer bonded explosives (Chen et al., 2004).

### 5.2.2 Structural complications

As described in the above, anomalous geophysical behavior is often simply ascribed to ‘damage’, which would mean that wave speed deficits resulted from fractures and cracks. However, the geological structures near and within impact structures are heterogenous at all scales. In the Chicxulub structure, for example, melt dykes dissect blocks of the displaced target granitoids. However, given that they were fluid when emplaced and cooled later to relatively crack-free igneous rock, it is difficult to argue that this material is damaged. At field observation scales, however, the longer-wavelength, bulk geophysical signatures sense the damaged granitoids and the intruded melts as one effective medium. Since different, but mixed, components of the structure will have anomalous properties for varying reasons, one cannot so readily assert that the anomalies can all be credited solely to damage. This heterogeneity will complicate the interpretation of damage levels in impact structures using geophysical responses.

To provide additional insight into this problem, we study core samples obtained from the peak ring of ICDP/IODP Expedition 364 (Figure 5.1). We focus on characterization of the pore space using different methods, and then measure the elastic waves speeds on the samples subjected to confining pressures. We attempt to model the laboratory observations using different rock physics models. We see quite different behavior and pore character between the differing lithological components suggesting that the geophysical anomalies cannot so readily be explained completely by damage. We are trying to better understand the pore structure and seismic response of these highly attenuating granitoids, as current



models and theories lean heavily on the non-interacting pore assumption; these models break down rapidly when applied to these pervasively damaged specimens.

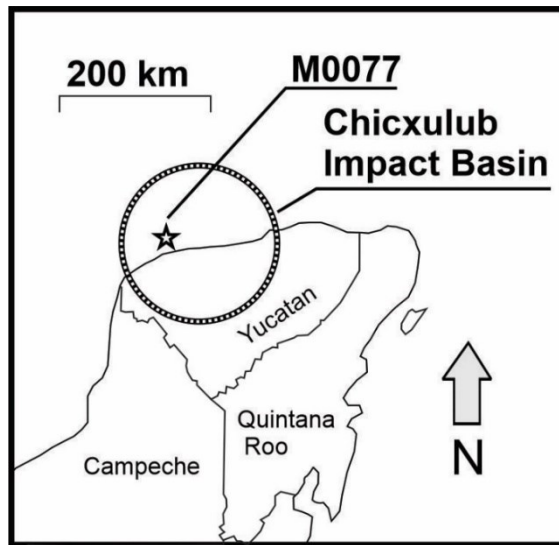


Figure 5.1. Chicxulub Impact Crater location shown with respect to site M0077.

## 5.3 Methods & Results

### 5.3.1 Acquisition

#### *Expedition 364 Coring and logging*

Detailed information about the coring, geophysical logging operations, and on the measurements made on the samples during archiving may be found in Gulick et al., 2017a; Lofi et al., 2018. Briefly, diamond coring in the borehole continued nearly continuously from 506.5 meters to 1335 meters below sea floor (mbsf). Here, we differentiate sections along the borehole within the mechanical context developed by Nixon (2021d), (Figure 5.2 a) relative to simplified lithologies within M0077a (Figure 5.2b), and samples selected for analysis hereafter (Figure 5.2c). These include post impact sediments above the suevite/transitional unit contact (STUC) at 617 mbsf (Figure 5.2b) overlain by a 35 m thick zone of seismically stiff reworked sediments (LID) (582 - 617 mbsf, Figure 5.2a) and underlain by a 105 m of melt

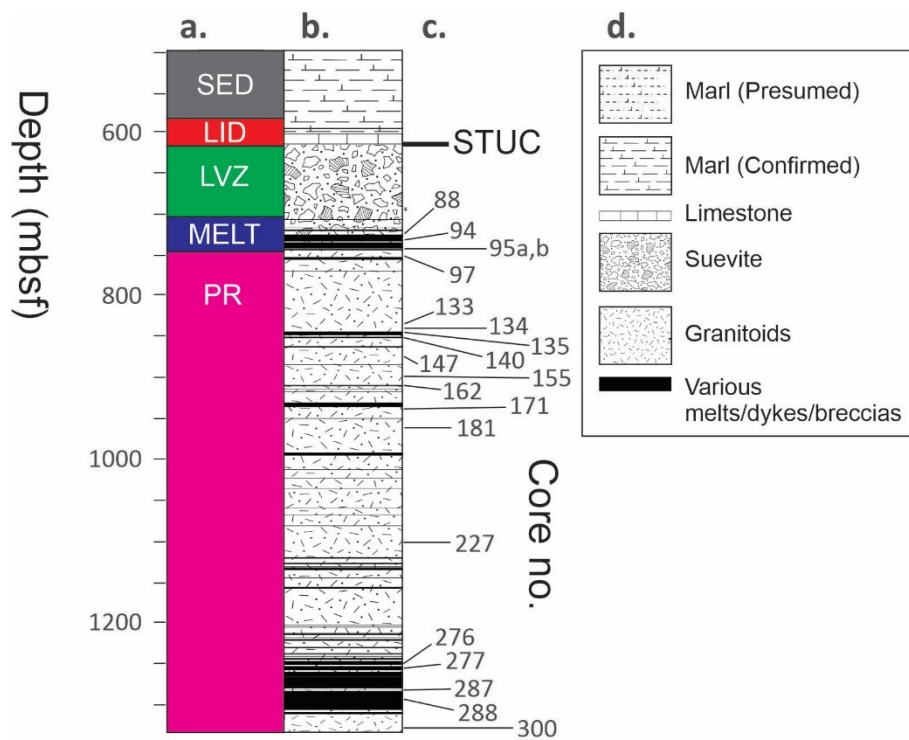


Figure 5.2. Sampling points in M0077a. a) Mechanically distinct seismic zones from Nixon et al., (2022, in press). b) Simplified lithostratigraphy from Gulick et al., 2017. c) Core numbers and point in hole from which samples here were taken. d) Legend for lithostratigraphy.

bearing breccia impactite (MELT) (617 – 722 mbsf, Figure 5.2b), an 85 m thick seismic low velocity zone LVZ of reworked materials (582 - 705 mbsf, Figure 5.2a), 25 m of predominantly altered shock melt (722 – 747 mbsf, Figure 5.2b), the 42 m thick seismic MELT zone (705-747 mbsf, Figure 5.2a), and below 747 mbsf the displaced peak ring materials (PR) and variously intersected by melt dikes (Figure 5.2a,b). The peak ring rocks have exceptionally low seismic wavespeeds and high porosities (Christeson et al., 2018), and are the focus of sample characterization hereafter.

### *Sample Selection*

The On-Shore Science Party (OSP) has already made extensive measurements on discrete samples, including quantitative XRD modal analysis, whole rock XRF elemental analysis,  $\gamma$ - $\gamma$  attenuation density, and bulk dry and grain densities following moisture and density protocols normally applied. These measurements, however, are not on the exact materials we have selected and many of these measurements are repeated here for consistency to our samples. During the onshore science party, a total of 20 half-cylinder, 10 cm long samples of the core were selected for further analysis. These samples included a variety of different rock types that we classify here as suevite (impact melt-bearing breccia), melt (any kind of non-brecciated melt rock), or shocked granitoid as compiled in Table 5.1 and shown in Figure 5.2c.

Sampling bias is a perennial problem in experimental rock physics and mechanics, and this issue persists here. The characteristics making these granitoids interesting also makes their study challenging. The shocked granite has been heavily damaged, some parts more than others. As such, it was necessary to select samples which were intact; this is a necessary sampling bias as it would not be possible to execute many of the following tests with the more heavily damaged (and often crumbling) samples. Even with carefully chosen 'intact' samples, further sub-sampling was still problematic. For example, 'plucking' was a major issue in thin section polishing, and when coring samples for physical properties tests, the sample would often crumble or break apart on pre-existing zones of weakness. An effort was made to select

homogenous samples (**Error! Reference source not found.**), targeting major units of melt rock and granites that were either very proximal or very distal to the selected melt rock units. Quantitative X-Ray diffraction analysis has been previously performed on M0077a core (Gulick et al., 2017a), with results relevant to samples analyzed here summarized in **Error! Reference source not found.**; it must be recognized that only 1 such modal analyses was made in each 1-meter segment of the core and this may differ from the samples selected here.

Thin sections were made from a representative set of samples for use on both an optical petrographic microscope and a scanning electron microscope for purposes of pore characterization. The images are described later to show examples of the differing pore structures within the material. Optical microscope images were made using a Nikon SMZ 800 stereomicroscope with attached camera.

Scanning electron microscope images were made using a Hitachi TP 4000Plus SEM operating at 15 kV in primary back scattered electron mode.

As noted above, porosities were measured on discrete samples at the onshore science party using He-pycnometry and comparison weighing of dry and saturated samples. Here we examine the specific samples collected for this study using both He-pycnometry and Hg-injection porosimetry in our own laboratory.

### 5.3.2 Porosimetry

#### *Helium Pycnometry*

He-pycnometry is a popular and nondestructive method that exploits Boyle's ideal gas law to determine the density of the solid portion of porous materials and powders. This is accomplished via helium gas expansion by expanding helium gas at pressure  $P_1$  in known volume  $V_1$  into a second chamber volume  $V_2$  containing the sample with unknown solid volume  $V_S$ :

$$V_s = V_1 + \frac{V_2}{1 - \frac{P_1}{P_2}} \quad (5.1)$$

*Helium pycnometry equation.*

the grain, or solid, density is then simply the ratio of the measured mass of the sample to this volume  $V_s$ . By using the grain density from the aforementioned pycnometry, and calculating bulk density from samples with simple geometry, total porosity is then simply:

$$\phi = \frac{\rho_{grain} - \rho_{bulk}}{\rho_{grain}} \quad (5.2)$$

*Porosity as a function of density.*

The procedure is to place the rock sample in a helium chamber of known volume and pressure ( $V_1, P_1$ ) then open a valve connecting to a second chamber ( $V_2$ ) and measure the new, lower pressure with the entire apparatus now filled with helium. Due to helium's near ideal gas behavior and excellent pore penetration,  $V_s$  is an accurate measure of grain volume. Grain density measurements made with a 35 cm<sup>3</sup> sample cup using a Accupyc-II Series™ (Micromeritics) pycnometer are shown for 9 granitoid and 7 rock melt samples<sup>2</sup> (Figure 5.3, Table 5.1).

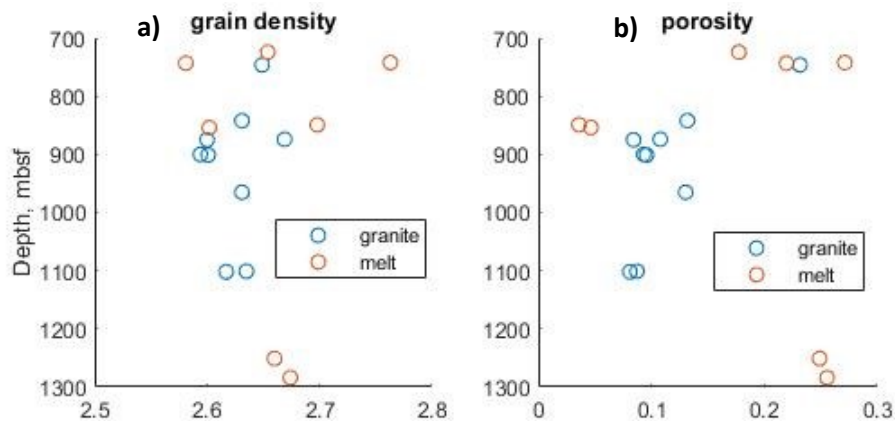


Figure 5.3. Helium pycnometry results. a) Grain density. b) Porosity.

<sup>2</sup> These measurements were made by C. Gucwa and G. daVila, Purdue University.

Sample	Lithology	He Pycnometry			Hg Injection Porosimetry		
		Grain Density	Bulk Density (Dry)	Porosity %	Grain Density	Bulk Density (Dry)	Porosity %
88r3a	Melt	2.654	2.028	23.6	err	err	26.03
88r3b		-	-	-	2.630	2.070	21.02
94r2	Melt	2.581	2.030	21.3	2.620	2.040	21.97
		2.763	-	-	-	-	-
95r3a	Granite	2.6119	-	-	2.4946	2.3597	5.4072
95r3b		2.6492	-	-	-	-	-
97r3	Granite	2.669	-	-	-	-	-
133r1	Granite	2.6307	2.37	9.9	-	-	-
134r2	Granite	2.6621	-	-	-	-	-
135r2	Melt	2.6977	2.746	-1.8	-	-	-
140r1	Melt	2.6015	-	-	-	-	-
147r1a	Granite	2.6687	2.448	8.3	err	err	8.42
147r1b		2.600	-	-	2.5464	2.320	8.893
155r2a	Granite	2.594	2.337	9.9	err	err	9.68
155r2b		2.601	-	-	2.5304	2.3865	5.6868
162r1	Melt	2.8113	-	-	-	-	-
171r2	Granite	-	-	-	-	-	-
181r2	Granite	2.631	2.203	16.3	-	-	-
227r2	Granite	2.6351	2.374	9.9	2.58	2.40	7.03
276r3	Suevite	2.66	-	-	2.6169	2.0699	20.9024
277r3	Suevite	2.7019	-	-	2.4148	2.0424	15.4236
287r1	Suevite	2.6739	-	-	2.6359	2.0239	23.2156
288r1	Suevite	-	-	-	-	-	-
300r2	Granite	-	2.243	-	2.580	2.340	9.36

Table 5.1 Summary of petrophysical measurements, M0077a samples.

### Mercury Injection Porosimetry

Mercury injection porosimetry, although invasive and destructive to the sample, offers unique advantages in pore characterization. This method can only reach interconnected pores and thus can, with an appropriate model, elucidate permeability characteristics; other methods of porosimetry do not differentiate whether pore volume is connected. More importantly, however, the method can provide indications of what the distribution of various pore sizes might be within the sample. The method relies on injecting a non-wetting liquid, most usually Hg, at progressively higher pressures. Essentially, the greater the pressure, the larger the capillary force that may be overcome and hence the smaller the pore throat diameter that may be breached. In this method, the porous material is considered to contain open pores that are connected to each other in a 3D network via 'pore throats' following descriptions by Wardlaw et al. (1987; 1981). Capillary forces resist the flow of Hg past the pinch points

of the pore throats, but these are overcome once the pressure in the Hg exceeds a value depends on the dimensions of the pore throat's aperture. Using a highly idealized cylindrical geometry, Washburn (1921), (eqn. 5.3) applied the Young-Laplace relationship between the pressure  $P_L$  required to push a fluid through a tube of diameter  $D_p$  taken to be that for the pore throat (ASTM, 2018).

$$D_p = \frac{4\sigma\cos\theta}{P_L} \quad (5.3)$$

*Washburn's equation.*

where  $\theta = 130^\circ$  and  $\sigma = 486.5$  mN/m are, respectively, the Hg-solid-air contact angle and Hg-air surface tension most often employed; this equation is widely utilized in Hg-injection porosimetry. Alternatively, for a planar crack-like pore the depth and breadth of which are large relative to its aperture  $w$ , the relevant formula is (Lenormand et al., 1983):

$$w = \frac{2\sigma}{P_L} \quad (5.4)$$

*Lenormand crack width.*

which differs by ~30 % with regard to the largest opening. In the measurement, by increasing pressure, Hg is forced through progressively smaller and smaller pore throats until the connected pore space is filled, and hence the volume of this injected Hg may be used to estimate the porosity. In addition, however, the volume of Hg injected is measured as a function of the pressure which can then provide, via eqn. 5.3, an indication of the fraction of the porosity with dimensions close to that of the corresponding pore throats.

Hg-injection measurements were made using an AutoPore IV<sup>TM</sup> (Micromeritics) that reaches a peak pressure of 413 MPa (60 kpsi), allowing Hg to enter pore throats as small as ~ 3 nm. This method is costly, and three melt rock samples and three granitoid samples could be measured with results shown

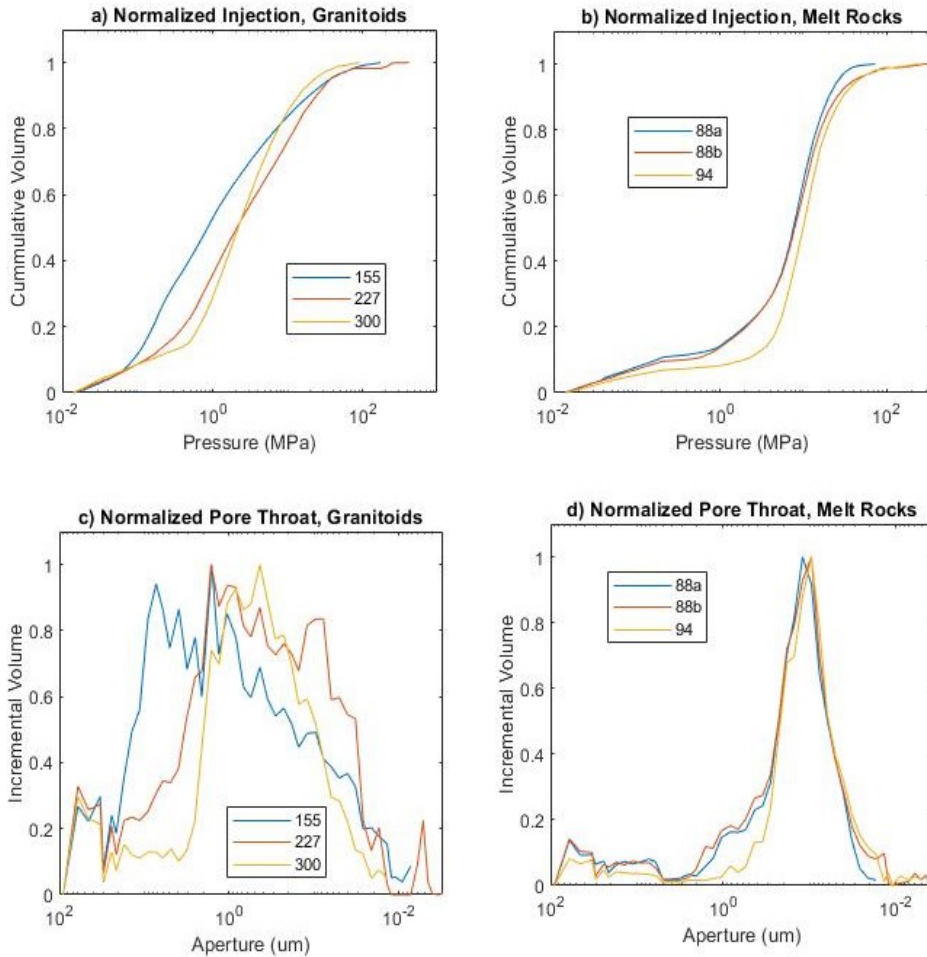


Figure 5.4. Mercury injection porosimetry. a) Granitoid injection curves. b) Melt rock injection curves. c) Granitoid pore throat distribution. d) Melt rock pore throat distribution.

in Figure 5.4<sup>3</sup> and Table 5.1. The behavior of these plots is clearly different between the granitoids and the melt rocks.

The granitoids show a gradual accumulation of mercury with pressure (Figure 5.4a) that indicates a broad pore throat distribution (Figure 5.4c) when displayed incrementally. This distribution decays exponentially with diameter (note the logarithmic independent axis). The saw-tooth shape of the distributions largely start around 0.1-1  $\mu\text{m}$ , although the porosity in sample 155 begins near an upper

<sup>3</sup> The Hg-injection measurements were assisted by B. King and R.S. Kofman at the University of Alberta and C. Gucwa and G. Davila at Purdue University.



limit at  $\sim 10 \mu\text{m}$ . It is important to note that in the independent axis in Figure 5.4c the pore apertures are calculated using the cylindrical assumption of eqn. 5.3, as is standard practice (ASTM, 2018), but given that the pore space in the granitoids is predominantly crack-like the apertures could be approximately  $\frac{3}{4}$  these values according to eqn. 5.4. In contrast, the melt rocks accumulate most of their mercury saturation rapidly around 10 MPa (Figure 5.4b), corresponding to a narrower pore throat aperture distribution ranging from  $1 \mu\text{m}$  to  $0.05 \mu\text{m}$  and centered near  $0.1 \mu\text{m}$  (Figure 5.4d).

### 5.3.3 Ultrasonic Wavespeeds

#### *Experimental Configuration.*

Wave speeds were determined using the long-standing ultrasonic pulse transmission technique in which an ultrasonic pulse is launched into the sample from a transmitting transducer to be recorded by a receiver. Details of the procedures used here may be found in Cholach et al. (2005), and a brief overview is given here. Longitudinal and shear mode piezoelectric ceramics (PZT 840, American Piezo Ceramics) with resonant frequencies of  $1 \text{ MHz} \pm 5\%$  and preferentially generating P- and S-wave signals, respectively, were sandwiched between machined aluminum endcaps and an impedance-matched

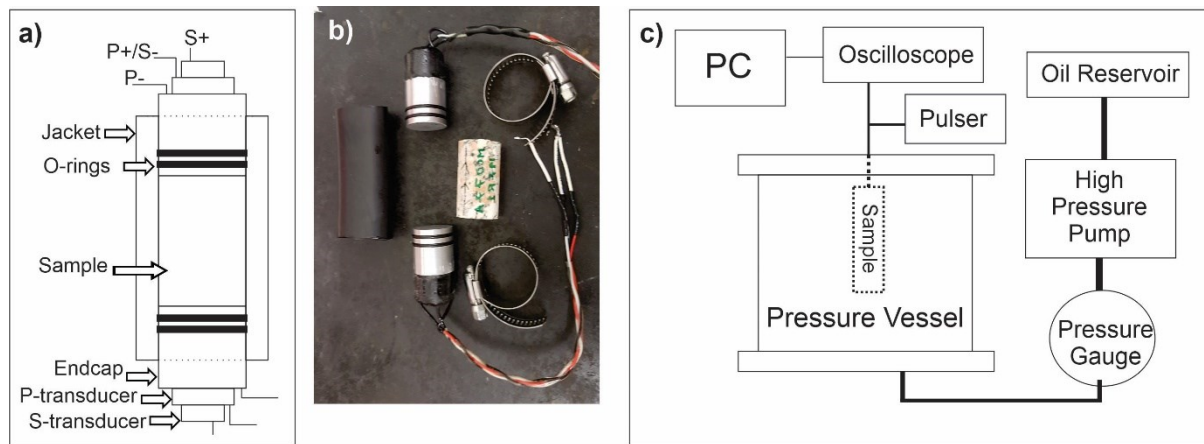


Figure 5.5. Ultrasonic confining pressure experimental configuration. a) Assembled sample schematic. b) Photograph of components prior to assembly. c) Fully assembled experimental configuration schematic.

damper. The circular longitudinal mode ceramic has a diameter of 20 mm and is attached directly to the Al endcaps. The square S-wave transducer has a width of 15 mm and is located directly on top of the P-transducer (Figure 5.5a), (APC, 2021). A pressure-dependent time delay-time calibration is determined for the pair of transducers by placing them end-to-end and cycling the confining pressure.

Cylindrical plugs (25.4 mm diameter) were cut from the core half-rounds selected (Figure 5.5b), their ends machined to be parallel, dried for at least 24 hours at 50°C, and inserted into an impermeable and pliant PVC jacket with the end caps inserted and clamped linearly on either end (Figure 5.5a). This assembly was lowered into 300 MPa capacity pressure vessel containing hydraulic oil for the pressure medium (Figure 5.5c). Confining pressure  $P_c$  was controlled with a combination of an air driven pump and a hand operated intensifier with the pressure obtained manually from a calibrated gauge (Heise).

The transmitter was activated by a 5-ns rise time, 300 V, step pulse (Model 5077C, Panametrics) with the received pulses sampled every 20 ns on a digital oscilloscope (Model TDS2012C, Tectronix) for 50  $\mu$ s. Each saved record was the stabilized stacked average of 200 pulses. The frequency at which a waveform was recorded depended on pressure, with measurements typically taken at 3 MPa pressure increments at lower pressures increasing to 25 MPa increments at the highest pressures. The samples were taken to a peak pressure of 200 MPa and records were further taken during pressurization as a check on hysteresis that may indicate the sample had been damaged during the test.

#### *Ultrasonic Processing and Wave Speed Determination.*

Due to noise interference, which was most significant at low pressures, a Matlab™ software package was developed to automatically sweep through the filtered ultrasonic traces (Nixon, 2021c) using the clear transmitted pulse at the peak pressure of 200 MPa. This issue appears to be related to the fact that at low pressures these materials highly attenuate the signal, and the purpose of this additional processing was to optimize the isolation of the pulse at lower pressure. Briefly, a Blackmann-Harris

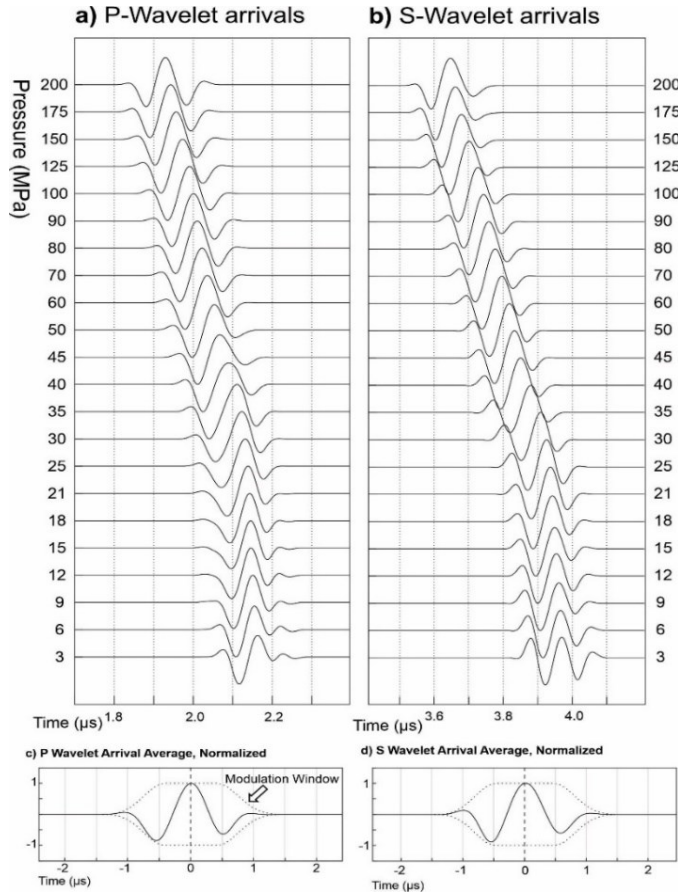


Figure 5.6. Sample 155 waveform windowing. a) P-wavelet arrivals. b) S-wavelet arrivals. c) Average P-wavelet. d) Average S-wavelet. Note that the pressure axis is not linear.

tapered window centered on the clear pulse obtained at 200 MPa isolated a starting pilot trace, which was subsequently cross-correlated with each of the records obtained at lower pressures, chosen initially via the wavelet arrival in the 200 MPa record for each sample. The program then modulates the 200 MPa trace which is cross correlated (CCF) with the next lowest pressure. Using the same window parameters, the window is then advanced by the time value associated with the central peak of the CCF and repeated for the next pair. Advancement of the modulation window by the previous iteration's CCF peak value is repeated for every trace, with the extracted waveforms shown in Figure 5.6a,b. As an additional quality control measure, the software averages all the windowed wavelets (Figure 5.6c,d). The pulse transit time is declared at the peak amplitude following procedures discussed in Molyneux & Schmitt (2000), and subsequently corrected for the appropriate calibrated transducer delay time. The

velocity is calculated simply as the ratio of the sample length to this transit time. No correction for changes in the sample length on pressurization were made as these are expected to be small and the correction less than the 20 ns sampling period. The resulting  $V_p$  and  $V_s$  are shown from both the pressurization and depressurization cycles in Figure 5.7a,c. It is worth commenting that the transit times, and hence the wavespeeds shown in Figure 5.7, result from strict application of the time picking criteria above, but this leads to some unlikely trends in the velocities at low pressures with some of the samples that are likely due to incorrect transit time picks when the procedure could not overcome the noise. This results in the unlikely cases where the sample shows a local maximum in the waves speeds at confining pressures below 40 MPa; it is unlikely that all values obtained at low confining pressures are correct. Although such an unexpected behavior could result from new damage, that these local maxima again appear on depressurization suggest that they result from higher noise levels. Although the windowed wavelets may appear clean after processing, the raw waveforms below ~40MPa are generally overwhelmed by noise, and following a continuous waveforms through from the more reliable signal at high pressures down to lower pressure is sometimes questionable. This is unfortunate, as the actual overburden and effective pressures experienced within M0077a falls within the range of 0-30 MPa. We are currently investigating remedies to this issue, which may include fitting a curve to reliable measurements above 40 MPa and extrapolating downward.

#### *Corrections for Fluid Saturation*

The wavespeeds were measured on dry rock samples, but this in the field we expect that the rocks are fully saturated with seawater; the laboratory measurement cannot be fully representative of the in situ seismic or sonic measurements. The simplest way to effect this correction is to use Gassmann's (1951) relations that describe the undrained static moduli for a fully fluid saturated porous material.

Application of Gassmann's equations assume that pore saturation does not affect shear modulus  $\mu$  of

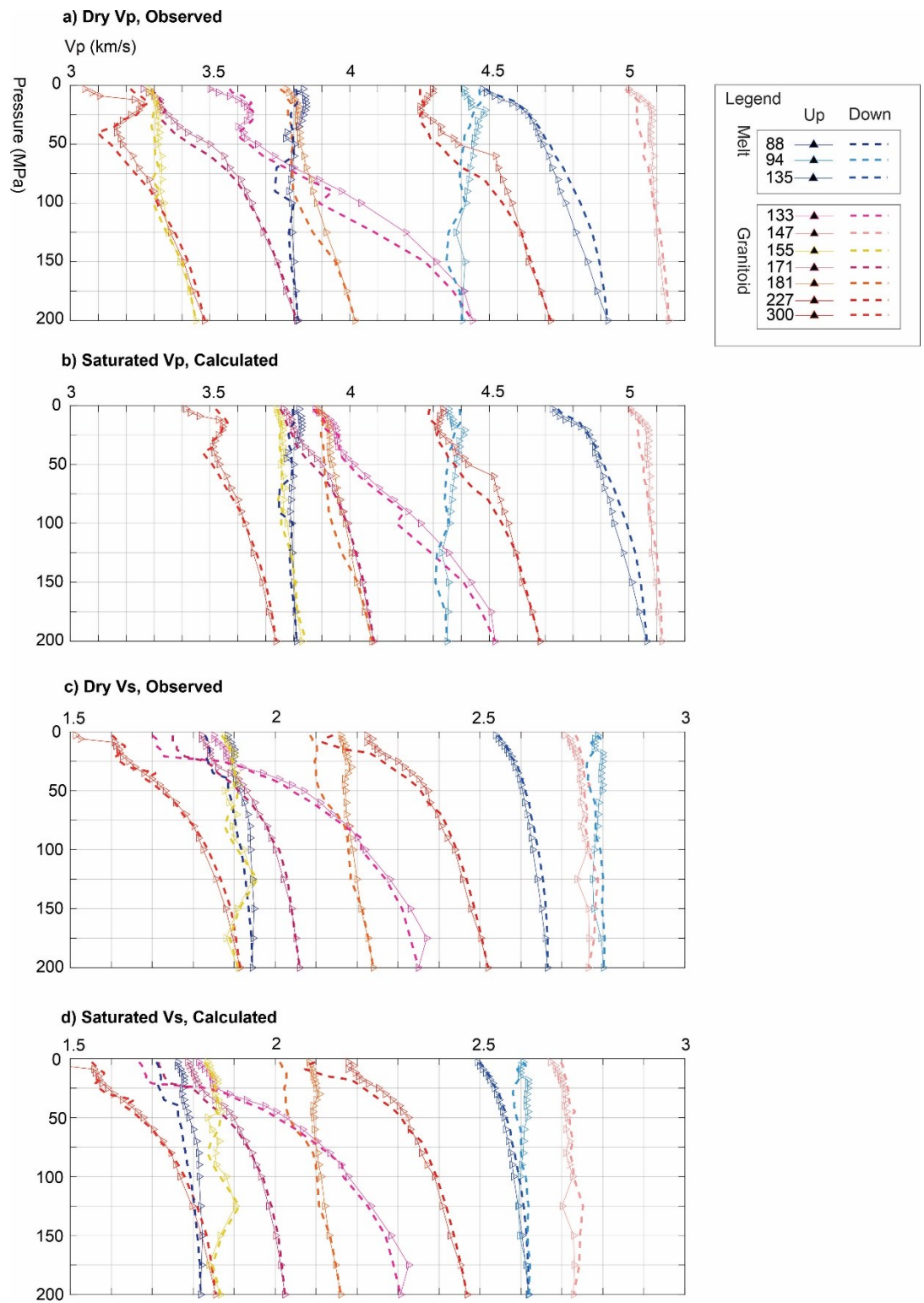


Figure 5.7. Confining pressure wavespeed curves up to 200 MPa.  
 a) Dry  $V_p$ . b) Saturated  $V_p$ . c) Dry  $V_s$ . d) Saturated  $V_s$ .

the dry rock, that porosity is independent of saturating fluid, that frequency effects are negligible, and the rock frame is not chemically affected by fluid saturation. In dry materials, the effect of frequency dispersion on the velocities (and corresponding elastic moduli) are small (e.g., Schijns et al, 2018), and the dry (i.e., air saturated) shear  $\mu_l$  and bulk  $K_1$  frame moduli in terms of the observed dry, but pressure-dependent, wave speeds  $V_P$  and  $V_S$  and the dry bulk density  $\rho_{dry}$  are

$$\mu_1(P_c) = \rho_{dry} V_S^2(P_c) \quad (5.5)$$

and

$$K_1(P_c) = \rho_{dry} \left[ V_P^2(P_c) - \frac{4}{3} V_S^2(P_c) \right] \quad (5.6)$$

Thus, the ultrasonic wavespeeds have been adjusted with Gassmann's equation using a rearranged version of Avseth et al. (2005), assuming seawater saturation, under the somewhat dubious assumption of fixed porosity and density with increasing pressure (Table 5.2). Gassmann's equation is shown

Sample	$K_R$ (GPa)	$\Phi_{mad}$	$\rho_{dry\ lab}$ (g/cc)	Length (mm)	Diameter (mm)	Mass (g)
133	48.95	0.125	2.40	18.99	25.18	22.4
135	89.42	0.066	2.72	55.96	24.87	74.6
147	48.56	0.100	2.381	43.34	25.18	52.8
171	47.95	0.138	2.277	43.11	25.13	51.1
181	45.61	0.131	2.288	56.41	25.15	61.7
287				72.2	24.83	70.3
300	48.69	0.094	2.382	16.99	24.80	18.4

Fluid	$K_f$ (GPa)	$\rho$ (g/cc)
Air	1.42E-4	negligible
Water	2.34	1.024

Table 5.2. Physical properties of Gassmann adjusted samples.

rearranged for saturated bulk moduli (eqns. 5.8, 5.9), where  $K_{1,2}$  = fluid 1 & 2 saturation bulk moduli (air & seawater),  $K_R$  = undamaged mineral bulk modulus, and  $K_{f1,2}$  = fluid 1 & 2 bulk moduli allows for calculation of a scaling factor  $\gamma$

$$\gamma = \frac{K_1}{K_R - K_1} - \frac{K_{f1}}{\varphi(K_R - K_{f1})} + \frac{K_{f2}}{\varphi(K_R - K_{f2})} \quad (5.7)$$

with the sea water saturated bulk modulus then given by

$$K_2 = \frac{K_R \gamma}{1 + \gamma} \quad (5.8)$$

and with the corresponding lack of change to the saturated shear modulus

$$\mu_2 = \mu_1 \quad (5.9)$$

The corrected sea-water saturated compressional  $V_{psat}$  (Figure 5.7b) and shear  $V_{ssat}$  (Figure 5.7d) wave speeds are correspondingly

$$V_{ssat} = \sqrt{\frac{\mu_2}{\rho_{sat}}} \quad (5.10)$$

and

$$V_{psat} = \sqrt{\frac{K_2 - 4\mu_2/3}{\rho_{sat}}} \quad (5.11)$$

with saturated bulk density depending on porosity  $\phi$ , the density of seawater  $\rho_w$ , and of the rock's dry bulk density  $\rho_{dry}$ :

$$\rho_{sat} = \phi \rho_w + \rho_{dry} \quad (5.12)$$

For the mineral frame elastic moduli, we use the Voigt-Reuss-Hill (VRH) average (Hill, 1952) as previously reported in Nixon (2021d). We use elastic moduli (Bass, 1995) for only the 7 primary constituent mineral phases (Table 5.3) from the X-ray diffraction (XRD) core analyses reported in Gulick et al. (2017b, Table T5) and Gulick et al. (2017d, Table T4). The complete XRD mineralogy for the samples discussed here, including clays and other minor constituents omitted for the calculations here, is

available in the supplementary information (**Error! Reference source not found.**). The VRH bulk modulus,  $K_R$ , is

$$K_R = \frac{1}{2} \left( \sum \phi_i(z) K_i + \left[ \sum \frac{\phi_i(z)}{K_i} \right]^{-1} \right) \quad (5.13)$$

And the VRH shear modulus,  $\mu_R$ , is

$$\mu_R = \frac{1}{2} \left( \sum \phi_i(z) \mu_i + \left[ \sum \frac{\phi_i(z)}{\mu_i} \right]^{-1} \right) \quad (5.14)$$

where  $\phi_i(z)$  is the  $i^{\text{th}}$  volumetric modal fractions of mineral (z), with its corresponding bulk ( $K_i$ ) or shear ( $\mu_i$ ) modulus (Table 5.3).

Mineral	Quartz	Albite	Microcline	Sanidine	Orthoclase	Anorthite	Augite
$\rho$ (kg/m <sup>3</sup> )	2648	2610	2567	2520	2571	2765	3320
$K$ (GPa)	37.8	56.9	55.4	58.8	62	84.2	95
$\mu$ (GPa)	44.3	28.6	28.1	30.1	29.3	39.9	59

Table 5.3. Isotropic elastic moduli and density for primary constituent minerals in M0077a peak ring (Bass 1995).



## 5.4 Discussion

### 5.4.1 Character of Pore Space

Second only to the magnitude of porosity itself, the geometry of a rock's pore space greatly influences its physical properties. It is well known that for the same porosity, the dry frames of rocks with equant (rounded) pores are much stiffer than those containing cracks. Pore dimensions and shapes, too, will control the availability of these rocks to shelter microscopic organisms. Here, we study the pore characteristics by contrasting several different methods including He-pycnometry and Hg-injection porosimetry, described above, supplemented with microscopic imaging.

The main purpose of He-pycnometry is to provide a measure of the density of the solid portion of the rock which is then used to infer a bulk density based on the sample's dimensions; but He-pycnometry cannot reveal any additional information regarding pore characteristics. The Hg-porosimeter, in contrast, provides the division of the pore spaces broadly in terms of its pore throat dimensions (Figure 5.4) that may then be used to infer the distribution of pore sizes. Neither of these methods, however, can directly provide information on pore shapes and this can only be accommodated using microscopic observations. The porosities observed by He-pycnometry range from about 0.05 to as much as 0.3 (Figure 5.3b), and there appears to be no noticeable differences between the granitoid, the melt, and suevite. The Hg-porosimetry, however, suggests that the pore structures within the damaged granites are significantly different from those in the melt rich rocks. The distribution for the melt rocks clearly peak at slightly less than  $1 \mu\text{m}$  and have nearly disappeared by about  $50 \mu\text{m}$  (Figure 5.4d), in contrast, the pore throat distributions for the granites are much broader range from about 100 microns down to nanometer scale approaching the  $3 \text{ nm}$  ultimate resolution of the machine (Figure 5.4c). For first order effects, one would expect the velocity deficits/damage to be related to the total scalar measure of porosity, and a better description of the exact orientation and nature of porosity would contribute to second order effects. Currently, it unknown is whether isotropic elastic effects exist in the shock

affected texture. However, the wavespeeds measured under confining pressure (Figure 5.7) vary greatly in both magnitude and their rate of change with confining pressure; there also does not appear to be any strong differences in these behaviours for a given classification.

As the effect of increasing velocity under pressure is known to be related to pore density, aspect ratio, and orientation, and the orientation with respect shock propagation at time of impact are unknown, the highly heterogeneous results presented here may be in part due to local anisotropy.

*Comparison of Hg measurements to other similar materials.*

The Hg-injection technique has seen wide application in to predicting the influence of capillary effects on mixed fluid saturations porous sedimentary rock, but this method is only rarely used to investigate igneous and metamorphic rock. Recently, Staněk & Géraud (2019) describe a series of measurements on fresh and altered granites in the vicinity of faults. Their incremental distributions are qualitatively similar to those reported here. Staněk and Géraud's fresh, unaltered granites display a broad-sawtooth distribution similar to Figure 5.4c, while the altered materials display a distinct peak akin to Figure 5.4. Revil et al. (2017) report measurements in a suite of 21 basalts obtained from a borehole drilled through a sequence of flows, but the pore space in these rocks is vesicular (spherical) and these do not compare well to the results shown in Figure 5.7.

#### 5.4.2 Damage Parameters

Modelling for undamaged granites mineralogically like those tested here places undamaged  $V_p$  at  $\sim 6$  km/s, and  $V_s$  at  $\sim 4$  km/s. The actual wavespeeds measured here for  $V_p$  and  $V_s$  range from  $\sim 3$  to 5, and  $\sim 1.5$  to 2.7 kms/s, respectively (Figure 5.7). These velocity deficits can be numerically characterized by damage parameterization,  $D_p$ ,  $D_s$ , (Figure 5.8),(Ahrens & Rubin, 1993; Grady & Kipp, 1993; Nixon, 2021d), where  $D = 0$  represents a flawless rock, and  $D = 1$  represents complete structural failure:

$$D_P = 1 - \frac{M_d}{M_o} = 1 - \frac{\rho}{\rho_o} \left( \frac{V_P}{V_{Po}} \right)^2 \quad (5.15)$$

*Grady Kipp compressional-wavespeed damage parameter.*

and

$$D_S = 1 - \frac{\mu_d}{\mu_o} = 1 - \frac{\rho}{\rho_o} \left( \frac{V_S}{V_{So}} \right)^2 \quad (5.16)$$

*Grady Kipp shear-wavespeed damage parameter.*

It should be stressed that the analysis in Figure 5.7 has been applied strictly to samples prepared parallel to the vertical axis of the borehole, as velocity results from other axes are currently unavailable. We expect the total amount of damage to be the primary contributing factor to  $D$ , whether by mineralogical alteration, introduction of porosity, or both. Figure 5.8 shows a broad distribution of  $D$  in the granites, ranging from 0.3 to 0.8. It is likely that the total void space within these samples is the primary contributing factor to  $D$ , and more complete overlap of porosity measurements with the ultrasonically investigated samples will help to elucidate this hypothesis.

Previous work has found preferred orientation to shock texture in granitoid samples from M0077a (Rae, 2019), and it is worthwhile to consider the implications here. First, the orientation of damage fabric would affect the overall magnitude of  $D$ ; this could, in part, explain the broad distribution of  $D$  magnitude, as the original orientation of the target rock with respect to the impact is entirely unknown. However,  $D$ 's response to confining pressure should be more dependent on damage fabric orientation, as is observed by microcrack orientation's effect on anisotropy in rocks (e.g., Dewhurst & Siggins, 2006; Sayers & Van Munster, 1991). In the granitoids investigated here,  $D$ 's slope with increasing pressure, at higher more reliable pressures, appears to be similar between many samples, with 2 exceptions: 1) Sample 147 is an obvious outlier, with the lowest  $D_p$  and  $D_s$  out of any sample investigated here. As such,

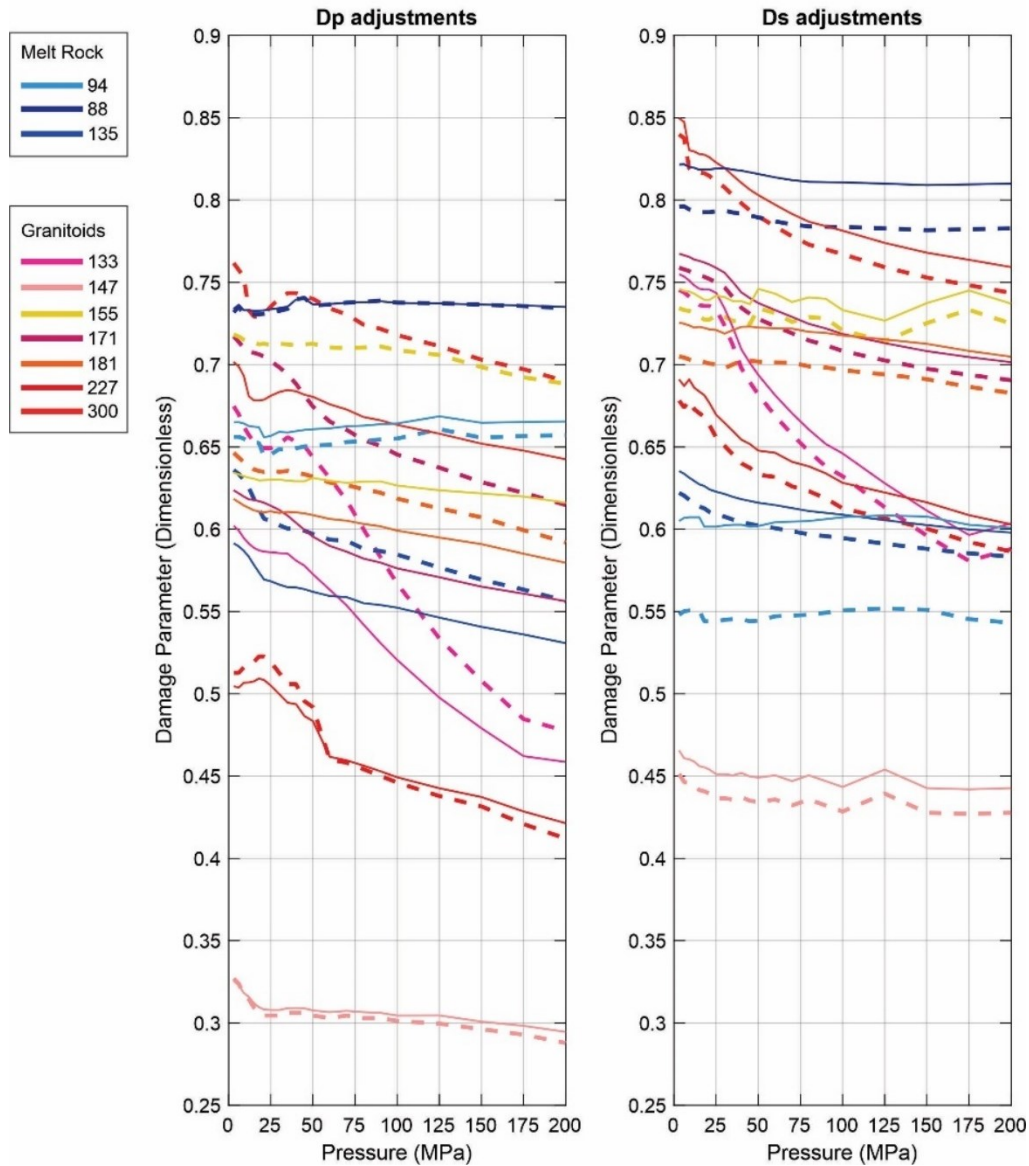


Figure 5.8. Grady Kipp damage parameters under confining pressure, dashed line for dry and solid after gasman adjustments.

its weak decrease of  $D$  with pressure is supportive of the hypothesis that the relationship between  $D$  and pressure is controlled in part by total damage. Additionally, sample 147 has been a favorite of sampling as it tolerates manipulation quite well in comparison to the other granites (see section 5.3.1). Sample 133 has an overall magnitude of  $D$  somewhat representative of the average of the group. However, sample 133 also has the steepest slope of  $D$  reduction with pressure. Although one sample is

not enough to draw conclusions, this could be a hint that sample 133 has and/or is aligned with an orientation that causes wavespeeds to increase under confining pressure.

The apparent ‘damage’ as shown for this suite of samples shows no clear relation to the lithology. More precisely, the damage parameters for the cracked and displaced granitoids do not differ significantly from those for the emplaced undamaged, but altered, melt rocks and suevites. This may complicate the use of remotely sensed seismic wave speeds to infer damage levels at depth within impact structures.

### 5.4.3 Elastic Moduli

The dry velocities ranges shown in Figure 5.7 have been inverted for elastic moduli and are compared against expected moduli for mineralogically similar undamaged rock (Figure 5.9). We observe that, in general, the measured shear modulus,  $\mu$ , is proportionately more depressed than the bulk modulus,  $K$ , in each individual sample, and the shear moduli shows less variability under confining pressure. Taken together, this may suggest that  $\mu$  is more sensitive than  $K$  to intragranular shock effects, and  $K$  is more

Mineralogical Estimates vs Real Measurements for Elastic Moduli in Shocked Granitoids of M0077a

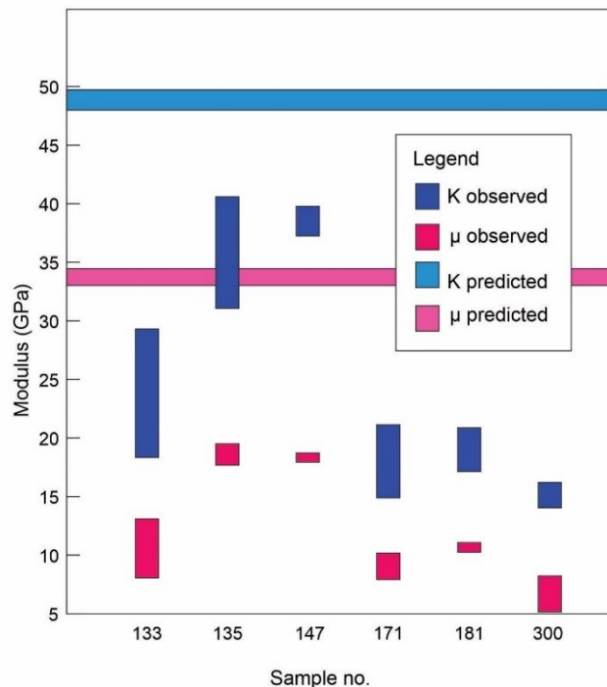


Figure 5.9. Elastic moduli ranges observed under confining pressure.

resistant to confining pressure deformation. Under confining pressure, cracks and other pores will close. The observation that  $\mu$  is less affected by confining pressure than  $K$  may suggest an irregular/rough surface within the pores, where increasing contact due to pressure between the high points in the intra-pore microtopography contributes more significantly to  $K$  than  $\mu$ . Further evidence for pore roughness is suggested by hysteresis observed in the velocity/pressure data. Sample 135, which has a particularly pronounced  $K$  range to  $\mu$  range ratio (Figure 5.9), also has particularly well resolved elevated velocities at pressures above  $\sim 40$  MPa (Figure 5.10). This hysteresis has long been observed (e.g., Gardner et al, 1965) but the physical understanding of it remains incomplete (e.g., Guyer & Johnson, 1999). This observation has implications for interpretation, as the stress history of a highly damaged rock may be built into observable seismic properties: A specimen which was damaged near the surface and then migrated downward to its current resting depth could appear similar to a more damaged specimen that took a path through higher confining pressure before transport to the same resting depth. In the context of impact craters, with peak pressures experienced on the scale of GPa and vertical transport fluxes on the order of tens of kilometers, the lingering effects of hysteresis on in situ physical properties may be very significant.

#### 5.4.4 Pore characterization implications

As already noted, optical petrographic microscope and scanning electron microscope images from thin sections of a melt rock (135R2), a damaged granitoid (97R3), and a suevite (288R2) are provided for comparison in Figure 5.11. Care must be taken to avoid overgeneralizing the interpretation of these images, as all of these samples display some level of alteration, but they are broadly consistent with the earlier pore throat distributions from the Hg-injection porosimetry of Figure 5.8. The SEM image for the granitoid (Figure 5.11f) shows that this material contains numerous cracks with differing widths that are apparent as magnification is increased (not shown). The pores in the melt (Figure 5.11b,c) and the

suevite (Figure 5.11h,i), in contrast, are generally significantly more equant and is also supports the Hg-injection observations of a narrowly range of pore throat diameters.

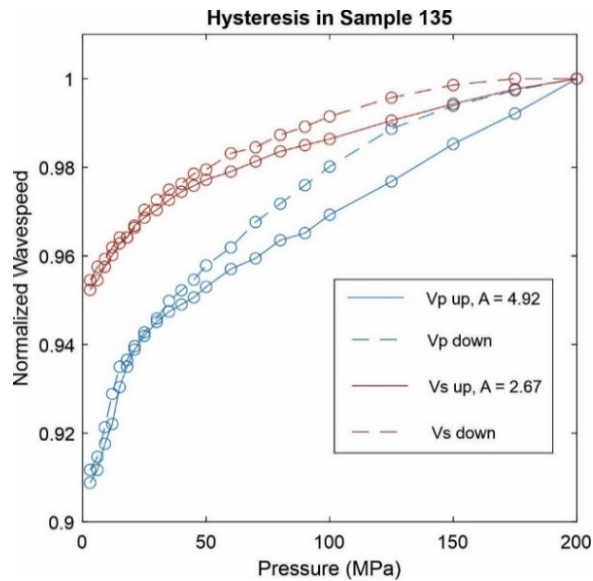


Figure 5.10. Normalized wavespeed curves under confining pressure, both increasing (solid) and decreasing (dashed) directions.

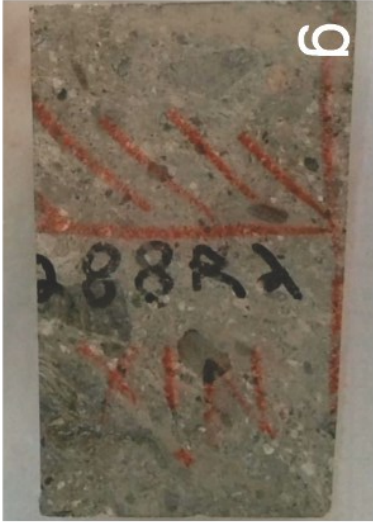


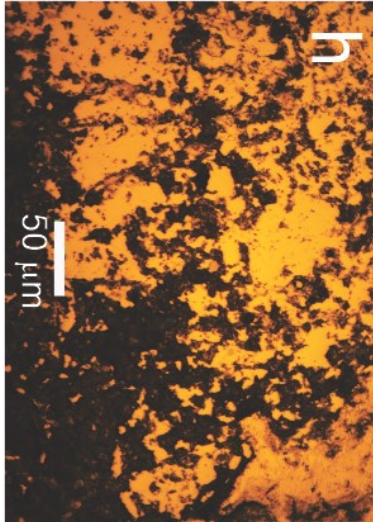
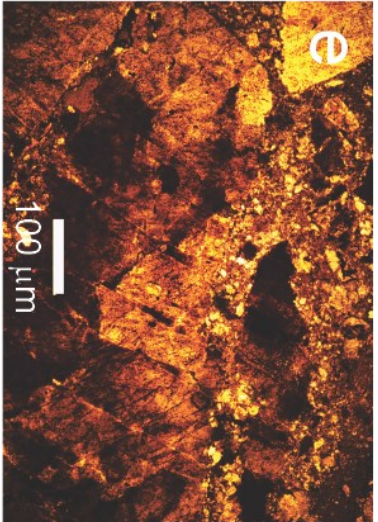
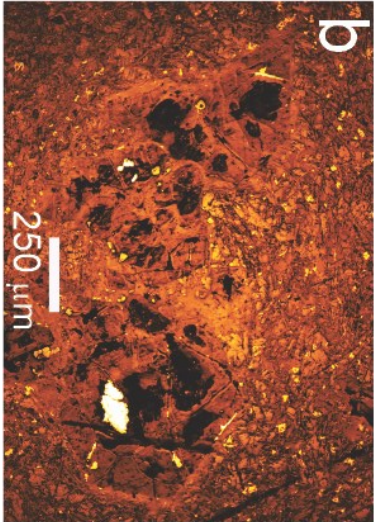
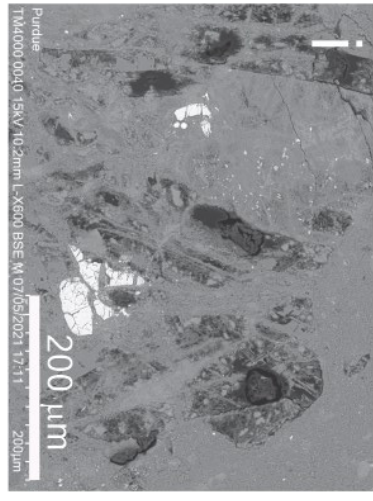
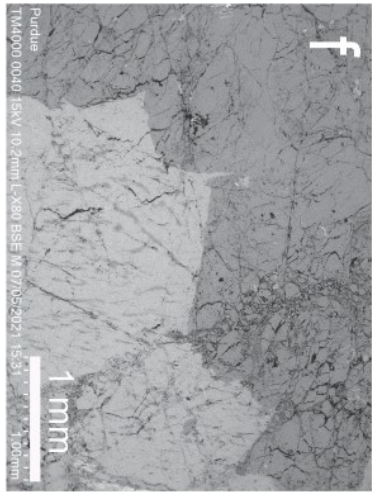
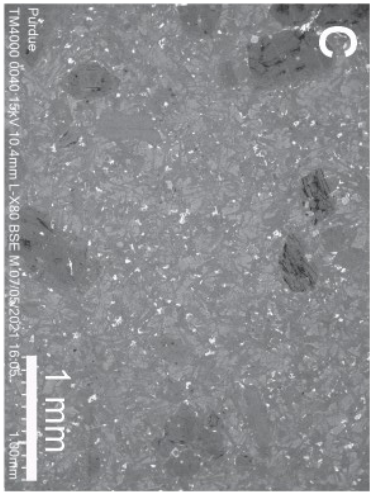
The broad distribution of apparent pore throat diameter includes a significant contribution from length scales of 1 to 10  $\mu\text{m}$  (Figure 5.4c), similar to that of unicellular organisms (Taheri-Araghi et al., 2015). The availability of fracture networks on the micrometer scale are further confirmed by scanning electron microscopy (Figure 5.11). Although the melt rocks and most granitoids in this study have a small fraction of pores at this scale, sample 155 has a particularly pronounced contribution to pore throat at the magnitude that could accommodate life. The search for niche life within M0077a has received some attention already, with a sulfate nutrient source within the post-impact hydrothermal system evidenced by pyrite framboids and isotopic ratios (Kring & Bach, 2021; Kring et al., 2021). These results may be applicable to the search for life on Mars, where appropriate conditions for microbial life may exist deep within impact structures in the present day.

## 5.5 Conclusion

A large inventory of confining pressure wavespeeds has been compiled on the nonlinear behaviour of shocked rocks. Considering that the shock affected depth is similar to crater radius, in this case approximately 100 km, the intense pressure dependence should be carefully considered with respect to seismic reflectivity surveys. In addition, the effects of hysteresis could help to constrain which route a particular sample took to its final in situ resting place. When this velocity data is supplemented and integrated with currently ongoing petrophysical measurements, it may be possible to create an empirical model linking the pressure response to quantified pore behaviour, and then hopefully new shocked rock physics theory can be developed to account for observations.

*Figure 5.11. (opposing page) Microscopy on samples representative of lithology. MELT sample 135R2: a) sample photograph, b) OM reflected light, not polarized, c4X, c) SEM 80X; PR granitoid sample 97R3: d) sample photograph, e) OM transmitted light, polarized, 10X, f) SEM 80X; Suevite sample 288R2: g) sample photograph, h) OM reflected light, not polarized, 20X, i) SEM 600X. All SEM collected are primary back scattered electron images collected at 15kV on polished thin sections. The petrographic optical and SEM images are all from the same thin sections.*



Suevite	Granitoid	Melt	Photograph	Optical Microscope	SEM
 <p>g</p>	 <p>d</p>	 <p>e</p>	 <p>h</p> <p>50 <math>\mu</math>m</p>	 <p>e</p> <p>100 <math>\mu</math>m</p>	 <p>b</p> <p>250 <math>\mu</math>m</p>
 <p>i</p> <p>200 <math>\mu</math>m</p> <p>Purdue TM4000 00410 15kV 10.2mm L-X800 BSE M.07/05/2021 17:11</p>	 <p>f</p> <p>1 mm</p> <p>Purdue TM4000 00410 15kV 10.2mm L-X800 BSE M.07/05/2021 15:51</p>	 <p>c</p> <p>1 mm</p> <p>Purdue TM4000 00410 15kV 10.4mm L-X800 BSE M.07/05/2021 16:05</p>			

## 6. Conclusion

### 6.1 Future Work.

#### 6.1.1 Attenuation

Chapter 3 is an immediate springboard for further work, as attenuation is of particular interest because it provides additional information regarding in situ material conditions and materials. The nature of a waveform is significantly altered by attenuation as it propagates, and better understanding this property could be applied to extensive datasets which already exist. In chapter 3, we began to quantify attenuation within M0077a, yet the true potential of this dataset has not yet been realized. An attenuating medium will reduce the amplitude of a wavelet, as shown below (Figure 6.1). However, a wavelet is a sum of superposition and part of the peak amplitude's apparent decay is due to velocity dispersion. Therefore, more complete analyses of attenuation in this dataset should include numerical

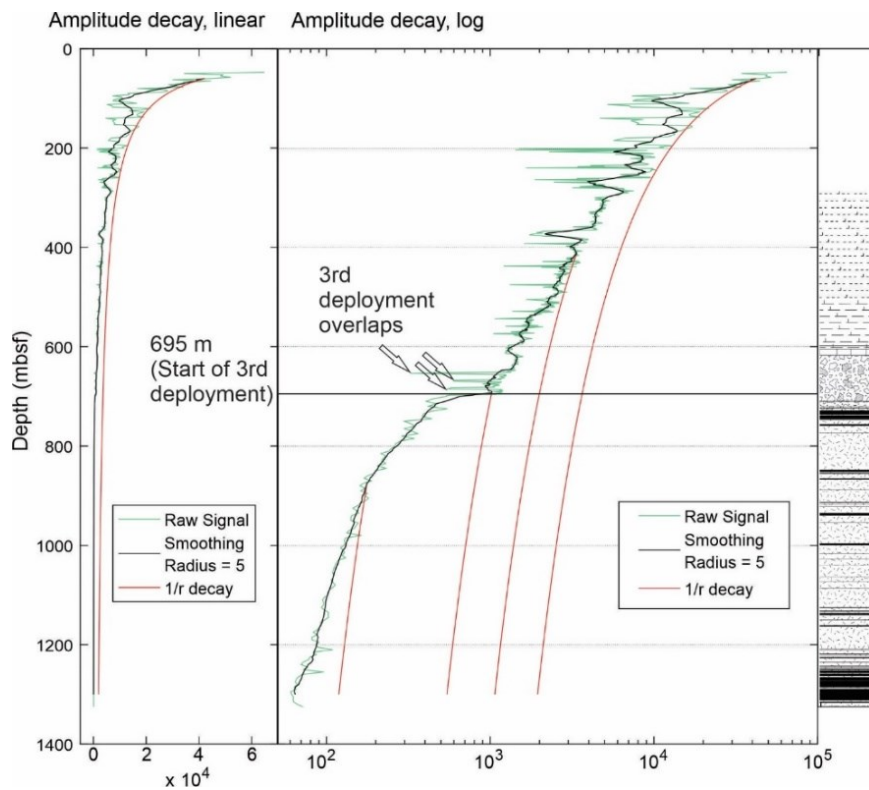


Figure 6.1. Peak amplitude loss in the VSP of M0077a.

integration of the entire wavelet's amplitude throughout hole the VSP in hole M0077a. It would not be very difficult to add this step to the windowing subroutine within the software package already available (section 6.4c).

The spectral ratio method utilized in chapter 3 shows that the damaged peak ring granitoids in M0077a are highly attenuating. However, limiting the "reference" wavelet to the upper portion is dubious, and the available software package (section 6.4c) is able to generate a matrix of Q values using any reference trace within the borehole to find Q at any other point (Figure 6.2). While this matrix is valuable in that it

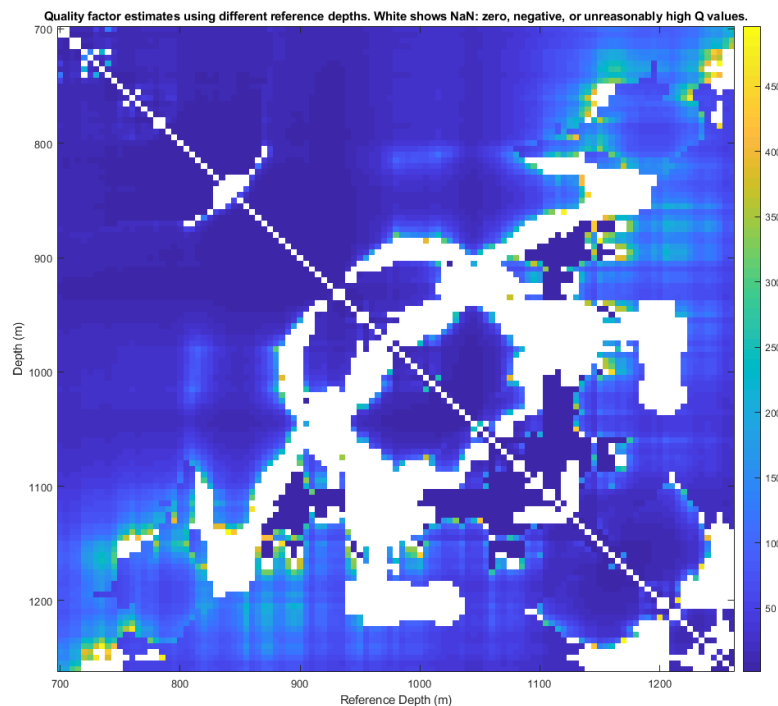


Figure 6.2. Q matrix, using variable band method.

in support of the low Q-factors published in chapter 3, the discontinuous and spotty data coverage makes these results questionable. Inspecting Figure 6.2, the data appears fairly consistent and smooth above 900 m. However below roughly 940 m, gaps in coverage suddenly appear and are problematic. It turns out that there is a natural high frequency filtering layer at precisely 936 m depth (Figure 6.3). I originally become interested the lithology at 930-940 m depth due to apparent blockage and reflection

of tube waves in the raw VSP (Figure 6.3a, RHS). Inspection of the line scans reveal that the lithology at 936m is rather highly fragmented with no cohesion between the fragments (Figure 6.3d), which is surprising at nearly a km below the Earth's surface! While the fact that these fragments are uncemented after 66 Ma has its own implications with regard to hydrology, the main effect concerning discussions here is the highly effective removal of any frequencies above 50 Hz (Figure 6.3b,c). This effect is not limited to the tube waves, as visual inspection of the raw VSP above and below 936 m depth (Figure 6.3a) reveals a removal of high frequency noise, as well. As the depth of 936m precisely matches where the spectral ratio matrix starts having problems (Figure 6.2), further work on attenuation within the M0077a VSP will need to incorporate the effects of this natural filtering layer and similar yet less obvious layers. Additionally, the 936 m natural filtering layer could be utilized to constrain dimensional parameters of squish/squirt flow in inter and intra granular modes of attenuation.

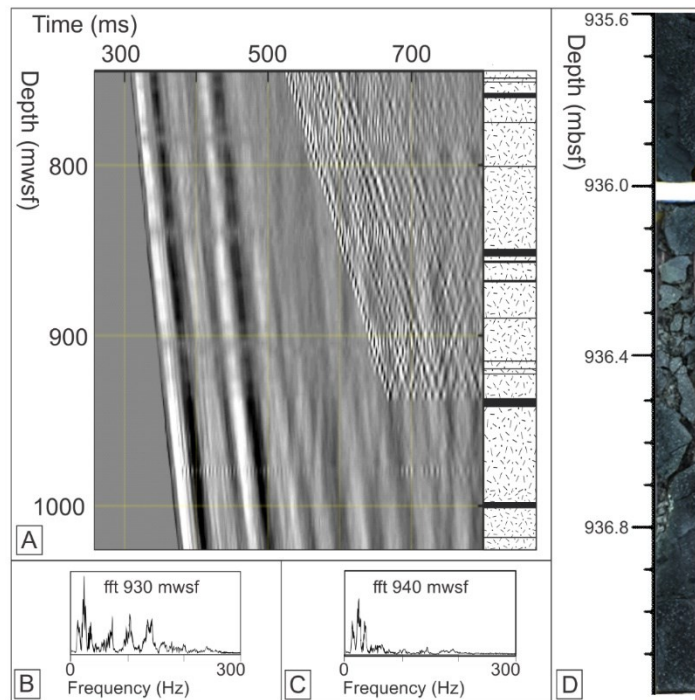


Figure 6.3. Natural filtering layer at 936 mbsf.

### 6.1.2 Pore Structure Inversion.

The pore structure of the shocked granitoids within M0077a are diverse and complex. The mercury porosimetry described in chapter 5 is a good start, but the pore throat characterization only quantifies the 'choke point' of interconnected pores. I have made many attempts to invert our available data into some sort of pore parameterization, but this line of inquiry with existing theory generally produced nonsensical results. However, by assuming porosity exclusively due to 'penny-shaped' cracks, I wrote a software package (section 6.4e) to analytically invert with via Kuster-Toksoz equations for average pore aspect ratio (Figure 6.4). Although the Kuster Toksoz software package includes parameters for other pore geometries and varying contributions from other pore types, I found that incorporating pore types other than penny cracks gave unrealistic results. The main takeaway from Figure 6.4 is that porosity within the peak ring appears to be dominated by long wide and flat cracks. This interpretation is supported by preliminary investigations via electron microscopy (Figure 5.11).

The main deficiency with pre-existing effective medium theories is the assumptions that inclusions and/or pores are diffuse and do not interact with each other. Previous workers have attempted to push the limits of effective medium theory with a numerical approach, known as differential effective medium (DEM) theory, however it is not clear that even DEM will suffice for these extensively damaged specimens where cracks and pore are clearly connected in the microscopic images. In addition to the extensive interconnected pore structure, there are intragranular pores which may not necessarily be accessible with laboratory measurements, and mineralogical alteration with poorly understood elastic properties.



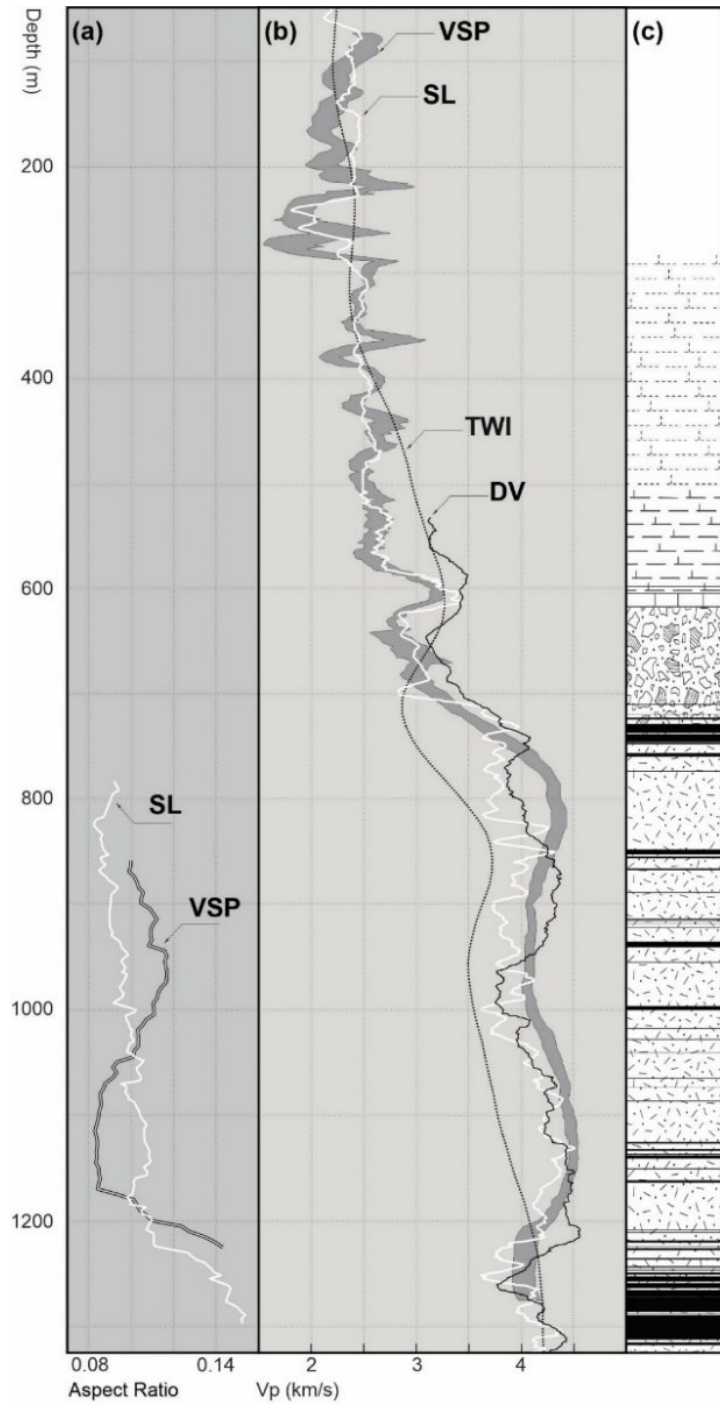


Figure 6.4. Kuster Toksoz pore aspect ratio inversion.

The results from chapter 5 may require the development of an entirely new theoretical framework of rock physics for highly damaged media, but given the extent of uncertainty and unknowns, this will need to be built statistically from extensive testing on a far larger sample set. Fortunately, there is ~500 m of shocked granitoid available for testing, and petrophysical experimentation on enough samples to establish an empirical relationship is possible. Thus, I propose a strategy as follows:

- 1) Complete ultrasonic, helium, and mercury tests on all M0077a granitoid samples currently in Experimental Geophysics Group's possession at Purdue.

([https://purdue0-my.sharepoint.com/:x/r/personal/schmitt\\_purdue\\_edu/\\_layouts/15/Doc.aspx?sourcedoc=%7BAE5142D8-CA2C-4B57-A6F4-3BF3AF671F92%7D&file=Chicxulub\\_Data\\_Summary\\_July2021.V2.xlsx&action=default&mobileredirect=true](https://purdue0-my.sharepoint.com/:x/r/personal/schmitt_purdue_edu/_layouts/15/Doc.aspx?sourcedoc=%7BAE5142D8-CA2C-4B57-A6F4-3BF3AF671F92%7D&file=Chicxulub_Data_Summary_July2021.V2.xlsx&action=default&mobileredirect=true))

- 2) Fit a rough empirical model to the data from step 1.
- 3) Obtain enough granitoid samples from M0077a to be statistically relevant, and repeat the measurements from step 1.
- 4) Publish a statistically relevant empirical model to the new larger dataset.
- 5) Let the theoretician/modeler community do the rest.

### 6.1.3 Thin Sections

The question of wavespeed anisotropy is presently unanswered in the M0077a impactite samples. Granites, although made of highly anisotropic minerals, have the emergent property of isotropy when combined into a polycrystalline aggregate where, on average, the grains are randomly oriented with respect to one another in the rock mass. It is important to note that analyses of thin sections (Rae et al., 2019) and borehole and core images (Ross et al., 2021) indicate preferred directions at scales ranging from cracks to faults within the peak ring; this favouring is expected to make the material anisotropic to seismic waves. One question that might be addressed in part with the existing samples is whether shock effects introduce anisotropy and subsequently if this information might be used to reconstruct a specific sample's orientation at the time of impact. The determination of wavespeed anisotropy at

ultrasonic frequencies is a specialty of the Experimental Geophysics Group. Unfortunately, due to IODP sampling policies, we were unable to obtain full-round (unsplit) samples for machining into polyhedra for this purpose. To further this goal, efforts were made to find collaborators (Uppsala University) with the equipment, and sample preparation to carry out electron back scatter diffraction (EBSD) analysis on the thin sections. In March 2020, however, after 2 years of preparation, I visited Uppsala for to perform EBSD analysis on these samples. Unfortunately, after introduction to the equipment, I had to rush home on the first available flight just before COVID-19 lockdown. This work remains to be done.

EBSD harnesses the wave properties of matter by collecting diffraction patterns of back-scattered electrons from a highly polished thin section in a scanning electron microscope vacuum chamber. These patterns can then be interpreted to identify mineral phase, grain boundaries, and crystallographic orientation to microscopic resolution. Processing this data can then provide elastic moduli for any desired direction within the plane of the thin section. My experimental design uses triplanar ( $xy$ ,  $yz$ ,  $xz$ ) thin sections from the same visually homogenous samples, so that elastic parameters could be calculated twice for each of the three principal axes. Some may prefer the term triaxial, as an axis defines a plane, but I prefer triplanar for clarity of experimental design. Three samples have been prepared this way, for a total of 9 exotic and labor-intensive thin sections (Figure 6.5).

One key knowledge gap, however, is that the elastic parameters of impactite minerals and glasses are nearly non-existent, and we have single axis velocity measurements (chapter 5) on a significant collection of these impactites. This experiment would be foundational by answering the following questions:

- 1) Can EBSD detect and map shock alteration in minerals?
- 2) Does shock mineral alteration induce polycrystalline elastic moduli anisotropy?

Question 2 is of particular interest, as the majority of previous analysis I have performed on this topic revolve around porosity as the key variable.



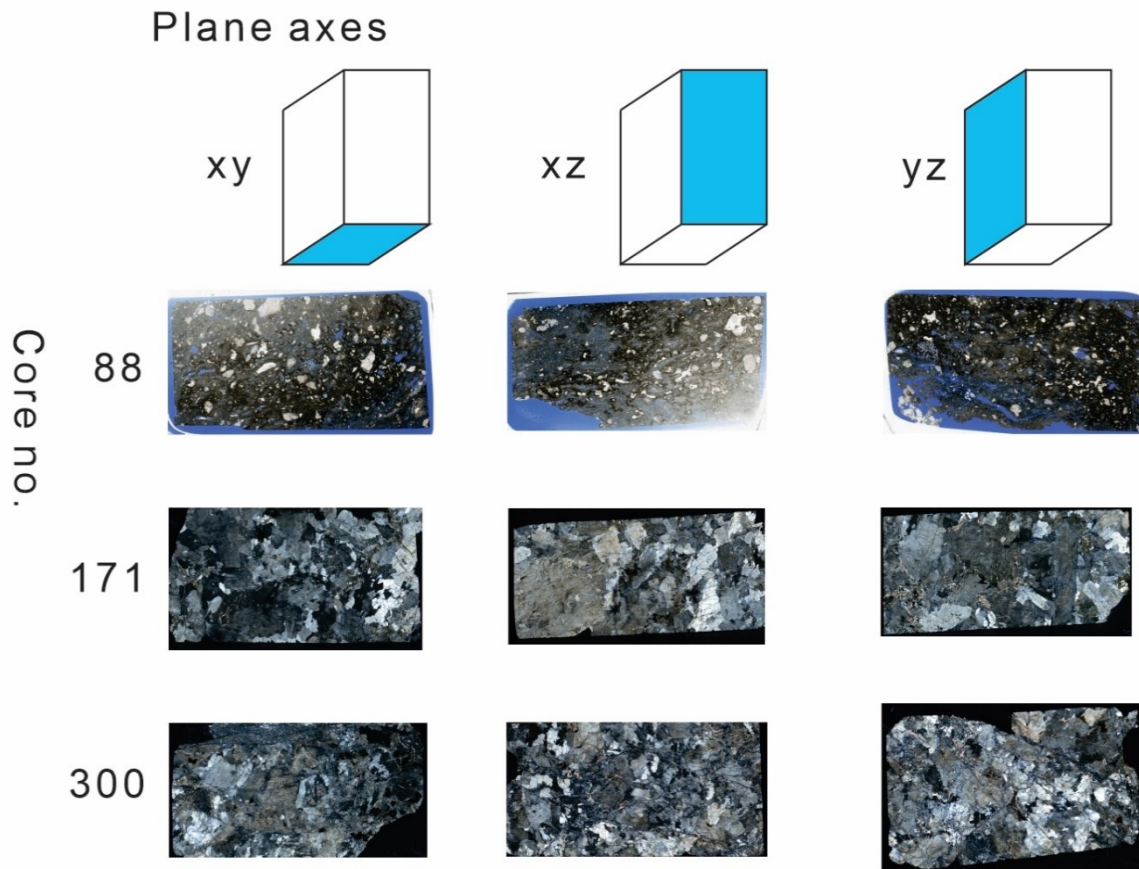


Figure 6.5. Triplanar thin sections prepared for EBSD analysis. 88 suevite sample shown under plane polarized light, 171 & 300 granitoid samples shown under cross polarized light.

## 6.2 Concluding Remarks

This thesis describes field and laboratory measurements on unique samples and extremely rare seismic data. The in-situ measurements from borehole M0077a within Chicxulub's peak ring presented here are highly unusual. Both  $V_p$  and  $V_s$  seismic wavespeeds are depressed by  $\sim 1/3$  of what would be expected for mineralogically similar unshocked granite. The anomalous wavespeeds are inextricably linked to alterations resulting from the K/Pg hypervelocity impact, which includes both immediate shock damage/alterations and subsequent alterations from the impact induced hydrothermal system.

Attenuation in undamaged crystalline rocks is typically quite minimal, with Q values reaching as high as  $\sim 1000$ . However, Q within M0077a is 2 to 3 orders of magnitude less, with spectral ratios analysis on the P-wavelet first arrival ranging from 10 to possibly as high as 100. These values are low and should therefore be treated with caution as the spectral ratios method utilized here is imperfect and can be tainted with noise. With the data and software presented here, one could easily apply the spectral ratio method to other portions of the VSP, which include the upper 2 deployments of the VSP P wavelet (Figure 4.5), and shear wavelets (Figure 4.7). Analysis of the shear wavelet is of particular interest due to the large discrepancy between  $D_p$  and  $D_s$  seen in chapter 4. The concept of damage parameterization introduced here (Figure 4.13) may be particularly insightful, as shock physics code used to model hypervelocity impacts often track damage parameters and can grant insight into exactly where within the initially hemispherical target a particular rock originated. In the VSP data analyzed here,  $D_s$  appears to be much higher than  $D_p$ , which, when considered along somewhat analogous Lunar Basalt impact simulations by Wiggins, et al., (2019), may suggest the peak ring materials originated closer to ground zero than currently believed. However, this interpretation is extremely tentative and will need to be further constrained by hydrocode simulations more tuned to the actual conditions at Chicxulub.

The seismic detailed seismic reflectivity and velocity model presented here has already been used to improve surface seismic inversions and interpretations (Christeson, et. al, 2021), and improve iSALE

hydrocode hypervelocity impact modelling (Morgan, et al., 2016). We have confirmed that the character of the seismic reflectivity at site M0077 results from tuning of reflections originating at abrupt impedance contrasts: The seismic LID, and top & bottom of the LVZ. The carbonate LID is significantly stiffer mechanically than later subsequent sedimentary deposition, and its contrast with the underlying suevites dominates the initial arrival of the peak ring's primary reflection. Although reasons for this sharp mechanical contrast between the LID and subsequent sedimentation remain unclear, hydrological alteration is a likely contributing factor. As the Chicxulub Impact Basin has a nearly exclusive Marine history, better understanding the seismic response in context of hydrological alteration and highly anomalous Poisson's ratios could have applications in the search for evidence of ancient water in similar basins on Mars.

These highly anomalous physical properties warrant close petrophysical investigation, as current rock physics models are insufficient for characterization. Laboratory investigations of M0077a samples have begun to scratch the surface of this new weird shocked-rock physics, yet much work remains to be done. We have shown here the heterogeneous response to confining pressure of both wavespeed magnitude and slope, which, when considered with the lack of knowledge of the initial orientation of the target rock with respect to the K/Pg shock wave, this heterogeneity may be an expression of local anisotropy. We have seen a tremendously broad distribution of pore throat diameter in the granitoids, which obeys no clear pattern, yet is contrasted by the melt rocks which have a fairly homogenous pore throat distribution. Although it is clear more testing is needed, the clear differences in pore characterization between melt rock and granitoids are intriguing. The overall magnitude of porosity (~10%) and the seismic impedance of both are similar, and in the VSP data, no clear reflections are seen originating from major melt rock layers. While the differences in porosity character likely result from differences in modes of emplacement and response to shock effects, the conclusions here are highly tentative and more data is necessary before empirical and theoretical relations can be applied.

I have provided herein a handbook for researching the emerging field of shocked rock physics. While the results presented here are certainly unusual and interesting, this thesis is only begins to scratch the surface of the sheer volume of research that can be accomplished with these unique data and samples.

### **6.3 Permissions**

IODP (Figure 1.7), Google (Figure 1.4), SEG (Figure 1.9), AGU (Figure 2.16), and NASA, (Figures 2.1, 2.8, 3.20, 3.22, and 3.23) all have statements available online permitting academic reproduction of the figures used here without prior consent. Elsevier, Earth Impact Database, and Lunar and Planetary Institute have explicitly granted permission for academic reproduction of Figure 1.5, Figure 1.3, and Figures 3.17, 3.18, & 3.19, respectively. Specific records of permissions are available upon request.

## 6.4 Data Sets

A - Nixon, Kofman, and Schmitt, (2021). *Replication Data for "Borehole Seismic Observations from the Chicxulub Impact Drilling: Implications for Seismic Reflectivity and Impact Damage"*. UAlberta Dataverse.

Replication data for chapters 3 & 4

[doi:10.7939/DVN/D1YY4A](https://doi.org/10.7939/DVN/D1YY4A)

B - Nixon, (2021). *Borehole Attenuation Processing Package*, UAlberta Dataverse. .

[doi%3A10.7939%2FDVN%2FJGPORP](https://doi.org/10.7939/2FDVN%2FJGPORP)

C - Nixon, (2021). *Ultrasonic Correlation Processing Package*, UAlberta Dataverse.

[doi%3A10.7939%2FDVN%2FXCRNHN](https://doi.org/10.7939/2FDVN%2FXCRNHN)

D - Nixon, (2021). *Kuster-Toksoz Porosity Inversion Processing Package*, UAlberta Dataverse.

[doi%3A10.7939%2FDVN%2FCSRLGE](https://doi.org/10.7939/2FDVN%2FCSRLGE)

## 7. Works Cited.

### Articles

Abdelhedi, M., Aloui, M., Mnif, T., & Abbas, C. (2017). Ultrasonic velocity as a tool for mechanical and physical parameters prediction within carbonate rocks. *Geomechanics and Engineering*, 13(3), 371-384.

Ackermann, H., Godson, R., & Watkins, J. (1975). Seismic refraction technique used for subsurface investigations at Meteor Crater, Arizona. *Journal of Geophysical Research*, 80(5), 765-775.

Adams, L., & Williamson, E. (1923). On the compressibility of minerals and rocks at high pressures. *Journal of the Franklin Institute*, 195, 475-529.

Agarwal, A., Kontny, A., Srivastava, D., & Greiling, R. (2016). *Shock pressure estimates in target basalts of a pristine crater: A case study in the Lonar Crater, India*. Geological Society of America Bulletin, 128(1-2), 19-28.

Agosta, F., Prasad, M., & Aydin, A. (2007). Physical properties of carbonate fault rocks, Fucino Basin (Central Italy): implications for fault seal in platform carbonates. *Geofluids*, 7(1), 19-32.

Ahrens, T., & Rubin, A. (1993). Impact-induced tensional failure in rock. *Journal of Geophysical Research-Planets*, 98(E1), 1185-1203.

Ai, H. (2006). Shock-induced damage in rocks: application to impact cratering. *California Inst. of Technology*, PhD thesis.

Ai, H., & Ahrens, T. (2007). Effects of shock-induced cracks on the ultrasonic velocity and attenuation in granite. *Journal of Geophysical Research-Solid Earth*, 112(B1), 9.

Albertsson, T., Semenov, D., & Henning, T. (2014). Chemodynamical deuterium fractionation in the early solar nebula: The origin of water on earth and in asteroids and comets. *The Astrophysical Journal*, 784(1), 39.

Altman, N., & Krzywinski, M. (2015). Points of significance: simple linear regression. *Nature Methods*, 12(11), 999-1000.

Alvarez, L., Alvarez, W., Asaro, F., & Michel, H. (1980). Extraterrestrial cause for the Cretaceous-Tertiary extinction. *Science*, 208(4448), 1095-1108.

- Ames, D., Jonasson, I., Gibson, H., & Pope, K. (2006). Impact-generated hydrothermal system—constraints from the large Paleoproterozoic Sudbury Crater, Canada. *Biological processes associated with impact events* (pp. 55-100). Springer.
- Amidror, I. (2013). Mastering the discrete Fourier transform in one, two or several dimensions: pitfalls and artifacts. Springer.
- Anders, E., Ganapathy, R., Krähenbühl, U., & Morgan, J. (1973). Meteoritic material on the Moon. *The Moon*, 8(1-2), 3-24.
- Anderson, D., & Kanamori, H. (1968). Shock-wave equations of state for rocks and minerals. *Journal of Geophysical Research*, 73(20), 6477-6502.
- Angenheister, G., & Pohl, J. (1974). Beiträge der angewandten geophysik zur Auswahl des borepunktes der forschungsbohrung Nordlingen 1973. *Geological Bavarica*, 72, 59-63.
- Angenheister, G., & Pohl, J. (1976). Results of seismic investigations in the Ries Crater area (Southern Germany). *Explosion Seismology in Central Europe*, (pp. 290-302). Springer.
- APC. (2021). Physical and piezoelectric properties of APC materials. *APC international*. Retrieved Oct 12 from <https://www.americanpiezo.com/apc-materials/physical-piezoelectric-properties.html>
- Artemieva, N., Morgan, J., & Party, E. (2017). Quantifying the release of climate-active gases by large meteorite impacts with a case study of Chicxulub. *Geophysical Research Letters*, 44(20), 10,180-110,188.
- ASTM. (2018). ASTM D4404-Standard test method for determination of pore volume and pore volume distribution of soil and rock by mercury injection porosimetry. *Physical-Chemical Interactions of Soil and Rock* (Vol. ASTM International 1-8, pp. D18.06 - D18.06).
- Atten, S. (2004). MSc-attenuation. *University of Alberta*. MSc thesis.
- Avseth, P., Mukerji, T., & Mavko, G. (2005). Quantitative seismic interpretation. *Cambridge University Press*.
- Baker, D., Head, J., Collins, G., & Potter, R. (2016). The formation of peak-ring basins: Working hypotheses and path forward in using observations to constrain models of impact-basin formation. *Icarus*, 273, 146-163.



Balch, A., Lee, M., Miller, J., & Ryder, R. (1982). The use of vertical seismic profiles in seismic investigations of the earth. *Geophysics*, 47(6), 906-918.

Bass, J. (1995). Elasticity of minerals, glasses, and melts. Mineral Physics and Crystallography: A Handbook of Physical Constants, (pp. 45-63). *American Geophysical Union*,

Bauer, J. (1979). Experimental shock metamorphism of mono- and polycrystalline olivine-A comparative study. *Lunar and Planetary Science Conference Proceedings*.

Bell, C., Morgan, J., HAMPSON, G., & TRUDGILL, B. (2004). Stratigraphic and sedimentological observations from seismic data across the Chicxulub impact basin. *Meteoritics & Planetary Science*, 39(7), 1089-1098.

Ben-Zion, Y., & Sammis, C. (2003). Characterization of fault zones. *Pure and Applied Geophysics*, 160(3), 677-715.

Benson, P., Schubnel, A., Vinciguerra, S., Trovato, C., Meredith, P., & Young, R. (2006). Modeling the permeability evolution of microcracked rocks from elastic wave velocity inversion at elevated isostatic pressure. *Journal of Geophysical Research-Solid Earth*, 111(B4), 11.

Berge, P., Berryman, J., & Bonner, B. (1993). Influence of microstructure on rock elastic properties. *Geophysical Research Letters*, 20(23), 2619-2622.

Biot, M. (1956). Theory of elastic waves in a fluid-saturated porous solid. 1. Low frequency range. *The Journal of the Acoustical Society of America*, 28, 168-178.

Biot, M. (1956). Theory of propagation of elastic waves in a fluid-saturated porous solid. II. Higher frequency range. *The Journal of the Acoustical Society of America*, 28(2), 179-191.

Birch, F. (1960). The velocity of compressional waves in rocks to 10 kilobars: 1. *Journal of Geophysical Research*, 65(4), 1083-1102.

Boadu, F. K. (1998). Inversion of fracture density from field seismic velocities using artificial neural networks. *Geophysics*, 63(2), 534-545.

Bohor, B., Betterton, W., & Krogh, T. (1993). Impact-shocked zircons: discovery of shock-induced textures reflecting increasing degrees of shock metamorphism. *Earth and Planetary Science Letters*, 119(3), 419-424.

Bourbié, T., Coussy, O., Zinszner, B., & Junger, M. C. (1992). Acoustics of porous media. *U.S. Department of Energy, Office of Scientific and Technical Information*

Bralower, T., Cosmidis, J., Heaney, P., Kump, L., Morgan, J., Harper, D., Lyons, S., Freeman, K., Grice, K., & Wendler, J. (2020). Origin of a global carbonate layer deposited in the aftermath of the Cretaceous-Paleogene boundary impact. *Earth and Planetary Science Letters*, 548, 116476.

Brenguier, F., Boué, P., Ben-Zion, Y., Vernon, F., Johnson, C., Mordret, A., Coutant, O., Share, P., Beaucé, E., & Hollis, D. (2019). Train traffic as a powerful noise source for monitoring active faults with seismic interferometry. *Geophysical Research Letters*, 46(16), 9529-9536.

Bunch, T., & Cohen, A. J. (1964). Shock deformation of quartz from two meteorite craters. *Geological Society of America Bulletin*, 75(12), 1263-1266.

Caine, J., Evans, J., & Forster, C. (1996). Fault zone architecture and permeability structure. *Geology*, 24(11), 1025-1028.

Camargo-Zanoguera, A., & Suarez-Reynoso, G. (1994). Evidencia sísmica del cráter impacto de Chicxulub. *Bol. de la Asociación Mexicana de Geofísicos de Exploración*, 34, 1-28.

Campos-Enriquez, J., Chavez-Garcia, F., Cruz, H., Acosta-Chang, J., Matsui, T., Arzate, J., Unsworth, M., & Ramos-Lopez, J. (2004). Shallow crustal structure of Chicxulub impact crater imaged with seismic, gravity and magnetotelluric data: inferences about the central uplift. *Geophysical Journal International*, 157(2), 515-525.

Canales-Garcia, I., Urrutia-Fucugauchi, J., & Aguayo-Camargo, E. (2018). Seismic imaging and attribute analysis of Chicxulub Crater central sector, Yucatan Platform, Gulf of Mexico. *Geologica Acta*, 16(2), 215-235.

Canup, R., & Asphaug, E. (2001). Origin of the Moon in a giant impact near the end of the Earth's formation. *Nature*, 412(6848), 708-712.

Casanova-Arenillas, S., Rodríguez-Tovar, F., & Martínez-Ruiz, F. (2020). Applied ichnology in sedimentary geology: Python scripts as a method to automatize ichnofabric analysis in marine core images. *Computers & Geosciences*, 136, 104407.

Catchings, R., Powars, D., Gohn, G., Horton Jr, J., Goldman, M., & Hole, J. (2008). Anatomy of the Chesapeake Bay impact structure revealed by seismic imaging, Delmarva Peninsula, Virginia, USA. *Journal of Geophysical Research: Solid Earth*, 113(B8).

Chaki, S., Takarli, M., & Agbodjan, W. (2008). Influence of thermal damage on physical properties of a granite rock: porosity, permeability and ultrasonic wave evolutions. *Construction and Building Materials*, 22(7), 1456-1461.

- Chao, E., Fahey, J., Littler, J., & Milton, D. (1962). Stishovite, SiO<sub>2</sub>, a very high pressure new mineral from Meteor Crater, Arizona. *Journal of Geophysical Research*, 67(1), 419-421.
- Chao, E., Shoemaker, E., & Madsen, B. (1960). First natural occurrence of coesite. *Science*, 132(3421), 220-222.
- Chen, J., Xu, Z., Yu, Y., & Yao, Y. (2014). Experimental characterization of granite damage using nonlinear ultrasonic techniques. *Ndt & E International*, 67, 10-16.
- Chen, P., Dai, K., Huang, F., & Ding, Y. (2004). Ultrasonic evaluation of the impact damage of polymer bonded explosives. *Journal of Beijing Institute of Technology*, 13(3), 242-246.
- Cheng, C., & Toksöz, M. (1979). Inversion of seismic velocities for the pore aspect ratio spectrum of a rock. *Journal of Geophysical Research: Solid Earth*, 84(B13), 7533-7543.
- Cheng, C., Toksöz, M., & Willis, M. (1982). Determination of in situ attenuation from full waveform acoustic logs. *Journal of Geophysical Research: Solid Earth*, 87(B7), 5477-5484.
- Chiang, E., & Youdin, A. (2010). Forming planetesimals in solar and extrasolar nebulae. *Annual Review of Earth and Planetary Sciences*, 38, 493-522.
- Cholach, P., Molyneux, J., & Schmitt, D. (2005). Flin Flon Belt seismic anisotropy: elastic symmetry, heterogeneity, and shear-wave splitting. *Canadian Journal of Earth Sciences*, 42(4), 533-554.
- Christensen, N. (1996). Poisson's ratio and crustal seismology. *Journal of Geophysical Research: Solid Earth*, 101(B2), 3139-3156.
- Christeson, G., Morgan, J., & Gulick, S. Mapping the Chicxulub Impact Stratigraphy and Peak Ring Using Drilling and Seismic Data. *Journal of Geophysical Research: Planets*, e2021JE006938.
- Christeson, G., Collins, G., Morgan, J., Gulick, S., Barton, P., & Warner, M. (2009). Mantle deformation beneath the Chicxulub impact crater. *Earth and Planetary Science Letters*, 284(1-2), 249-257.
- Christeson, G., Gulick, S., Morgan, J., Gebhardt, C., Kring, D., Le Ber, E., Lofi, J., Nixon, C., Poelchau, M., & Rae, A. (2018). Extraordinary rocks from the peak ring of the Chicxulub impact crater: P-wave velocity, density, and porosity measurements from IODP/ICDP Expedition 364. *Earth and Planetary Science Letters*, 495, 1-11.

Christeson, G., Gulick, S., Morgan, J., Gebhardt, C., Kring, D., Le Ber, E., Lofi, J., Nixon, C., Poelchau, M., Rae, A., Rebolledo-Vieyra, M., Riller, U., Schmitt, D., Wittmann, A., Bralower, T., Chenot, E., Claeys, P., Cockell, C., Coolen, M., Ferriere, L., Green, S., Goto, K., Jones, H., Lowery, C., Mellett, C., Ocampo-Torres, R., Perez-Cruz, L., Pickersgill, A., Rasmussen, C., Sato, H., Smit, J., Tikoo, S., Tomioka, N., Urrutia-Fucugauchi, J., Whalen, M., Xiao, L., & Yamaguchi, K. (2018). Extraordinary rocks from the peak ring of the Chicxulub impact crater: P-wave velocity, density, and porosity measurements from IODP/ICDP Expedition 364. *Earth and Planetary Science Letters*, 495, 1-11.

Christeson, G., Nakamura, Y., Buffler, R., Morgan, J., & Warner, M. (2001). Deep crustal structure of the Chicxulub impact crater [Article]. *Journal of Geophysical Research-Solid Earth*, 106(B10), 21751-21769.

Cochran, E., Li, Y., Shearer, P., Barbot, S., Fialko, Y., & Vidale, J. (2009). Seismic and geodetic evidence for extensive, long-lived fault damage zones. *Geology*, 37(4), 315-318.

Cockell, C., Schaefer, B., Wuchter, C., Coolen, M., Grice, K., Schnieders, L., Morgan, J., Gulick, S., Wittmann, A., & Lofi, J. (2021). Shaping of the present-day deep biosphere at Chicxulub by the impact catastrophe that ended the Cretaceous. *Frontiers in Microbiology*, 12, 1413.

Coes Jr, L. (1953). A new dense crystalline silica. *Science*, 118(3057), 131-132.

Collins, G. S. (2014). Numerical simulations of impact crater formation with dilatancy. *Journal of Geophysical Research-Planets*, 119(12), 2600-2619.

Collins, G., Melosh, H., & Ivanov, B. (2004). Modeling damage and deformation in impact simulations. *Meteoritics & Planetary Science*, 39(2), 217-231.

Collins, G., Melosh, H., Morgan, J., & Warner, M. (2002). Hydrocode simulations of Chicxulub crater collapse and peak-ring formation. *Icarus*, 157(1), 24-33.

Collins, G., Morgan, J., Barton, P., Christeson, G., Gulick, S., Urrutia, J., Warner, M., & Wunnemann, K. (2008). Dynamic modeling suggests terrace zone asymmetry in the Chicxulub crater is caused by target heterogeneity. *Earth and Planetary Science Letters*, 270(3-4), 221-230.

Collins, G., Patel, N., Davison, T., Rae, A., Morgan, J., & Gulick, S. (2020). A steeply-inclined trajectory for the Chicxulub impact. *Nature communications*, 11(1), 1-10.

Cooper, M., Kovach, R., & Watkins, J. (1974). Lunar near-surface structure. *Reviews of Geophysics*, 12(3), 291-308.

- Croft, S. (1985). The scaling of complex craters. *Journal of Geophysical Research: Solid Earth*, 90(S02), C828-C842.
- Dainty, A., & Toksoz, M. (1977). Elastic wave-propagation in a highly scattering medium - diffusion approach. *Journal of Geophysics-Zeitschrift Fur Geophysik*, 43(1-2), 375-388.
- Daly, R., Schultz, P., Lassiter, J., Loewy, S., Thompson, L., & Spray, J. (2018). Contrasting meteoritic signatures within the Clearwater East and Clearwater West impact structures: the view from osmium isotopes. *Geochimica et Cosmochimica Acta*, 235, 262-284.
- David, C., Menéndez, B., & Darot, M. (1999). Influence of stress-induced and thermal cracking on physical properties and microstructure of La Peyratte granite. *International Journal of Rock Mechanics and Mining Sciences*, 36(4), 433-448.
- De Carli, P., & Jamieson, J. (1959). Formation of an amorphous form of quartz under shock conditions. *The Journal of Chemical Physics*, 31(6), 1675-1676.
- De Carli, P., & Milton, D. (1965). Stishovite: Synthesis by shock wave. *Science*, 147(3654), 144-145.
- de Graaff, S., Kaskes, P., Déhais, T., Goderis, S., Debaille, V., Ross, C., Gulick, S., Feignon, J., Ferrière, L., & Koeberl, C. (2021). New insights into the formation and emplacement of impact melt rocks within the Chicxulub impact structure, following the 2016 IODP-ICDP Expedition 364. *GSA Bulletin*. 134 (1-2): 293–315.
- Debono, L. (2018). A Targeted Investigation of the Upper Contact Unit of the Sudbury Igneous Complex in the North Range, Sudbury Impact Structure, Canada. *Western University*, MSc thesis.
- Demidenko, Y. B. (1969). Vertical seismic profiling. *International Geology Review*, 11(7), 803-824.
- DESA, U. (2019). World Population Prospects 2019. *United Nations, Department of Economic and Social Affairs*.
- Dewhurst, D., & Siggins, A. (2006). Impact of fabric, microcracks and stress field on shale anisotropy. *Geophysical Journal International*, 165(1), 135-148.
- Dickmann, T., Hecht-Méndez, J., Krüger, D., Sapronova, A., Unterlaß, P., & Marcher, T. (2021). Towards the integration of smart techniques for tunnel seismic applications. *Geomechanics and Tunnelling*, 14(5), 609-615.
- Dietz, R. S. (1947). Meteorite Impact Suggested by the Orientation of Shatter-Cones at the Kentland, Indiana, Disturbance. *Science*, 105(2715), 42.

Digges, T., Rosenberg, S., & Geil, G. (1966). Heat treatment and properties of iron and steel. *The National Bureau of Standards*.

Ding, Y., Liu, Z., Qiu, C., & Shi, J. (2007). Metamaterial with simultaneously negative bulk modulus and mass density. *Physical review letters*, 99(9), 093904.

Dörfler, M., & Kenkmann, T. (2020). Central uplift collapse in acoustically fluidized granular targets: Insights from analog modeling. *Meteoritics & Planetary Science*, 55(2), 441-456.

Doukhan, J., & Trépiéd, L. (1985). Plastic deformation of quartz single crystals. *Bulletin de minéralogie*, 108(1), 97-123.

Dresen, G., & Guéguen, Y. (2004). Damage and rock physical properties. *International Geophysics Series.*, 89, 169-218.

Dunn, M., & Ledbetter, H. (1995). Poissons ratio of porous and microcracked solids - theory and application to oxide superconductors. *Journal of Materials Research*, 10(11), 2715-2722.

Eberli, G., Baechle, G., Anselmetti, F., & Incze, M. (2003). Factors controlling elastic properties in carbonate sediments and rocks. *The Leading Edge*, 22(7), 654-660.

Ebert, M., Poelchau, M., Kenkmann, T., & Schuster, B. (2020). Tracing shock-wave propagation in the Chicxulub crater: Implications for the formation of peak rings. *Geology*, 48(8), 814-818.

Eitel, M., Gilder, S., Spray, J., Thompson, L., & Pohl, J. (2016). A paleomagnetic and rock magnetic study of the Manicouagan impact structure: Implications for crater formation and geodynamo effects. *Journal of Geophysical Research: Solid Earth*, 121(2), 436-454.

Elbra, T., Kontny, A., Pesonen, L., Schleifer, N., & Schell, C. (2007). Petrophysical and paleomagnetic data of drill cores from the Bosumtwi impact structure, Ghana. *Meteoritics & Planetary Science*, 42(4-5), 829-838.

Engelhardt, W., Hörz, F., Stöffler, D., & Bertsch, W. (1968). Observations on quartz deformation in the breccias of West Clearwater Lake, Canada, and the Ries Basin, Germany. In *Shock metamorphism of natural materials*, (pp 475-482). *Mono Book Corporation*,

Engelhardt, W., & Bertsch, W. (1969). Shock induced planar deformation structures in quartz from the Ries crater, Germany. *Contributions to Mineralogy and Petrology*, 20(3), 203-234.

Englund, K., & Roen, J. (1963). Origin of the Middlesboro basin, Kentucky. *USGS Prof Pap*, 450, E20-E22.

Euler, L. (1980). The Rational Mechanics of Flexible Or Elastic Bodies 1638-1788: Introduction to Vol. X and XI. *Springer Science & Business Media*.

Falls, S., & Young, R. (1998). Acoustic emission and ultrasonic-velocity methods used to characterise the excavation disturbance associated with deep tunnels in hard rock. *Tectonophysics*, 289(1-3), 1-15.

Feignon, J., Ferrière, L., Leroux, H., & Koeberl, C. (2020). Characterization of shocked quartz grains from Chicxulub peak ring granites and shock pressure estimates. *Meteoritics & Planetary Science*, 55(10), 2206-2223.

Filiberto, J., & Schwenzer, S. (2018). Volatiles in the Martian Crust. *Elsevier*.

Flynn, G., Keller, L., Feser, M., Wirick, S., & Jacobsen, C. (2003). The origin of organic matter in the solar system: Evidence from the interplanetary dust particles. *Geochimica et Cosmochimica Acta*, 67(24), 4791-4806.

French, B. (2021). Remains of paleoflora in the breccias of the Onaping formation, Sudbury Impact Structure, Ontario, Canada. *Geological Journal*, (1), 17-31.

French, B. (1998). Traces of catastrophe: A handbook of shock-metamorphic effects in terrestrial meteorite impact structures. *Lunar and Planetary Institute*.

French, B., & Koeberl, C. (2010). The convincing identification of terrestrial meteorite impact structures: What works, what doesn't, and why. *Earth-Science Reviews*, 98(1-2), 123-170.

French, R., & Hokett, S. (1998). Evaluation of Recharge Potential at Crater U5a (WISHBONE). *U.S. Department of Commerce National Technical Information Service*.

Gal'perin, E. (1974). Vertical seismic profiling (Vol. 12). *Society of exploration geophysicists*.

Ganley, D. (1981). A method for calculating synthetic seismograms which include the effects of absorption and dispersion. *Geophysics*, 46(8), 1100-1107.

Gardner, G., Wyllie, M., & Droschak, D. (1965). Hysteresis in the velocity-pressure characteristics of rocks. *Geophysics*, 30(1), 111-116.

Gassmann, F. (1951). Über die elastizität poroser medien. *Vierteljahrsschrift der Naturforschenden Gesellschaft in Zurich*, 96, 1-23.

Gattacceca, J., Zylberman, W., Coulter, A., Demory, F., Quesnel, Y., Rochette, P., Osinski, G., & Edwige, B. (2019). Paleomagnetism and rock magnetism of East and West Clearwater Lake impact structures. *Canadian Journal of Earth Sciences*, 56(9), 983-993.

Ghasemi, S., Khamehchiyan, M., Taheri, A., Nikudel, M., & Zalooli, A. (2020). Crack evolution in damage stress thresholds in different minerals of granite rock. *Rock Mechanics and Rock Engineering*, 53(3), 1163-1178.

Gischler, E., & Lomando, A. (1999). Recent sedimentary facies of isolated carbonate platforms, Belize-Yucatan system, Central America. *Journal of Sedimentary Research*, 69(3), 747-763.

Glombick, P., Schmitt, D., Xie, W., Bown, T., Hathway, B., & Banks, C. (2014). The Bow City structure, southern Alberta, Canada: The deep roots of a complex impact structure? *Meteoritics & Planetary Science*, 49(5), 872-895.

Goderis, S. (2019). The final settling of meteoritic matter on the peak-ring of the Chicxulub impact structure at Site M0077 of IODP-ICDP Expedition 364. *Large Meteorite Impacts and Planetary Evolution IV*, 2136, 1 – 2.

Goderis, S., Sato, H., Ferrière, L., Schmitz, B., Burney, D., Kaskes, P., Vellekoop, J., Wittmann, A., Schulz, T., & Chernozhkin, S. (2021). Globally distributed iridium layer preserved within the Chicxulub impact structure. *Science advances*, 7(9), eabe3647.

Göllner, P., Wüstemann, T., Bendschneider, L., Reimers, S., Clark, M., Gibson, L., Lightfoot, P., & Riller, U. (2019). Thermo-mechanical interaction of a large impact melt sheet with adjacent target rock, Sudbury impact structure, Canada. *Meteoritics & Planetary Science*, 54(6), 1228-1245.

Golos, E., Fang, H., & van der Hilst, R. (2020). Variations in Seismic Wave Speed and VP/VS Ratio in the North American Lithosphere. *Journal of Geophysical Research: Solid Earth*, 125(12), e2020JB020574.

Goltrant, O., Leroux, H., Doukhan, J., & Cordier, P. (1992). Formation mechanisms of planar deformation features in naturally shocked quartz. *Physics of the Earth and Planetary Interiors*, 74(3-4), 219-240.

Grady, D., & Kipp, M. (1987). Dynamic rock fragmentation in B. K. Atkinson (Ed.), *Fracture Mechanics of Rock*. Academic Press, 429-475.



Grady, D. E., & Kipp, M. E. (1993). Dynamic Fracture and Fragmentation. In J. R. Asay & M. Shahinpoor (Eds.), *High-Pressure Shock Compression of Solids*, (pp 265-322). *Springer New York*.

Grieve, R., Robertson, P., & Dence, M. (1981). Constraints on the formation of ring impact structures, based on terrestrial data. Multi-ring basins: Formation and evolution, *Lunar and Planetary Science Conference*, (A82-39033 19-91), 37-57.

Grieve, R., Ames, D., Morgan, J., & Artemieva, N. (2010). The evolution of the Onaping Formation at the Sudbury impact structure. *Meteoritics & Planetary Science*, 45(5), 759-782.

Grieve, R., & Osinski, G. (2020). The Upper Contact Unit of the Sudbury Igneous Complex in the Garson region: Constraints on the depth of origin of a peak ring at the Sudbury impact structure. *Meteoritics & Planetary Science*, 55(8).

Griggs, D., & Blacic, J. (1965). Quartz: anomalous weakness of synthetic crystals. *Science*, 147(3655), 292-295.

Gudlaugsson, S. T. (1993). Large impact crater in the Barents Sea. *Geology*, 21(4), 291-294.

Guerin, G., & Goldberg, D. (1996). Acoustic and elastic properties of calcareous sediments across a siliceous diagenetic front on the eastern US continental slope. *Geophysical Research Letters*, 23(19), 2697-2700.

Güldemeister, N., Wünnemann, K., & Poelchau, M. (2015). Scaling impact crater dimensions in cohesive rock by numerical modeling and laboratory experiments. *Geological Society of America Special Papers*, 518, 17-29.

Gulick, S., Christeson, G., Barton, P., Grieve, R., Morgan, J., & Urrutia-Fucugauchi, J. (2013). Geophysical characterization of the Chicxulub impact crater. *Reviews of Geophysics*, 51(1), 31-52.

Gulick, S., Morgan, J., Mellett, C. & the Expedition 364 Scientists, 2016. Expedition 364 Preliminary Report: Chicxulub: Drilling the K-Pg Impact Crater. *International Ocean Discovery Program*.

Gulick, S., Morgan, J., Mellett, C., Green, S., Bralower, T., Chenot, E., Christeson, G., Claeys, P., Cockell, C., Coolen, M., Ferrière, L., Gebhardt, C., Goto, K., Jones, H., Kring, D., Lofi, L., Lowery, C., Ocampo-Torres, R., Perez-Cruz, L., Pickersgill, A., Poelchau, M., Rae, A., Rasmussen, C., Rebolledo-Vieyra, M., Riller, U., Sato, H., Smit, J., Tikoo, S., Tomioka, N., Urrutia-Fucugauchi, J., Whalen, M., Wittmann, A., Yamaguchi, K., Xiao, L., & Zylberman, W. (2017a). Expedition 364 Methods. *Proceedings of the International Ocean Discovery Program, Issue. I. O. D. Program*.

Gulick, S., Morgan, J., Mellett, C., Green, S., Bralower, T., Chenot, E., Christeson, G., Claeys, P., Cockell, C., Coolen, M., Ferrière, L., Gebhardt, C., Goto, K., Jones, H., Kring, D., Lofi, L., Lowery, C., Ocampo-Torres, R., Perez-Cruz, L., Pickersgill, A., Poelchau, M., Rae, A., Rasmussen, C., Rebolledo-Vieyra, M., Riller, U., Sato, H., Smit, J., Tikoo, S., Tomioka, N., Urrutia-Fucugauchi, J., Whalen,

M., Wittmann, A., Yamaguchi, K., Xiao, L., & Zylberman, W. (2017b). Site M0077: Lower Peak Ring. *Proceedings of the International Ocean Discovery Program, Issue. I. O. D. Program.*

Gulick, S., Morgan, J., Mellett, C., Green, S., Bralower, T., Chenot, E., Christeson, G., Claeys, P., Cockell, C., Coolen, M., Ferrière, L., Gebhardt, C., Goto, K., Jones, H., Kring, D., Lofi, L., Lowery, C., Ocampo-Torres, R., Perez-Cruz, L., Pickersgill, A., Poelchau, M., Rae, A., Rasmussen, C., Rebolledo-Vieyra, M., Riller, U., Sato, H., Smit, J., Tikoo, S., Tomioka, N., Urrutia-Fucugauchi, J., Whalen, M., Wittmann, A., Yamaguchi, K., Xiao, L., & Zylberman, W. (2017c). Site M0077: Post-Impact Sedimentary Rocks. *Proceedings of the International Ocean Discovery Program, Issue. I. O. D. Program.*

Gulick, S., Morgan, J., Mellett, C., Green, S., Bralower, T., Chenot, E., Christeson, G., Claeys, P., Cockell, C., Coolen, M., Ferrière, L., Gebhardt, C., Goto, K., Jones, H., Kring, D., Lofi, L., Lowery, C., Ocampo-Torres, R., Perez-Cruz, L., Pickersgill, A., Poelchau, M., Rae, A., Rasmussen, C., Rebolledo-Vieyra, M., Riller, U., Sato, H., Smit, J., Tikoo, S., Tomioka, N., Urrutia-Fucugauchi, J., Whalen, M., Wittmann, A., Yamaguchi, K., Xiao, L., & Zylberman, W. (2017d). Site M0077: Upper Peak Ring. *Proceedings of the International Ocean Discovery Program, Issue. I. O. D. Program.*

Gulick, S., Barton, P., Christeson, G., Morgan, J., McDonald, M., Mendoza-Cervantes, K., Pearson, Z., Surendra, A., Urrutia-Fucugauchi, J., & Vermeesch, P. (2008). Importance of pre-impact crustal structure for the asymmetry of the Chicxulub impact crater. *Nature Geoscience*, 1(2), 131-135.

Gulick, S., Bralower, T., Ormö, J., Hall, B., Grice, K., Schaefer, B., Lyons, S., Freeman, K., Morgan, J., & Artemieva, N. (2019). The first day of the Cenozoic. *Proceedings of the National Academy of Sciences*, 116(39), 19342-19351.

Gulley, A., Kaipio, J., Eccles, J., & Malin, P. (2017). A numerical approach for modelling fault-zone trapped waves. *Geophysical Journal International*, 210(2), 919-930.

Guyer, R., & Johnson, P. (1999). Nonlinear mesoscopic elasticity: Evidence for a new class of materials. *Physics today*, 52(4), 30-36.

Hamilton, E. (1979). Vp-Vs and poisson ratios in marine-sediments and rocks. *Journal of the Acoustical Society of America*, 66(4), 1093-1101.

Hardage, B. (1981). An examination of tube wave noise in vertical seismic profiling data. *Geophysics*, 46(6), 892-903.

Hardage, B. (1985). Vertical seismic profiling (Vol. 14). *Geophysical Press London.*

Harris, F. (1978). On the use of windows for harmonic analysis with the discrete Fourier transform. *Proceedings of the IEEE*, 66(1), 51-83.

- Hashin, Z., & Shtrikman, S. (1962). On some variational principles in anisotropic and nonhomogeneous elasticity. *Journal of the Mechanics and Physics of Solids*, 10(4), 335-342.
- Hauri, E., Saal, A., Rutherford, M., & Van Orman, J. (2015). Water in the Moon's interior: Truth and consequences. *Earth and Planetary Science Letters*, 409, 252-264.
- Hawkins, W., & Wohletz, K. (1997). Visual inspection for CTBT Verification. *Office of Scientific & Technical Information Technical Reports*.
- Hayatsu, R., Matsuoka, S., Scott, R., Studier, M., & Anders, E. (1977). Origin of organic matter in the early solar system—VII. The organic polymer in carbonaceous chondrites. *Geochimica et Cosmochimica Acta*, 41(9), 1325-1339.
- He, T., & Schmitt, D. (2006). P- and S-wave velocity measurement and pressure sensitivity analysis of AVA response. *Physics*.
- Head, J. (2010). Transition from complex craters to multi-ringed basins on terrestrial planetary bodies: Scale-dependent role of the expanding melt cavity and progressive interaction with the displaced zone. *Geophysical Research Letters*, 37(2).
- Heap, M., Gilg, H., Byrne, P., Wadsworth, F., & Reuschle, T. (2020). Petrophysical properties, mechanical behaviour, and failure modes of impact melt-bearing breccia (suevite) from the Ries impact crater (Germany). *Icarus*, 349, 16, Article Unsp 113873.
- Heiken, G., Vaniman, D., & French, B. (1991). Lunar Sourcebook, a user's guide to the Moon. *Lunar and Planetary Institute*.
- Hilbert, M., & López, P. (2011). The world's technological capacity to store, communicate, and compute information. *Science*, 332(6025), 60-65.
- Hildebrand, A., Pilkington, M., Ortiz-Aleman, C., Chavez, R., Urrutia-Fucugauchi, J., Connors, M., Ganiell-Castro, E., Camara-Zi, A., Halpenny, J., & Niehaus, D. (1998). Mapping Chicxulub crater structure with gravity and seismic reflection data. *Geological Society, London, Special Publications*, 140(1), 155-176.
- Hildebrand, A., & Stansberry, J. (1992). K/T boundary ejecta distribution predicts size and location of Chicxulub crater. *Lunar and Planetary Science Conference*.
- Hildebrand, A., Penfield, G., Kring, D., Pilkington, M., Camargo Z., Jacobsen, S., & Boynton, W. (1991). Chicxulub crater: a possible Cretaceous/Tertiary boundary impact crater on the Yucatan Peninsula, Mexico. *Geology*, 19(9), 867-871.
- Hill, R. (1952). The elastic behaviour of a crystalline aggregate. *Proceedings of the Physical Society. Section A*, 65(5), 349.

Hilpert, M., Jirka, G., & Plate, E. (2000). Capillarity-induced resonance of oil blobs in capillary tubes and porous media. *Geophysics*, 65(3), 874-883.

Hinds, R., Anderson, N., & Kuzmiski, R. (1996). VSP interpretive processing: Theory and practice. *Society of Exploration Geophysicists*.

Honniball, C., Lucey, P., Li, S., Shenoy, S., Orlando, T., Hibbitts, C., Hurley, D., & Farrell, W. (2021). Molecular water detected on the sunlit Moon by SOFIA. *Nature Astronomy*, 5(2), 121-127.

Hooke, R. (1678). De potentia restitutiva, or of spring explaining the power of springing bodies, vol. 1678. London, UK: *John Martyn*, 23.

Hu, X., Song, X., Liu, Y., Cheng, Z., Ji, J., & Shen, Z. (2019). Experiment investigation of granite damage under the high-temperature and high-pressure supercritical water condition. *Journal of Petroleum Science and Engineering*, 180, 289-297.

Huber, M., & Koeberl, C. (2017). Accretionary lapilli from the Sudbury impact event. *Meteoritics & Planetary Science*, 52(6), 1257-1276.

Hunze, S., & Wonik, T. (2007). Lithological and structural characteristics of the Lake Bosumtwi impact crater, Ghana: Interpretation of acoustic televiwer images. *Meteoritics & Planetary Science*, 42, 779-792.

Indares, A., & Dunning, G. (2018). Metamorphic Evolution of the central Grenville Province (Manicouagan area): a review. *Government of Quebec Report MM2017-01*, 20.

Ireland, M., Goultly, N., & Davies, R. (2010). Influence of pore water chemistry on silica diagenesis: evidence from the interaction of diagenetic reaction zones with polygonal fault systems. *Journal of the Geological Society*, 167(2), 273-279.

Ishii, E., Sanada, H., Iwatsuki, T., Sugita, Y., & Kurikami, H. (2011). Mechanical strength of the transition zone at the boundary between opal-A and opal-CT zones in siliceous rocks. *Engineering Geology*, 122(3-4), 215-221.

Ivanov, B., & Kostuchenko, V. (1997). Block oscillation model for impact crater collapse. *Lunar and Planetary Science Conference*.

Ivanov, B., Deniem, D., & Neukum, G. (1997). Implementation of dynamic strength models into 2D hydrocodes: Applications for atmospheric breakup and impact cratering. *International Journal of Impact Engineering*, 20(1-5), 411-430.

- Japsen, P. (1998). Regional velocity-depth anomalies, North Sea Chalk: a record of overpressure and Neogene uplift and erosion. *AAPG bulletin*, 82(11), 2031-2074.
- Jiang, H., Zhang, J., & Jiang, R. (2017). Stress evaluation for rocks and structural concrete members through ultrasonic wave analysis. *Journal of Materials in Civil Engineering*, 29(10), 04017172.
- Johnson, B., Milliken, R., Lewis, K., & Collins, G. (2021). Impact generated porosity in Gale crater and implications for the density of sedimentary rocks in lower Aeolis Mons. *Icarus*, 366, 114539.
- Johnson, D. (1986). Recent developments in the acoustic properties of porous media. *Frontiers in Physical Acoustics*, 93(1984), 255-290.
- Johnston, D., Toksöz, M., & Timur, A. (1979). Attenuation of seismic waves in dry and saturated rocks: II. Mechanisms. *Geophysics*, 44(4), 691-711.
- Jolly, R. (1953). Deep-hole geophone study in Garvin County, Oklahoma. *Geophysics*, 18(3), 662-670.
- Juhlin, C., & Pedersen, L. (1987). Reflection seismic investigations of the Siljan impact structure, Sweden. *Journal of Geophysical Research: Solid Earth*, 92(B13), 14113-14122.
- Kanasewich, E. R. (1974). Time Series Analysis in Geophysics. *University of Alberta Press*.
- Kanbur, Z., Louie, J., Chávez-Pérez, S., Plank, G., & Morey, D. (2000). Seismic reflection study of Upheaval Dome, Canyonlands National Park, Utah. *Journal of Geophysical Research: Planets*, 105(E4), 9489-9505.
- Karakostas, F., Schmerr, N., Maquire, R., Kim, D., Huang, Q., Kawamura, T., Ondera, K., Longonne, P., Giardini, D., & Banerdt, W. B. (2020). DI024-0010 - S-coda wave analysis of InSight seismic data to determine the scattering and intrinsic attenuation in the crust of Mars. *AGU Fall Meeting*. Online.
- Karp, T., Milkereit, B., Janle, P., Danour, S., Pohl, J., Berckhemer, H., & Scholz, C. (2002). Seismic investigation of the Lake Bosumtwi impact crater: preliminary results. *Planetary and Space Science*, 50(7-8), 735-743.
- Kaskes, P., De Graaff, S., Déhais, T., Goderis, S., Feignon, J., Ferrière, L., Koeberl, C., Smit, J., & Claeys, P. (2019). Geochemical and petrographic characterization of the suevite sequence within the IODP-ICDP Exp. 364 core of the Chicxulub peak ring. *Large Meteorite Impacts and Planetary Evolution VI: Lunar and Planetary Institute*, 2136, 5085.

Kaskes, P., de Graaff, S., Feignon, J., Déhais, T., Goderis, S., Ferrière, L., Koeberl, C., Smit, J., Wittmann, A., & Gulick, S. (2021). Formation of the crater suevite sequence from the Chicxulub peak ring: A petrographic, geochemical, and sedimentological characterization. *GSA Bulletin*.

Kawohl, A., Whymark, W., VanderWal, J., Whymark, W., Hall, M., Bite, A., & Frimmel, H. (2021). Impactites East Of The Sudbury Igneous Complex—A Reconnaissance Study. *Lunar and Planetary Science Conference*.

Keiswetter, D., Black, R., & Steeples, D. (1996). Seismic reflection analysis of the Manson impact structure, Iowa. *Journal of Geophysical Research: Solid Earth*, 101(B3), 5823-5834.

Kenkmann, T., Deutsch, A., Thoma, K., Ebert, M., Poelchau, M., Buhl, E., Carl, E., Danilewsky, A., Dresen, G., Dufresne, A., Durr, N., Ehm, L., Grosse, C., Gulde, M., Guldemeister, N., Hamann, C., Hecht, L., Hiermaier, S., Hoerth, T., Kowitz, A., Langenhorst, F., Lexow, B., Liermann, H., Luther, R., Mansfeld, U., Moser, D., Raith, M., Reimold, W., Sauer, M., Schafer, F., Schmitt, R., Sommer, F., Wilk, J., Winkler, R., & Wunnemann, K. (2018). Experimental impact cratering: A summary of the major results of the MEMIN research unit. *Meteoritics & Planetary Science*, 53(8), 1543-1568.

Kenkmann, T., Poelchau, M., & Wulf, G. (2014). Structural geology of impact craters. *Journal of Structural Geology*, 62, 156-182.

Kennett, B. (1974). Reflections, Rays, And Reverberations. *Bulletin of the Seismological Society of America*, 64(6), 1685-1696.

Kieffer, S., & Simonds, C. (1980). The role of volatiles and lithology in the impact cratering process. *Reviews of Geophysics*, 18(1), 143-181.

King, D. (2019). The impact-generated hydrothermal system of the East Clearwater Lake impact structure, Quebec, Canada. *Western University*, MSc thesis.

King, D., & Petruny, L. (2003). Application of stratigraphic nomenclature to terrestrial impact-derived and impact-related materials. In *Impact markers in the stratigraphic record*, Springer. 41-64.

Kneib, G. (1995). The statistical nature of the upper continental crystalline crust derived from in situ seismic measurements. *Geophysical Journal International*, 122(2), 594-616.

Koeberl, C. (1993). Chicxulub crater, Yucatan: tektites, impact glasses, and the geochemistry of target rocks and breccias. *Geology*, 21(3), 211-214.

Koeberl, C., Milkereit, B., Overpeck, J., Scholz, C., Amoako, P., Boamah, D., Danuor, S., Karp, T., Kueck, J., & Hecky, R. (2007). An international and multidisciplinary drilling project into a young complex impact structure: The 2004 ICDP Bosumtwi Crater Drilling Project—An overview. *Meteoritics & Planetary Science*, 42(4-5), 483-511.

Kommedal, J., & Tjøstheim, B. (1989). A Study of Different Methods of Wavefield Separation for Application to VSP Data 1. *Geophysical Prospecting*, 37(2), 117-142.

Kovach, R., & Watkins, J. (1973). Apollo 17 seismic profiling - probing lunar crust. *Science*, 180(4090), 1063-1064.

Kring, D., Hildebrand, A., & Boynton, W. (1991). The Petrology of an Andestic Melt Rock and a Polymict Breccia from the Interior of the Chicxulub Structure, Yucatan, Mexico. *Lunar and Planetary Science Conference*.

Kring, D. (2005). Hypervelocity collisions into continental crust composed of sediments and an underlying crystalline basement: Comparing the Ries (~ 24 km) and Chicxulub (~ 180 km) impact craters. *Geochemistry*, 65(1), 1-46.

Kring, D., & Bach, W. (2021). Hydrogen Production from Alteration of Chicxulub Crater Impact Breccias: Potential Energy Source for a Subsurface Microbial Ecosystem. *Astrobiology*, 21(12), 1547-1564

Kring, D., Claeys, P., Gulick, S., Morgan, J., & Collins, G. (2017). Chicxulub and the exploration of large peak-ring impact craters through scientific drilling. *GSA Today*, 27(10), 4-8.

Kring, D., Tikoo, S., Schmieder, M., Riller, U., Rebolledo-Vieyra, M., Simpson, S., Osinski, G., Gattacceca, J., Wittmann, A., Verhagen, C., Cockell, C., Coolen, M., Longstaffe, F., Gulick, S., Morgan, J., Bralower, T., Chenot, E., Christeson, G., Claeys, P., Ferriere, L., Gebhardt, C., Goto, K., Green, S., Jones, H., Lofi, J., Lowery, C., Ocampo-Torres, R., Perez-Cruz, L., Pickersgill, A., Poelchau, M., Rae, A., Rasmussen, C., Sato, H., Smit, J., Tomioka, N., Urrutia-Fucugauchi, J., Whalen, M., Xiao, L., & Yamaguchi, K. (2020). Probing the hydrothermal system of the Chicxulub impact crater. *Science advances*, 6(22), 9.

Kring, D., Whitehouse, M., & Schmieder, M. (2021). Microbial sulfur isotope fractionation in the Chicxulub hydrothermal system. *Astrobiology*, 21(1), 103-114.

Krogh, T., Kamo, S., Sharpton, V., Marin, L., & Hildebrands, A. (1993). U–Pb ages of single shocked zircons linking distal K/T ejecta to the Chicxulub crater. *Nature*, 366(6457), 731-734.

Kusaba, K., Syono, Y., Kikuchi, M., & Fukuoka, K. (1985). Shock behavior of zircon: Phase transition to scheelite structure and decomposition. *Earth and Planetary Science Letters*, 72(4), 433-439.

Kuster, G., & Toksöz, M. (1974). Velocity and attenuation of seismic waves in two-phase media: Part I. Theoretical formulations. *Geophysics*, 39(5), 587-606.

Labo, J. (1987). Borehole Geophysics Techniques and Application. In A Practical Introduction to Borehole Geophysics: An Overview of Wireline Well Logging Principles for Geophysicists. *Society of Exploration Geophysicists*, 1-12.

Lafrance, B., Legault, D., & Ames, D. (2008). The formation of the Sudbury breccia in the North Range of the Sudbury impact structure. *Precambrian Research*, 165(3-4), 107-119.

Lakes, R. (2017). Negative-Poisson's-ratio materials: auxetic solids. *Annual review of materials research*, 47, 63-81.

Lamé, G. (1852). Leçons sur la théorie mathématique de l'élasticité des corps solides. *Bachelier*.

Lamontagne, M., Keating, P., & Toutin, T. (2000). Complex faulting confounds earthquake research in the Charlevoix Seismic Zone, Québec. *Eos, Transactions American Geophysical Union*, 81(26), 289-293.

Langenhorst, F., & Deutsch, A. (1993). Orientation of planar deformation features (PDFs) in quartz. *Lunar and Planetary Science Conference*.

Langenhorst, F., & Deutsch, A. (1994). Shock experiments on pre-heated  $\alpha$ - and  $\beta$ -quartz: I. Optical and density data. *Earth and Planetary Science Letters*, 125(1-4), 407-420.

Langenhorst, F., Deutsch, A., Stoeffler, D., & Hornemann, U. (1992). Effect of temperature on shock metamorphism of single-crystal quartz. *Nature*, 356(6369), 507-509.

Lasue, J., Clifford, S., Conway, S., Mangold, N., & Butcher, F. (2019). Chapter 7 - The Hydrology of Mars Including a Potential Cryosphere. In J. Filiberto & S. P. Schwenzer (Eds.), *Volatiles in the Martian Crust*, (pp 185-246). *Elsevier*,

Latham, G., Ewing, M., Press, F., Sutton, G., Dorman, J., Nakamura, Y., Toksoz, N., Wiggins, R., Derr, J., & Duennebi, F. (1970). Passive Seismic Experiment. *Science*, 167(3918), 455-457.

Learner, R., Thorne, A., & Brault, J. (1996). Ghosts and artifacts in Fourier-transform spectrometry. *Applied optics*, 35(16), 2947-2954.

Lee, D., Halliday, A., Snyder, G., & Taylor, L. (1997). Age and origin of the Moon. *Science*, 278(5340), 1098-1103.



- Lee, M., & Balch, A. (1983). Computer processing of vertical seismic profile data. *Geophysics*, 48(3), 272-287.
- Lefticariu, M., Perry, E., Ward, W., & Lefticariu, L. (2006). Post-Chicxulub depositional and diagenetic history of the northwestern Yucatan Peninsula, Mexico. *Sedimentary Geology*, 183(1-2), 51-69.
- Lemieux, Y., Tremblay, A., & Lavoie, D. (2003). Structural analysis of supracrustal faults in the Charlevoix area, Quebec: relation to impact cratering and the St-Laurent fault system. *Canadian Journal of Earth Sciences*, 40(2), 221-235.
- Lenormand, R., Zarcone, C., & Sarr, A. (1983). Mechanisms of the displacement of one fluid by another in a network of capillary ducts. *Journal of Fluid Mechanics*, 135, 337-353.
- Leroux, H., Reimold, W., Koeberl, C., Hornemann, U., & Doukhan, J. (1999). Experimental shock deformation in zircon: A transmission electron microscopic study. *Earth and Planetary Science Letters*, 169(3-4), 291-301.
- Levin, F., & Lynn, R. (1958). Deep-hole geophone studies. *Geophysics*, 23(4), 639-664.
- Lewis, K., Peters, S., Gonter, K., Morrison, S., Schmerr, N., Vasavada, A., & Gabriel, T. (2019). A surface gravity traverse on Mars indicates low bedrock density at Gale crater. *Science*, 363(6426), 535-537.
- Li, H., Dong, Z., Yang, Y., Liu, B., Chen, M., & Jing, W. (2018). Experimental study of damage development in salt rock under uniaxial stress using ultrasonic velocity and acoustic emissions. *Applied Sciences*, 8(4), 553.
- Li, M., & Zhao, Y. (2014). Chapter 7 - Prestack Seismic Inversion and Seismic Attribute Analysis. In M. Li & Y. Zhao (Eds.), *Geophysical Exploration Technology*, Elsevier, 199-219.
- Liu, C., & Ahrens, T. (1997). Stress wave attenuation in shock-damaged rock. *Journal of Geophysical Research-Solid Earth*, 102(B3), 5243-5250.
- Liu, L., Ji, H., Elsworth, D., Zhi, S., Lv, X., & Wang, T. (2020). Dual-damage constitutive model to define thermal damage in rock. *International Journal of Rock Mechanics and Mining Sciences*, 126, 104185.
- Liu, Z., & Sun, S. (2015). The differential Kuster–Toksöz rock physics model for predicting S-wave velocity. *Journal of geophysics and engineering*, 12(5), 839-848.

Lofi, J., Smith, D., Delahunty, C., Le Ber, E., Brun, L., Henry, G., Paris, J., Tikoo, S., Zylberman, W., Pezard, P., Celerier, B., Schmitt, D., Nixon, C., & the Expedition 364 Scientists, (2018). Drilling-induced and logging-related features illustrated from IODP-ICDP Expedition 364 downhole logs and borehole imaging tools. *Scientific Drilling*, 24, 1-13.

Lognonne, P., Banerdt, W., Pike, W., Giardini, D., Christensen, U., Garcia, R., Kawamura, T., Kedar, S., Knapmeyer-Endrun, B., Margerin, L., Nimmo, F., Panning, M., Tauzin, B., Scholz, J., Antonangeli, D., Barkaoui, S., Beucler, E., Bissig, F., Brinkman, N., Calvet, M., Ceylan, S., Charalambous, C., Davis, P., van Driel, M., Drilleau, M., Fayon, L., Joshi, R., Kenda, B., Khan, A., Knapmeyer, M., Lekic, V., McClean, J., Mimoun, D., Murdoch, N., Pan, L., Perrin, C., Pinot, B., Pou, L., Menina, S., Rodriguez, S., Schmelzbach, C., Schmerr, N., Sollberger, D., Spiga, A., Stahler, S., Stott, A., Stutzmann, E., Tharimena, S., Widmer-Schmidrig, R., Andersson, F., Ansan, V., Beghein, C., Bose, M., Bozdog, E., Clinton, J., Daubar, I., Delage, P., Fuji, N., Golombek, M., Grott, M., Horleston, A., Hurst, K., Irving, J., Jacob, A., Knollenberg, J., Krasner, S., Krause, C., Lorenz, R., Michaut, C., Myhill, R., Nissen-Meyer, T., ten Pierick, J., Plesa, A. C., Quantin-Nataf, C., Robertsson, J., Rochas, L., Schimmel, M., Smrekar, S., Spohn, T., Teanby, N., Tromp, J., Vallade, J., Verdier, N., Vrettos, C., Weber, R., Banfield, D., Barrett, E., Bierwirth, M., Calcutt, S., Compaire, N., Johnson, C., Mance, D., Euchner, F., Kerjean, L., Mainsant, G., Mocquet, A., Manfredi, J., Pont, G., Laudet, P., Nebut, T., de Raucourt, S., Robert, O., Russell, C., Sylvestre-Baron, A., Tillier, S., Warren, T., Wiczorek, M., Yana, C., & Zweifel, P. (2020). Constraints on the shallow elastic and anelastic structure of Mars from InSight seismic data. *Nature Geoscience*, 13(3), 213-220.

Long, A., & Ascent, D. (2020). World Economic Outlook. *International Monetary Fund*.

Lopez Ramos, E. (1975). Geological Summary of the Yucatan Peninsula. In A. E. M. Nairn & F. G. Stehli (Eds.), *The Gulf of Mexico and the Caribbean*. *Springer US*, 257-282.

Lowell, S., Shields, J., Thomas, M., & Thommes, M. (2012). Characterization of porous solids and powders: surface area, pore size and density, (Vol. 16). *Springer Science & Business Media*.

Lowery, C., Bralower, T., Owens, J., Rodríguez-Tovar, F., Jones, H., Smit, J., Whalen, M., Claeys, P., Farley, K., & Gulick, S. (2018). Rapid recovery of life at ground zero of the end-Cretaceous mass extinction. *Nature*, 558(7709), 288-291.

Lowery, C., Morgan, J., Gulick, S., Bralower, T., & Christeson, G. (2019). Ocean drilling perspectives on meteorite impacts. *Oceanography*, 32(1), 120-134.

Lyons, S., Karp, A., Bralower, T., Grice, K., Schaefer, B., Gulick, S., Morgan, J., & Freeman, K. (2020). Organic matter from the Chicxulub crater exacerbated the K-Pg impact winter. *Proceedings of the National Academy of Sciences*, 117(41), 25327-25334.

Mackenzie, G., Maguire, P., Denton, P., Morgan, J., & Warner, M. (2001). Shallow seismic velocity structure of the Chicxulub impact crater from modelling of Rg dispersion using a genetic algorithm. *Tectonophysics*, 338(2), 97-112.

Mallick, S., & Frazer, L. (1988). Rapid computation of multioffset vertical seismic profile synthetic seismograms for layered media. *Geophysics*, 53(4), 479-491.

Malvern, L. (1969). Introduction to the Mechanics of a Continuous Medium. *Prentice-Hall*.

Martínez-Martínez, J., Fusi, N., Galiana-Merino, J., Benavente, D., & Crosta, G. (2016). Ultrasonic and X-ray computed tomography characterization of progressive fracture damage in low-porous carbonate rocks. *Engineering Geology*, 200, 47-57.

Marton, G., & Buffler, R. (1994). Jurassic reconstruction of the Gulf of Mexico Basin. *International Geology Review*, 36(6), 545-586.

Mayr, S., Burkhardt, H., Popov, Y., & Wittmann, A. (2008). Estimation of hydraulic permeability considering the micro morphology of rocks of the borehole YAXCOPOIL-1 (Impact crater Chicxulub, Mexico). *International Journal of Earth Sciences*, 97(2), 385-399.

Mayr, S., Wittmann, A., Burkhardt, H., Popov, Y., Romushkevich, R., Bayuk, I., Heidinger, P., & Wilhelm, H. (2008). Integrated interpretation of physical properties of rocks of the borehole Yaxcopoil-1 (Chicxulub impact structure). *Journal of Geophysical Research*, 113(B7).

McCall, N., Gulick, S., Hall, B., Rae, A., Poelchau, M., Riller, U., Lofi, J., & Morgan, J. (2021). Orientations of planar cataclastic zones in the Chicxulub peak ring as a ground truth for peak ring formation models. *Earth and Planetary Science Letters*, 576, 117236.

McIntyre, D. (1962). Impact metamorphism at Clearwater lake, Quebec. *Journal of Geophysical Research*, 67, 1647.

McLaren, A., Retchford, J., Griggs, D., & Christie, J. (1967). Transmission electron microscope study of Brazil Twins and dislocations experimentally produced in natural quartz. *Physica Status Solidi (b)*, 19(2), 631-644.

Meadows, D., & Davies, R. (2009). Predicting porosity reduction due to silica diagenesis using seismic reflection data. *Marine and Petroleum Geology*, 26(8), 1543-1553.

Means, W. (1976). Hookean Behavior. In *Stress and Strain*, (pp. 240-253). *Springer*.

Meillieux, D. (2009). Wellbore Seismic and Core Sample Measurement Analysis: Integrated Geophysical Study of The Lake Bosumtwi Impact Structure. *University of Alberta*, MSc thesis.

Meister, R., Robertson, E., Werre, R., & Raspet, R. (1980). Elastic-Moduli Of Rock Glasses Under Pressure To 8-Kilobars And Geophysical Implications. *Journal of Geophysical Research*, 85(NB11), 6461-6470.

Melosh, H., & Gaffney, E. (1983). Acoustic fluidization and the scale dependence of impact crater morphology. *Journal of Geophysical Research: Solid Earth*, 88(S02), A830-A834.

Melosh, H. (1989). *Impact cratering: A geologic process*. New York: Oxford University Press.

Melosh, H., Ryan, E., & Asphaug, E. (1992). Dynamic Fragmentation In Impacts - Hydrocode Simulation Of Laboratory Impacts. *Journal of Geophysical Research-Planets*, 97(E9), 14735-14759.

Michel, P., & Morbidelli, A. (2007). Review of the population of impactors and the impact cratering rate in the inner solar system. *Meteoritics & Planetary Science*, 42(11), 1861-1869.

Molnár, F., Watkinson, D., & Everest, J. (1999). Fluid-inclusion characteristics of hydrothermal Cu–Ni–PGE veins in granitic and metavolcanic rocks at the contact of the Little Stobie deposit, Sudbury, Canada. *Chemical Geology*, 154(1-4), 279-301.

Molyneux, J., & Schmitt, D. (2000). Compressional-wave velocities in attenuating media: A laboratory physical model study. *Geophysics*, 65(4), 1162-1167.

Monroy-Rios, E., & Beddows, P. (2015). Hydrogeothermal Convective Circulation Model for the Formation of the Chicxulub Ring of Cenotes in the Yucatan Peninsula, Mexico. *AGU Fall Meeting Abstracts*.

Montalbetti, J. & Kanasewich, E. (1970). Enhancement of Teleseismic Body Phases with a Polarization Filter. *Geophysical Journal International*, 21(2), 119-129.

Moore, B., Jaglinski, T., Stone, D., & Lakes, R. (2006). Negative incremental bulk modulus in foams. *Philosophical magazine letters*, 86(10), 651-659.

Moos, D., & Zoback, M. (1983). In situ studies of velocity in fractured crystalline rocks. *Journal of Geophysical Research*, 88(NB3), 2345-2358.

Moreno-Gómez, M., Martínez-Salvador, C., Moulahoum, A., Liedl, R., Stefan, C., & Pacheco, J. (2019). First Steps into an Integrated Karst Aquifer Vulnerability Approach (IKAV). Intrinsic Groundwater Vulnerability Analysis of the Yucatan Karst, Mexico. *Water*, 11(8), 1610.

Morgan, J., Gulick, S., Mellett, C., Green, S., & the Expedition 364 Scientists. (2017). Chicxulub: Drilling the K-Pg Impact Crater: Proceedings of the International Ocean Discovery Program, 364. *International Ocean Discovery Program*.

Morgan, J., Gulick, S., Mellett, C., Green, S., & the Expedition 364 Scientists. (2016). Chicxulub: Drilling the K-Pg Impact Crater *International Ocean Discovery Program*.

Morgan, J., & Warner, M. (1999). Chicxulub: The third dimension of a multi-ring impact basin. *Geology*, 27(5), 407-410.

Morgan, J., Warner, M., Brittan, J., Buffler, R., Camargo, A., Christeson, G., Denton, P., Hildebrand, A., Hobbs, R., & Macintyre, H. (1997). Size and morphology of the Chicxulub impact crater. *Nature*, 390(6659), 472-476.

Morgan, J., Warner, M., Collins, G., Grieve, R., Christeson, G., Gulick, S., & Barton, P. (2011). Full waveform tomographic images of the peak ring at the Chicxulub impact crater. *Journal of Geophysical Research: Solid Earth*, 116(B6).

Morgan, J., Warner, M., Collins, G., Melosh, H., & Christeson, G. (2000). Peak-ring formation in large impact craters: Geophysical constraints from Chicxulub. *Earth and Planetary Science Letters*, 183(3-4), 347-354.

Morgan, J., Gulick, S., Bralower, T., Chenot, E., Christeson, G., Claeys, P., Cockell, C., Collins, G., Coolen, M., Ferrière, L., Gebhardt, C., Goto, K., Jones, H., Kring, D., Le Ber, E., Lofi, J., Long, X., Lowery, C., Mellett, C., Ocampo-Torres, R., Osinski, G., Perez-Cruz, L., Pickersgill, A., Poelchau, M., Rae, A., Rasmussen, C., Rebolledo-Vieyra, M., Riller, U., Sato, H., Schmitt, D., Smit, J., Tikoo, S., Tomioka, N., Urrutia-Fucugauchi, J., Whalen, M., Wittmann, A., Yamaguchi, K., & Zylberman, W. (2016). The formation of peak rings in large impact craters. *Science*, 354(6314), 878.

Morgan, J., Warner, M., Collins, G., Melosh, H., & Christeson, G. (2000). Peak-ring formation in large impact craters: geophysical constraints from Chicxulub. *Earth and Planetary Science Letters*, 183(3-4), 347-354.

Moser, D., Poelchau, M. H., Stark, F., & Grosse, C. (2013, Jan). Application of nondestructive testing methods to study the damage zone underneath impact craters of MEMIN laboratory experiments [Article]. *Meteoritics & Planetary Science*, 48(1), 87-98. <https://doi.org/10.1111/maps.12000>

Moser, D., Cupelli, C., Barker, I., Flowers, R., Bowman, J., Wooden, J., & Hart, J. (2011). New zircon shock phenomena and their use for dating and reconstruction of large impact structures revealed by electron nanobeam (EBSD, CL, EDS) and isotopic U–Pb and (U–Th)/He analysis of the Vredefort dome. *Canadian Journal of Earth Sciences*, 48(2), 117-139.

Müller, T. M., Gurevich, B., & Lebedev, M. (2010). Seismic wave attenuation and dispersion resulting from wave-induced flow in porous rocks—A review. *Geophysics*, 75(5), 75A147-175A164.

Müller, W., & Défourneaux, M. (1968). Deformationsstrukturen in Quarz als Indikator für Stoßwellen: eine experimentelle Untersuchung an Quarzeinkristallen. *Zeitschrift für Geophysik*, 34, 483-504.

Müller, W., & Hornemann, U. (1969). Shock-induced planar deformation structures in experimentally shock-loaded olivines and in olivines from chondritic meteorites. *Earth and Planetary Science Letters*, 7(3), 251-264.

Newman, P., & Worthington, M. (1982). In-situ investigation of seismic body wave attenuation in heterogeneous media. *Geophysical Prospecting*, 30(4), 377-400.

Niessen, F., Gebhardt, A., Kopsch, C., & Wagner, B. (2007). Seismic investigation of the El'gygytgyn impact crater lake (Central Chukotka, NE Siberia): preliminary results. *Journal of Paleolimnology*, 37(1), 49-63.

Nixon, C. (2021a). Borehole Attenuation Processing Package. *UAL Dataverse*. <https://doi.org/doi:10.7939/DVN/JGPORP>

Nixon, C. (2021b). Kuster Toksoz modelling matlab code. *UAL Dataverse*. <https://doi.org/doi:10.7939/DVN/CSRLGE>

Nixon, C. (2021c). Matlab code for ultrasonic wavespeed analysis. *UAL Dataverse*. <https://doi.org/doi:10.7939/DVN/XCRNHN>

Nixon, C., Kofman, R., & Schmitt, D., (2021d). Replication Data for "Borehole Seismic Observations from the Chicxulub Impact Drilling: Implications for Seismic Reflectivity and Impact Damage". *UAL Dataverse*. <https://doi.org/doi:10.7939/DVN/D1YY4A>

Nixon, C., Kofman, R., Schmitt, D., Gulick, S., Christeson, G., Sastrup, S., Lofi, J., & Morgan, J. (2020). Assessment of Rock Damage Using Seismic Methods: Wave Speeds and Attenuation from Borehole Measurements in the Chicxulub Impact Structure. *54th US Rock Mechanics/Geomechanics Symposium*.

Nixon, C., Kofman, R., Schmitt, D., Lofi, J., Gulick, S., Christeson, G., Sastrup, S., & Morgan, J. (2017). High Resolution Vertical Seismic Profile from the Chicxulub IODP/ICDP Expedition 364 Borehole: Wave Speeds and Seismic Reflectivity. *AGU Fall Meeting Abstracts*.

Njiekak, G., & Schmitt, D. (2019). Effective Stress Coefficient for Seismic Velocities in Carbonate Rocks: Effects of Pore Characteristics and Fluid Types. *Pure and Applied Geophysics*, 176(4), 1467-1485.

Nobes, D., Murray, R., Kuramoto, S., Pisciotto, K., & Holler, P. (1992). Impact of silica diagenesis on physical property variations. *Proceedings of the Ocean Drilling Program, Scientific Results*.

O'Callaghan, J., Linnen, R., Lightfoot, P., & Osinski, G. (2017). Mineralogical And Geochemical Characteristics Of Sudbury Breccia Adjacent To Footwall Cu-Ni-PGE Sulfide Veins and Structures In The Creighton and Coleman Deposits. *The Canadian Mineralogist*, 55(5), 909-943.

O'Connell, R., & Budiansky, B. (1974). Seismic velocities in dry and saturated cracked solids. *Journal of Geophysical Research*, 79(35), 5412-5426.

O'Connell, R., & Budiansky, B. (1977). Viscoelastic properties of fluid-saturated cracked solids. *Journal of Geophysical Research*, 82(36), 5719-5735.

O'Keefe, J., & Ahrens, T. (1982). Cometary and meteorite swarm impact on planetary surfaces. *Journal of Geophysical Research: Solid Earth*, 87(B8), 6668-6680.

Okeefe, J., & Ahrens, T. (1993). Planetary Cratering Mechanics. *Journal of Geophysical Research-Planets*, 98(E9), 17011-17028.

Onwuemeka, J., Lui, Y., & Harrington, R. (2021). Crustal velocity variations and constraints on material properties in the Charlevoix Seismic Zone, eastern Canada. *Journal of Geophysical Review*.

Ormö, J., Gulick, S., Whalen, M., King Jr, D., Sturkell, E., & Morgan, J. (2021). Assessing event magnitude and target water depth for marine-target impacts: Ocean resurge deposits in the Chicxulub M0077A drill core compared. *Earth and Planetary Science Letters*, 564, 116915.

Osinski, G., Brunner, A., Collins, G., Cohen, B., Coulter, A., Elphic, R., Grieve, R., Hodges, K., Horne, A., & Kerrigan, M. (2015). Revisiting the West Clearwater Lake Impact Structure, Canada. *Lunar and Planetary Science Conference*.

Osinski, G., Grieve, R., Hill, P., Simpson, S., Cockell, C., Christeson, G., Ebert, M., Gulick, S., Melosh, H., & Riller, U. (2020). Explosive interaction of impact melt and seawater following the Chicxulub impact event. *Geology*, 48(2), 108-112.

Osinski, G., & Pierazzo, E. (2012). Impact cratering: Processes and products. *John Wiley & Sons*.

Ostertag, R. (1983). Shock experiments on feldspar crystals. *Journal of Geophysical Research: Solid Earth*, 88(S01), B364-B376.

Paillet, F., & Cheng, C. (1991). Acoustic Waves in Boreholes. *CRC Press*.

Pandit, B., & Tozer, D. (1970). Anomalous propagation of elastic energy within moon. *Nature*, 226(5243), 335.

Penfield, G. (1981). Definition of a major igneous zone in the central Yucatan platform with aeromagnetism and gravity. *Society of Exploration Geophysicists Annual Meeting*.

Phillips, R., Arvidson, R., Boyce, J., Campbell, D., Guest, J., Schaber, G., & Soderblom, L. (1991). Impact craters on Venus: Initial analysis from Magellan. *Science*, 252(5003), 288-297.

Phinney, W., Simonds, C., Cochran, A., & McGee, P. (1978a). Geology of the West Clearwater, Quebec Impact Structure, Part Iii: SEM Petrology of Very Fine-Grained Units. *Lunar and Planetary Science Conference*.

Phinney, W., Simonds, C., Cochran, A., & McGee, P. (1978b). West clearwater, Quebec impact structure, part II: petrology. *Lunar and Planetary Science Conference Proceedings*.

Pike, R. (1977). Size-dependence in the shape of fresh impact craters on the Moon. Impact and explosion cratering: Planetary and terrestrial implications. *Proceedings of the Symposium on Planetary Cratering Mechanics*.

Pilkington, M., & Grieve, R. (1992). The geophysical signature of terrestrial impact craters. *Reviews of Geophysics*, 30(2), 161-181.

Pilkington, M., Pesonen, L., Grieve, R., & Masaitis, V. (2002). Geophysics and petrophysics of the Popigai impact structure, Siberia. In *Impacts in Precambrian shields*. 87-107, Springer.

Poisson, S. (1838). *Traité de mécanique*. Société belge de librairie.

Pollack, J., Kasting, J., Richardson, S., & Poliakov, K. (1987). The case for a wet, warm climate on early Mars. *Icarus*, 71(2), 203-224.

Pope, K., Ocampo, A., & Duller, C. (1993). Surficial geology of the Chicxulub impact crater, Yucatan, Mexico. *Earth, Moon, and Planets*, 63(2), 93-104.

Pope, K., Ocampo, A., Kinsland, G., & Smith, R. (1996). Surface expression of the Chicxulub crater. *Geology*, 24(6), 527-530.

Popov, Y., Mayr, S., Romushkevich, R., Burkhardt, H., & Wilhelm, H. (2014). Comparison of petrophysical properties of impactites for four meteoritic impact structures. *Meteoritics & Planetary Science*, 49(5), 896-920.

Qingyun, D., Fei, L., Jianguo, Y., Zhiyong, X., & Rodriguez, J. (2018). Buried Impact Features on Mercury as Revealed by Gravity Data. *Journal of Geophysical Research: Planets*, 123(11), 3005-3019.



Rae, A., Collins, G., Grieve, R., Osinski, G., & Morgan, J. (2017). Complex crater formation: Insights from combining observations of shock pressure distribution with numerical models at the West Clearwater Lake impact structure. *Meteoritics & Planetary Science*, 52(7), 1330-1350.

Rae, A., Collins, G., Morgan, J., Salge, T., Christeson, G., Leung, J., Lofi, J., Gulick, S., Poelchau, M., Rillee, U., Gebhardt, C., Grieve, R., & Osinski, G. (2019). Impact-Induced Porosity and Microfracturing at the Chicxulub Impact Structure. *Journal of Geophysical Research-Planets*, 124(7), 1960-1978.

Rae, A., Collins, G., Poelchau, M., Riller, U., Davison, T., Grieve, R., Osinski, G., Morgan, J., Gulick, S., Morgan, J., Chenot, E., Christeson, G., Claeys, P., Cockell, C., Coolen, M., Ferriere, L., Gebhardt, C., Goto, K., Green, S., Jones, H., Kring, D., Lofi, J., Lowery, C., Ocampo-Torres, R., Perez-Cruz, L., Pickersgill, A., Poelchau, M., Rae, A., Rasmussen, C., Rebolledo-Vieyra, M., Riller, U., Sato, H., Smit, J., Tikoo, S., Tomioka, N., Urrutia-Fucugauchi, J., Whalen, M., Wittmann, A., Xiao, L., Yamaguchi, K., & the Expedition 364 Scientists, (2019). Stress-Strain Evolution During Peak-Ring Formation: A Case Study of the Chicxulub Impact Structure. *Journal of Geophysical Research-Planets*, 124(2), 396-417.

Raina, A., Chakraborty, A., Ramulu, M., & Jethwa, J. (2000). Rock mass damage from underground blasting, a literature review, and lab-and full scale tests to estimate crack depth by ultrasonic method. *Fragblast*, 4(2), 103-125.

Raiskila, S., Elbra, T., Öhman, T., & Pesonen, L. (2008). Petrophysical and palaeomagnetic studies of the Keurusselkä impact structure, central Finland. *Large Meteorite Impacts and Planetary Evolution IV*, 1423, 3056.

Raith, M., Ebert, M., Pinkert, K., & Grosse, C. U. (2018). Nondestructive imaging of hypervelocity impact-induced damage zones beneath laboratory-created craters by means of ultrasound travel-time tomography. *Meteoritics & Planetary Science*, 53(8), 1756-1772.

Ramos, E. (1975). Geological summary of the Yucatan Peninsula. In *The Gulf of Mexico and the Caribbean* (pp. 257-282). Springer.

Rasmussen, C., Stockli, D., Ross, C., Pickersgill, A., Gulick, S., Schmieder, M., Christeson, G., Wittmann, A., Kring, D., & Morgan, J. (2019). U-Pb memory behavior in Chicxulub's peak ring—Applying U-Pb depth profiling to shocked zircon. *Chemical Geology*, 525, 356-367.

Rebolledo-Vieyra, M., Marin, L., Trejo-García, A., & Sharpton, V. (2011). The Chicxulub Impact Crater and its Influence on the Regional Hydrogeology in Northwest Yucatan, Mexico. *Gulf of Mexico origin, waters, and biota*, 3, 279-290.

Reimold, W., Grieve, R., & Palme, H. (1981). Rb-Sr dating of the impact melt from East Clearwater, Quebec. *Contributions to Mineralogy and Petrology*, 76(1), 73-76.

Reimold, W., & Stöffler, D. (1978). Experimental shock metamorphism of dunite. *Lunar and Planetary Science Conference Proceedings*.

Rempe, M., Mitchell, T., Renner, J., Nippres, S., Ben-Zion, Y., & Rockwell, T. (2013). Damage and seismic velocity structure of pulverized rocks near the San Andreas Fault. *Journal of Geophysical Research-Solid Earth*, 118(6), 2813-2831.

Rempe, M., Mitchell, T., Renner, J., Smith, S., Bistacchi, A., & Di Toro, G. (2018). The Relationship Between Microfracture Damage and the Physical Properties of Fault-Related Rocks: The Gole Larghe Fault Zone, Italian Southern Alps. *Journal of Geophysical Research-Solid Earth*, 123(9), 7661-7687.

Reuß, A. (1929). Berechnung der fließgrenze von mischkristallen auf grund der plastizitätsbedingung für einkristalle. *ZAMM-Journal of Applied Mathematics and Mechanics/Zeitschrift für Angewandte Mathematik und Mechanik*, 9(1), 49-58.

Revil, A., Breton, M., Niu, Q., Wallin, E., Haskins, E., & Thomas, D. (2017). Induced polarization of volcanic rocks. 2. Influence of pore size and permeability. *Geophysical Journal International*, 208(2), 814-825.

Riller, U. (2005). Structural characteristics of the Sudbury impact structure, Canada: Impact-induced versus orogenic deformation—A review. *Meteoritics & Planetary Science*, 40(11), 1723-1740.

Riller, U., Poelchau, M., Rae, A., Schulte, F., Collins, G., Melosh, H., Grieve, R., Morgan, J., Gulick, S., Lofi, J., Diaw, A., McCall, N., Kring, D., Morgan, J., Gulick, S., Green, S., Lofi, J., Chenot, E., Christeson, G., Claeys, P., Cockell, C., Coolen, M., Ferrière, L., Gebhardt, C., Goto, K., Jones, H., Kring, D., Xiao, L., Lowery, C., Ocampo-Torres, R., Perez-Cruz, L., Pickersgill, A., Poelchau, M., Rae, A., Rasmussen, C., Rebolledo-Vieyra, M., Riller, U., Sato, H., Smit, J., Tikoo-Schantz, S., Tomioka, N., Whalen, M., Wittmann, A., Yamaguchi, K., Fucugauchi, J., Bralower, T., & the Expedition 364 Scientists, (2018). Rock fluidization during peak-ring formation of large impact structures. *Nature*, 562(7728), 511-518.

Robert, F. (2001). The origin of water on Earth. *Science*, 293(5532), 1056-1058.

Robertson, P. (1975a). Experimental shock metamorphism of maximum microcline. *Journal of Geophysical Research*, 80(14), 1903-1910.

Robertson, P. (1975b). Zones of shock metamorphism at the Charlevoix impact structure, Quebec. *Geological Society of America Bulletin*, 86(12), 1630-1638.

Robertson, P., & Grieve, R. (1975). Impact structures in Canada-Their recognition and characteristics. *Journal of the Royal Astronomical Society of Canada*, 69, 1-21.

Rodríguez-Tovar, F., Lowery, C., Bralower, T., Gulick, S., & Jones, H. (2020). Rapid macrobenthic diversification and stabilization after the end-Cretaceous mass extinction event. *Geology*, 48(11), 1048-1052.

Rondot, J. (1971). Impactite of the charlevoix structure, Quebec, Canada. *Journal of Geophysical Research*, 76(23), 5414-5423.

Rondot, J. (2000). Charlevoix and Sudbury as gravity-readjusted impact structures. *Meteoritics & Planetary Science*, 35(4), 707-712.

Ross, C., Stockli, D., Rasmussen, C., Gulick, S., de Graaff, S., Claeys, P., Zhao, J., Xiao, L., Pickersgill, A., & Schmieder, M. (2021). Evidence of Carboniferous arc magmatism preserved in the Chicxulub impact structure. *GSA Bulletin*.

Rostron, B., White, D., Chalaturnyk, R., Sorenson, J., Hawkes, C., Worth, K., & Young, A. (2015). An Overview of the Aquistore Project: Canada's First CO<sub>2</sub> Storage Project Associated With a Commercial-Scale Coal-Fired Power Plant. *International Conference and Exhibition, Melbourne, Australia*.

Roussel, D., & Brown, G. (2009). A field guide to the geology of Sudbury, Ontario. *Ontario Ministry of Northern Development, Mines and Forestry*.

Salguero-Hernández, E., Pérez-Cruz, L., & Urrutia-Fucugauchi, J. (2020). Seismic attribute analysis of Chicxulub impact crater. *Acta Geophysica*, 68, 627–640.

Salminen, J., Donadini, F., Pesonen, L., Masaitis, V., & Naumov, M. (2006). Paleomagnetism and petrophysics of the Jänisjärvi impact structure, Russian Karelia. *Meteoritics & Planetary Science*, 41(12), 1853-1870.

Sayers, C., & Van Munster, J. (1991). Microcrack-induced seismic anisotropy of sedimentary rocks. *Journal of Geophysical Research: Solid Earth*, 96(B10), 16529-16533.

Schaal, R., & Hörz, F. (1977). Shock metamorphism of lunar and terrestrial basalts. In. *Pergamon Press*.

Schaefer, B., Grice, K., Coolen, M., Summons, R., Cui, X., Bauersachs, T., Schwark, L., Böttcher, M., Bralower, T., & Lyons, S. (2020). Microbial life in the nascent Chicxulub crater. *Geology*, 48(4), 328-332.

Schijns, H., Jackson, I., & Schmitt, D. (2018). Shear Modulus Dispersion in Cracked and Fluid-Saturated Quartzites: Experimental Observations and Modeling. *Journal of Geophysical Research-Solid Earth*, 123(4), 2825-2840.

Schmieder, M., Jourdan, F., Tohver, E., & Cloutis, E. (2014).  $^{40}\text{Ar}/^{39}\text{Ar}$  age of the Lake Saint Martin impact structure (Canada)—Unchaining the Late Triassic terrestrial impact craters. *Earth and Planetary Science Letters*, 406, 37-48.

Schmitt, D. R. (2015). Geophysical properties of the near surface earth: Seismic properties.

Schmitt, D., Milkereit, B., Karp, T., Scholz, C., Danuor, S., Meillieux, D., & Welz, M. (2007). In situ seismic measurements in borehole LB-08A in the Bosumtwi impact structure, Ghana: Preliminary interpretation. *Meteoritics & Planetary Science*, 42(4-5), 755-768.

Scholz, C., Karp, T., Brooks, K., Milkereit, B., Amoako, P., & Arko, J. (2002). Pronounced central uplift identified in the Bosumtwi impact structure, Ghana, using multichannel seismic reflection data. *Geology*, 30(10), 939-942.

Schön, J. (2015). Physical properties of rocks: Fundamentals and principles of petrophysics. *Elsevier*.

Schubnel, A., Benson, P., Thompson, B., Hazzard, J., & Young, R. (2006). Quantifying damage, saturation and anisotropy in cracked rocks by inverting elastic wave velocities. *Pure and Applied Geophysics*, 163(5-6), 947-973.

Schulte, F., Wittmann, A., Jung, S., Morgan, J., Gulick, S., Kring, D., Grieve, R., Osinski, G., & Riller, U. (2021). Ocean resurge-induced impact melt dynamics on the peak-ring of the Chicxulub impact structure, Mexico. *International Journal of Earth Sciences*, 1-18.

Scott, D., & Hajnal, Z. (1988). Seismic signature of the Haughton structure. *Meteoritics*, 23(3), 239-247.

Sheriff, R., & Geldart, L. (1995). Exploration seismology. *Cambridge university press*.

Shirole, D., Walton, G., Ostrovsky, L., Masoumi, H., & Hedayat, A. (2018). Non-linear ultrasonic monitoring of damage progression in disparate rocks. *International Journal of Rock Mechanics and Mining Sciences*, 111, 33-44.

Short, N. (1968). Nuclear-explosion-induced microdeformation of rocks: An aid to the recognition of meteorite impact structures. *Shock metamorphism of natural materials*, 1, 185-210.

Short, N. (1965). A comparison of features characteristic of nuclear explosion craters and astroblemes. *Annals of the New York Academy of Sciences*, 123(2), 573-616.

Short, N. (1970). Progressive shock metamorphism of quartzite ejecta from the Sedan nuclear explosion crater. *The Journal of Geology*, 78(6), 705-732.

Silva, J., Worsley, T., & Lusk, B. (2019). Practical assessment of rock damage due to blasting. *International Journal of Mining Science and Technology*, 29(3), 379-385.

Simmons, G., & Wang, H. (1971). Single crystal elastic constants and calculated aggregate properties. *MIT Press*.

Simonds, C., Phinney, W., McGee, P., & Cochran, A. (1978). West Clearwater, Quebec impact structure, Part I: Field geology, structure and bulk chemistry. *Proceedings of the Ninth Lunar and Planetary Science Conference*.

Simpson, S., Osinski, G., Longstaffe, F., Schmieder, M., & Kring, D. (2020). Hydrothermal alteration associated with the Chicxulub impact crater upper peak-ring breccias. *Earth and Planetary Science Letters*, 547, 116425.

Sjogren, B., Ofsthus, A., & Sandberg, J. (1979). Seismic Classification of Rock Mass Qualities. *Geophysical Prospecting*, 27(2), 409-442.

Smeulders, D. (2005). Experimental evidence for slow compressional waves. *Journal of Engineering Mechanics*, 131(9), 908-917.

Smidt, J. (2009). Table of elastic constants for isotropic media. *The Leading Edge*, 28(1), 116-117.

Smith, V., Warny, S., Grice, K., Schaefer, B., Whalen, M., Vellekoop, J., Chenot, E., Gulick, S., Arenillas, I., & Arz, J. (2020). Life and death in the Chicxulub impact crater: a record of the Paleocene–Eocene Thermal Maximum. *Climate of the Past*, 16(5), 1889-1899.

Smith, V., Warny, S., Jarzen, D., Demchuk, T., Vajda, V., & Gulick, S. (2020). Paleocene–Eocene palynomorphs from the Chicxulub impact crater, Mexico. Part 2: angiosperm pollen. *Palynology*, 44(3), 489-519.

Smith, V., Warny, S., Jarzen, D., Demchuk, T., Vajda, V., & the Expedition 364 Scientists. (2020). Palaeocene–Eocene miospores from the Chicxulub impact crater, Mexico. Part 1: spores and gymnosperm pollen. *Palynology*, 44(3), 473-487.

Smith, V., Warny, S., Vellekoop, J., Vajda, V., Escarguel, G., & Jarzen, D. (2021). Palynology from ground zero of the Chicxulub impact, southern Gulf of Mexico. *Palynology*, 45(2), 283-299.

Soderblom, J., Evans, A., Johnson, B., Melosh, H., Miljković, K., Phillips, R., Andrews-Hanna, J., Bierson, C., Head, J., Milbury, C., Neumann, G., Nimmo, F., Smith, D., Solomon, S., Sori, M., Wieczorek, M., & Zuber, M. (2015). The fractured Moon: Production and saturation of porosity in the lunar highlands from impact cratering. *Geophysical Research Letters*, 42(17), 6939-6944.

Spray, J. (2021). Earth Impact Database. Planetary and Space Science center. Retrieved Oct 7 from [http://www.passc.net/EarthImpactDatabase/New%20website\\_05-2018/Index.html](http://www.passc.net/EarthImpactDatabase/New%20website_05-2018/Index.html)

Spray, J., Kelley, S., & Rowley, D. (1998). Evidence for a late Triassic multiple impact event on Earth. *Nature*, 392(6672), 171-173.

Spray, J., & Thompson, L. (2008). Constraints on central uplift structure from the Manicouagan impact crater. *Meteoritics & Planetary Science*, 43(12), 2049-2057.

Spray, J., Thompson, L., Biren, M., & O'Connell-Cooper, C. (2010). The Manicouagan impact structure as a terrestrial analogue site for lunar and martian planetary science. *Planetary and Space Science*, 58(4), 538-551.

Staněk, M., & Géraud, Y. (2019). Granite microporosity changes due to fracturing and alteration: secondary mineral phases as proxies for porosity and permeability estimation. *Solid Earth*, 10(1), 251-274.

Stephen, R., & Harding, A. (1983, 1983). Travel time analysis of borehole seismic data. *Journal of Geophysical Research*, 88(NB10), 8289-8298.

Stewart, R. (1984). VSP interval velocities from travelttime inversion. *Geophysical Prospecting*, 32(4), 608-628.

Stewart, R., Huddleston, P., & Kan, T. (1984). Seismic versus sonic velocities: A vertical seismic profiling study. *Geophysics*, 49(8), 1153-1168.

Stierman, D., & Kovach, R. (1979). An in situ velocity study: The Stone Canyon Well. *Journal of Geophysical Research: Solid Earth*, 84(B2), 672-678.

Stishov, S., & Popova, S. (1961). A new dense modification of silicon oxide. *Geokhimiya*, 10, 923-926.

Stöffler, D. (1966). Zones of impact metamorphism in the crystalline rocks of the Nördlinger Ries crater. *Contributions to Mineralogy and Petrology*, 12(1), 15-24.

Stöffler, D. (1984). Glasses formed by hypervelocity impact. *Journal of Non-Crystalline Solids*, 67(1-3), 465-502.

Stöffler, D., & Grieve, R. (2007) Impactites, Chapter 2.11 in Fettes, D. and Desmons, J. (eds.) *Metamorphic Rocks: A Classification and Glossary of Terms, Recommendations of the International Union of Geological Sciences*, Cambridge University Press, Cambridge, UK, 82-92, 111-125, and 126-242.

Stöffler, D., & Grieve, R. (1994). Classification and nomenclature of impact metamorphic rocks: A proposal to the IUGS subcommission on the systematics of metamorphic rocks. *Lunar and Planetary Science Conference*.

Stöffler, D., Hamann, C., & Metzler, K. (2018). Shock metamorphism of planetary silicate rocks and sediments: Proposal for an updated classification system. *Meteoritics & Planetary Science*, 53(1), 5-49.

Stöffler, D., Keil, K., & RD, S. (1991). Shock metamorphism of ordinary chondrites. *Geochimica et Cosmochimica Acta*, 55(12), 3845-3867.

Stöffler, D., & Langenhorst, F. (1994). Shock metamorphism of quartz in nature and experiment: I. Basic observation and theory. *Meteoritics*, 29(2), 155-181.

Stork, A., Nixon, C., Hawkes, C., Birnie, C., White, D., Schmitt, D., & Roberts, B. (2018). Is CO<sub>2</sub> injection at Aquistore aseismic? A combined seismological and geomechanical study of early injection operations. *International Journal of Greenhouse Gas Control*, 75, 107-124.

Sun, Q., Zhang, W., Xue, L., Zhang, Z., & Su, T. (2015). Thermal damage pattern and thresholds of granite. *Environmental Earth Sciences*, 74(3), 2341-2349.

Swanson, E., Wilson, J., Broome, S., & Sussman, A. (2020). The Complicated Link Between Material Properties and Microfracture Density for an Underground Explosion in Granite. *Journal of Geophysical Research-Solid Earth*, 125(11), 15, e2020JB019894.

Taheri-Araghi, S., Bradde, S., Sauls, J., Hill, N., Levin, P., Paulsson, J., Vergassola, M., & Jun, S. (2015). Cell-size control and homeostasis in bacteria. *Current biology*, 25(3), 385-391.

Tani, R., Tomioka, N., Kayama, M., Chang, Y., Nishido, H., Das, K., Rae, A., Ferrière, L., Gulick, S., & Morgan, J. (2018). Microstructural observations of quartz from the basement rocks of the Chicxulub impact structure and shock pressure estimation. *AGU Fall Meeting Abstracts*.

Thompson, L., & Spray, J. (2017). Dynamic interaction between impact melt and fragmented basement at Manicouagan: The suevite connection. *Meteoritics & Planetary Science*, 52(7), 1300-1329.

Thurber, C., Zhang, H., Waldhauser, F., Hardebeck, J., Michael, A., & Eberhart-Phillips, D. (2006). Three-dimensional compressional wavespeed model, earthquake relocations, and focal mechanisms for the Parkfield, California, region. *Bulletin of the Seismological Society of America*, 96(4B), S38-S49.

Timms, N., Kirkland, C., Cavosie, A., Rae, A., Rickard, W., Evans, N., Erickson, T., Wittmann, A., Ferrière, L., Collins, G., & Gulick, S. (2020). Shocked titanite records Chicxulub hydrothermal alteration and impact age. *Geochimica et Cosmochimica Acta*, 281, 12-30.

Timms, N., Pearce, M., Erickson, T., Cavosie, A., Rae, A., Wheeler, J., Wittmann, A., Ferrière, L., Poelchau, M., & Tomioka, N. (2019). New shock microstructures in titanite (CaTiSiO<sub>5</sub>) from the peak ring of the Chicxulub impact structure, Mexico. *Contributions to Mineralogy and Petrology*, 174(5), 38.

Trepmann, C., Götte, T., & Spray, J. (2005). Impact-related Ca-metasomatism in crystalline target-rocks from the Charlevoix structure, Quebec, Canada. *The Canadian Mineralogist*, 43(2), 553-567.

Trepmann, C., & Spray, J. (2006). Shock-induced crystal-plastic deformation and post-shock annealing of quartz: microstructural evidence from crystalline target rocks of the Charlevoix impact structure, Canada. *European Journal of Mineralogy*, 18(2), 161-173.

Urrutia-Fucugauchi, J., Pérez-Cruz, L., Morgan, J., Gulick, S., Wittmann, A., Lofi, J., & the Expedition 364 Scientists. (2019). Peering inside the peak ring of the Chicxulub Impact Crater—its nature and formation mechanism. *Geology today*, 35(2), 68-72.

Uyanık, O., Sabbağ, N., Uyanık, N., & Öncü, Z. (2019). Prediction of mechanical and physical properties of some sedimentary rocks from ultrasonic velocities. *Bulletin of Engineering Geology and the Environment*, 78(8), 6003-6016.

Van Gaever, Q. (2019). Petrography and geochemistry of the chicxulub impact melt. *Ghent University*, MSc thesis.

Vermeesch, P., & Morgan, J. (2004). Chicxulub central crater structure: Initial results from physical property measurements and combined velocity and gravity modeling. *Meteoritics & Planetary Science*, 39(7), 1019-1034.

Vermeesch, P., & Morgan, J. (2008). Structural uplift beneath the Chicxulub impact structure. *Journal of Geophysical Research-Solid Earth*, 113(B7), 10, Article B07103.

Voight, W. (1928). Lehrbuch der kristallphysik. *Teubner, Leipzig*.

von Engelhardt, W. (1967). Chemical composition of Ries glass bombs. *Geochimica et Cosmochimica Acta*, 31(10), 1677-1689.

Wang, J., Zuo, J., Sun, Y., & Wen, J. (2021). The effects of thermal treatments on the fatigue crack growth of Beishan granite: an in situ observation study. *Bulletin of Engineering Geology and the Environment*, 80(2), 1541-1555.



- Wang, X.-Q., Schubnel, A., Fortin, J., David, E., Guéguen, Y., & Ge, H.-K. (2012). High Vp/Vs ratio: Saturated cracks or anisotropy effects? *Geophysical Research Letters*, 39(11).
- Wang, X., Wang, E., & Liu, X. (2019). Damage characterization of concrete under multi-step loading by integrated ultrasonic and acoustic emission techniques. *Construction and Building Materials*, 221, 678-690.
- Wang, Y.-C., & Lakes, R. (2005). Composites with inclusions of negative bulk modulus: extreme damping and negative Poisson's ratio. *Journal of composite materials*, 39(18), 1645-1657.
- Wang, Z., Tian, N., Wang, J., Liu, J., & Hong, L. (2018). Experimental study on damage mechanical characteristics of heat-treated granite under repeated impact. *Journal of Materials in Civil Engineering*, 30(11), 04018274.
- Ward, W., Keller, G., Stinnesbeck, W., & Adatte, T. (1995). Yucatán subsurface stratigraphy: Implications and constraints for the Chicxulub impact. *Geology*, 23(10), 873-876.
- Wardlaw, N., Li, Y., & Forbes, D. (1987). Pore-throat size correlation from capillary pressure curves. *Transport in porous media*, 2(6), 597-614.
- Wardlaw, N., & McKellar, M. (1981). Mercury porosimetry and the interpretation of pore geometry in sedimentary rocks and artificial models. *Powder technology*, 29(1), 127-143.
- Washburn, E. W. (1921). Note on a method of determining the distribution of pore sizes in a porous material. *Proceedings of the National Academy of Sciences of the United States of America*, 7(4), 115.
- Watanabe, T., & Sassa, K. (1996). Seismic attenuation tomography and its application to rock mass evaluation. *International Journal of Rock Mechanics and Mining Sciences & Geomechanics Abstracts*.
- Watson, B. (2003). Han Feizi: basic writings. *Columbia University Press*.
- Watt, J. (1979). Hashin-Shtrikman bounds on the effective elastic moduli of polycrystals with orthorhombic symmetry. *Journal of Applied Physics*, 50(10), 6290-6295.
- Watt, J. (1986). Hashin-Shtrikman bounds on the effective elastic moduli of polycrystals with trigonal (3, 3) and tetragonal (4, 4, 4 m) symmetry. *Journal of Applied Physics*, 60(9), 3120-3124.

Weide, D., & Faber, M. (1985). Soils and Quaternary geology of the southwestern United States (Vol. 203). *Geological Society of America*.

Whalen, M., Gulick, S., Lowery, C., Bralower, T., Morgan, J., Grice, K., Schaefer, B., Smit, J., Ormö, J., & Wittmann, A. (2020). Winding down the Chicxulub impact: The transition between impact and normal marine sedimentation near ground zero. *Marine Geology*, 430, 106368.

White, D., Harris, K., Roach, L., Roberts, B., Worth, K., Stork, A., Nixon, C., Schmitt, D., Daley, T., & Samson, C. (2017). Monitoring results after 36 ktonnes of deep CO<sub>2</sub> injection at the Aquistore CO<sub>2</sub> storage site, Saskatchewan, Canada. *Energy Procedia*, 114, 4056-4061.

Wiggins, S., Johnson, B., Bowling, T., Melosh, H., & Silber, E. (2019). Impact Fragmentation and the Development of the Deep Lunar Megaregolith. *Journal of Geophysical Research-Planets*, 124(4), 941-957.

Wilks, R. (2016). Geochemical and petrographic study of melt veins at the West Clearwater Lake Impact Structure, Canada. *Western University*, MSc thesis.

Winkler, K., & Nur, A. (1982). Seismic attenuation: Effects of pore fluids and frictional-sliding. *Geophysics*, 47(1), 1-15.

Winkler, R., Luther, R., Poelchau, M., Wunnemann, K., & Kenkmann, T. (2018). Subsurface deformation of experimental hypervelocity impacts in quartzite and marble targets. *Meteoritics & Planetary Science*, 53(8), 1733-1755.

Wittmann, A., Cavosie, A., Timms, N., Ferrière, L., Rae, A., Rasmussen, C., Ross, C., Stockli, D., Schmieder, M., Kring, D., Zhao, J., Xiao, L., Morgan, J., & Gulick, S. (2021). Shock impedance amplified impact deformation of zircon in granitic rocks from the Chicxulub impact crater. *Earth and Planetary Science Letters*, 575, 117201.

Wong, J., Hurley, P., & West, G. (1983). Crosshole seismology and seismic imaging in crystalline rocks. *Geophysical Research Letters*, 10(8), 686-689.

Wood, C., & Head, J. (1976). Comparison of impact basins on Mercury, Mars and the Moon. *Lunar and Planetary Science Conference Proceedings*.

Wordsworth, R. (2016). The climate of early Mars. *Annual Review of Earth and Planetary Sciences*, 44, 381-408.

Wu, J., Milkereit, B., & Boerner, D. (1995). Seismic imaging of the enigmatic Sudbury Structure. *Journal of Geophysical Research: Solid Earth*, 100(B3), 4117-4130.

Wuenschel, P. (1976). The vertical array in reflection seismology—Some experimental studies. *Geophysics*, 41(2), 219-232.

Wulff, A., Hashida, T., Watanabe, K., & Takahashi, H. (1999). Attenuation behaviour of tuffaceous sandstone and granite during microfracturing. *Geophysical Journal International*, 139(2), 395-409.

Wyatt, K. (1981). Synthetic vertical seismic profile. *Geophysics*, 46(6), 880-891.

Xia, K., & Ahrens, T. (2001). Impact induced damage beneath craters. *Geophysical Research Letters*, 28(18), 3525-3527.

Xie, W. (2014). Seismic characterization of a possible buried impact structure near Bow City Southern Alberta. *University of Alberta*, MSc thesis.

Yamamura, K., Sano, O., Utada, H., Takei, Y., Nakao, S., & Fukao, Y. (2003). Long-term observation of in situ seismic velocity and attenuation. *Journal of Geophysical Research: Solid Earth*, 108(B6).

Yang, S.-Q., Ranjith, P., Jing, H.-W., Tian, W.-L., & Ju, Y. (2017). An experimental investigation on thermal damage and failure mechanical behavior of granite after exposure to different high temperature treatments. *Geothermics*, 65, 180-197.

Young, T. (1807). A course of lectures on natural philosophy and the mechanical arts: in two volumes (Vol. 2). *Johnson*.

Yu, H., Liu, Y., Harrington, R., & Lamontagne, M. (2016). Seismicity along St. Lawrence Paleorift faults overprinted by a meteorite impact structure in Charlevoix, Québec, Eastern Canada. *Bulletin of the Seismological Society of America*, 106(6), 2663-2673.

Zahnle, K., Schenk, P., Levison, H., & Dones, L. (2003). Cratering rates in the outer Solar System. *Icarus*, 163(2), 263-289.

Zhang, W., Sun, Q., Zhang, Y., Xue, L., & Kong, F. (2018). Porosity and wave velocity evolution of granite after high-temperature treatment: a review. *Environmental Earth Sciences*, 77(9), 1-13.

Zhao, J., Xiao, L., Gulick, S., Morgan, J., Kring, D., Fucugauchi, J., Schmieder, M., de Graaff, S., Wittmann, A., & Ross, C. (2020). Geochemistry, geochronology and petrogenesis of Maya Block granitoids and dykes from the Chicxulub Impact Crater, Gulf of México: Implications for the assembly of Pangea. *Gondwana Research*, 82, 128-150.

Zhao, J., Xiao, L., Xiao, Z., Morgan, J., Osinski, G., Neal, C., Gulick, S., Riller, U., Claeys, P., & Zhao, S. (2021). Shock-deformed zircon from the Chicxulub impact crater and implications for cratering process. *Geology*, 49(7), 755-760.

Zhou, K.-p., Bin, L., Li, J.-l., Deng, H.-w., & Feng, B. (2015). Microscopic damage and dynamic mechanical properties of rock under freeze–thaw environment. *Transactions of Nonferrous Metals Society of China*, 25(4), 1254-1261.

Zoeppritz, K. (1919). VIIb. Über Reflexion und Durchgang seismischer Wellen durch Unstetigkeitsflächen., VIIb. On reflection and transmission of seismic waves by surfaces of discontinuity, *Nachrichten von der Königlichen Gesellschaft der Wissenschaften zu Göttingen*.

Zuo, J.-P., Wei, X., Shi, Y., Liu, C., Li, M., & Wong, R. (2020). Experimental study of the ultrasonic and mechanical properties of a naturally fractured limestone. *International Journal of Rock Mechanics and Mining Sciences*, 125, 104162.

## **Appendix**

### **Appendix A - Supplementary Methods for Chapter 3**

#### **Software Package**

A software package (see section 6.4c) was written and stitched together in a single function which first takes the flattened VSP traces, time base, depth, and P-velocities, and asks for user input every step of the way. If the user is not happy with a processing step, parameters can be changed until the user feels the results of that step are suitable for further processing. This was very valuable for fine tuning the project as a single run of the program takes ~ 2 minutes.

The program is built with an optional automatic frequency truncating function. There are several “holes” in the spectrum and the signal becomes quite faint after that. Since the first spectral “hole” slowly shifts with depth, I thought it would be valuable to incorporate this observation into the processing. An emphasis of this report will be the comparison of a fixed bandwidth vs. a variable bandwidth analysis.

#### **Windowing**

A pre-designed Blackmann-Harris window was used as outlined in Atten 2004; However, I used a different set of coefficients from the original Harris (1978) paper which gives fatter tails on the modulation window ( $a_0=0.40217$   $a_1=0.49703$   $a_2=0.09392$   $a_3 = 0.00183$ ). I updated  $a_0$  to 0.40494 for closer intersection to zero). Messing around with these coefficients and attempting to add more terms did not go well and I realized that these extremely specific values were published for a reason. Figure A 1 shows the effects of modulation on the signal spectra. At first glance, one may be concerned there is ringing in the frequency domain as a processing artifact. However, close comparison of the raw and windowed signal spectra (Figure A 1, bottom) seems to show similar peaks in both. Figure A 1 shows the window applied to the entire dataset. Window start and end times of 0.17 and 0.26 seconds were used for further processing.

## Trouble region

From roughly 800 to 950 m there is an odd region of the signal which persists throughout the processing (Figure A 2). This corresponds roughly to the clast free melt and will be discussed throughout the report.

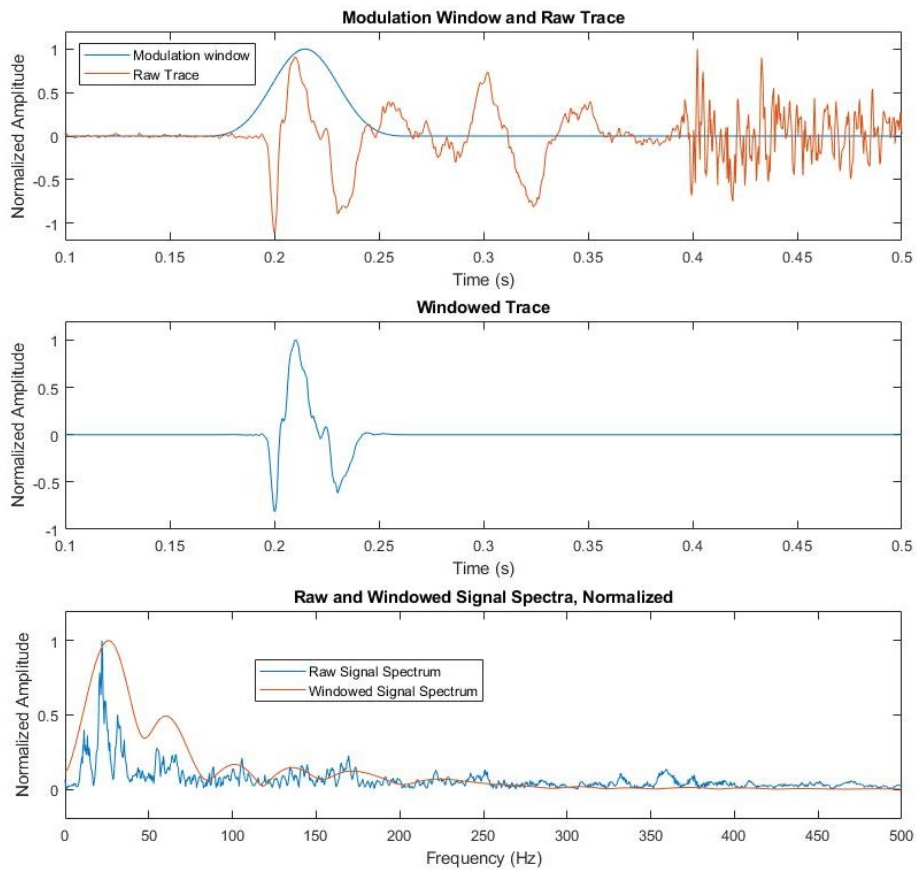


Figure A 1. Effects of windowing on one particular trace at 698 m depth.

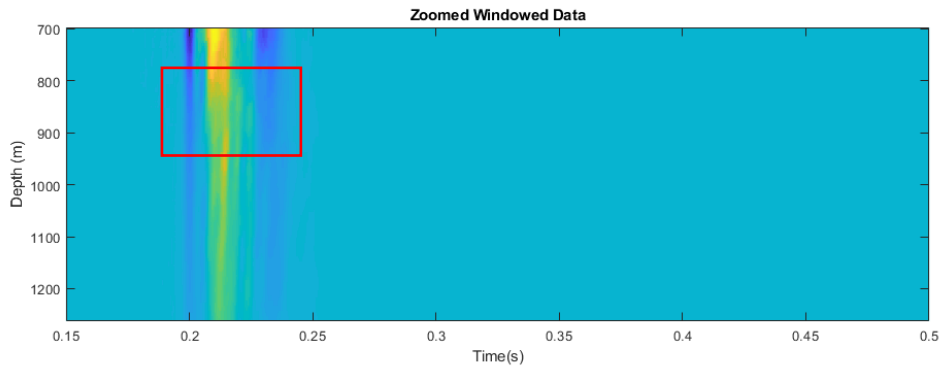
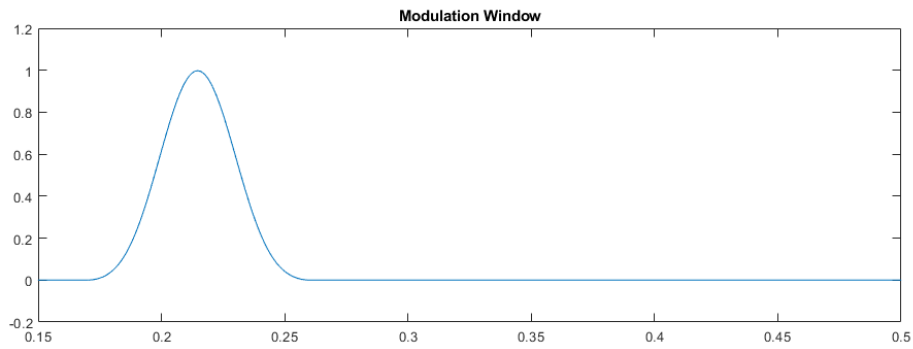
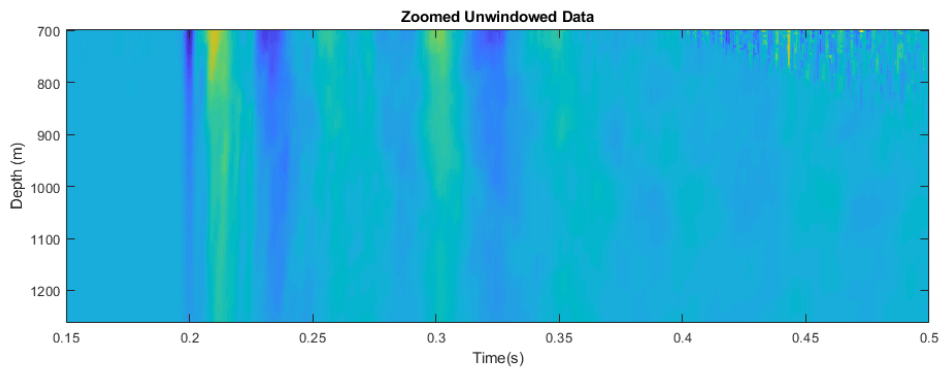
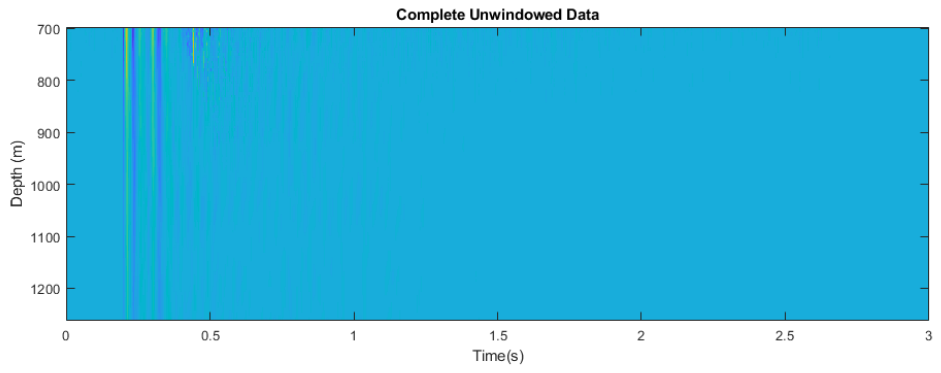


Figure A 2. Windowing performed on the full VSP. Trouble region in red box.

## Spectral Decay

This is the first step in the processing where fixed and variable bandwidth begin to diverge. The user defines the spectral band to be used for further processing. A bottom cutoff frequency of 7 Hz was used for both methods, but an upper cutoff of 80 was used for the fixed band (Figure A 3, LHS) and 85 Hz for the variable band (Figure A 3, RHS).

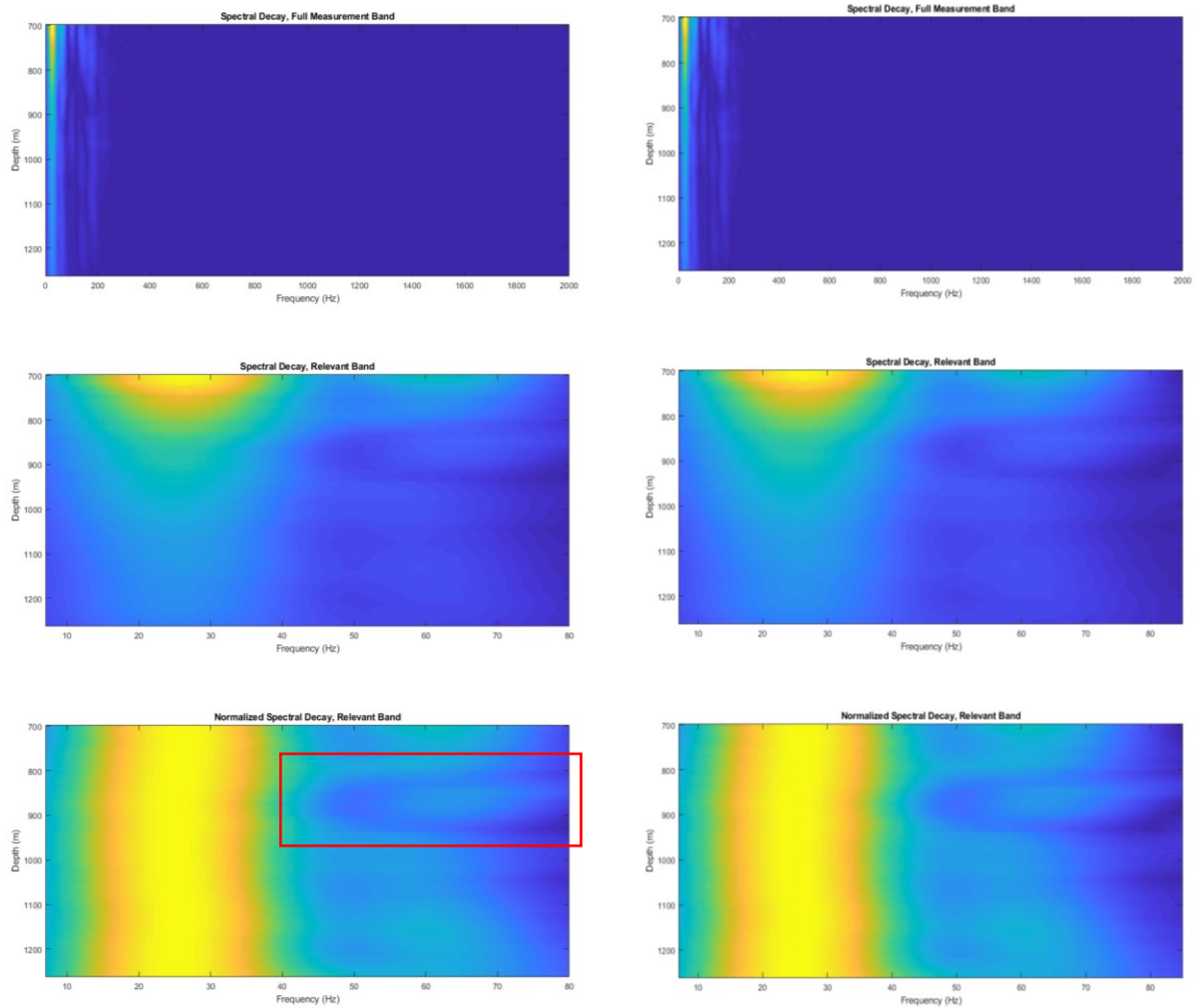


Figure A 3. LHS: Fixed band spectral decay. 7 to 80 Hz used in all further processing. Trouble region in red box. RHS: Variable band spectral decay. 7 to 85 Hz used for auto cutoff algorithm.



The code creates an interim square dimensioned cell structure where a vector of the frequency ratios is temporarily stored for every reference depth. That is, “At each frequency, calculate the simple ratio. Divide the second amplitude by the first amplitude for every frequency sample” (Atten 2004). The dimensions of this structure are then depth by depth with the values along the main diagonal obviously being all ones, as the trace is using itself as a reference. The next step is to take the natural log of these values and apply a linear fit. The code will give a regularly spaced 10 by 10 array of these log frequency ratio plots with best fit lines as a quality control measure (Figure A 4), and the user is given the option to loop back to bandwidth selection and reprocess.

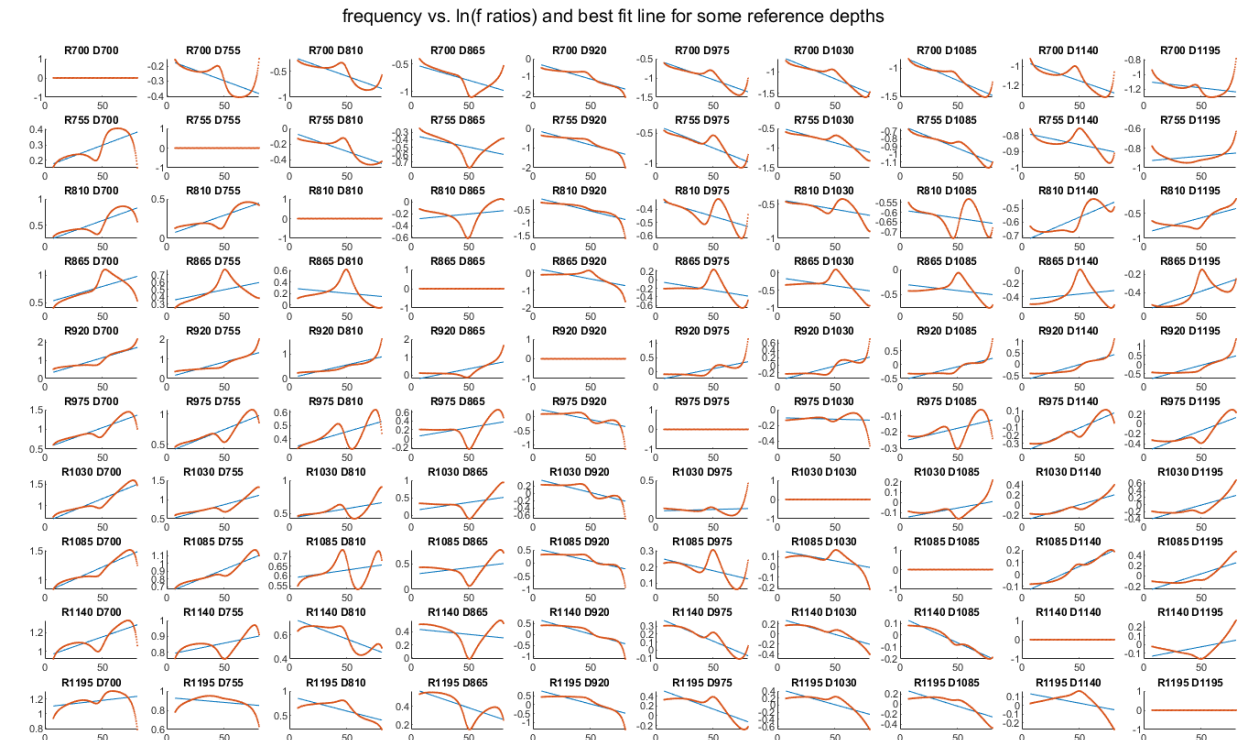


Figure A 4. Logarithmic spectral ratio plots with best fit lines (fixed band).

### Variable band

Given that the fixed band frequently produces dubious results, especially when using deeper reference traces, I developed a simple algorithm to try and use the more linear part of the logarithm charts. This is

following the observation that after hitting a deep local minimum, the ratios would often skyrocket to unreasonable values shortly after. Given the depth of the hole and the faintness of high frequency components in the signal, I felt it prudent to make an effort to chase that minimum ratio value and ignore the portion of the curve to the right where it jumps.

The algorithm is quite simple. In the case where the reference trace is above the trace being analyzed, all frequencies above the deep minimal trough in the log (spectral ratio) chart are thrown away. In the opposite case (reference trace being below the trace being analyzed), things are opposite, and the same rejection is applied to all frequencies above the first maximum. Figure A 5 shows the interim results of this variable band selection method with the same data as the fixed band in Figure A 4. Although they look quite similar, the variable band in Figure A 5 does produce smoother data and many of the slopes that are positive when they should be negative (or vice versa) in Figure A 4 have been corrected.

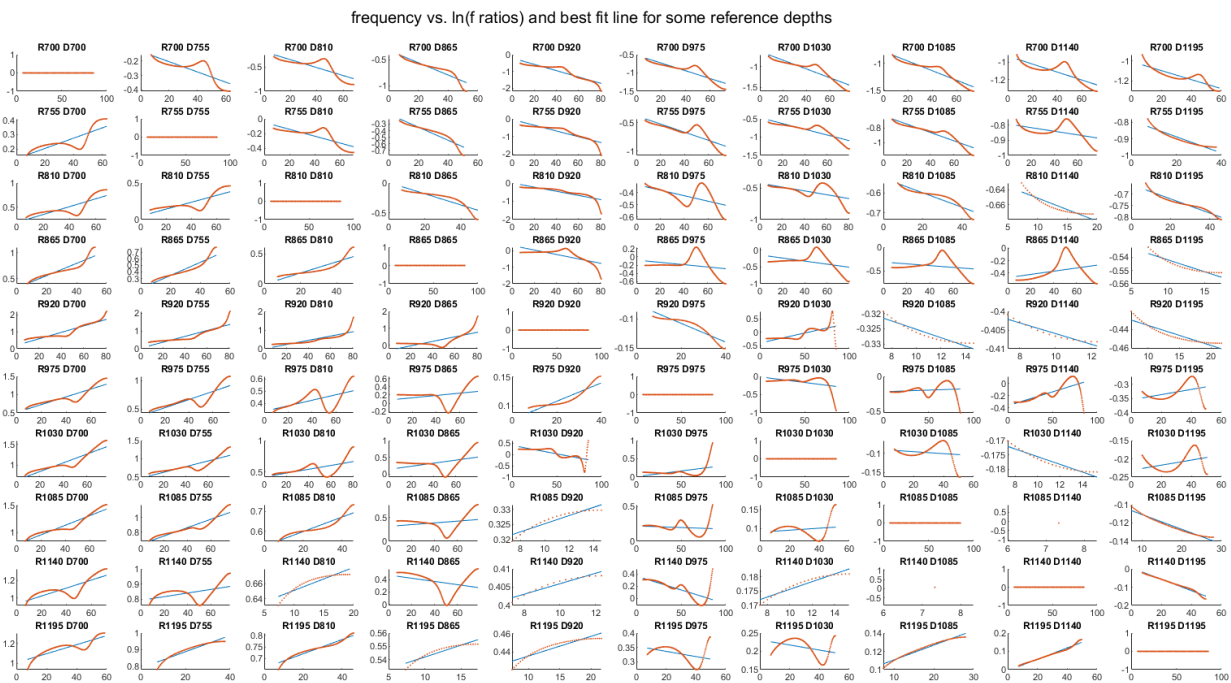


Figure A 5. Logarithmic spectral ratio plots with best fit lines (variable band).

## Slope Matrix

The best fit slopes of Figures A 4 & A 5 are shown in Figure A 6, except this is for the entire dataset whereas Figures A 4 & A 5 only show intermittent depths. There are hotspots approximately corresponding to spectral dead zones at ~810, 920, and 1040 mbsf. The variable band method (Figure A 6b) does smooth the hotspots somewhat, but introduces digitized hotspots of its own.

## Q-factor matrix.

Using equation 2.3 from Atten 2004 (Below),

$$\ln \frac{A(x,f)}{A(x_0,f)} = -\frac{\pi \Delta x}{Qv} f + \ln G \quad (A 1)$$

a quick rearrangement and substitution gives:

$$Q = \frac{-\pi \Delta x}{mv_p} \quad (A 2)$$

A final simple calculation step in the program converts Figure A 6 **Error! Reference source not found.** into the Q factor matrices (Figure A 7). The matrices are symmetric, as expected. The processing isn't perfect, particularly with real data, so I added a section of code to convert any negative Q values to NaN as well as any Q-values over a user defined threshold (in this report, 500). Without this step, the figure becomes washed out by an extremely wide range of negative and positive Q values.

At first glance, the fixed band method (Figure A 7a) has trouble crossing the antidiagonal. It is not clear if this is an intrinsic property of the processing method, or something about this dataset. However, all

reference traces do agree that Q increases overall with depth. Exactly how quickly is unclear. The 800 to 950 m trouble spot is now manifesting as a NaN<sup>4</sup> glob off the main diagonal.

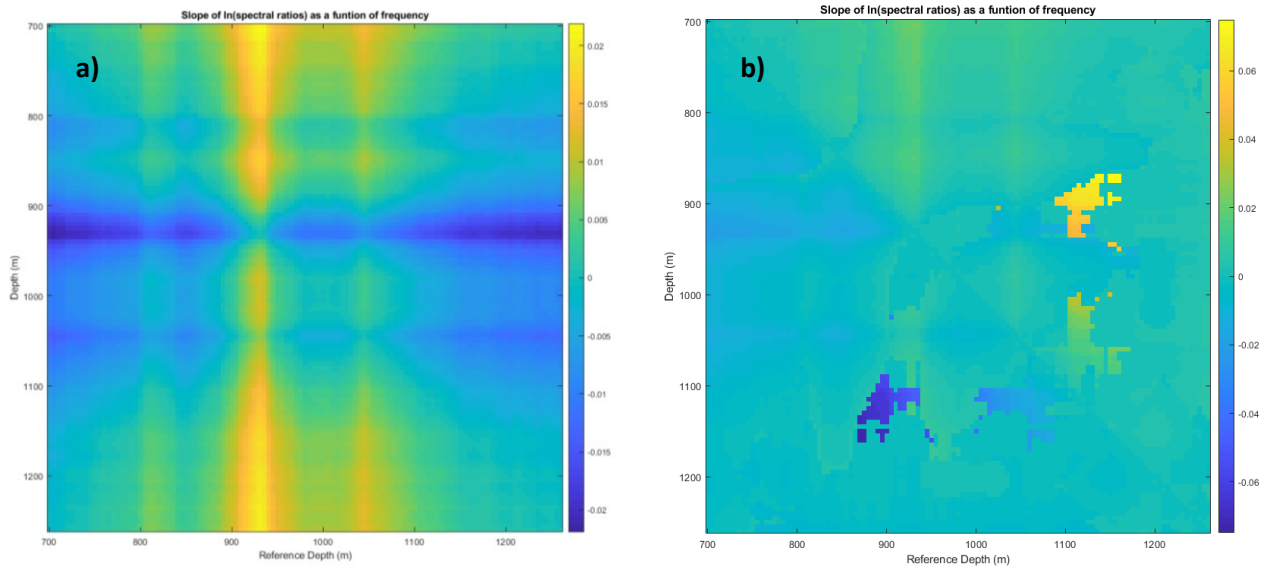


Figure A 6. *ln(spectral ratio)* plot. a) Fixed band. b) Variable band.

The variable band method (Figure A 7b) overall gives lower Q estimates, particularly at depth. However, both methods agree with the increase in Q with depth. The variable band method still has trouble on the wiggly line near the antidiagonal, but can fill in approximately half of the NaN zones in Figure A 7a. Are these results to be trusted? I don't know. I think we should still publish the comparison. The non-continuous hotspots from Figure A 6b manifest as low Q values in Figure A 7b and I think it would be safe to throw those regions away. Overall, I think the variable band method is quite useful as it fills in areas problematic for processing

---

<sup>4</sup> NaN – “Not a Number” Matlab concept, in this case used where actual values are unrealistic and rejected.

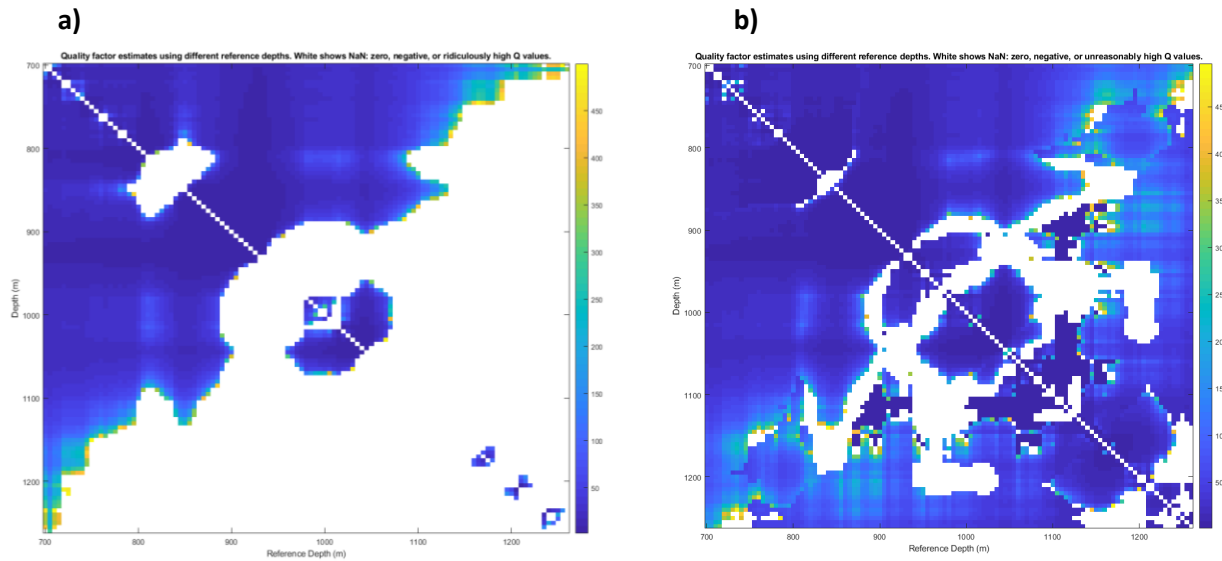


Figure A 7. Q factor matrix. a) Fixed band. b) Variable band.

## Results

I took the top 4 reference depths of each Q matrix and plotted the upper and lower estimates of each against the color lithostratigraphy (Figure A 8). They agree pretty well in some places, but disagree in others. Most notably, they disagree at the top of the CF melt and toward the bottom after the onset of felsite and breccias. I am skeptical of the spike in the fixed band result at the onset of CF melt as the same result is not seen in the other main layer of CF melt right below. It is rather conspicuous that the fixed band spike at ~850m is associated with the center of the trouble region. Also, the fixed band result shoots up quite rapidly after the tonalite layer whereas the variable band result seems to be less chaotic and more related to lithology. I think I believe the variable band method more, but as I said before, we should publish both.

The trouble region associated with the upper CF melt caused some headache in processing, but may be insightful in itself. I think this hole is trying to tell us something, perhaps it can guide further research.

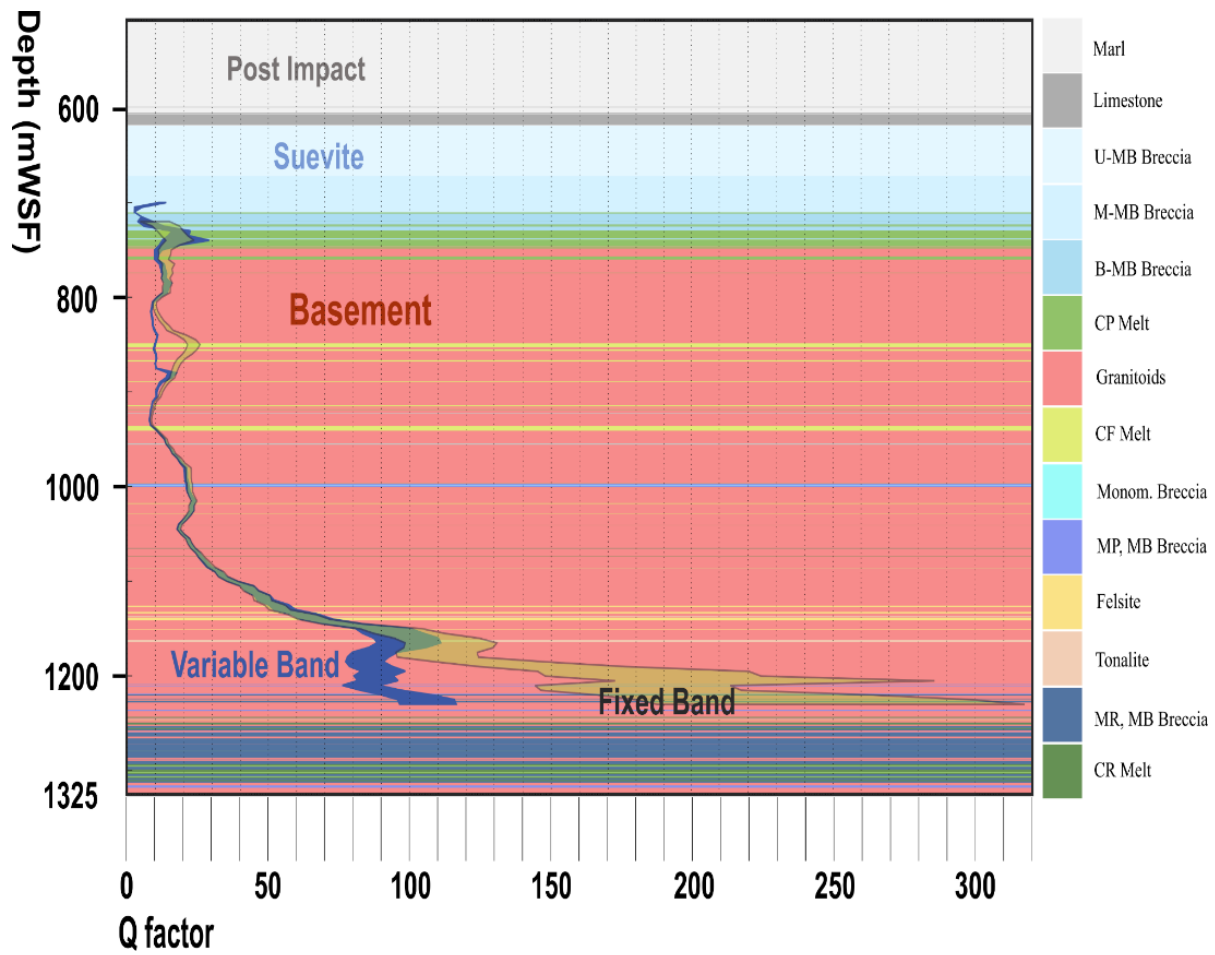


Figure A 8. Q factor results, both methods compared with lithostratigraphy.

## Appendix B - Supplementary Methods for Chapter 4

*The following methods have been published as an electronic supplement to Chapter 4*

### Vertical Seismic Profiling (VSP)

A VSP essentially consists of measuring the seismic wavefield at a variety of depths within the earth.

The technique developed from 'check-shots', in which the time taken by a seismic wave to arrive at a known depth was directly measured in order to calibrate those depths that had otherwise only been estimated indirectly from analysis of reflection moveout velocity analyses (Hardage, 1985). A VSP includes measurements at many depths, which allows for precise determination of the depths and dips of reflecting events; this allows distinguishing primary reflections from multiples and the potential for direct in situ measurement of seismic wave speeds and attenuation. The VSP records, too, retain significant strength and frequency-content relative to corresponding surface reflection data, as surface cultural noise is reduced and the wave need only pass through the highly attenuating near surface overburden once.

While there are many VSP source-receiver geometries, here we employ the simplest 'zero-offset' method and it is useful to provide a brief description of the method. For the reader desiring more information, several primary texts describe vertical seismic profile geometries and data processing in detail (Hardage, 1985; Hinds et al., 1996). The method consists of a repeatable seismic source placed at a negligible horizontal offset distance, providing signal for detectors at depth in a vertical borehole (Figure A 9), with the wave front passing the detectors as it travels downward nearly parallel to the borehole. Similarly, upward-going reflected and scattered signals pass the detectors a second time.

For purposes of illustration, a basic seismic amplitude trace at the topmost receiver recorded for a simple 3-layer model, highlighted in bold (Figure A 10a), shows the first down going arrival followed by

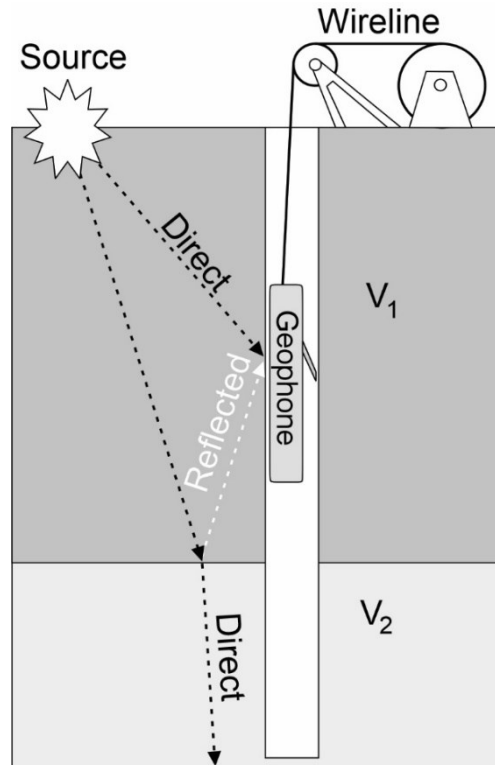


Figure A 9. Geometry of zero-offset VSP showing direct downward going propagation and upward-going reflections.

two upgoing primary reflections originating at the interfaces between the three layers. The survey is continued for each additional shot point by lowering the receiver a depth interval ( $\Delta z$ ) and recording the subsequent response. If one plots each detector's time-series recording at its depth on the z-axis and the actual time series along the x-axis, the resulting composite image is the raw VSP (Figure A 10a). As the travel direction for the zero-offset approximation is perfectly vertical, processing is relatively simple and seismic arrivals in the raw VSP lay along straight lines with the tracking of the down going direct wave and upward going reflection forming the opposing arms of an isosceles triangle.

The raw VSP profile of Figure A 10a may be further processed by wavefield separation into upward and downward propagating wavefields and it is useful to briefly outline this process as it is important for both calibrating the depth to reflectors and for providing the down-going wavelet pulses necessary for



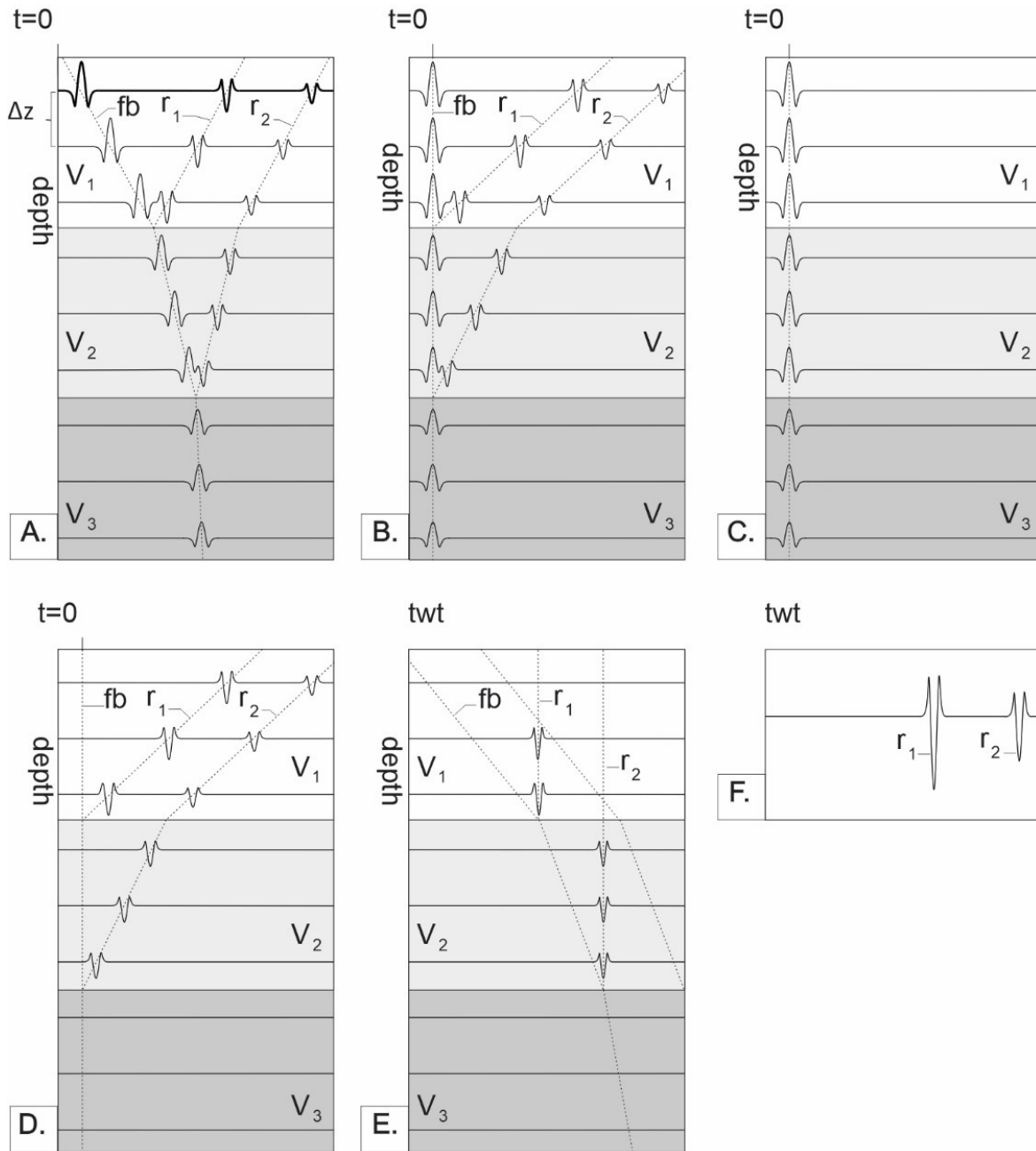


Figure A 10. Major VSP processing steps. A. A typical shot record is shown for a 3-layer model with a near surface receiver (top, bold). The raw VSP is shown with lines superimposed for first breaks (fb) and the reflections from layer 2 & 3. ( $r_1$ ,  $r_2$ ) B. Each trace is left shifted so the fb coincides with the origin. C. Down-going wavefield is estimated. D. Down-going wavefield is subtracted from total VSP, only reflections remain. E. Each trace is double right-shifted. F. All traces are summed to provide a 2-way travel time reflector profile that is directly comparable to the corresponding surface seismic trace.

attenuation analysis. The basic steps are: i) picking of the one-way pulse arrival times from the raw profile (Figure A 10a), ii) time-shifting of the traces so that they align at the same arbitrary time in order to assist with further processing (Figure A 10b), iii) application of a filter, most commonly a median or an FK filter, although alternate approaches are available, that provides an estimate of the initial down-going pulse (Figure A 10c), iv) separation of the up-going wavefield (Figure A 10d) by subtracting the down-going estimate (Figure A 10c) from the time-flattened panel (Figure A 10b), v) reshifting the traces by twice the original picked arrival times in order to move the pulses to their expected normal incidence 2-way time (twt) (Figure A 10e) at which point the coherent reflecting events will align, and finally, vi) collapsing times along an appropriately chosen 'corridor' by stacking to estimate of the 2-wave reflectivity that may be directly compared to surface seismic data (Figure A 10f).

#### **Acquisition Details.**

VSP acquisition was conducted from the lift ship Myrtle, with the drill floor ~17 m above a 13 m thick water column, in a prominent region of the peak ring structure near the intersection of 3 horizontal seismic profiles CHIXR3, CHIX10, and CHIX17B (Gulick et al., 2017). The hole was drilled in three stages, with rapid rotary drilling to 503.6 mbsf, PQ3-dimension coring to 701.7 mbsf, and finally switching to standard PQ3 coring to the bottom hole at 1334.69 mbsf (Lofi et al., 2018). Geological intervals are summarized in Table A 1. It is important to note this here as geophysical logging followed by the VSP both deployed in open hole at the end of each stage (Figure 4.5) and prior to placement of temporary casing; these operational constraints did influence some aspects of the VSP recording.

Data acquisition was carried out with a 3-component wall locking wireline geophone system (Sercel SlimwaveTM) with five 3-component sondes at 15 m spacing. The seismic signals were transduced with 15 Hz geophones and digitized onboard the sondes for transmission to the surface, thus avoiding wireline

induction noise. The signal was digitized at 250  $\mu$ s interval sampling for 3000 ms. No instrumental gains or filtering were used for any of the surveys. The orientations of the sondes, and hence the polarization directions of the two horizontal receivers, are unknown. Each record was individually stored, with a minimum of 5 shots taken at each station. These were stacked after editing of poor-quality records to provide the final set of traces for each depth with the raw vertical component data shown in Figure 4.5, with the unprocessed horizontal components provided in Figure A 11.

Subunit	Top Depth (mbsf)	Dominant Lithology
1A	505.7	marlstone
1B	530.18	marlstone & limestone
1C	537.8	marlstone & limestone
1D	559.75	marlstone & limestone
1E	580.89	limestone
1F	607.27	limestone
1G	616.58	mud-wackestone
2A	617.33	suevite
2B	664.52	suevite
2C	712.84	suevite
3A	721.61	impact melt rock
3B	737.56	impact melt rock
4	747.02	granitoid
4*	*	suevite
4*	*	impact melt rock
4*	*	granitoid
4*	*	dolerite

*Table A 1. Table of Interpreted Geological Intervals. \*Unit 4 was not divided into subunits; these values are calculated for depths within Unit 4 where core description identified the dominant lithology.*

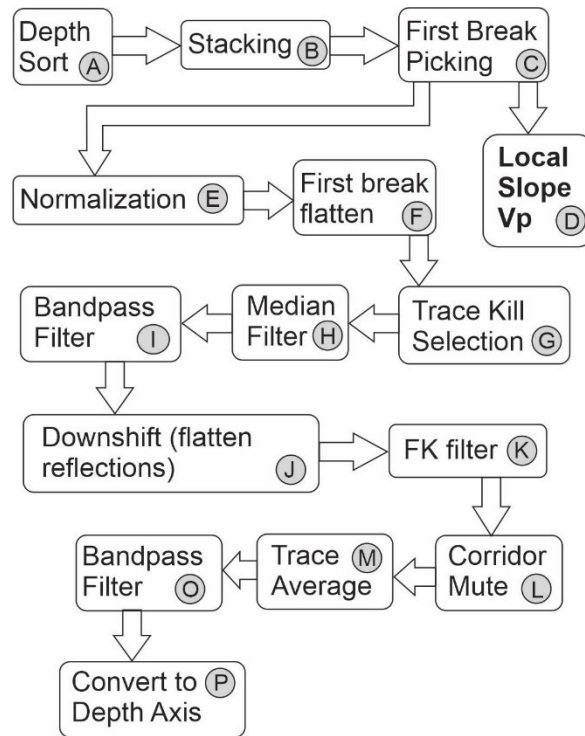


Figure A 11. Vertical component processing flow. a,b) Traces sorted by approximate depth and stacked to improve signal to noise ratio. c) First breaks of initial p-wave arrival are manually selected. d)  $V_p$  is calculated with a local slope differential algorithm, radius is 10 sample points. e) Dataset is normalized by first break amplitude. f) VSP is static shifted to align first break points. g) Poorly coupled noisy traces are removed prior to further processing. h) Median filter is applied for wavefield separation. i) Bandpass filter to remove high frequency noise. j) Remaining wavefield is double shifted so reflectors are flattened. k) Vertical box rejection FK filters are applied to aid in reflector visualization. l) 150 ms corridor mute is applied to eliminate multiples m) Reflector wavefield is averaged. o) Additional bandpass filter applied to reduce high frequency noise in result giving reflector profile in two way travel time. p) Reflector profile is resampled by first break data to convert to depth scale.

An airgun seismic source (Sercel 30/30 cubic inch mini-GITM) was activated at a nominal water depth of 2-m, offset 10 m from the borehole. The gun was activated by a 13.8 MPa (2000 psi) maintained air pressure and, in the first two deployments, controlled by computer (Hotshot), and manually for the final deployment. The manual control did not allow for control of the pulse signature and as such this differed in the final deployment as is evident in the raw records in Figure 4.5. Regardless, during each individual deployment the signature remained uniform. Additional details of the acquisition are

summarized in Table A 2.

VSP equipment parameters, hole M0077A	
Hole depth	1335 mbsf
VSP depth range	47.5-1325 mbsf
Recording system Supplied by	Sercel Slimwave™ U Alberta
Sercel Sonde spacing	15 m
No. triaxial sondes	4
Geophone Frequency response	>15 Hz
Airgun Source Supplied by	Sercel mini GITM U Texas
Source Offset	~10 m
Acquisition deployments	3
Record length	3000 ms
Sampling interval	250 $\mu$ s
Repeated Shots per station	5 to 10
Station Intervals	1.25 m, 2.5 m, 5 m

*Table A 2. Details of Seismic Acquisition.*

### **Processing of Vertical Component**

The basic method of processing VSP data was introduced earlier with the goal to provide an estimate of the downgoing and upgoing wavefields to use in calibrating the seismic response as well as providing data for attenuation analysis. The detailed processing flow developed here (Figure A 11) and processing was carried out using the VISTA™ (Schlumberger) Version 2013.026.5536. This included basic quality control and trace energy equalization for the purpose of improving visualization of the fainter traces toward the bottom of the hole.

This set of first arrival times is used to ‘flatten’ the profile to an arbitrary datum time. The purpose of this flattening is to align the down going traces to assist in estimation of the down going pulse signature. Additionally, the trace was normalized to the maximum amplitude of the wavelet’s first break.

Presumably due to poor coupling, certain traces ‘rang’ with a very high oscillatory amplitude after the first break; this ringing drowned out the useful signal and thus the problematic traces were removed prior to further processing (Figure A 12a,b) Due to the different source wavelets and spacings used in

the upper and lower portions of the VSP, separate median filters were designed and applied to both the upper (31 traces  $\times$  3 time samples) and lower (5 traces  $\times$  5 times samples) to produce an estimate of the down-going wavefield (Figure A 11h) that is then subtracted from the time shifted original data to yield the upgoing wavefield (Figure A 12d). An Ormsby bandpass filter was then applied to reduce noise at frequencies not relevant to the seismic bandwidth (1,10,100,120 Hz) (Figure A 11i).

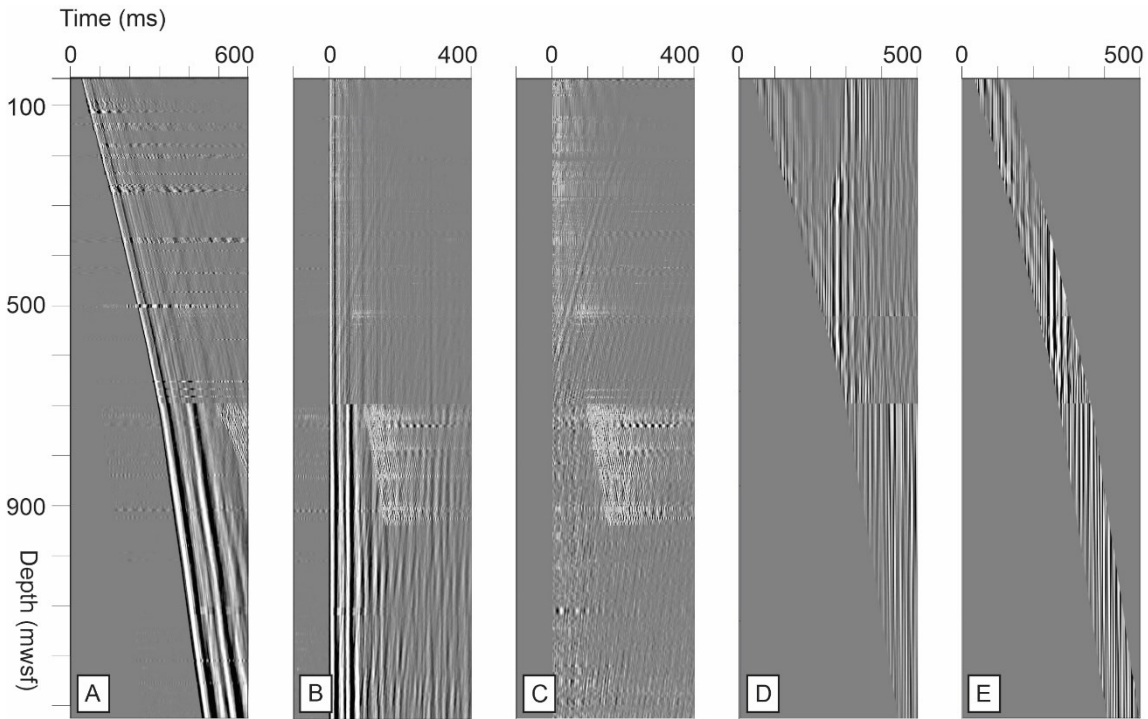


Figure A 12. VSP vertical component processing. a) Raw VSP data. b) Flattened VSP (Figure A 11f). c) Upgoing wavefield (Figure A 11h). d) Flattened reflection wavefield, post-F-K filter (Figure A 11k). e) Corridor mute (Figure A 11l).

The first arrival time data was fit with a 10<sup>th</sup> order polynomial in order to give a monotonically increasing function which was used to convert the TWT reflector profile into a depth axis which could be compared against real lithostratigraphy. The entire survey was then downshifted by twice the upshift amount in order to flatten the now separated reflected wavefield. Although the reflections are clearly discernible by eye, scattered energy within the peak ring makes discerning the exact origin of reflections difficult. Additionally, the aggressive removal of poorly coupled traces within the upper region of the VSP has made visual recognition of reflected wavelets difficult. In order to enhance visual recognizability of the

reflected wavefield, a vertical box rejection FK filter was applied (Figure A 11k). Other than subtle differences in the peak amplitudes, this did not affect the outcome of the finished product. In order to reduce the effect of multiples, a 100 ms corridor mute was applied prior to averaging all traces together (Figure A 12e). The resulting product is a single seismic trace in two-way travel time (TWT), (Figure 4.9c). When simply plotted versus depth, the first arrival travel times show 4 distinct linear trends with depth that display changes in slope that, including the water column, allow the structure to be divided into five average velocity zones as summarized in Table A 3. This simpler block structure is used in determining amplitude corrections later.

Velocity Zone	Depth Range mbsl	Average velocity m/s	Geology
1	0 - 13	1500	Seawater
2	13 – 293	2285 ± 14	Upper Cenozoic
3	293 - 603	2597 ± 4	Lower Cenozoic
4	603 - 738	2970 ± 21	Suevite
5	738 and below	4238 ± 11	Peak Ring

*Table A 3. Block velocity model derived from regression of linear segments of the transit time versus depth curve.*

### **Horizontal Components and Processing**

In addition to the vertical component geophone, each sonde contains two additional geophones with horizontal polarizations radial and tangential to the borehole axis. The true orientation of these cannot be controlled and without additional information from, say, offset source locations, cannot be unambiguously determined. As expected from the geometry of the experiment, the amplitudes observed in these are significantly reduced relative to the vertical component. The profiles for the two uncorrected horizontal components (Figure A 13) do, however, display the first arriving P-wave originating directly from the source: a distinct S-wave arrival S1 above the K-Pg contact likely due to

conversions at the sea-floor, a second, irregular, S-wave arrival S2 within the peak ring, and tube waves. The character of the wavefield also changes abruptly within the peak ring below 750 mbsf.

The greatest amplitudes observed in both the raw horizontal component panels of Figure 4.7 fall along the S1 and S2 trends and horizontal processing flow is shown in Figure A 14.

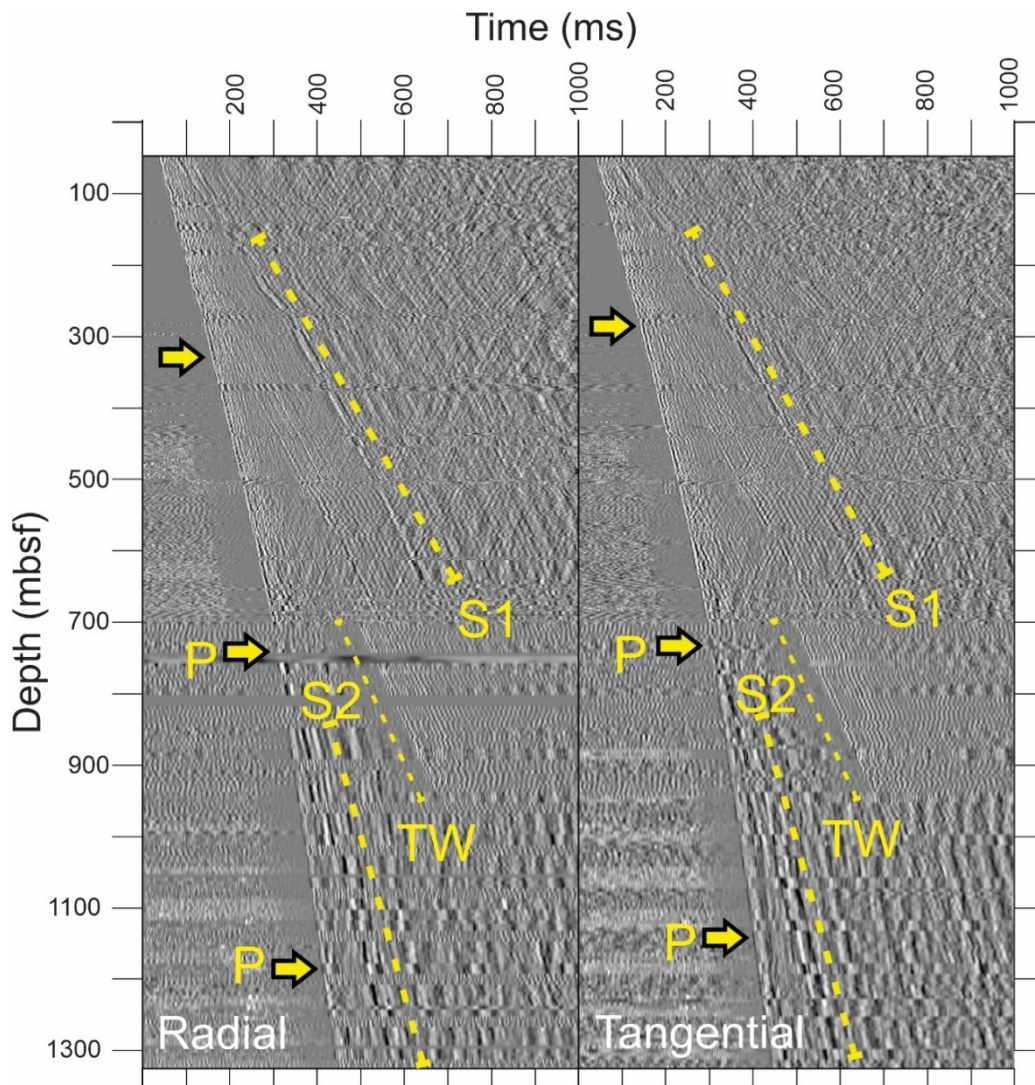


Figure A 13. Raw radial and tangential components. P: directly arriving P-wave, S1: S-wave originating from conversions near the sea floor, S2: Irregular S-wave arrival through the peak ring, TW: Tube wave. Each trace scaled by a 200 ms automatic gain control.



### Additional Information

Correlation coefficients between entire traces have been calculated for combinations of the real VSP and synthetic traces (Table A 4). As expected, the coefficient between the true VSP trace and both synthetics are fairly high, and the correlation between the real VSP and closest real line (CHIX17b) is higher than the other two lines. Owing to significant horizontal heterogeneity, the traces cannot be expected to correlate perfectly.

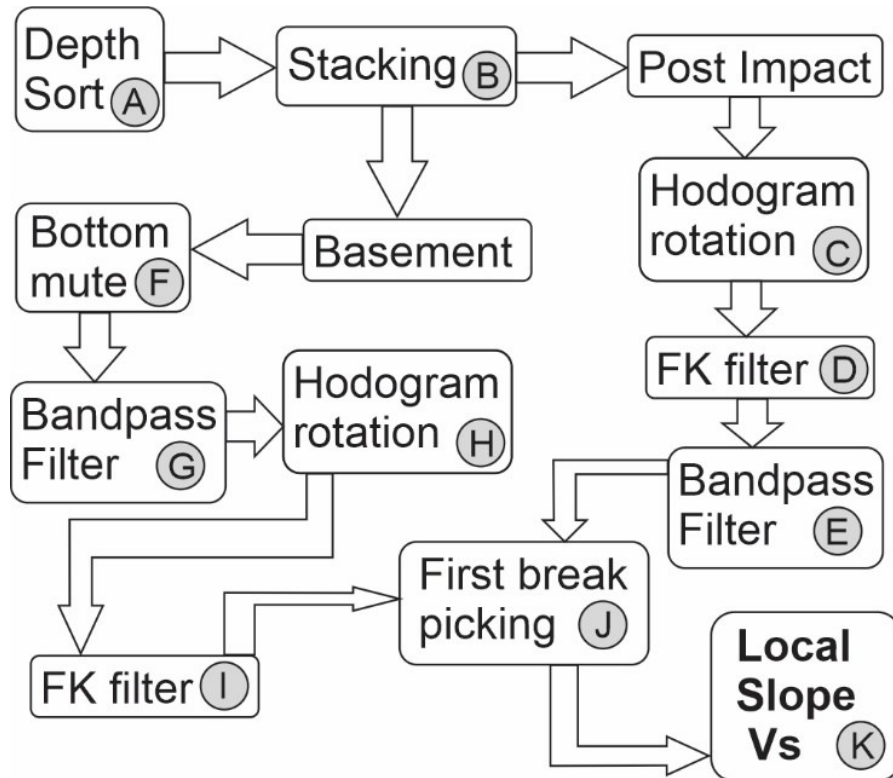


Figure A 14. Horizontal components processing flow. a,b) Traces sorted by approximate depth and stacked to improve SNR. c,d,e) Carbonate sediment specific processing: Hodogram algorithm first, then FK and bandpass filtering to enhance desired signal. f,g,h,i) Crystalline basement specific processing: High amplitude tube waves muted and Ormsby filter prior to hodogram algorithm. FK filters applied to enhance signal. j,k) First coherent extrema followed down through enhanced s-wave and local slope differential algorithm applied. Panel c) is expanded in Figure 4.7 in the main text.

	C VSP Real	D VSP Synthetic	E Surface Synthetic
C VSP Real	1		
D VSP Synthetic	0.6919	1	
E Surface Synthetic	0.5786	0.6647	1
F CHIX17b Real	0.4068	0.3127	0.2405
G CHIX10 Real	0.1802	0.2200	0.0407
H CHIXR3 Real	0.0174	0.1263	0.0576

Table A 4. Correlation coefficient values for entire traces compared against each other.

Acronym	Meaning	First Appearance
VSP	Vertical Seismic Profile	page 2, line 23
K-Pg	Cretaceous-Paleogene Boundary	page 6, line 95
STUC	Suevite-Transitional Unit Contact at 617.33 mbsf	page 9, line 140
LFR	Low Frequency and irregular Reflector	page 9, line 143
IODP	International Ocean Discovery Program	page 4, line 74
ICDP	International Continental scientific Drilling Program	page 4, line 74
GR	natural Gamma Radiation log	page 13, line 231
MSCL	Multi Sensor Core Logging	page 16, line 271
VRH	Voigt-Reuss-Hill	page 25, line 397
SED	carbonate SEDiments at 0-582 mbsf	page 15, figure 4 caption
LID	seismically stiff carbonate layer at 582-617.33 mbsf	page 14, line 249
LVZ	Low Velocity Zone at 617.33-705.5 mbsf	page 14, line 254
MELT	MELT sheet at 705.5-748 mbsf	page 15, line 266
PR	Peak Ring granitoid basement at 748 mbsf to total hole depth	page 15, line 266

Table A 5. Main text acronym reference.

## Acknowledgements

This research used samples and data provided by IODP. Samples can be requested at <http://web.iodp.tamu.edu/sdrm>. Expedition 364 was jointly funded by the European Consortium for Ocean Research Drilling (ECORD) and the International Continental Scientific Program, with contributions and logistical support from the Yucatan State Government and Universidad Nacional Autónoma de México (UNAM). The downhole seismic chain and wireline system is funded by grants to DRS from the Canada Foundation for Innovation and the Alberta Enterprise and Advanced Education Grants Program. Special thanks to Randy Kofman for his tireless expertise.

## **Appendix C - Supplementary Methods for Chapter 5.**

*An abbreviated version of the following methods has been published as:*

*Invited.* Nixon, C. G., & Schmitt, D. R. (2020). Windowed Cross Correlation Sweep to Extract Ultrasonic Waveforms from Noisy Data for Laboratory Velocities. Geoconvention, Calgary.

### **Ultrasonic Processing.**

The method described hereafter, which is an improvement over first break picking, worked for all the samples, but some worked better than others. The prototypical step by step results will be presented for sample 135r2, for which the method worked best. Final velocity results are shown in chapter 5 (Figure 5.7).

A software package (see section 6.4d) was developed to automatically sweep through the ultrasonic traces, beginning at 200 MPa where the signal is clearest. The user chooses a starting and finishing point for the window based on where the signal is at 200 MPa. The user also selects how many sample points will be used in the tapered ends of the Blackmann Harris window. The program then modulates the 200 MPa trace and runs a cross correlation from the 200 MPa trace with the next lowest pressure. Using the same window parameters. The window is then advanced by the time value associated with the central peak of the cross-correlation function and cross correlation is repeated for the next pair. Advancement of the modulation window by the previous iteration's peak value is repeated for every trace. The automatically windowed wavelets for P up, P down, S up, and S down are shown (Figure A 15a) as well as the corresponding correlation functions (Figure A 15b). As an additional quality control measure, the software averages all the windowed wavelets for the P and S. This was useful for adjusting initial window parameters for subsequent runs. In general, I tried to get the average as a "trough-peak-trough" with the peak in the center of the window. The average post-windowing wavelet is shown within the modulation envelope (Figure A 16).

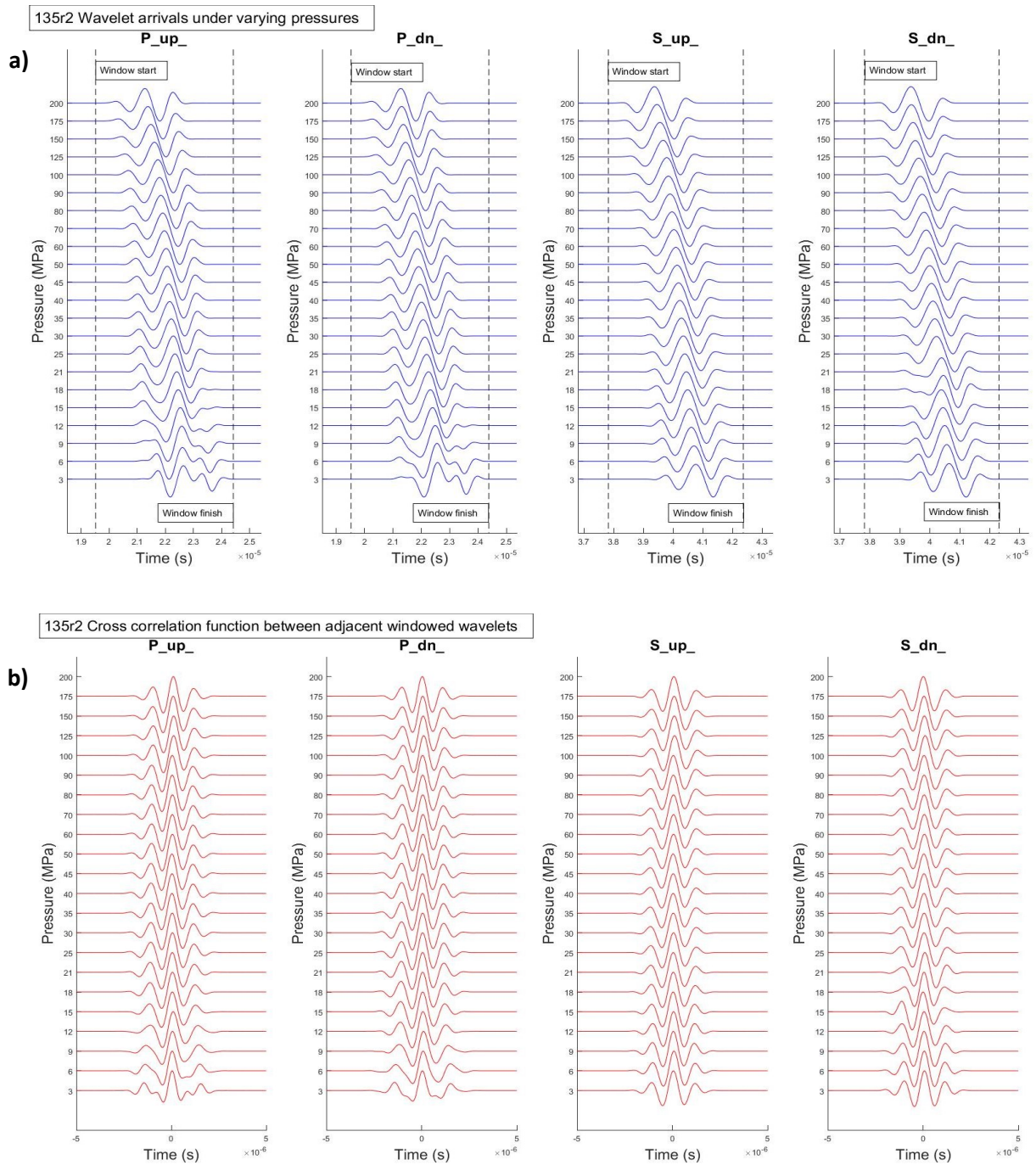


Figure A 15. a) Windowed wavelet arrivals for sample 135. Window varies from top to bottom. The start of the first window and finish of the last window are shown by dotted lines. b) Cross correlation functions using the advancing sweep method for sample 135.

After the automatic window advancement is completed, a broader fixed window is applied. The start and end times for this window are the user defined start time and the finish time at 3 MPa after the automatic cross correlation sweep is applied. The 200 MPa trace is then used as a reference and correlated with every other trace in the run. The wavelet averages from **Error! Reference source not found.** are also superimposed on this as a quality control measure (Figure A 17a). Cross correlations using the reference trace are also shown (Figure A 17b), but we note that the functions are not as crisp.

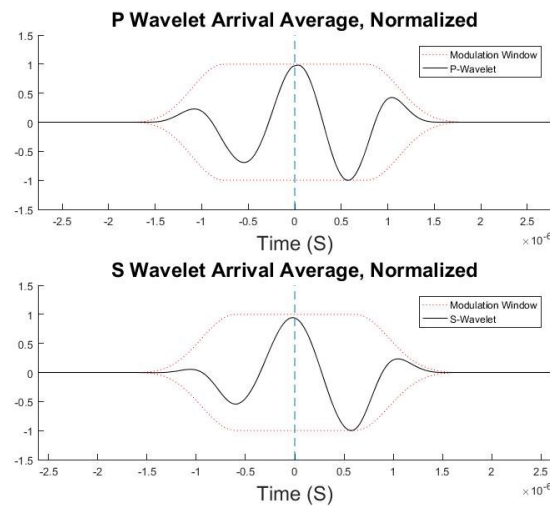


Figure A 16. P and S windowed wavelet averages.

The peak cross correlation value time is recorded as the “lag time” between traces and all 4 runs are shown compared for the adjacent pairs method (Figure A 18a). The lag times are also shown compared to the results for using a fixed reference trace (Figure A 18b). The results are similar, although the sweep method developed here gives smoother results and is clearly superior at low pressures with noise problems.

As the signal is quite clear at peak pressure, the velocity at 200 MPa was calculated via a hand picked first break. This first break amount was then advanced by the cross-correlation lag time for each trace to get subsequent velocities, with results shown for sample 135 (Figure A 19a) and all samples (Figure 5.7). Additionally, the shear velocities from the sweep method are shown compared to the more primitive

first break results (Figure A 19b). Although the sweep method is only a small improvement over simple first break picking for this sample, we must stress that the sample selected for this proof of concept analysis had by far the best data. Use of the sweep method is much more important in other samples with less clear wavelets at low pressure

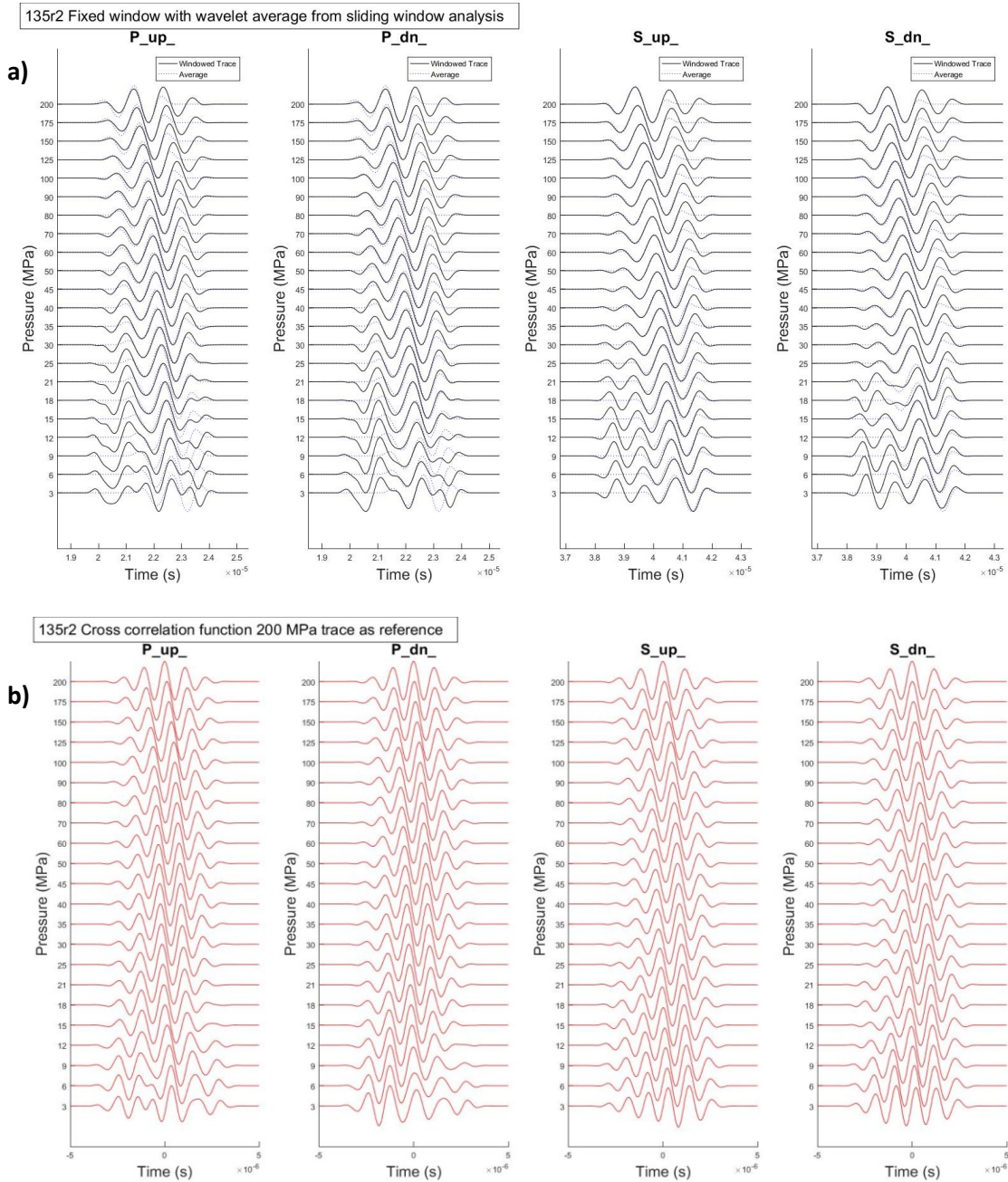


Figure A 17. a) Fixed window waveforms with average value from Figure A 16 superimposed. Sample 135.

b) Correlation functions for fixed window waveforms using a single reference trace.



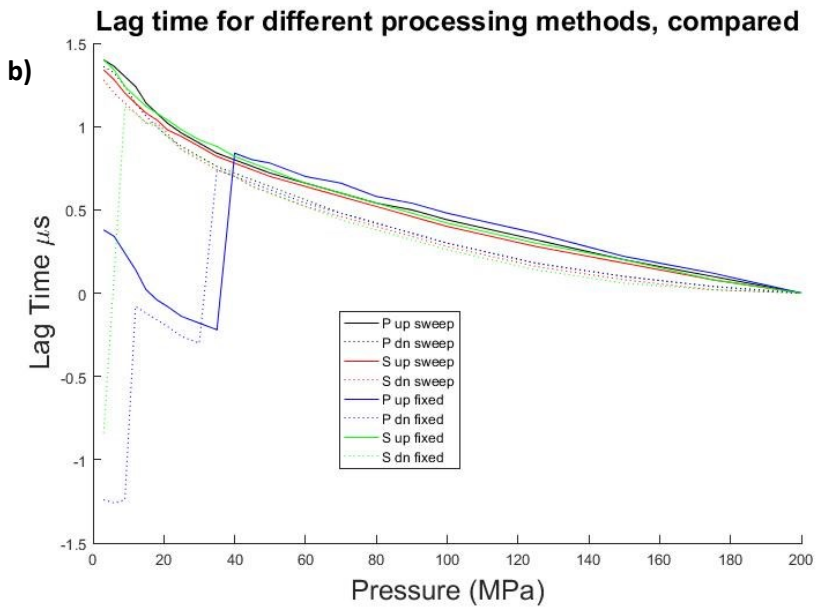
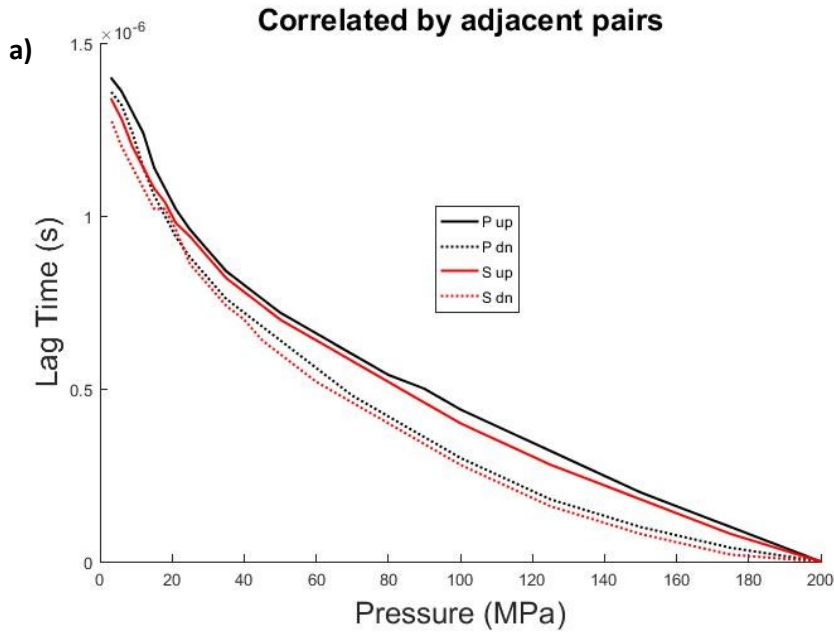


Figure A 18. a) Lag times from 200 MPa for each run. Sample 135. b) Lag times for sweep and fixed window processing methods compared. Sample 135.

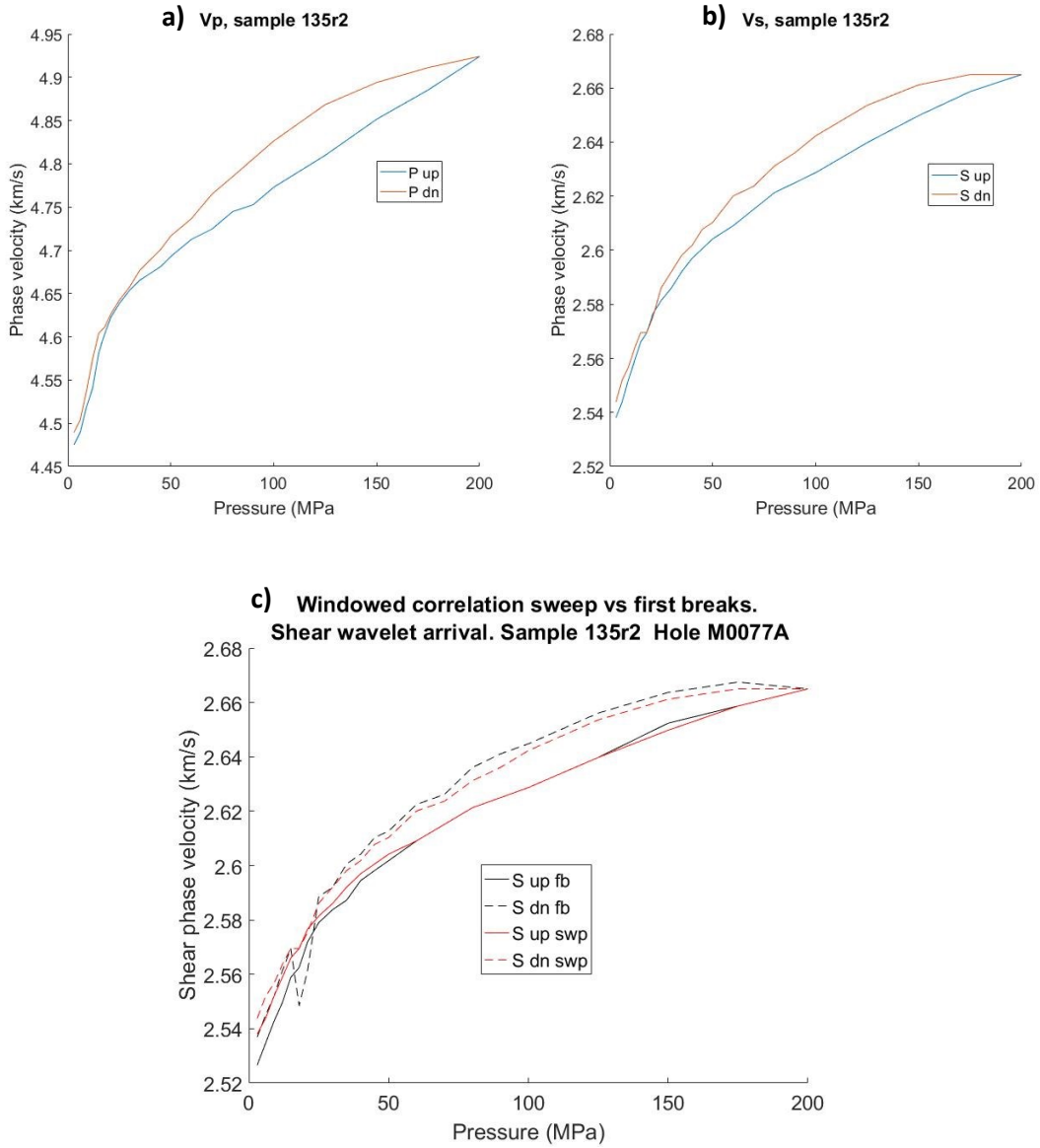


Figure A 19. a) Velocity results for sample 135 using the advancing window sweep method. Sample 135. b) c)  $V_s$  results for 135. First break and correlation sweep compared.



## Geological details

IGSN IBCR0364...	Core Number.	Depth (mbsf)	Geological Description
EXUM401	88r3	724.68- 724.76	Black melt with green schlieren that also entrains angular fragments of black melt. Target clasts include gneisses
EXNT401	94r2	742.37 – 752.37	Dark gray impact melt, clast poor. Partially digested basement clasts
EXDW401	95r3a	746.70- 746.78	Black melt with green schlieren and gneiss target clasts
EXCW401	95r3b	746.07 – 746.14	Large granite clast surrounded by impact melt. Up to 2cm orange feldspar
EXOY401	97r3	752.80 – 752.90	Coarse grained shock target granite, slightly fractured
EXTJ501	133r1	841.76 – 841.88	Coarse grained homogenous granite, k-feldspar up to 4cm. network of thin white veins
EXKK501	134r1	844.92 – 845.00	Coarse grained homogenous granite, k-feldspar up to 5cm. White fill shear fractures throughout
EXMM501	135r2	849.66– 849.76	Dolerite black to green with up to 1 cm rounded aggregates (Looks like Melt)
EX2O501	140r1	853.97 – 854.07	Greenish dolerite, pervasively veined, dark grey to black veins
EXTT501	147r1	874.72 – 874.81	Coarse grained granite, weakly deformed epidote veins. Knot of biotite.
EXIX501	155r2	900.97 – 901.06	Coarse grained homogenous granite, K-Feldspar grains up to 3 cm
EX12601	162r1	912.95- 913.05	Dolerite, near contact with granitoid. Several subhorizontal shearbands.
EXK9601	171r2	941.49 - 941.59	Coarse grain size granite, strongly deformed and altered. Parallel fractures and filled with fine cataclasite veins
EXMF601	181r2	964.75 - 964.84	Homogenous coarse grained granite, K-feldspar up to 3 cm.
EX07701	227r2	1102.39 – 1102.47	Coarse grained granite with subvertical shear and dilational fracturing.
EXW3901	276r3	1251.42 – 1251.49	Melt poor polymictic suevite. Gneiss, granite and schist clasts.
EXJ5901	277r3	1255.31– 1255.38	Highly polymict suevite. Clasts include highly deformed granite, clast rich impact melt rock, gneiss, dolerite.
EXGB901	287r1	1283.79 – 1283.89	Suevite dominated by granite clasts.
EXWC901	288r2	1288.42 – 1288.48	Polymict breccia suevite. Granite, Gneiss and melt clasts.
EXAN901	300r2	1324.24– 1324.32	Strongly deformed coarse grained granite, distinctly different species from others in study. Grains up to 1cm.

Table A 6. Sample depths and geological interpretations.

Core no.	Minerals by volume fraction.									
88	Albite	Diopside	Sanidine	Basanite	Saponite					
	32	13	22	18	15					
94	Quartz	Cristobalite	Anorthite	Ferrosilite	Gypsum	Sanidine	Magnetite	Forsterite	Corundum	Saponite
	5	2	36	9	1	11	4	4	2	24
95	Quartz	Orthoclase	Andesite	Nepheline	Saponite					
	7	11	56	5	22					
97	Quartz	Albite	Microcline	Calcite	Muscovite	Phlogopite	Kaolinite			
	23	47	11	1	6	10	2			
133	Quartz	Albite	Microcline	Annite	Clinochlore					
	33	27	35	1	3					
134	Quartz	Microcline	Sanidine	Nimite	Calcite	Muscovite	Phlogopite			
	28	22	30	8	1	8	3			
135	Anorthite	Augite	Cristobalite	Natrolite	Saponite	Biotite	Clinochlore			
	26	31	2	1	19	2	19			
140	Albite	Anorthite	Talc	Diopside	Saponite	Phlogopite	Nimite			
	18	12	5	12	21	5	26			
147	Quartz	Albite	Microcline	Illite	Nimite					
	26	29	14	22	9					
155	Quartz	Albite	Microcline	Ankerite	Biotite	Clinochlore				
	28	34	23	1	10	4				
162 (used 163)	Quartz	Albite	Microcline	Calcite	Phlogopite	Clinochlore				
	28	34	16	1	13	7				
171	Albite	Anorthite	Aerinite	Paragonite	Chamosite					
	22	16	29	13	10					
181	Quartz	Albite	Microcline	Phlogopite	Clinochlore					
	51	14	16	16	3					
227	Quartz	Albite	Microcline	Cristobalite	Ferrierite	Calcite	Anorthoclase	Sodalite	Muscovite	Clinochlore
	45	10	13	1	4	1	16	1	6	4
276	Quartz	Albite	Microcline	Biotite						
	46	27	15	12						
277	Quartz	Albite	Ferrosilite	Saponite	Chlorite					
	54	18	7	9	11					
287	Quartz	Albite	Microcline	Aerinite	Biotite	Lizardite				
	22	36	25	4	10	2				
288	Quartz	Albite	Microcline	Saponite	Annite	Chlorite				
	14	66	13	1	3	3				
300	Quartz	Albite	Microcline	Calcite	Annite	Vermiculite				
	40	38	18	1	2	1				

Table A 7. Mineralogy from Expedition 364 Onshore Science Party.

## Appendix D - Publications

The research conducted for this thesis forms part of the international research collaboration IODP Expedition 364, led by Professor S.P.S. Gulick at the University of Texas, Institute of Geoscience and J.V. Morgan at Imperial College, London, with Professor D.R. Schmitt being the lead collaborator at the University of Alberta. I provide here an overview of the publications contributed from the work described in this thesis as well as my contribution to the Aquistore CO<sub>2</sub> Sequestration project that required significant effort but is not presented here.

### Peer Reviewed Publications (First Author)

C. Nixon, Schmitt, D., Kofman, R., Lofi, J., Gulick, S., Saustrup, S., Christeson, G., and Kring, D., (2022). Borehole Seismic Observations from the Chicxulub Impact Drilling: Implications for Seismic Reflectivity and Impact Damage. *In press at Geochemistry, Geophysics, and Geosystems.*

*Nixon was primarily responsible for data analysis and manuscript composition. Schmitt was the supervisory author, assisting conceptualization and manuscript composition. Lofi was primarily responsible for initial processing and manuscript composition regarding sonic logging. Nixon, Schmitt, Kofman, Lofi, Gulick, and Saustrup were responsible for offshore data acquisition. All authors were involved with manuscript edits. This manuscript is reproduced here as chapter 4.*

C. Nixon, R. Kofman, D. Schmitt, S. Gulick, G. Christeson, S. Saustrup, J. Lofi, and J. Morgan, (2020). Assessment of Rock Damage Using Seismic Methods: Wave Speeds and Attenuation from Borehole Measurements in the Chicxulub Impact Structure. *54th US Rock Mechanics/Geomechanics Symposium*, OnePetro.

[onepetro.org/ARMAUSRMS/proceedings-abstract/ARMA20/All-ARMA20/ARMA-2020-1307/447518](https://onepetro.org/ARMAUSRMS/proceedings-abstract/ARMA20/All-ARMA20/ARMA-2020-1307/447518)

*Nixon was primarily responsible for data analysis and manuscript composition. Schmitt was the supervisory author, assisting conceptualization and manuscript composition. Nixon, Schmitt, Kofman, Lofi, Gulick, and Saustrup were responsible for offshore data acquisition. All authors were involved with manuscript edits. This manuscript is reproduced here as chapter 3.*

## Peer Reviewed Publications (Contributing Author)

A. Stork, C. Nixon, C. Hawkes, C. Birnie, D. White, D. Schmitt, and B. Roberts, (2018). Is CO<sub>2</sub> injection at Aquistore aseismic? A combined seismological and geomechanical study of early injection operations. *International Journal of Greenhouse Gas Control*, 75, 107-124.

[doi.org/10.1016/j.ijggc.2018.05.016](https://doi.org/10.1016/j.ijggc.2018.05.016)

*Nixon was responsible for downhole data collection & analysis, and contributed to manuscript composition & edits.*

G. Christeson, S. Gulick, J. Morgan, C. Gebhardt, D. Kring, E. Le Ber, J. Lofi, C. Nixon, M. Poelchau, A. Rae, M. Rebolledo-Vieyra, U. Riller, D. Schmitt, A. Wittmann, J. Bralower, E. Chenot, P. Claeys, C. Cockell, and K. Yamaguchi, (2018). Extraordinary rocks from the peak ring of the Chicxulub impact crater: P-wave velocity, density, and porosity measurements from IODP/ICDP Expedition 364. *Earth and Planetary Science Letters*, 495, 1-11.

[doi.org/10.1016/j.epsl.2018.05.013](https://doi.org/10.1016/j.epsl.2018.05.013)

*Nixon was responsible for offshore downhole seismic data collection & analysis, and contributed to core processing during the 1-month Onshore Science Party, as well as manuscript edits.*

J. Lofi, D. Smith, C. Delahunty, E. Le Ber, L. Brun, G. Henry, J. Paris, S. Tikoo, W. Zylberman, P. Pezard, B. Célérier, D. Schmitt, C. Nixon, and Expedition 364 Science Party, (2018). Drilling-induced and logging-related features illustrated from IODP–ICDP Expedition 364 downhole logs and borehole imaging tools. *Scientific Drilling*, 24, 1-13.

[doi.org/10.5194/sd-24-1-2018](https://doi.org/10.5194/sd-24-1-2018)

*Nixon was responsible for offshore downhole seismic data collection & analysis, and contributed to manuscript edits.*

D. White, K. Harris, L. Roach, B. Roberts, K. Worth, A. Stork, C. Nixon, D. Schmitt, T. Daley, and C. Samson, (2017). Monitoring results after 36 ktonnes of deep CO<sub>2</sub> injection at the Aquistore CO<sub>2</sub> Storage Site, Saskatchewan, Canada. *Energy Procedia*, 114, 4056-4061.

[doi.org/10.1016/j.egypro.2017.03.1546](https://doi.org/10.1016/j.egypro.2017.03.1546)

*Nixon was responsible for downhole data collection & analysis.*

## Peer Reviewed Publications (Contributed)

J. Morgan, S. Gulick, T. Bralower, E. Chenot, G. Christeson, P. Claeys, C. Cockell, G. Collins, M. Coolen, L. Ferrière, C. Gebhardt, K. Goto, H. Jones, D. Kring, E. Le Ber, J. Lofi, X. Long, C. Lowery, C. Mellet, R. Ocampo-Torres, G. Osinski, L. Perez-Cruz, A. Pickersgill, M. Poelchau, A. Rae, C. Rasmussen, M. Rebolledo-Vieyra, U. Riller, H. Sato, D. Schmitt, J. Smit, S. Tikoo, N. Tomioka, J. Urrutia-Fucugauchu, M. Whalen, A. Wittmann, K. Yamaguchi, and W. Zylberman, (2016). The formation of peak rings in large impact craters. *Science*, 354(6314), 878-882.

[DOI:10.1126/science.aah6561](https://doi.org/10.1126/science.aah6561)

*Nixon was not credited as an author here and was responsible for offshore downhole seismic data collection & analysis used in figure 2, and contributed to core processing throughout the 1-month Onshore Science Party used in figures 2 & 3.*

## Technical Reports

D. Schmitt, C. Nixon, and R. Kofman, (2019). Borehole Seismic Monitoring Experiments to nearly 3 km depth at the Aquistore CO2 Sequestration Site, Estevan, Saskatchewan. *Aquistore carbon sequestration project*. Estevan, SK.

J. Morgan, S. Gulick, C. Mellett, and the Expedition 364 Scientists, (2017). Proceedings of the International Ocean Discovery Program. Volume 364 Chicxulub: Drilling the K-Pg Impact Crater. *International Ocean Discovery Program*. Bremen, GE. <https://doi.org/10.14379/iodp.proc.364.2017>

*Nixon contributed to offshore downhole seismic data collection, provided downhole seismic analysis, contributed to manuscript composition in the downhole logging section of the Methods, Open Hole, Post-Impact Sedimentary Rocks, Upper Peak-Ring, and Lower Peak Ring chapters, was solely responsible for figures F4, F5, F15, F27, F28, F31, F33, F34, & F47, and contributed to core processing throughout the 1-month Onshore Science Party. Nixon is credited in this report as a “vertical seismic profile and logging contractor”.*

S. Gulick, J. Morgan, C. Mellett, and the Expedition 364 Scientists, (2016) International Ocean Discovery Program Expedition 364 Preliminary Report Chicxulub: drilling the K-Pg impact crater. *International Ocean Discovery Program*. Bremen, GE. <https://doi.org/10.14379/iodp.pr.364.2017>

*Nixon contributed to offshore downhole seismic data collection, provided downhole seismic analysis, contributed to manuscript composition in the downhole logging section, was solely responsible for figure F14, and contributed to core processing throughout the 1-month Onshore Science Party. Nixon is credited in this report as a “vertical seismic profile contractor”.*

## Conference Abstracts (First Author)

C. Nixon, D. Schmitt, B. King, and R. Kofman, (2020). Laboratory measurements of porosity parameterization and wavespeed dependence under confining pressure up to 200 MPa in shocked Chicxulub peak-ring granitoids. *AGU Fall Meeting*, Virtual. <https://ui.adsabs.harvard.edu/abs/2020AGUFMMR0160013N/abstract>

*Invited.* C. Nixon and D. Schmitt, (2020). Windowed Cross Correlation Sweep to Extract Ultrasonic Waveforms from Noisy Data for Laboratory Velocities. *CSEG Geoconvention*, Virtual. <https://geoconvention.com/wp-content/uploads/abstracts/2020/57986-seismic-characterization-and-laboratory-analysis-o.pdf>

C. Nixon, B. King, R. Kofman, E. Walton, M. Poelchau, and D. Schmitt, (2018). Nonlinear Seismic Wavespeeds Under Confining Pressure up to 200 MPa for Shocked Granitoids of the Chicxulub Impact Basin Peak Ring and Anisotropy Investigations. *AGU Fall Meeting*, Washington, DC. <https://ui.adsabs.harvard.edu/abs/2018AGUFMPP51D1168N/abstract>

C. Nixon, B. King, R. Kofman, and D. Schmitt, (2018). Shock metamorphosed Granite of the Chicxulub Impact Basin and very low seismic velocities: A case study. *CSEG Geoconvention*, Calgary, AB. [https://geoconvention.com/wp-content/uploads/abstracts/2018/189\\_GC2018\\_Shock\\_metamorphosed\\_Granite\\_of\\_Chicxulub\\_Impact\\_Basin.pdf](https://geoconvention.com/wp-content/uploads/abstracts/2018/189_GC2018_Shock_metamorphosed_Granite_of_Chicxulub_Impact_Basin.pdf)

C. Nixon, D. Schmitt, R. Kofman, and D. White, (2017). Technical Descriptions in Long-term 115°C Borehole Digital Micro-seismic Monitoring at the PTRC Aquistore CO2 Sequestration Project. *79th EAGE Conference and Exhibition*, Paris, France. <https://www.earthdoc.org/content/papers/10.3997/2214-4609.201701661>

*Invited.* C. Nixon, R. Kofman, D. Schmitt, J. Lofi, S. Gulick, G. Christeson, S. Sastrup, J. Morgan, (2017). High Resolution Vertical Seismic Profile from the Chicxulub IODP/ICDP Expedition 364 Borehole: Wave Speeds and Seismic Reflectivity. *AGU Fall Meeting*, New Orleans, LA. <https://ui.adsabs.harvard.edu/abs/2017AGUFM.P33D2909N/abstract>

C. Nixon, D. Schmitt, R. Kofman, D. White, A. Stork, M. Kendall, and K. Worth, (2017). *Experiences in Deep Downhole Digital Micro-seismic Monitoring near 3 km at the PTRC Aquistore CO2 Sequestration Project*. *CSEG Geoconvention*, Calgary, AB. [https://geoconvention.com/wp-content/uploads/abstracts/2017/303\\_GC2017\\_Experiences\\_in\\_Deep\\_Downhole\\_Digital\\_Micro-seismic\\_Monitoring.pdf](https://geoconvention.com/wp-content/uploads/abstracts/2017/303_GC2017_Experiences_in_Deep_Downhole_Digital_Micro-seismic_Monitoring.pdf)

C. Nixon, R. Kofman, D. Schmitt, S. Gulick, S. Sastrup, and J. Morgan, (2017). Vertical Seismic Profiling of the Chicxulub Impact Basin Peak Ring. *CSEG Geoconvention*, Calgary, AB. [https://geoconvention.com/wp-content/uploads/abstracts/2017/308\\_GC2017\\_Vertical\\_Seismic\\_Profiling\\_of\\_Chicxulub\\_Impact\\_Basin\\_Peak\\_Ring.pdf](https://geoconvention.com/wp-content/uploads/abstracts/2017/308_GC2017_Vertical_Seismic_Profiling_of_Chicxulub_Impact_Basin_Peak_Ring.pdf)

## Conference Abstracts (Contributing Author)

M. Unsworth, J. Chira, R. Yupa, Y. Antayhua-Vera, D. Calla-Pilco, B. Garcia, F. Baca, B. Lee, C. Nixon, D. Ramos-Palomino, and C. Valencia-Miraval, (2018). Magnetotelluric studies of the Andean subduction zone in southern Peru. *AGU Fall Meeting*, Washington, DC. <https://ui.adsabs.harvard.edu/abs/2018AGUFM.T31H0402U/abstract>

S. Gulick, J. Morgan, T. Bralower, E. Chenot, G. Christeson, P. Claeys, C. Cockell, M. Coolen, L. Ferrière, C. Gebhardt, K. Goto, S. Green, H. Jones, D. Kring, J. Lofi, C. Lowery, R. Ocampo-Torres, L. Perez-Cruz, A. Pickersgill, M. Poelchau, A. Rae, C. Rasmussen, M. Rebolledo-Vieyra, U. Riller, H. Sato, D. Schmitt, J. Smit, S. Tikoo, J. Urrutia-Fucugauchi, A. Wittmann, L. Xiao, K. Yamaguchi, J. Vellekoop, C. Neal, K. Grice, J. Ormö, J. Melosh, G. Collins, F. Rodríguez-Tovar, G. Osinski, D. Stockli, M. Schmieder, J. Snedden, K. Freeman, B. Hall, V. Smith, R. Grieve, C. Koeberl, S. Goderis, C. Nixon, V. Vajda, S. Warny, F. Schulte, N. Artemieva, A. Sluijs, N. McCall, B. Schaefer, A. Diaw, S. Lyons, K. O'Malley, J. Gattacceca, Y. Quesnel, C. Ross, J. Feignon, and Z. Zhu, (2018). Insights into impact processes and extinction mechanisms from IODP-ICDP Chicxulub crater drilling. *Geological Society of America Annual Meeting*, Indianapolis, IN. <https://lirias.kuleuven.be/2327066?limo=0>

G. Christeson, C. Gebhardt, S. Gulick, E. Le Ber, J. Lofi, J. Morgan, C. Nixon, A. Rae, and D. Schmitt (2017). Unusual physical properties of the Chicxulub crater peak ring: Results from IODP/ICDP Expedition 364. *AGU Fall Meeting*, New Orleans, LA. <https://ui.adsabs.harvard.edu/abs/2017AGUFM.P23H..02C/abstract>

B. King, C. Nixon, R. Kofman, and D. Schmitt, (2017). Quantitative Characterization of Chicxulub Impact Basin Peak Ring Materials. *AGU Fall Meeting*, New Orleans, LA. <https://ui.adsabs.harvard.edu/abs/2017AGUFM.P33D2910K/abstract>

C. Gebhardt, L. Perez-Cruz, E. Chenot, G. Christeson, E. Le Ber, J. Lofi, C. Nixon, and A. Rae, (2017). Preliminary Results From the Chicxulub Post-Impact Sediments: XRF and Physical Properties Data. *AGU Fall Meeting, New Orleans, LA*. <https://ui.adsabs.harvard.edu/abs/2017AGUFMPP23B1304G/abstract>

G. Christeson, C. Gebhardt, S. Gulick, E. Le Ber, J. Lofi, J. Morgan, C. Nixon, A. Rae, D. Schmitt, and IODP-ICDP Expedition scientists, (2017). Physical Properties of the Chicxulub Impact Breccia Drilled at IODP/ICDP Expedition 364 Hole M0077A. *Lunar and Planetary Science Conference*, The Woodlands, TX. <https://ui.adsabs.harvard.edu/abs/2017LPI....48.1444C/abstract>

A. Stork, C. Nixon, D. Schmitt, D. White, J. Kendall, and K. Worth, (2016). The seismic response at the Aquistore CO2 injection project, Saskatchewan, Canada. *Seismological Society of America Annual Meeting*, Reno, NV. [doi-org.login.ezproxy.library.ualberta.ca/10.1785/0220160046](https://doi.org/login.ezproxy.library.ualberta.ca/10.1785/0220160046)

D. Schmitt, C. Nixon, R. Kofman, D. White, and K. Worth, (2015). A Borehole Seismic System for Active and Passive Seismic Studies to 3 KM at Ptrc's Aquistore Project. *AGU Fall Meeting*, San Francisco, CA. <https://ui.adsabs.harvard.edu/abs/2015AGUFM.S21A2669S/abstract>

## Appendix E - IODP 364 OSP Logo Contest Entry

During the Post Cruise Onshore Science Party in Bremen, attendants were invited to submit a logo design for custom made T-shirts. Below is my entry (Figure A 20).



Figure A 20. Onshore Science Party T-Shirt Logo Contest Entry.